Optimization and coupling of perovskite nanocrystals with optical nanofibers for efficient integrated single-photon sources

Marianna d'Amato

THÈSE DE DOCTORAT
DE SORBONNE UNIVERSITÉ

Spécialité : Physique

École doctorale nº564: Physique en Île-de-France

réalisée au

Laboratoire Kastler Brossel
Physique quantique et applications

sous la direction de Alberto BRAMATI

présentée par

Marianna D'AMATO

pour obtenir le grade de :

DOCTEUR DE SORBONNE UNIVERSITÉ

Sujet de la thèse :

Optimization and coupling of perovskite nanocrystals with optical nanofibers for efficient integrated single-photon sources

soutenue le 13 Décembre 2023

devant le jury composé de :

Pr.	Jean-François ROCH	Rapporteur
Pr.	Nicolas JOLY	Rapporteur
Pr.	Maria CHAMARRO	Présidente de jury
MCF.	Carole DIEDERICHS	Examinatrice
Dr.	Marco BELLINI	Examinateur
Pr.	Alberto BRAMATI	Directeur de thèse
MCF.	Loïc LANCO	Membre invité

Contents

List of Figures

Nomenclature

ADC Analog-to-Digital Converter

APD Avalanche Photodiode

BBO Barium Borate

BEBID Blurred Electron Beam Induced Deposition

BS Non-polarizing Beamsplitter

CB Conduction Band

CCD Charge-Coupled Device

CEW Central Emission Wavelength

CFD Constant Fraction Discriminator

CW Continuous-Wave

DM Dichroic Mirror

DOS Density of Optical States

EDS Energy Dispersive X-ray Spectroscopy

FDTD Finite-Difference Time-Domain

FLID Fluorescence Lifetime-Intensity Distribution

FWHM Full Width at Half Maximum

GeV Germanium-Vacancy

GIS Gas Injection System

HBT Hanbury Brown and Twiss

HOM Hong, Ou, and Mandel

HRTEM High-Resolution Transmission Electron Microscopy

IR Infrared

KDP Potassium Dideuterium Phosphate

LDOS Local Density of Optical States

LED Light Emitting Diode

LHP Lead Halide Perovskite

NA Numerical Aperture

NC Nanocrystal

NIR Near Infrared

NV Nitrogen-Vacancy

OA Oleic Acid

OAm Oleylamine

ODE Octadecene

ONF Optical Nanofiber

PBS Polarizing Beamsplitter

PD Photodiode

PEI Polyethylenimine

PL Photoluminescence

PLQY Photoluminescence Quantum Yield

POT Plasma Oxygen Treatment

QD Quantum Dot

QIPC Quantum Information Processing and Computation

QY Quantum Yield

sCMOS Scientific Complementary Metal-oxide Semiconductor

SEM Scanning Electron Microscopy

SiV Silicon-Vacancy

SPDC Spontaneous Parametric Down Conversion

SPS Single-Photon Source

STEM-HAADF High-Angle Annular Dark-Field Scanning Transmission Electron Microscopy

SYNC Synchronization

TAC Time-to-Amplitude Converter

TCSPC Time-Correlated Single Photon Counting

TE Transverse Electric

TEM Transmission Electron Microscope

TM Transverse Magnetic

TTTR Time-Tagged Time-Resolved

UV Ultraviolet

VB Valence Band

VBM Valence Band Maximum

WLED White Light-Emitting Diode

WP Wave Plate

XRD X-ray Diffraction

Acknowledgments

This work was conducted at the Laboratoire Kastler Brossel (Paris, France), affiliated with Sorbonne Université, École Normale Supérieure, Collège de France, and the Centre national de la recherche scientifique (CNRS). First, I would like to thank the director, Prof. Antoine Heidmann, for welcoming me in such a great and inspiring working environment.

I am deeply thankful to my supervisor, Prof. Alberto Bramati, for his guidance throughout these three years and for the confidence he has placed in me. I am grateful for his scientific insight, availability, encouragement, and the numerous opportunities he has provided me, which have allowed me to work on diverse projects across different laboratories. This experience has been incredibly enriching.

My thesis was primarily funded by the ANR project IperNano^2, in collaboration with the Institut des NanoSciences de Paris (INSP). Spending nearly 20% of my time at INSP, I extend my thanks to Dr. Emmanuel Lhuillier for granting me access to the necessary research facilities and for his trust in me. My time at INSP equipped me with valuable knowledge and skills in chemistry and as a researcher, enhancing my scientific method and rigor.

A second part of my PhD was funded by the European project Nanobright in collaboration with the Istituto Italiano di Tecnologia in Italy. I am grateful to Dr. Ferruccio Pisanello for warmly welcoming me in Lecce and for his advice and encouragement. Working in his team was a wonderful experience.

Lastly, I extend my thanks to Prof. Cesare Soci of the Nanyang Technological University of Singapore and PhD student Qi Ying, with whom I had the pleasure of collaborating in the second part of my doctoral studies.

Working within this extensive network, where I met numerous researchers and PhD students, was significant and provided me with the opportunity to witness different aspects and visions of the scientific working process, acquire extensive knowledge,

and ensure interdisciplinary aspects in my thesis.

I would like to thank Pr. Jean François Roch and Pr. Nicolas Joly for reviewing my thesis, and Pr. Maria Chamarro, MCF Carole Diederichs, Dr. Marco Bellini, and MCF Loïc Lanco for being part of my jury. I am grateful to all of them for their careful attention to my research.

I express my gratitude to all my research group, which has grown over time, for accompanying me on this journey. In particular, I thank MCF Quentin Glorieux for his interest in my work and his motivation, as he carefully instills in us the best practices in science and scientific ethics and always encourages us to improve. I also extend my gratitude to Dr. Hanna Le Jeannic, who joined our group in my third year as a permanent member, for her enthusiasm, numerous scientific and personal advices, her attention, and her precious help during the writing process of articles and the thesis.

A special thanks to postdocs Dr. Chengjie Ding and Dr. Antonio Balena, with whom I spent a significant part of these years, and who have not only been the best colleagues one could wish for but also sincere friends whom I greatly cherish.

I would like to thank Althéa Housset and Lucien Belzane, former interns of the team and now doctoral students, for the time spent together transferring knowledge and advancing research. I am very optimistic about the future of this team!

Finally, I am grateful to many people outside of work, especially all the friends I have met during my time abroad here in France, who have become my family in Paris. I like the person I am becoming while living here.

Introduction

In his pioneering lecture *There's Plenty of Room at the Bottom: An Invitation to Enter a New Field of Physics* [1] at the California Institute of Technology on December 29, 1959, Richard Feynman envisioned the potential of manipulating matter at the nanoscale. While the term *nanotechnology* had yet to be coined, his ideas paved the way for the emergence of this field in the 1980s.

Over the past few decades, there has been a revolution in this domain, which has opened up entirely new avenues for exploring and harnessing quantum mechanical effects at atomic scale. The classical theories of information and computation, although highly successful, are insufficient for describing processes at the atomic and molecular level. In response to these scientific and technological challenges, Quantum Information Processing and Computation (QIPC) has emerged [2], finding applications in quantum communication [3, 4], in quantum metrology and sensing [5, 6], and in quantum computing [2].

Building blocks of QIPC are the quantum bits or *qubits*. Unlike classical bits, which can exist in one of two states (0 or 1), the qubit encodes the information in a superposition of states, denoted as $|\psi\rangle$:

$$|\psi\rangle = \alpha\,|0\rangle + \beta\,|1\rangle \tag{0.1}$$

where α and β correspond to amplitudes satisfying the condition $|\alpha|^2 + |\beta|^2 = 1$.

Various physical implementations for encoding the quantum information are under exploration, with each of them offering distinct advantages. These include atoms and ions [7] known for their long memory times and high gate fidelity, superconducting circuits [8] valued for their reconfigurability and speed, and defects in solids [9] known for their ease of operation.

Among the various options, photons are particularly promising as *flying qubits*. They allow the quantum information to be easily stored and encoded in their vari-

ous degrees of freedom, such as in photon polarization states or spatial paths, and they can be easily manipulated and detected. Weakly interacting with the environment, photons do not suffer from decoherence as matter-based qubits systems, and consequently do not require cryogenic operation and high vacuum conditions. Moreover, they offer a natural interface with optical telecommunications, as they can be transmitted over 100 km using fibers.

The quest for the ideal single-photon source (SPS), capable of emitting a single photon at a time in a pure quantum state, holds great promise for advancing quantum information processing and technology. In particular, solid-state SPSs offer the advantage of on-demand single photon generation, unlike heralded single photon sources. Furthermore, these SPSs, which resemble atom-like systems with discrete energy levels within their bandgap, are intriguing due to their superior brightness compared to atoms and ions. Among solid-state SPS options, promising candidates include organic molecules [10, 11] color centers in diamonds [12, 13], and epitaxially-grown [14] and colloidal quantum dots (QDs) [15]. Notably, the 2023 Nobel Prize in Chemistry has been awarded to Moungi G. Bawendi, Louis E. Brus, and Alexei Ekimov [16] for their pioneering works for the fabrication and development of colloidal QDs.

Colloidal QDs typically possess sizes that are smaller than or comparable to the bulk semiconductor's electron, hole, and/or exciton Bohr radii. As a result, they exhibit quantum confinement effects, which, in turn, results in size-dependent electronic and optical properties. Their distinctive characteristics make them versatile, finding applications in biology as optical materials for luminescent probes and in various light-emission applications.

Recently, colloidal QDs have emerged as platforms for quantum information science [17], answering essential demands like single-photon emission and optical coherence. Furthermore, their potential integration into nanophotonic devices like microcavities [18], waveguides [19], plasmonic resonators [20], and microlenses [21] represents a significant step towards the realization of compact, hybrid and efficient SPSs. However, they often display fluorescence intermittency, known as *blinking*, or permanent loss of emission due to degradation, referred to as *bleaching*. These issues pose challenges in their practical use.

Among various types of colloidal QDs, lead halide perovskite (LHP) nanocrystals (NCs) of the form $APbX_3$, (with A = $CH_3NH_3^+$ (referred to as MA), Cs^+, or $HC(NH_2)_2^+$ (referred to as FA), and X = Cl^-, Br^-, or I^-), have recently captured

the attention of the quantum optics community. Perovskite materials had already gained recognition for their remarkable performance in photovoltaics and various optoelectronic applications, including their use in light-emitting diodes [22]. In 2015, a significant milestone was reached with the successful synthesis of perovskite-based colloidal nanocrystals (NCs), showcasing their controllable tunability in size and composition [23]. These NCs exhibit single-photon emission at room temperature [24], along with long coherence times and short radiative lifetimes [25].

During my Ph.D., my research was centered on the development of a compact and efficient integrated single-photon source operating at room temperature. This was accomplished by integrating a perovskite NC with an optical tapered nanofiber (ONF), which is fabricated by stretching a single-mode optical fiber to subwavelength diameters. Originally designed for interfacing light with atomic clouds, ONFs have proven to be a versatile tool for a range of quantum photonics applications, offering advantages such as an intense evanescent field at their surface, exceptionally high transmission rates due to their fabrication methods, and compatibility with fiber networks. I pursued this goal through two main avenues. Firstly, I investigated various strategies to optimize perovskite NCs, addressing environmental instabilities while ensuring robust single-photon emission. Secondly, I optimized the nanofiber fabrication process to enable their practical and efficient utilization. To further enhance the device's efficiency, I explored the fabrication of plasmonic nanostructures directly on the nanofiber, using an innovative technique based on defocused electron beam-induced deposition (EBID). This method offered precise control over the composition, location, and shape of the nanostructures.

This manuscript is organized as follows:

- In **Chapter 1**, I introduce the theoretical framework of single-photon emission. I outline the characteristics of an ideal single-photon source, discuss the key parameters for evaluating real-world sources, and provide an overview of the systems used for generating single-photon emissions. Then, among semiconductor quantum emitters, I shift the focus to the description of perovskite NCs. I describe their chemical structure, electronic and optical properties, fabrication methods, and the main challenges associated with these NCs.

- In **Chapter 2**, I detail the fabrication process and the experimental setup and methods I used for characterizing the single-photon emitters.

- In **Chapter 3**, I present an in-depth characterization of $CsPbBr_3$ NCs, which served as the starting point for my optimization study. These NCs were synthesized using an unconventional protocol that demonstrated improved stability compared to the traditional synthesis method. I showcase their robust single-photon emission and explore the impact of quantum confinement on their single-photon purity. Furthermore, I investigate their stability under illumination and dilution. These results were published in ACS Photonics in 2020 [26].

- In **Chapter 4**, I delve into the synthesis of mixed-cation perovskite NCs, which are characterized by a stoichiometric mixture of monovalent cations. This approach aims to address the well-known stability issues of perovskites in achieving a stable photoluminescence in the red and near-infrared (NIR) spectral regions. Specifically, I report the characterization of confined organic-inorganic mixed-cations $Cs_{1-x}FA_xPbBr_3$ NCs, where a fraction of inorganic Cs cations are replaced with organic FA cations. This substitution results in a red-shift of the emission wavelength and an improvement in photo-stability compared to traditional mixed-halide systems. In this chapter, I also present the first generation of single photons from mixed-cation perovskite NCs. These findings were published in ACS Photonics in 2023 [27].

- In **Chapter 5**, I introduce an effective strategy for enhancing the stability and brightness of $CsPbBr_3$ NCs by incorporating Zn^{2+} ions at the Pb-site. This approach results in improved stability under dilution and illumination, even at excitation powers well above saturation, and in a reduced blinking behaviour on a sub-millisecond time scale. These results were published in Nano Letters [28].

- In **Chapter 6**, I present the ONF platform, outlining its advantages and applications. I describe the protocol for fabricating a single-mode optical tapered nanofiber, and detail the optimizations I made to this platform. I also describe the first coupling of a perovskite NC with a ONF, demonstrating how this integrated system works as a hybrid single photon source. Parts of these results were published in *ACS Photonics* in 2020 [26] and in an review in *Optical Materials* in 2023 [29].

- In **Chapter 7**, I finally introduce an innovative approach based on Electron Beam Induced Deposition (EBID) for creating metallic nano-fabrications on

ONFs. This method has the potential to enable the efficient coupling of emitted photons by harnessing the enhancement of the quantum emitter's spontaneous emission rate via Purcell effect. I describe the fabrication protocol, present the fabricated nano-structures (nanopillars and nanoantenna), and provide a detailed optical characterization, with a focus on the study of the spectra and the polarization of the scattered light. The content of this chapter has led to a patent application (under evaluation) and an article based on this work is currently in preparation.

List of publications

The work presented in this thesis has given rise to the following publications:

Publications

1. D'Amato, M., Belzane, L., Dabard, C., Silly, M., Patriarche, G., Glorieux, Q., Le Jeannic, H., Lhuillier, E., & Bramati, A. (2023). Highly photostable Zn-treated halide perovskite nanocrystals for efficient single photon generation. Nano Letters, 23(22), 10228-10235.

2. D'Amato, M., Tan, Q. Y., Glorieux, Q., Bramati, A., & Soci, C. (2023). Color-tunable mixed-cation perovskite single photon emitters. ACS Photonics, 10(1), 197-205.

3. Soci, C., Adamo, G., Cortecchia, D., Wang, K., Xiao, S., Song, Q., ... D'Amato, M., Lhuillier, E. & Bramati, A. (2023). Roadmap on perovskite nanophotonics. Optical Materials: X, 17, 100214.

4. Pierini, S., D'Amato, M., Goyal, M., Glorieux, Q., Giacobino, E., Lhuillier, E., Couteau, C., & Bramati, A. (2020). Highly photostable perovskite nanocubes: toward integrated single photon sources based on tapered nanofibers. ACS Photonics, 7(8), 2265-2272.

Conference proceedings

- Bramati, A., Pierini, S., D'Amato, M., Goyal, M., Glorieux, Q., Giacobino, E., Lhuillier, E.,& Couteau, C. (2021, August). Room temperature integrated single photon sources based on highly photostable perovskites nanocubes coupled to optical nanofibers. In Quantum Nanophotonic Materials, Devices, and Systems 2021 (Vol. 11806, p. 118060O). SPIE.

- Pierini, S., D'Amato, M., Joos, M., Glorieux, Q., Giacobino, E., Lhuillier, E., Couteau, C.,& Bramati, A. (2020, May). Hybrid devices for quantum nanophotonics. In Journal of Physics: Conference Series (Vol. 1537, No. 1, p. 012005). IOP Publishing.

I have presented the results of this thesis at the following conferences:

Invited talks

- INSP Workshop on Colloidal Nanocrystal, Paris, 2023 *Single photon emission from perovskite nanocrystals.* (1st Febraury 2023)
- Quantum Nanophotonic Materials, Devices, and Systems 2021. SPIE, San Diego, California (1st-05th August 2021) *Room temperature integrated single photonsources based on highly photostable perovskites nanocubes coupled to optical nanofibers.*

Posters

- Central European Workshop on Quantum Optics (CEWQO2023) Milan (3rd-7th July 2023). *Towards a room-temperature integrated single photon source based on perovskite nanocrystal coupled to optical nanofiber*
- 18th International Conference on Optics of Excitons in Confined Systems (OECS 2023) in Lecce, Italy (12nd-16th June 2023) *Towards a room-temperature integrated single photon source based on perovskite nanocrystal coupled to optical nanofiber*
- European Physical Society Forum 2022, Paris, (2nd-4th June 2022). *Room temperature integrated single photon sources based on highly photostable perovskites nanocubes coupled to optical nanofibers*

Chapter 1

Perovskite nanocrystals as single photon sources

Contents

Introduction

This chapter establishes the framework of this thesis, providing the theoretical and practical tools essential for understanding the following discussions and results. It comprises three distinct sections, each addressing essential elements of my research. Section 1.1 serves as an introduction to the realm of single photon sources. It elucidates the characteristics of an ideal single photon source, introduces the key parameters used to assess the deviation of real-world sources from the ideal ones, and provides an overview of the systems employed for achieving single photon emissions. In Section 1.2, the focus shifts to semiconductor quantum emitters, where we investigate their transition into a quantum confinement regime, where they behave as *artificial atoms* enabling single photon emission. The section also explores the carrier dynamics and the common issues that affect the single-photon emission in semiconductor QDs. Finally, Section 1.3 introduces *perovskite* semiconductor QDs, topic of this thesis, describing their chemical structure, electronic and optical properties, fabrication methods, and the major challenges associated with these emitters.

1.1 Single photon sources

An ideal single photon source can be represented as a two-level system. This system consists of two distinct states: a ground state $|g\rangle$ and an excited state $|e\rangle$, characterized by a radiative electromagnetic transition with energy $\hbar\omega_A$, as depicted in Figure 1.1a. An ideal source produces photons in the same pure quantum state and *on-demand*, meaning that when the system is efficiently prepared in the excited state, this source emits exactly one photon during each excitation cycle through spontaneous emission [30]. In practical scenarios, quantum emitters deviate from this ideal behavior. When evaluating the performance of a real-world single photon source, three crucial parameters are considered: single photon purity, brightness and indistinguishability, as summarized in Figure 1.1b.

1.1.1 Single photon purity

The essential requirement for a reliable single photon source is a negligible multi-photon probability in each wave packet. A way to access information about the photon statistics of the electromagnetic field is through the second-order correlation

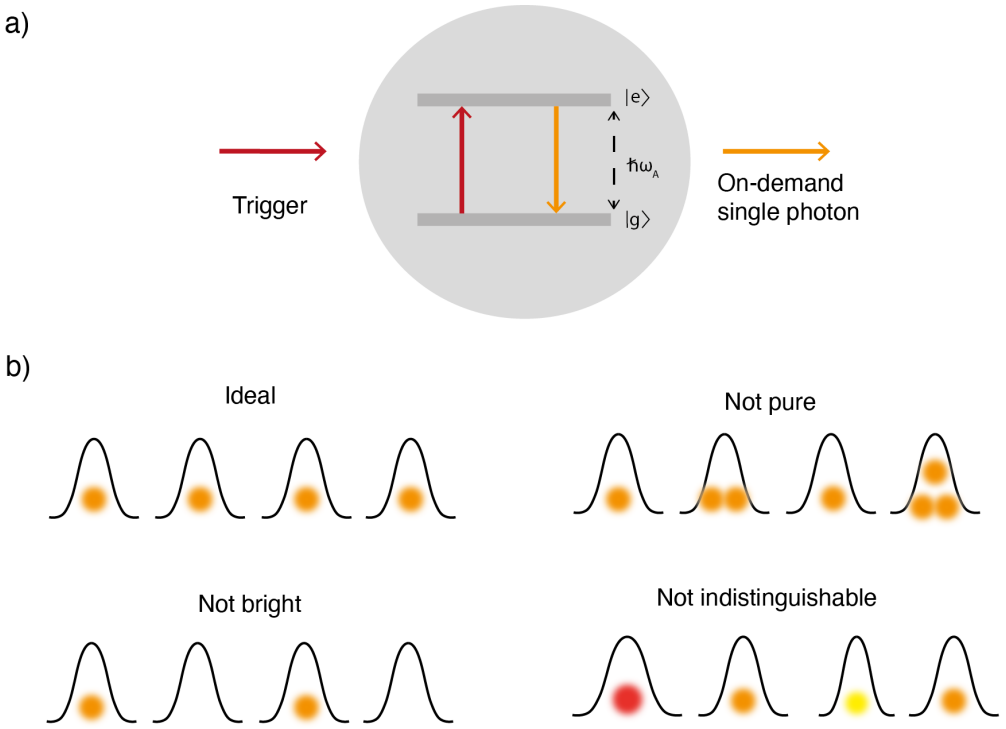

Fig. 1.1 ***Ideal single photon source.*** *a) Schematic of an on-demand SPS: when there is a need for single-photon emission, an external control mechanism is employed to bring the system to the excited state $|e\rangle$. The the system relaxes to the ground energy state $|g\rangle$ via spontaneous emission. b) Schematic of practical scenarios for SPSs deviating from the ideal behaviour.*

function [31]. This function can be expressed in terms of photon creation and annihilation operators $\hat{a}$ and $\hat{a}^\dagger$:

$$g^{(2)}(\tau) = \frac{\left\langle \hat{a}^\dagger(t)\hat{a}^\dagger(t+\tau)\hat{a}(t)\hat{a}(t+\tau)\right\rangle}{\langle \hat{a}^\dagger(t)\hat{a}(t)\rangle \langle \hat{a}^\dagger(t+\tau)\hat{a}(t+\tau)\rangle} \tag{1.1}$$

Given the photon number operator $\hat{n} = \hat{a}^\dagger\hat{a}$, Eq.1.1 can be written in terms of the mean and mean squared photon numbers:

$$g^{(2)}(\tau) = \frac{\langle n(n-1)\rangle}{\langle n\rangle^2} = 1 + \frac{(\Delta n)^2 - \langle n\rangle}{\langle n\rangle^2} \tag{1.2}$$

where $(\Delta n)^2 = \langle n^2\rangle - \langle n\rangle^2$ is the photon-number variance. This expression can be used to characterize the light based on its photon statistics [32]. I give here a few

examples of states of light:

- **Coherent light** A coherent state of light $|\alpha\rangle$, i.e. the state generated by a laser above threshold, can be written as a coherent superposition of number states $|n\rangle$ [33] as follows:

$$|\alpha\rangle = e^{-\alpha^2/2} \sum_{n=0}^{\infty} \frac{\alpha^n}{\sqrt{n!}} |n\rangle \tag{1.3}$$

  The statistics of coherent states is described by a Poisson distribution. As the coherent state $|\alpha\rangle$ is an eigenstate of the annihilation operator, the expected value of the photon number is therefore $\langle n\rangle = \alpha^2$, while the photon-number variance is $(\Delta n)^2 = \alpha^2 = \langle n\rangle$. From eq.1.2, we deduce that, for coherent light, $g^2(0) = 1$.

- **Thermal light** The thermal state, described by the black-body radiation, is an incoherent mixture of differente number states. The number of photons in a given state follows the Bose-Einstein statistics

$$P_n = \frac{\langle n\rangle^n}{(1 + \langle n\rangle)^{n+1}} \tag{1.4}$$

  where $\langle n\rangle$ is the average number of photons in the state. Since the variance for the thermal state is given by $(\Delta n)^2 = \langle n\rangle^2 + \langle n\rangle$, therefore the fluctuations in photon number are larger that the mean photon number. The statistics of thermal ligth states is then desbribed by a super-poissonian distribution. From eq.1.2, we obtain $g^2(0) = 2$, which is referred to as *photon bunching*.

- **Fock states** For Fock states $|n\rangle$ there is no uncertainty in the photon number and the photon-number variance is therefore $(\Delta n)^2 = 0$. These states have a statistics described by a sub-poissionian distribution. Eq.1.2 for Fock states becames:

$$g^2(\tau) = 1 - \frac{1}{\langle n\rangle} \tag{1.5}$$

  In the case of an ideal single photon sources emitting only one photon at time, we obtain $g^{(2)}(0) = 0$, which is referred as *antibunching*. In the case of two photons we have $g^{(2)}(0) = 0.5$.

The single photon purity can be measured with a Hanbury Brown and Twiss (HBT) setup [34]. In this setup a stream of photons is sent on a $50:50$ beam splitter

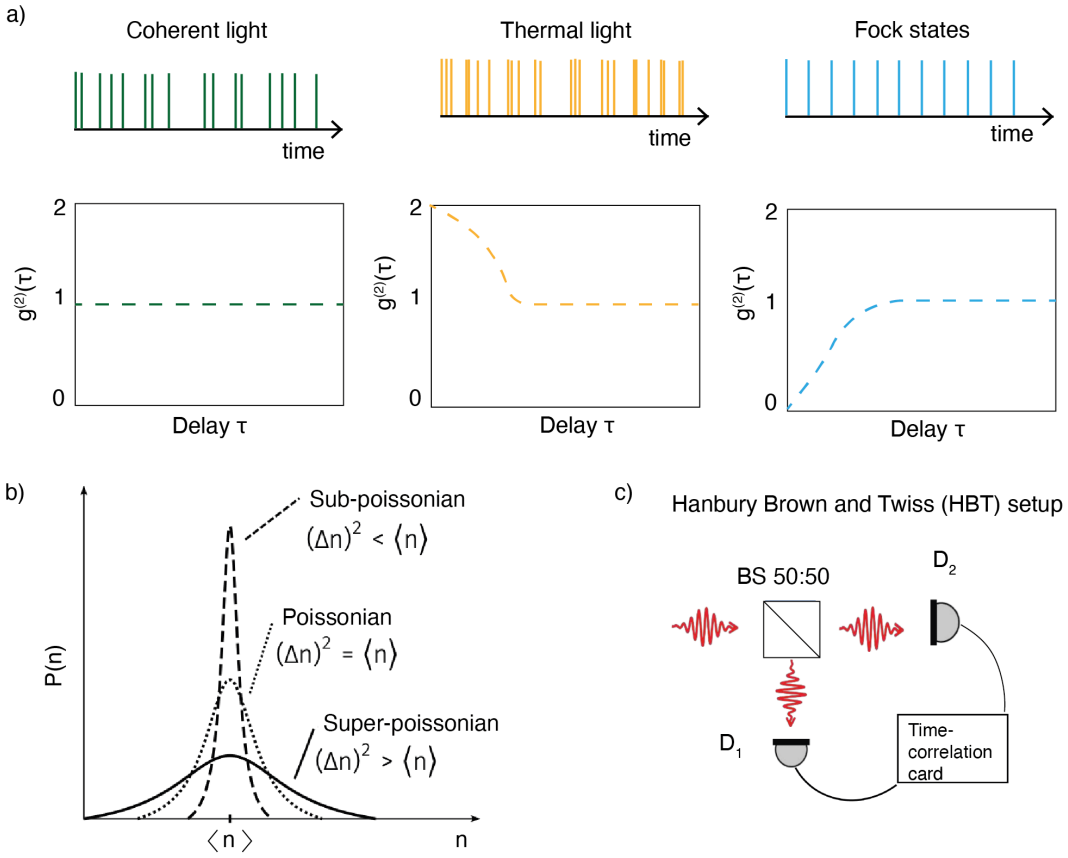

Fig. 1.2 ***Single photon purity*** *a) Distribution of photon arrival time and second-order correlation function $g^{(2)}(\tau)$ for coherent light, thermal light and Fock states. b) Photon statistics for coherent light (dotted line), thermal light (continuous line) and Fock states (dashed line). c) Schematic of the Hanbury Brown and Twiss setup used to measure the second-order correlation function $g^{(2)}(\tau)$.*

that equally divides it between the two ouputs, on two photon counting detectors D_1 and D_2. The resulting output signals are sent to correlation electronics that measure the time delay between the detection events in both detectors D_1 and D_2. The measure of the coincidences at $\tau = 0$ gives a direct measure of the second-order correlation function $g^{(2)}(\tau)$.

1.1.2 Brightness

A deterministic single-photon source is expected to deliver light pulses without any vacuum component $|0\rangle$. To quantify the performance of a source, we can define the brightness B as the probability efficiently of generating a single photon upon

triggering and not vacuum states. High brightness is desirable for applications such as quantum communication and quantum information processing, where high detection rates are needed to achieve high fidelity and high signal-to-noise ratio.

The brightness is an intrinsic property of the source. To correct for the losses η_{losses} in the experimental setup, we can define the brightness as:

$$B = \frac{R_{photons}}{\Gamma_{laser}\eta_{losses}} \tag{1.6}$$

where Γ_{laser} is the laser repetition rate and $R_{photons}$ is the detected photon count rate.

1.1.3 Indistinguishability

A light pulse can be decomposed as an ensemble of plane wave modes, where each mode is a quantized harmonic oscillator with defined polarization ϵ, spatial frequency k, and frequency $\omega = ck$, where c is the speed of light. The photon wavepacket is given by:

$$|\psi\rangle = \sum_{\mathbf{k},\epsilon,n} c_{\mathbf{k},\epsilon} |n\rangle_{\mathbf{k},\epsilon} \tag{1.7}$$

The number state of each mode — or Fock state — written as $|n\rangle_{\mathbf{k},\epsilon}$, corresponds to a pure state with exactly n photons in the mode. A single-photon light field is built exclusively on single-photon Fock states $|1\rangle_{\mathbf{k},\epsilon}$, with a total photon number of one.

Indistinguishable photons are photons that occupy the same spatio-temporal mode and this condition is reached when each wavepacket is a pure quantum state with defined coefficients $c_{\mathbf{k},\epsilon}$ and not a statistical mixture [30]. This indistinguishability is compromised if the two photons are distinguishable in certain degrees of freedom, for example if they have poor spectral, temporal or spatial mode overlaps as well as non-matching polarization states. The indistinguishability can be evaluated through Hong, Ou and Mandel (HOM) interference experiment [35].

In this thesis, I focused on studying single-photon sources that operate at room temperature. Due to the inherent challenges associated with achieving indistinguishable photons in such conditions, including factors like decoherence and thermal phonon interactions, the evaluation of indistinguishability was not a part of this study.

Other key properties

In addition to these three essential properties, other important criteria can be employed to assess the performance of a single photon source.

- **Photo-stability** of the emission: in some SPSs where non-radiative channels play a significant role, phenomena such as temporary intermittency of fluorescence, known as *blinking*, or permanent interruption of fluorescence, known as *bleaching*, can occur. Further details on these phenomena will be discussed in Section 1.2.3.1.

- **High Quantum Yield (QY)**: this is the probability of radiative emission per excitation-cycle [30] defined as:

$$QY = \frac{\Gamma_{rad}}{\Gamma_{rad} + \Gamma_{non-rad}} \tag{1.8}$$

  where Γ_{rad} represents the radiative decay channel and $\Gamma_{non-rad}$ accounts for all the non-radiative decay channels. In an ideal two-level system, the QY is equal to 1, indicating that every excitation will lead to the emission of a photon. However, in real single photon sources, the decay to the ground state can occur non-radiatively, leading to a reduced quantum yield.

- **High photons extraction efficiency** ($> 90\%$): this is essential to achieve high-efficient single-photon sources. A low extraction efficiency means that a significant fraction of the photons generated by the emitter is trapped inside the material or lost in the surrounding medium, reducing the total number of photons available for use. This, in turn, limits the achievable signal-to-noise ratio, which is crucial for the fidelity of quantum operations [36].

- **High repetition rate** ($>$ GHz) and then short optical transition radiative lifetime (ps regime). This is particularly important for applications that require a high photon flux [37], such as quantum key distribution.

- **Room temperature operation**: this is desirable for single photon sources because it allows for easy integration with other electronic and optical components, and eliminates the need for expensive and bulky cryogenic cooling systems.

- **Near-infrared (NIR) emission**: optical fibers used in long-distance communication have low losses and dispersion in the NIR region. Thus, NIR photons emitted from single photon sources can be easily transmitted over long distances without significant attenuation or distortion [38].

Achieving a single quantum emitter with all these properties is still a challenge. Therefore, the selection of the most suitable single photon source should be based on the specific application requirements.

1.1.4 Available single-photon sources

Considering the conditions required for a good SPS, a first category of sources used in quantum optics experiments are macroscopic sources, including:

- **Faint lasers**: room-temperature sources relying on strong attenuation of laser pulses to achieve the goal of only one photon per pulse. However, this technique delivers Poisson distributions of photons, from which multi-photon events can never be entirely suppressed [39]. Additionally, in case of strong attenuation, they potentially lead to empty pulses.

- **Spontaneous parametric down conversion (SPDC)** sources: based on the non-linear interaction of a pump laser in a χ^2 non-linear crystal, such as barium borate (BBO) or potassium dideuterium phosphate (KDP). In these sources, one pump photon is split into a signal and an idler photons, when energy and momentum conservation is satisfied [40]. However, the photon-pair creation is a random process and the efficiency of SPDC is extremely low, typically around few pairs over 10^6 incoming photons. As a result, the output signal of SPDC sources is inevitably a trade-off between high emission rates and low multi-photon probability, limiting their usefulness for certain applications. On the other hand, being a *heralded* source, which means that it emits two photons at a time, SPDC finds extensive use in quantum information and quantum metrology applications [41, 42].

A second category of sources consists in single quantum emitters which can be described as two-level systems, serving as on-demand sources of single-photon Fock states. In this category we can find:

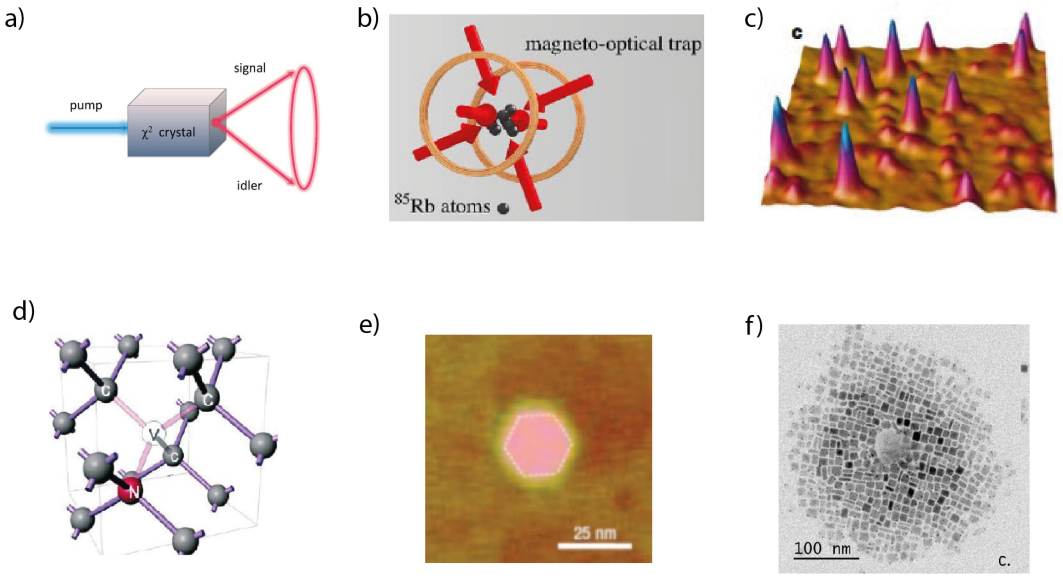

Fig. 1.3 ***Examples of single photon sources.*** *a) SPDC b) Atom and ions. Figure reported from [43]. c) Organic molecules Figure reported from [11] d) Color centers in diamond. e) Self-assembled quantum dots. f) Colloidal quantum dots.*

- **Atoms and ions**: their main advantage is that their states are perfectly reproducible and well-known, including the hyperfine structure of the levels. With the appropriate atom or ion, transitions can be observed throughout the visible and infrared (IR) ranges of the electromagnetic spectrum (for example, Cs at 852 nm and Rb at 780 nm). They allows for the generation of single photons with high purity and indistinguishability, but low brightness. Nevertheless, their use requires complex manipulation and trapping [44, 45], as well as costly equipment and ultra-high vacuum conditions.

- **Organic molecules**: the first solid-state systems on which the photon antibunching was demonstrate [46]. One of their major advantages is that they are intrinsically identical objects and can be easily fabricated using well-established and inexpensive chemical methods [10]. They operates at both room and cryogenic temperatures and they are suitable for integration into devices [18]. However, unlike atoms, molecules can exhibit a complex energy levels scheme and, if embedded in aqueous solutions or simply dispersed on a substrate, they experience bleaching, blinking, and low photo-stability, compromising their brightness. To overcome these instabilities, they can be embedded within a crystalline

matrix [10, 47], preserving their photo-physical properties.

- **Colors centers in diamonds** are other promising candidates as single photon sources. They include Nitrogen-Vacancy (NV) centers [48, 49], Silicon-Vacancy centers (SiV) [13, 50] and Germanium-Vacancy (GeV) [51] centers. They consist in substitutional atoms and carbon vacancies that behave as atom-like systems, with discrete energy levels in the diamond bandgap. Room-temperature operation is one of the main advantages of these systems, together with the high photostability and mechanical rigidity provided by the diamond lattice. However, achieving high brightness is a challenge, as the extraction of fluorescence light is hindered by diamond's high refractive index. These defect centers can be fabricated also in nanodiamonds, which can be used in colloidal solutions. This offers several advantages, as they can be readily deposited on various substrates, enabling integration into photonic nanostructures [52].

- **Semiconductor quantum dots** are semiconductor materials of nanometric size where the confinement of electrons and holes produces discrete exciton levels similar to atomic levels. They are classified in two types:

  - *Self-assembled* consisting of a small island of semiconductor embedded in a higher band gap semiconductor matrix, grown on a single-crystalline substrate via molecular beam epitaxy. Self-assembled InAs/GaAs QDs currently have the highest performance in terms of purity and indistinguishability at low temperature [14, 53, 54]. However, their operation at room temperature is less optimal and their fabrication requires the use of complex facilities and techniques.

  - *Colloidal* with a typical diameter < 100 nm and dispersed in solution. They have interesting optical properties, including absorption and emission spectra tunable with size and composition, high quantum yield, room temperature operation. These advantages, together with ease of fabrication, have attracted intensive interest. The most known are group II–VI semiconductor QDs, such as core-shell CdSe/ZnS. In my thesis, I focus on perovskite nanocrystals (NCs), which have garnered significant interest due to their exceptional properties for optoelectronic applications and their recent emergence as a novel quantum material for SPSs [24, 55].

Figure 1.3 illustrates examples of available SPS and Table 1.1.4 shows a comparison of the different quantum emitters in terms of brightness, indistinguishability, purity, room temperature operation and stability.

Source	Brightness	Indistinguishability	Purity	RT operation	Stability
Atoms and ions	✗	✓	✓	✗	✓
Color centers	✗	∼	✓	✓	✓
Organic molecules	✓	∼	✓	✓	✗
Self-assembled QDs	✓	∼	✓	✗	✓
Colloidal QDs	✓	∼	✓	✓	✗

Table 1.1: **Comparison between microscopic single photon sources**: ✓ for satisfied, ∼ for partially satisfied, and ✗ for not satisfied criteria.

1.2 Introduction to semiconductor QDs

1.2.1 Quantum confinement in semiconductor QDs

When a photon with sufficient energy is absorbed by a semiconductor, it can promote an electron from the valence band to the conduction band, leaving behind a positively charged effective particle known as a hole. This process creates an electron-hole (e-h) pair within the semiconductor. This e-h pair can form an *exciton*, which is a bound state of the electron and hole due to their mutual Coulombic attraction. This quasi-particle is characterized by the exciton binding energy (E_b), which represents the energy required to dissociate the exciton into free charge carriers, and the excitonic Bohr radius (a_B), which refers to the distance between the electron and hole. It ranges from few nm to few tens of nanometers (6 nm for CdSe, 21 nm for PbS and 40 nm for HgTe).

In semiconductors of macroscopic sizes (bulk semiconductor), the width of the energy gap that separates the conduction band from the valence band is a fixed parameter, which identify the material. The situation changes when the size of the semiconductor particle decreases towards the excitonic Bohr radius. In this case, the motion of electrons and holes is strongly spatially confined, *feeling* the presence of the particle boundaries. The electronic and optical properties of the system become dependent on its size. This strong dependence on the size is called *quantum confinement effect*. The dimensionality of the emitters has a strong impact on their electronic and

optical properties, as illustrated in Figure 1.4a. Two-dimensional (nanoplatelets or quantum wells) and one- dimensional structures (quantum nanorods or nanowires) imply the electrons are confined to only one (the thickness) or two dimensions separately. These nanostructures can be polarized as a result of their anisotropic structure. Meanwhile, zero-dimensional structures (quantum dots) imply the electrons are confined in all three dimensions.

Let's delve into more detail. When the QD's size is reduced, the energy gap increases, in particular leading to a blueshift of the emission wavelength. In addition to the increasing energy gap, quantum confinement leads to a collapse of the continuous energy band of the bulk material into discrete, atom-like energy levels, as shown in Figure 1.4b. The discrete structure of energy states leads to discrete absorption spectra.

1.2.2 Carrier dynamics in semiconductor QDs

In this paragraph, I will illustrate the main photo-physical dynamical processes occurring in semiconductor QDs, providing a brief but comprehensive understanding of the carrier dynamics. A schematic representation of these processes is reported in Figure 1.5, as a visual aid to facilitate the interpretation of the following discussions.

Upon photon absorption, the semiconductor NC is excited, resulting in the generation of bound and unbound electron-hole pairs, respectively excitons or charged carriers (positive or negative trions, biexcitons, etc.).

If the excitation is non-resonant ($h\nu > Eg$), the generated electrons and holes acquire excess kinetic energy, which can be referred to as *hot state* excitons for simplicity. This surplus of energy undergoes rapid dissipation through ultrafast processes, resulting in the formation of a *relaxed* excited state characterized by *cold state* excitons. This thermalization can occur via carrier-carrier scattering, with thermalization times ranging from 10 to less than 100 fs [57].

Subsequently, the charge carriers can thermalize with the lattice through intraband relaxation, a process commonly known as *cooling* [58]. The timescale for this cooling dynamics is typically around 100 fs [59]. At high photo-excitation densities, this effect can be dramatically increased by the phonon bottleneck effect [60], which resulted in a cooling lifetime of approximately 300 ps (picoseconds) in the case of perovskite NCs [61].

Following the completion of ultrafast processes, a competition arises between ra-

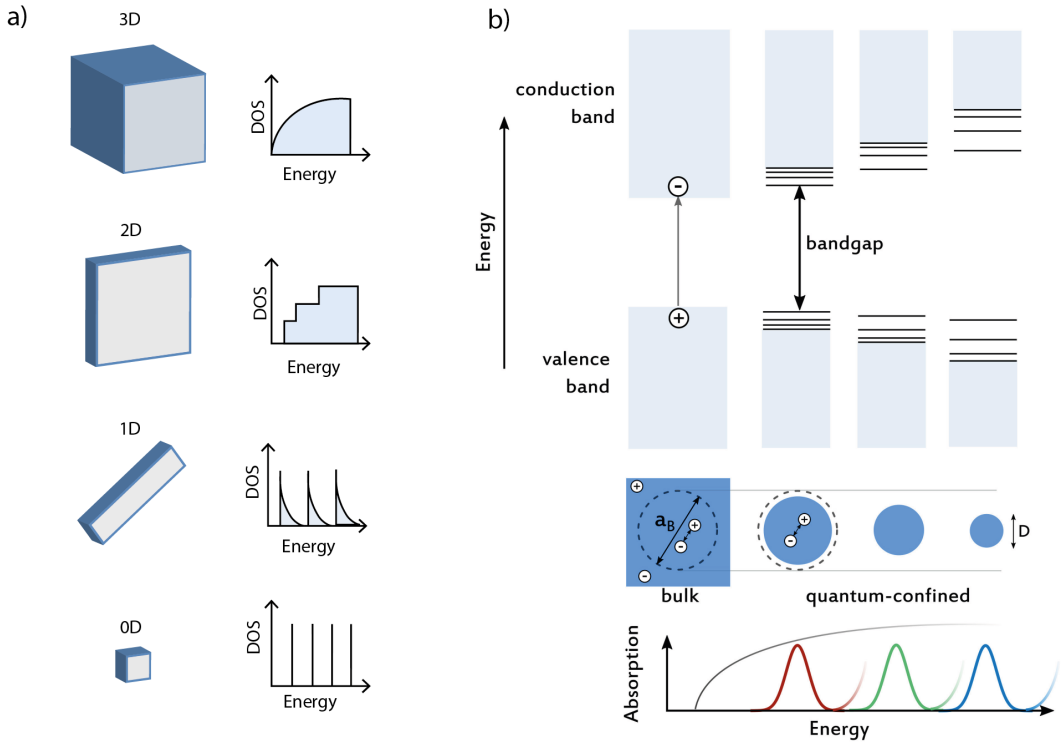

Fig. 1.4 ***Semiconductor dimensionality and quantum confinement*** *a) Schematic representation of the energy level structure of a bulk semiconductor and of semiconductor nanostructures with reduced dimensionality, from 2D (exciton is confined only in the thickness dimension), to 1D (exciton is confined in the diameter direction), to 0D (exciton is confined in all directions) (DOS: density of electronic states). b) Quantum confinement, leading to size-dependent optical and electrical properties that are distinct from those of parental bulk solids, occurs when the spatial extent of electronic wave functions is smaller than the Bohr exciton diameter (a_B). D is the QD's diameter. Figure reproduced from reference [56].*

diative decay and non-radiative decay pathways. If multiple excitons are generated in the NC, as in the case of high excitation fluences, radiative decay competes with Auger recombination [62]. Auger recombination involves the non-radiative transfer of energy from a photo-excited electron-hole pair to a third charge carrier (electron or hole), causing the latter to be excited to a higher-energy state. This results in the formation of a *hot state* exciton, which subsequently relaxes towards the band edge [63]. The Auger mechanism makes also possible ionization events that eject a carrier from the QD [64]. Auger recombination is typically a highly efficient mechanism, occurring on timescales ranging from tens to hundreds of picoseconds. As

long as Auger recombination remains feasible, it dominates over radiative recombination. This mechanism is particularly important in quantum dots, where it reduces multi-exciton events and enables single photon emission [24].

Finally, the *cold state* exciton undergoes recombination, which can occur through radiative or non-radiative processes. The exciton can recombine by emitting a photon with equivalent energy, returning the system to its ground state. This radiative recombination process for colloidal NCs typically occur in the nanosecond range (1-50 ns) [23]. Alternatively, non-radiative recombination processes lead to the production of heat, interband relaxation, or other non-radiative relaxation channels.

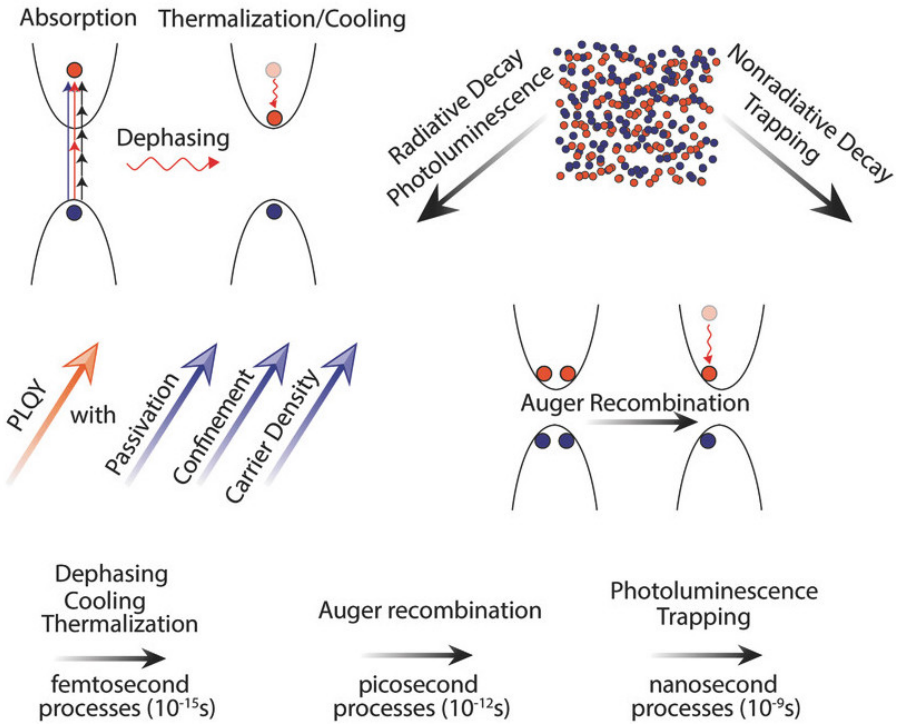

Fig. 1.5 ***Carrier dynamics in semiconductor NCs.*** *Photophysical processes that occur after excitation of light. Auger recombination and other nonradiative rates can compete with photoluminescence. Figure reproduced from reference [63].*

1.2.3 Issues in semiconductor QDs

1.2.3.1 Blinking and bleaching

Colloidal semiconductor emitters suffer from photoluminescence blinking. This phenomenon consists in a fluctuation of their fluorescence intensity between a high emissive state and a low-emissive state and it has been observed in a wide range of emitters, encompassing single molecules [65, 66], color centers in diamond [67, 68], semiconductor QDs [69, 70]. This phenomenon significantly constrains the practical use of these emitters in optoelectronic and quantum-technology applications, motivating efforts to mitigate it. Although the detailed mechanisms responsible for blinking are still subject to debate, it is generally agreed that fluorescence blinking is a direct consequence of charge trapping. Charge trapping involves the confinement of an electron or a hole at defect sites within the lattice or on the surface of the QDs. Consequently, this phenomenon impacts recombination processes and, consequently, the emitted photoluminescence. In the literature, two main models have been developed to establish a connection between charge trapping and the observed fluctuations during PL blinking, referred to as Type A and Type B models.

Type A blinking

Charge trapping in NCs (or QDs) can result in the formation of charged states, known as trions. Trions can be either positive or negative, depending on the trapped charge. While trions are optically active, they are prone to rapid Auger recombination [71]. In this process, the electron-hole (e-h) pairs within the NC recombine non-radiatively giving the energy to the unpaired charge left in the core. This process results in a low fluorescence signal. However, it's important to note that this low PL intensity period is reversible. Once the trapped charge return in the conduction or valence band, the nanocrystal return neutral and the Auger recombination is inhibited, resulting in an high PL intensity state.

Figure 1.6 illustrates the various steps involved in the type A blinking. Here, the periods of high PL intensity are referred to as *ON states*, while the periods of low PL intensity are referred to as *OFF states*.

- ON states are the result of continuous cycling photon absorption to create an exciton, followed by radiative recombination of e-h pair.
- ON to OFF switching occurs via thermal ionization or photoionization of a

charge carrier to a trap state [72], leaving a delocalized charge of opposite sign inside the NC.

- During OFF states, despite the subsequent absorption cycles, the resulting charged NC remains non-fluorescent or very low fluorescente, because emission is quenched by a competition between the fast non-radiative Auger recombination and radiative recombinations.

- OFF to ON switching occurs upon neutralization of the NC.

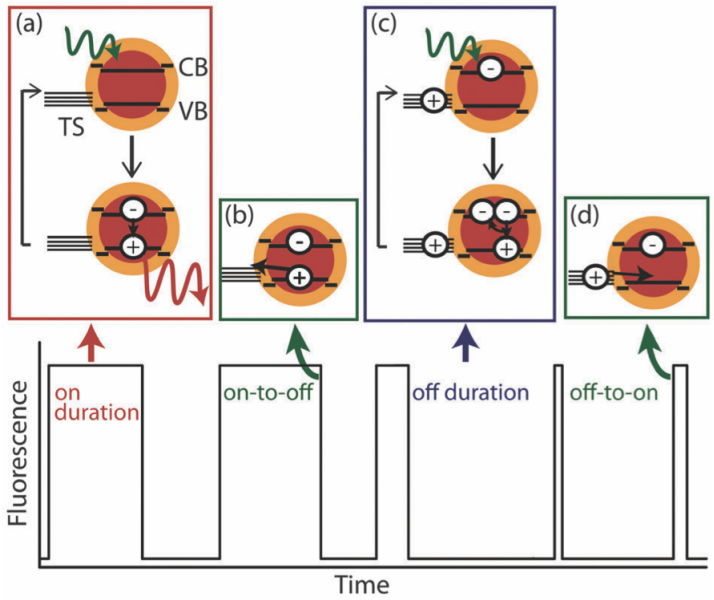

Fig. 1.6 ***Schematic description of type A blinking.*** *The NC conduction band edge (CB), valence band edge (VB), and surface trap states (TS) are labeled. Figure reproduced from reference [72].*

Type B blinking

In Type B blinking, the fluctuations in photoluminescence intensity are governed by the competition between the radiative recombination rate and the trapping rate, rather than the non-radiative rate [72]. The trapping rate fluctuates in time, causing the nanocrystal to enter an OFF state when the trapping rate becomes significantly faster than the radiative recombination rate. When in the OFF state, the NC is not permanently charged, and Auger recombination is not involved.

In Figure 1.7 the different steps are illustrated:

- ON states occur when the trapping rate is considerably slower than the fluorescence rate; the nanocrystal cycles between photon absorption and radiative recombination with the emission of a photon.
- ON to OFF switching occurs when the trapping rate becomes faster than the fluorescence rate.
- During OFF states, the nanocrystal cycles between photon absorption to create an exciton, fast removal of one charge carrier to a trap state and and non-radiative recombination of the electron and trapped hole
- OFF to ON switching occurs when the trapping rate becomes very slow again.

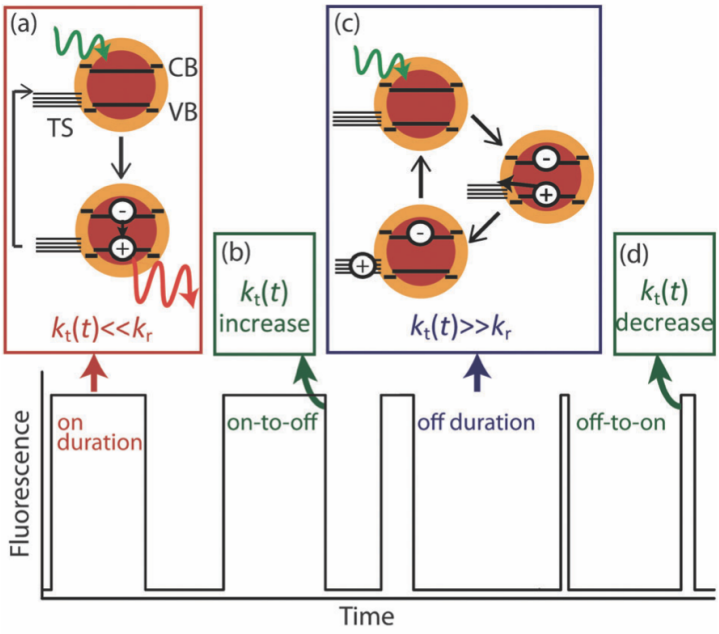

Fig. 1.7 ***Schematic description of type B blinking.*** *k_t is the trapping rate and k_r the recombination rate. The NC conduction band edge (CB), valence band edge (VB), and surface trap states (TS) are labeled. Figure reproduced from reference [72].*

One experimental method for distinguishing between these two types of blinking is the investigation of the correlation between fluctuations in photoluminescence intensity and lifetime. In Type A blinking, characterized by the competition between radiative recombination and Auger recombination in a charged exciton, correlated fluctuations in photoluminescence intensity and lifetime are expected. Indeed, when

a NC is in a charged state and Auger recombination introduces a rapid, non-radiative channel, this results in a shorter lifetime of the radiative state (typically a few nanoseconds or less) and in a reduction in photoluminescence intensity. In contrast, in type B blinking, characterized by the competition between the radiative recombination rate and the trapping rate, the significant changes in emission intensity are not accompanied by significant alterations in the emission lifetime.

Blinking is a reversible phenomenon, unlike photo-chemical degradation, which induces permanent bleaching of the emission, i.e. the emitters do not emit light any more and they become completely dark.

1.2.3.2 Not perfect saturation of the emission

In the previous sections we explored how the $g^{(2)}(0)$ is given by the number of coincidences detected at zero delay in a HBT setup, establishing that for an ideal single photon source $g^{(2)}(0) = 0$. However, for real-world quantum emitters multi-exciton events are possible, reducing the single photon purity. In this section, I will give a concise overview of how multi-exciton contributions significantly impacts the quality of single photon emission, following the formalism reported in references [73, 74], which can be consulted for futher details.

When excited with a pulsed laser, a NC absorbs a random number N of photons, leading to the creation of a number N_{eh} of excitons in the band-edge levels. The N_{eh} excitons are generated with a Poissonian probability :

$$P(N_{eh}, \langle N_{eh} \rangle) = \frac{\langle N_{eh} \rangle^{N_{eh}}}{N_{eh}!} e^{(-\langle N_{eh} \rangle)} \tag{1.9}$$

Here, the mean number $\langle N_{eh} \rangle$ of excitons is directly proportional to the excitation power. We can call QY_m the probability of m-exciton radiative recombination, which can be written as:

$$QY_m = \frac{\gamma_{R,m}}{\gamma_{R,m} + \gamma_{A,m} + \gamma_{NR,m}} \tag{1.10}$$

where $\gamma_{R,m}$ is the radiative recombination rate, $\gamma_{A,m}$ is the Auger recombination rate and $\gamma_{NR,m}$ takes into account other non-radiative decay channels different from Auger (i.e the energy transfer to phonons or to surface defects, etc.).

The mean number of photons emitted after a given excitation pulse can be mod-

eled [75] as follows:

$$N_{ph} = \sum_{N_{eh}=1}^{\infty} P(N_{eh},\langle N_{eh}\rangle) \sum_{m=1}^{N_{eh}} QY_m \tag{1.11}$$

In the case of colloidal semiconductor NCs, the highly efficient Auger recombination rate is the key driver of single photon emission. Since $\gamma_{A,m} >> \gamma_{R,m}$ for $m > 1$, Auger recombination effectively suppresses multi-exciton emission, resulting in negligible multi-exciton quantum yields (QY_m) for $m > 1$ and ensuring the efficient emission of single photons. This efficiency is the reason why colloidal NCs have been proposed as effective on-demand single photon sources at room temperature.

To gain a clearer understanding, let's begin by considering the scenario of an ideal single photon emitter.

In this case,the probability of emitting more than one photon per excitation pulse is zero, then $g^{(2)}(0) = 0$, and eq.1.11 reduces to:

$$N_{ph} = QY_1(1 - e^{(-\langle N_{eh}\rangle)}) \tag{1.12}$$

In this case a saturation of N_{ph} is expected.

In the case of multi-exciton events and without considering the Auger effect, the light emission has Poissonian statistics, and consequently a $g^{(2)}(0) = 1$. For such a *classical* source eq. 1.11 can be written as a linear relation:

$$N_{ph} = QY'\langle N_{eh}\rangle \tag{1.13}$$

where $QY_m = QY'$ is identical for any number m of excited electron-hole pairs.

In cases where a highly efficient Auger effect is at play, the emission of multi-excitons is effectively suppressed, even though the multi-exciton quantum yields are not entirely negligible. In such instances, within a low excitation regime, N_{ph} can be approximated by a combination of the exponential function from equation 1.12 and a linear component from equation 1.13, as shown in Figure 1.8. We can express it as follows:

$$N_{ph} \simeq QY_1((1 - e^{-\langle N_{eh}\rangle}) + \frac{QY_2}{QY_1}\langle N_{eh}\rangle) \tag{1.14}$$

where QY_1 and QY_2 are respectively the exciton and biexciton quantum yield. In such cases, single photon purity can be degradated due to the presence of biexciton contributions.

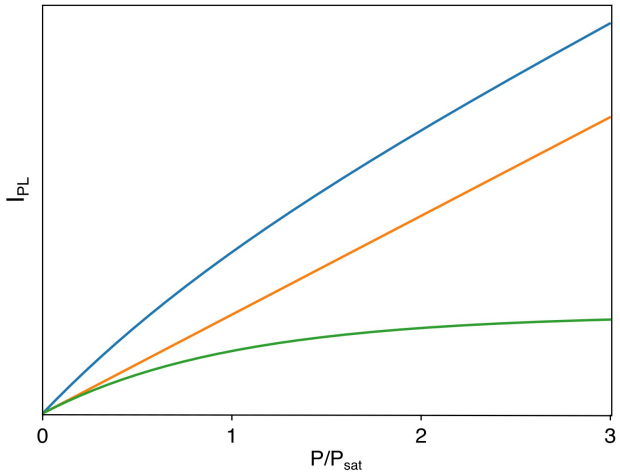

Fig. 1.8 ***Saturation of the emission*** *Comparison between the case of an ideal two level system, showing a perfect saturation (green line), the case of a multi-excitonic emission (orange line) and the case of highly efficient Auger effect with the partial suppression of multi-excitonic events (blue line).*

Experimentally it is useful to express this equation as a function of the laser excitation power P. P is proportional to $\langle N_{eh} \rangle$:

$$\langle N_{eh} \rangle = P/P_{sat} \tag{1.15}$$

where P_{sat} is saturation power, i.e. the power that corresponds to $\langle N_{eh} \rangle = 1$. Experimentally only a fraction of the photons emitted by a single nanocrystal can be collected and detected. This fraction, here referred to as photoluminescence intensity I_{PL}, is just proportional to N_{ph}:

$$I_{PL} = A(1 - e^{-\frac{P}{P_{sat}}}) + BP \tag{1.16}$$

where A is proportional to the exciton quantum yield QY_1 and B is proportional to the biexciton contribution QY_2/QY_1.

1.3 Perovskite nanocrystals (NCs)

Since pioneering works in the 80's-90's, lead halide perovskites (LHPs) have made remarkable progress in optoelectronics and photonics. These materials have demonstrated exceptional performance in various applications such as photovoltaic and photodetectors, light-emitting devices, lasers, and scintillators. As the field progresses, LHPs are becoming an increasingly established material platform, surpassing the performances of traditional semiconductors and making them a highly attractive option for quantum photonics, particularly as single-photon sources. However, advancing this field requires addressing several challenges that intersect chemistry, physics, materials science, and engineering.

1.3.1 Chemical structure and stability

The term *perovskite* refers to compounds that exhibit a crystalline structure described by the chemical formula ABX_3, where A and B represent respectively monovalent and divalent cations and X is a halide anion. In the cubic three-dimensional (3D) crystal structure, as shown in Figure 1.9a, the B cation is located at the body center of the octahedron composed of six halide anions $[BX6]_4$. The octahedra are linked with each other by sharing the vertex and the A cation is located in center of this network [76].

To conserve the structural stability, the type of A cations that can fit this close-packing of ions is limited by the Goldschmidt's tolerance factor, defined by the following relationship between the ionic radii of ions A, B, and X [77]:

$$t_F = \frac{r_A + r_X}{\sqrt{2}(r_B + r_X)} \tag{1.17}$$

Figure 1.9b shows that a favorable condition for obtaining a perovskite structure requires that t_F values lie between 0.8 and 1. Deviating from this interval, either with larger or smaller values, prevent the formation of stable perovskite structures.

Considering these constraints, only a limited number of compositions can lead to stable structures:

- **The A site**: the A cation options include organic monovalent cations like formamidinium ($HC(NH_2)_2^+$, referred as FA) or methylammonium ($CH_3NH_3^+$, referred as MA), as well as inorganic elements like cesium (Cs). Depending

on the organic or inorganic nature of the A cation, perovskites are classified as either hybrid or inorganic respectively. Other candidates such as sodium (Na), potassium (K), and rubidium (Rb) are too small, while imidazolium (IA), ethylammonium (EA), and guanidinium (GA) are too large.

- **The B site**: the B sites are occupied by divalent metals from group 14 of the periodic table, such as lead (Pb^{2+}), tin (Sn^{2+}), or germanium (Ge^{2+}).The 2+ indicates that these metal ions have lost two electrons, resulting in a positive charge of +2. Among these, lead ions has been widely employed due to its superior performance and stability compared to tin and germanium. The latter two are more sensitive to temperature and humidity or have an unstable nature in the 2+ oxidation state.

- **The X site**: the X halide anion can be chlorine (Cl), bromine (Br), or iodine (I). Among these options, bromine has been most effectively utilized due to its better stability under ambient operating conditions. However, iodine is also of interest due to its potential for achieving red light emission.

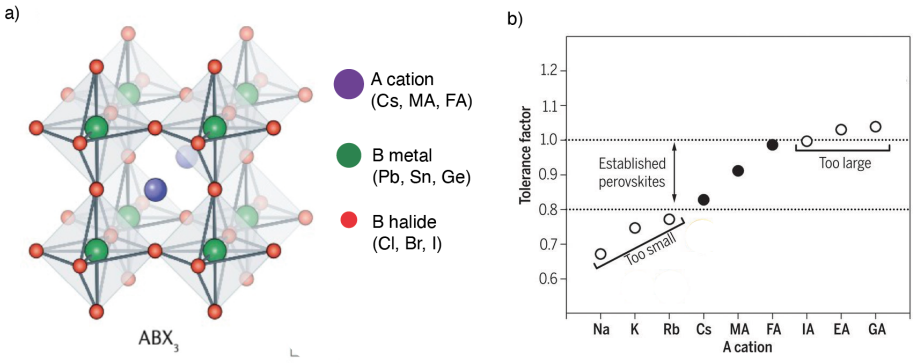

Fig. 1.9 ***Crystalline structure and stabily in perovskites*** *a) Crystalline structure: A is an inorganic or organic movovalent cation, B is a divalent metal cation and X is a halide anion. b) Tolerance factor of perovskite with A cations that are too small (Na, K, Rb), established (Cs, MA, FA), or too large [imidazolium (IA), ethylamine (EA), guanidinium (GA)].*

I will concentrate on investigating inorganic and hybrid organic-inorganic lead bromide perovskite nanocrystals. These nanocrystals will be synthesized using Pb^{2+} for the B cation and Br^{-} for the X halide. The A cation will be Cs^{+} ($CsPbBr_3$ NCs), FA ($FAPbBr_3$ NCs), or a combination of both ($Cs_{1-x}FA_xPbBr_3$ NCs).

1.3.2 Electronic and optical properties of perovskites

Perovskite materials exhibit direct band gaps, making them advantageous for optical devices. In such semiconductor, a photon with energy equal to the band gap energy (E_g) can readily generate an electron-hole pair without a phonon involvement in the process of excitation and de-excitation.

1.3.2.1 Band structure in perovskites NCs

The band structure of ABX_3 perovskites, shown in Figure 1.10a, has been investigated in several works [71, 78]. In these materials, the conduction band minimum (CBM) primarily arises from the p-orbitals of the B metal, while the valence band maximum (VBM) is strongly influenced by the p-orbitals of the halide X ions. Consequently, the bandgap energy is strongly influenced by the composition of the X halide, whereas the contribution from the A cation is relatively minor [79]. To visualize this clearly, I use as example the case of CsPbBr3, which serves as a starting point of my studies.

As shown in Figure 1.10b, in the valence band, strong hybridization occurs between the Pb 6s and Br 4p orbitals and their antibonding interaction leads to the formation of the upper valence band. Conversely, the conduction band is formed through the coupling between the empty Pb 6p orbitals.

Lead halide perovskite exhibit a binding energy (E_b) typically ranging from several to a few tens of meV (2.23 in the case of bulk $CsPbBr_3$) and depending on the composition and dimensionality of the material.

1.3.2.2 Tolerance to structural defects

More interestingly, perovskite NCs are found to be highly defect-tolerant, meaning that they can maintain their excellent electronic and optical properties even with a high density of defects [80]. In general, in semiconductor NCs, surface defects can act as electronic traps [81], affecting carrier mobility, lifetime, and recombination rate even at low concentrations. Due to the lacking of bonding-antibonding interaction between the conduction bands and valence bands, the energy levels of structural defects fall mostly within the conduction band or valence band, rather than within the bandgap itself, as shown in Figure 1.10c. Therefore, these defects are at worst shallow and do not form mid-gap trap states, preserving a clean bandgap [82, 83]. For this peculiar defect-tolerant nature, perovskite NCs exhibit high luminescence

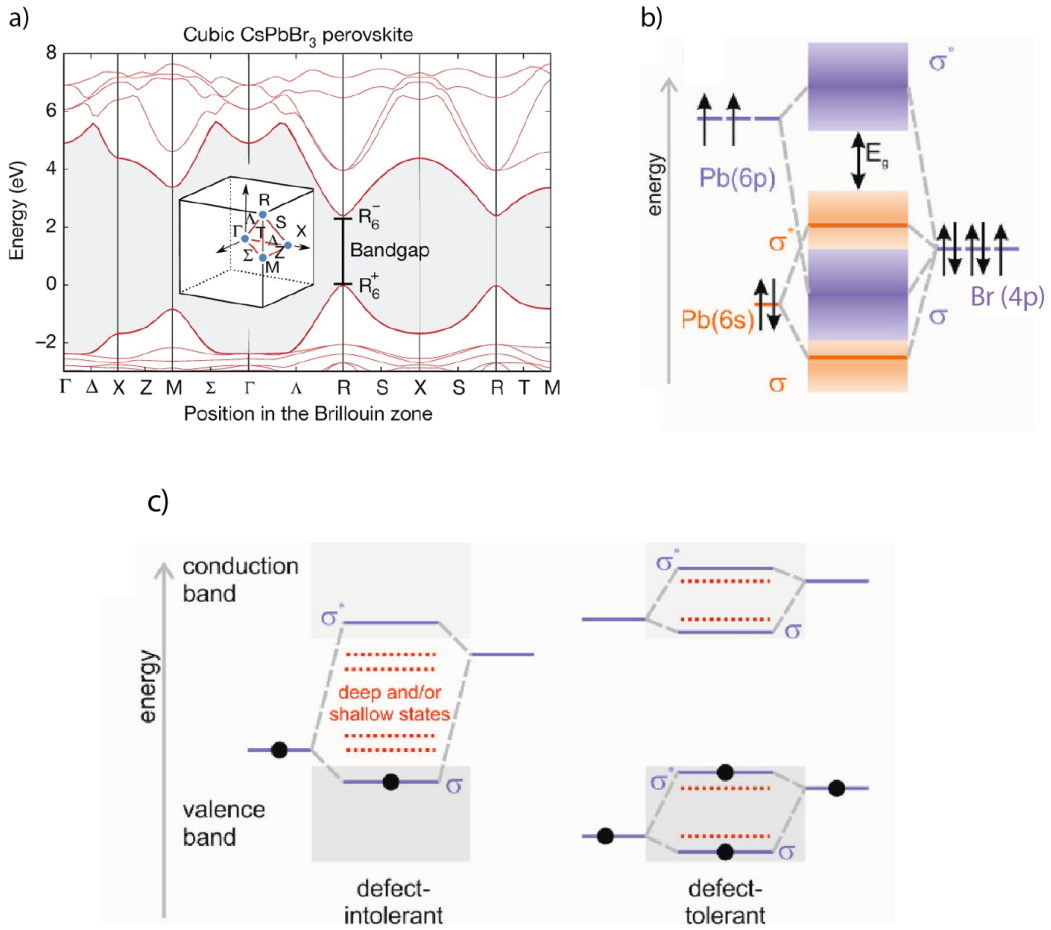

Fig. 1.10 ***Band structure and tolerance to defects.*** *a) Band structure of cubic $CsPbBr_3$ perovskite. The inset shows the first Brillouin zone of the cubic crystal lattice. The electronic bandgap is indicated in the band structure at the R point. Figure reproduced from reference [71]. b) Simplified depiction of the bonding in $CsPbB_3$ NCs (adapted from reference [80]). The band gap is formed between two sets of antibonding orbitals: the top of the valence band (VB) is primarily composed of antibonding states from the 6s orbital of Pb and the 4p orbital of Br, while the bottom of the conduction band (CB) consists of the antibonding states from the 6p orbital of Pb and the 4s orbital of Br. Bonding and antibonding orbitals are denoted as σ and σ^*, respectively. c) Schematics of two cases of a band-structure in semiconductors: defect-intolerant (conventional, left) and ideal hypothetical defect-tolerant (right). Figure reproduced from reference [71].*

even without surface passivation, which is otherwise a necessity for conventional QDs (such as CdSe and InP).

1.3.2.3 Tunability with composition and size

Through composition bandgap engineering, it is possible to tune the bandgap energies and emission spectra of perovskite NCs over the entire visible spectrum, spanning from 410 to 700 nm. The pioneering work by Kovalenko and colleagues [23] demonstrated this capability, as reported in Figure 1.11. The synthesized cubic-shaped $CsPbX_3$ NCs were characterized by remarkable photoluminescence (PL) properties, featuring high quantum yields (QY) ranging from 50% to 90% and narrow emission line widths of 12 to 42 nm. Time-resolved photoluminescence decay measurements of CsPbX3 NCs, as seen in Figure 2d, reveal radiative lifetimes spanning from 1 to 30 ns, with faster emission observed for wider-gap NCs.

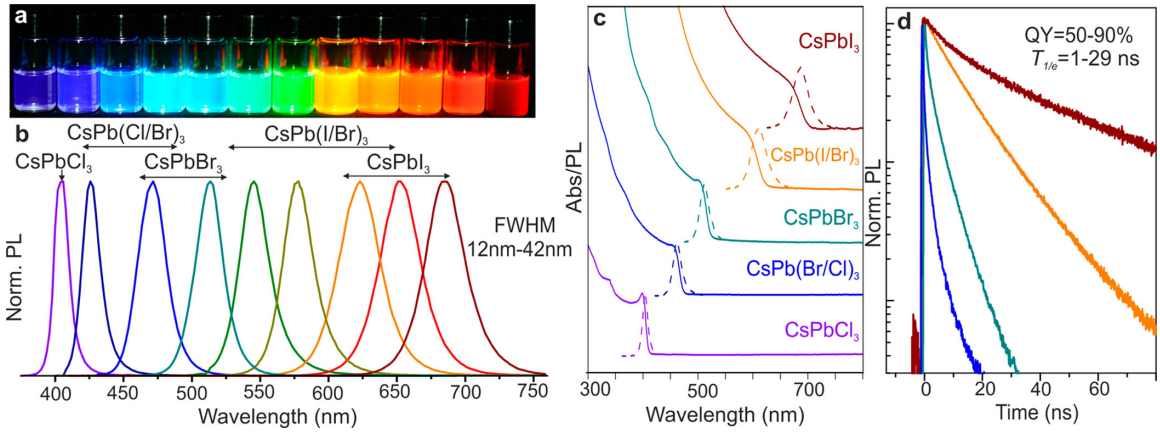

Fig. 1.11 ***Tunabilility with composition in $CsPbX_3$ NCs*** *CsPbX3 NCs (X = Cl, Br, I) composition-tunable bandgap energies covering the entire visible spectral region with narrow and bright emission: a) colloidal solutions in toluene under UV lamp ($\lambda = 365nm$); b) representative PL spectra; c) typical optical absorption and PL spectra; d) time-resolved PL decays. Figures reproduced from reference [23]*

Furthermore, one can tune the absorbance and emission spectra of perovskite NCs by varying the NC size, exploiting quantum size-induced effects. Notably, for CsPbBr3 with an excitonic Bohr diameter of 7 nm, it is possible to achieve strong confinement for sized below this value, as depicted in Figure 1.12.

1.3.3 Synthesis of perovskite NCs

Over the last two decades, extensive research efforts have been dedicated to develop reliable and straightforward techniques for producing high-quality QDs. Among the

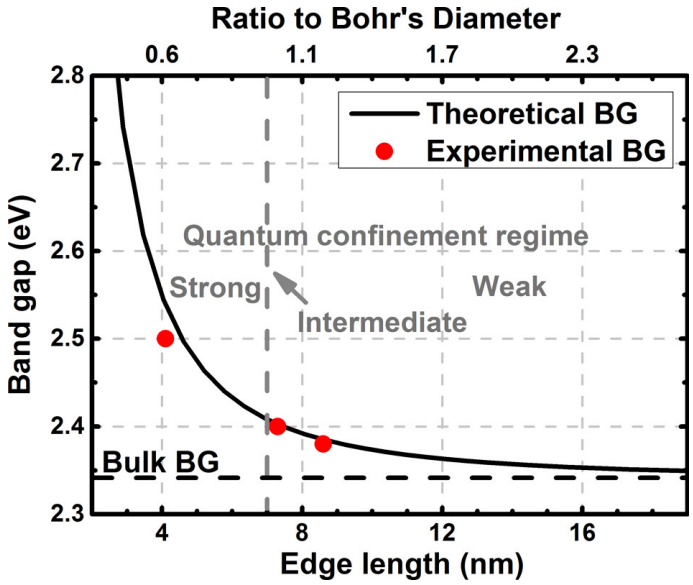

Fig. 1.12 ***Tunabilility with composition in perovskite NCs*** *Experimental versus theoretical (effective mass approximation) particle size-dependent bandgap energy of $CsPbBr_3$ NCs. The quantum confinement regimes is noted in relation to the Bohr diameter (a_b = 7 nm). Figure reproduced from reference [84].*

various methods, the hot-injection approach has emerged as a highly viable route for the fabrication of colloidal perovskite NCs with minimal size dispersion. This method offers practical benefits in terms of ease of implementation and cost-effectiveness.

The hot-injection method involves several essential components, each with a critical role to play:

- **cation and anion molecular precursors**, which are responsible for providing the necessary monomers (atoms) for NC's formation.
- **solvents** that dissolve and disperse the components involved in the growth process.
- **surface ligands** which are molecular compounds that dynamically bind and unbind to the NC surface, effectively modulating the nucleation and growth processes of the NCs. Additionally, these ligands serve to protect and passivate the NC surface, providing stability by preventing degradation and agglomeration. The choice of ligands can significantly influence the stability of the NCs.

The hot-injection method comprises three essential steps, illustrated in Figure 1.13:

1. **Degassing**: cation molecular precursor, surface ligands, and a high boiling point coordinating solvent are combined in a three-neck flask. This mixture is kept under vacuum at an elevated temperature (150-180°) to remove oxygen, water, and impurities.

2. **Hot Injection**: after degassing, the atmosphere is switched to an inert gas (such as Ar or N_2) to further increase the temperature. Once the temperature stabilizes at the reaction temperature (∼180°), the anion precursors are swiftly injected into the reaction bath. The reaction temperature varies depending on the target material system, desired size, precursor reactivity, and other factors. The rapid injection of anion precursor triggers the nucleation, leading to the assembly of freely dispersed atoms. The nucleation is soon terminated due to the temperature drop upon the addition of room temperature precursor, initiating the growth of the nanocrystals by adding atoms to existing nuclei.

3. **Quenching of the reaction**: to stop the growth of the nanocrystals, an excess of ligands is typically injected into the system to prevent the precursors atoms from accessing the nanocrystals. The flask is then cooled in an ice bath.

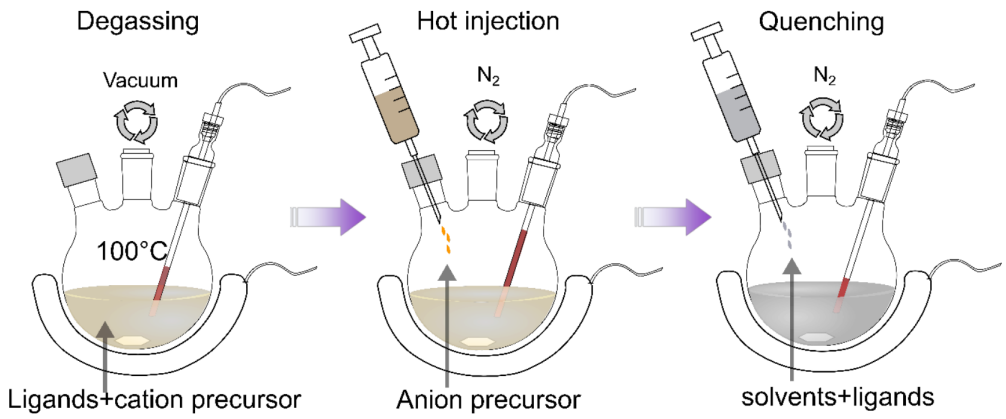

Fig. 1.13 ***Hot injection method.*** *Typical hot injection synthesis of colloidal nanocrystals including degassing of solvents and precursors, hot injection in an inert atmosphere and the quenching of reaction.*

1.3.3.1 Adaptation of hot-injection protocol for CsPbBr3 NCs

The adaptation of the hot-injection method for halide perovskite NCs was initially pioneered by Kovalenko and colleagues [23] in 2015, specifically targeting $CsPbX_3$ (X=Br, Cl, I) perovskite compositions. This synthesis method involves the use of ligands such as oleic acid (OA), octadecene (ODE), and oleylamine (OAm).

In the following, I will provide a concise overview of the key steps of this protocol, with a specific focus on $CsPbB_3$ NCs, as it serves as the foundation for the optimizations discussed in this thesis.

- **Preparation of Cs-OA precursor solution**: initially, a cesium-oleate (Cs-OA) precursor solution is prepared by mixing Cs_2CO_3, oleic acid (OA), and octadecene (ODE). This mixture is heated in a protective atmosphere, typically nitrogen.

- **Dissolution of PbBr2 precursor**: a PbBr2 precursor is then dissolved in a three-neck flask containing octadecene (ODE), oleylamine (OAm), and oleic acid (OA). OA and OAm play crucial roles in solubilizing $PbBr_2$ and stabilizing the nanocrystals as surfactants.

- **Injection of Cs-OA precursor solution**: after complete dissolution of the $PbBr_2$ salt, the Cs-OA precursor solution is rapidly injected into the mixture at a temperature within the range of 140 to 200 °C.

- **Rapid cooling and re-dispersion in toluene**: after waiting several seconds, the solution is rapidly cooled down to room temperature using an ice bath. The resulting NCs are redispersed in toluene.

While this method yields colloidal $CsPbBr_3$ NCs with bright luminescence, it presents challenges in controlling their size, mainly due to the rapid dynamic (a few seconds) of the process. Then, this protocol typically yields nanocrystals with average sizes ranging from approximately 10 to 15 nm. Controlling the growth to achieve nanocrystals with an average size smaller than 7 nm, which corresponds to the excitonic Bohr radius for perovskites, and would place them in a strong confinement regime, is a more challenging task.

Additionally, at room temperature and in contact with air, these nanocrystals are particularly sensitive to light and moisture, resulting in their degradation and subsequent photobleaching, as explained in next section.

1.3.4 Enviromental instability

In the previous sections, we observed that perovskite NCs exhibit an exceptional combination of spectral tunability, straightforward solution synthesis and robust single photon emission. Nevertheless, they also face significant challenges, primarily stemming from their salt-like nature, making them prone to solvent lability. Additionally, they exhibit environmental-induced instabilities, especially in ambient conditions.

In fact, due to the dynamic nature of the ligands, they bind relatively weakly to the NCs' surface. This weak binding makes the loss of ligands during purification and dilution steps very common. Consequently, perovskite nanocrystals become poorly passivated and vulnerable to vacancies on their surfaces, as illustrated in Figure 1.14a. These surface defects serve as centers for non-radiative decay pathways, adversely affecting their photoluminescence.

Furthermore, when exposed to a combination of light, oxygen, and moisture, perovskite nanocrystals undergo photon-oxidation processes and consequent photon-induced structural reorganization, leading to their chemical degradation. As illustrated in Figure 1.14b in the case of $CsPbI_3$ NCs, this results in the etching of the nanocrystal surface layer by layer, starting from the outermost layer and leading to a reduction in NC's size. This size reduction results in an increase in the band-gap energy and a corresponding shift in emission towards the blue, irreversibly ending in emission bleaching.

These drawbacks significantly limit the potential applications of perovskite NCs in quantum technology, where stability is crucially linked to the indistinguishability and coherence of single photons. To address these issues, substantial efforts have been devoted to enhancing the stability of LHPs. This has been pursued through improved ligand passivation [85–88], by growing a surrounding shell [89–91] or by embedding the NCs in a protective matrix to prevent exposure to moisture [92], as illustrated in Figure 1.14c.

In this study, we aim to enhance the stability of $CsPbBr_3$ perovskite NCs without resorting to traditional polymeric matrices, which are not suitable for the NC's deposition on an optical nanofiber. To achieve this, as discussed in Chapter 3, we will implement specific modifications to the conventional synthesis protocol detailed in Section 1.3.3.1, as reduced cesium oleate content, additional ligands and extented reaction time. Additionally, as discussed in Chapter 5, we will employ a Zn^{2+} doping of the B cation to increase the NCs' stability.

.

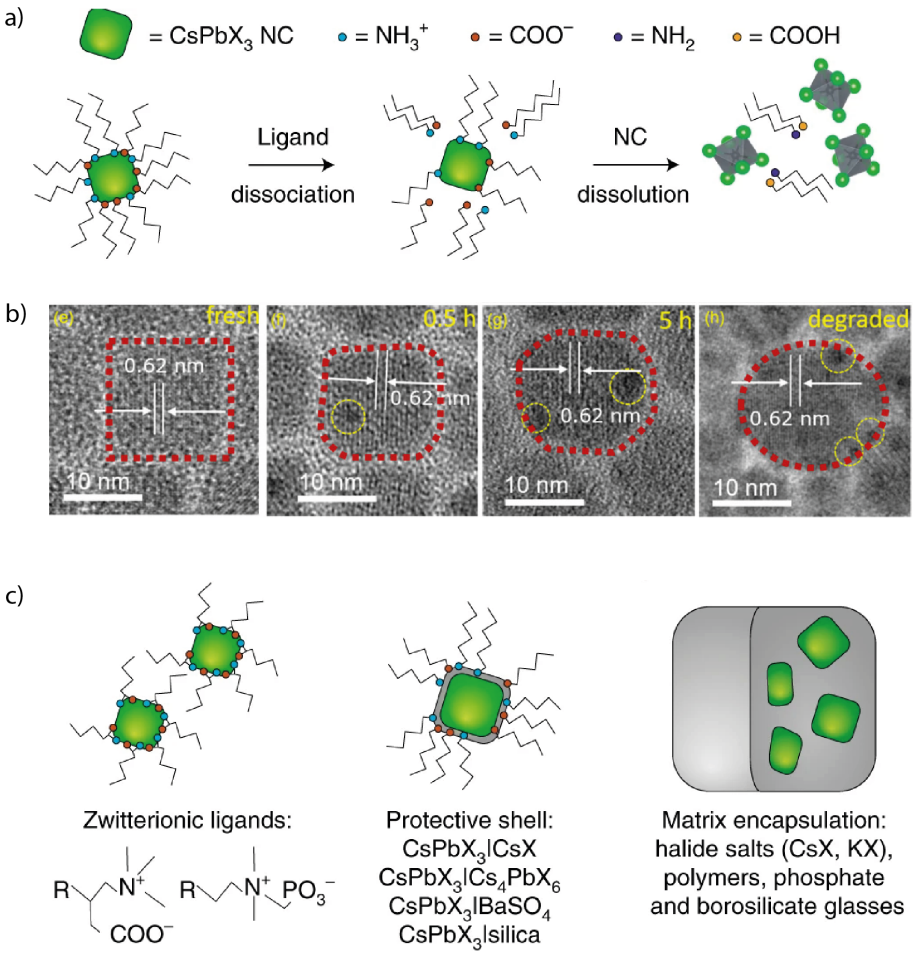

Fig. 1.14 ***Enviromental-induced instability in perovskite NCs*** *a) LHP NCs can lose their colloidal stability due to the desorption of weakly bound ligands. Figure reported from reference [82]. b) Effect of combination of light, oxygen and moisture on $CsPbI_3$ perovskites NCs: transmission electron microscopy (TEM) images showing the reduction of the NC's diameter over time. Figure reported from reference [93]. c) Strategies for attaining stable surface coverage by ligands include using zwitterionic long-chain molecules; overcoating with dielectric shells or compositionally matched salts and matrix-encapsulation into polymers. Figure reported from reference [82].*

Conclusion

In this chapter, I have provided a comprehensive overview of the essential elements necessary to grasp the core concepts of this thesis.

- I defined the characteristics of an ideal single photon source and introduced the key parameters used to evaluate deviations from this ideal in real-world sources, such as single photon purity, brightness and indistinguishability. Additionally, I provided an overview of the systems used for generating single photon emissions.
- Among these systems, I focused on semiconductor nanocrystals, the category to which the perovskite quantum emitters discussed in this thesis belong. In this context, I introduced the fundamental notions of quantum confinement, elucidating the carrier dynamics and the typical optical phenomena that can constrain emission stability and single photon purity in these emitters.
- Finally, I presented the perovskite NCs at the core of this thesis. Beginning with an exploration of the perovskite crystal structure, I delved into their electronic band structure, highlighted their tolerance to defects, and described the tunability of their emission wavelength with size and composition. I then detailed the synthesis method, their instability issues when exposed to illumination and moisture, and the primary strategies employed to mitigate these challenges.

Chapter 2

Experimental setup and methods

Contents

Introduction

In this chapter, I describe the experimental setup employed for characterizing the single photon emitters discussed in this thesis. Section 2.1 outlines the preparation process of the samples after their synthesis. Section 2.2 provides a comprehensive overview of the experimental setup, covering both the wide-field and confocal schemes that were utilized to characterize the prepared samples. Section 2.3 details the steady-state measurements conducted to study the optical properties and stability of the emitters, and Section 2.4 discusses the time-resolved measurements performed to examine their quantum properties and blinking behavior and explains the associated data processing procedures.

2.1 Sample preparation and conservation techniques

After the synthesis via the hot-injection method, described in Section 1.3.3, the perovskite solutions can be stored in vials, shielded from both light and moisture, for several weeks without undergoing significant degradation. For sample preparation, a small amount of the nanocrystal (NC) solution is deposited onto a glass coverslip for microscopic observation. To reduce the NC concentration, the original solution can be diluted with toluene before deposition. The chosen glass coverslips (Thorlabs CG00C) exhibited minimal auto-fluorescence and possessed a thickness ranging from 85 to 115 µm, allowing the use of an oil objective with a high numerical aperture for improved light collection.

The deposition was carried out using the spin-coating technique, wherein the sample is rotated at a high speed, as illustrated in Figure 2.1, typically at around 1000 - 1500 rotations per minute (rpm). The centrifugal force facilitates the uniform spreading of the NCs, reducing the formation of clusters and enabling simultaneous drying via solvent evaporation to form a thin substrate film. The film's thickness depends on various parameters, including angular speed, acceleration, process duration, and the quantity (and possibly viscosity) of the deposited solution. For the samples presented in this thesis, approximately 50 µL of solution were deposited onto the glass coverslip, with a velocity of 1000 rpm, an acceleration of 1000 rps/s, and a process duration of 100 s.

After the fabrication, the samples were stored at room temperature (around 20 °C), protected from light and moisture. It is important to note that, in general,

the deposited samples have a limited storage duration and typically remain stable for a few days or a week. Beyond this time, bleaching can become increasingly evident. To ensure measurement comparability, fresh samples were prepared daily.

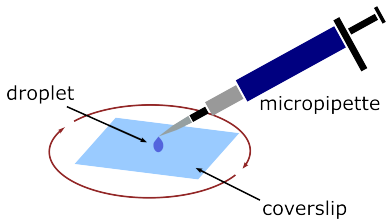

Fig. 2.1 ***Spin-coating technique.*** *The sample is rotated at high speed (around* 1000 *rotation per second).The centrifugal force facilitates the uniform spreading of the NCs, reducing the formation of agglomerates and enabling simultaneous drying via solvent evaporation to form a thin substrate film.*

2.2 Experimental setup

The experimental setup used for characterizing the nanocrystals (NCs) is illustrated in Figure 2.2. The perovskite samples are placed on a microscope (Nikon Eclipse Ti) equipped with a motorized stage (MadCityLabs) with high resolution x-y plane displacement, enabling investigation of the entire sample.

Two different excitation schemes are employed. In the first scheme, the NCs are observed using wide-field fluorescence microscopy, which provides an overview of the sample and facilitates the systematic selection of individual emitters for further characterization. In the second scheme, a pulsed laser light in a confocal configuration is employed to selectively excite a specific targeted NC. For both wide-field and confocal schemes, the excitation light is reflected towards the sample by means of a dichroic mirror placed at an incident angle of 45° to the incoming light. An objective lens is used to both focus the excitation light and back-collecting the NC's fluorescence. A high numerical aperture ($NA = 1.4$) infinity-corrected oil objective with a $100X$ magnification is employed to obtain high (diffraction-limited) spatial resolution[1].

[1]In oil objectives, a tiny droplet of oil is deposited between the front lens of the objective and the glass coverslip, replacing the air gap commonly found in air objectives. The oil used has a refractive index of 1.515, which is closer to the refractive index of the glass coverslip (n = 1.523) than air. This adjustment results in an increased maximum angle of the cone of light that can enter the front lens of the objective. This characteristic is described by the numerical aperture (NA) of the objective.

The emitted light collected by the objective is filtered to remove residual pump laser light, and directed to the detection setup. The NC's photoluminescence (PL) can be measured using both steady-state (time-averaged) and time-resolved techniques. In the case of steady-state measurements, the collected light can be imaged on a camera (HAMAMATSU ORCA Flash 4.0 LT) or sent to a spectrometer (Princeton Instrument Acton SP 2500) equipped with a CCD camera (Princeton Instrument Pixis 400). Alternatively, for time-resolved measurements, the collected light is sent using a flip mirror to a pair of avalanche photodiodes (APDs) (Excelitas SPCM-AQRH-14-FC) in a Hanbury Brown-Twiss (HBT) configuration to record single photon events. The aforementioned excitation schemes and PL measurement techniques, including steady-state and time-resolved PL, are described in detail in the following paragraphs.

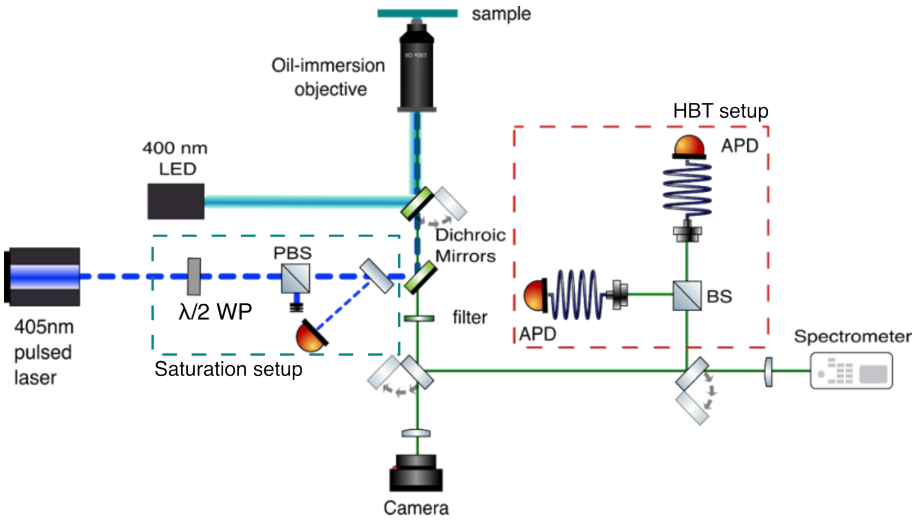

Fig. 2.2 ***Experimental setup for microscope analysis.*** *In wide-field configuration, a LED light is reflected by a dichroic mirror with cut-on at 435 nm and sent to the sample, via a microscope objective with high numerical aperture ($NA = 1.4$) . For the excitation of a single nanocrystal, a pulsed laser light is reflected towards the microscope objective with a 415 nm dichroic mirror. The collected light is further filtered to remove spurious excitation and then sent optionally to the camera, to the spectrometer or to the HBT setup. DM: dichroic mirror, BS: non polarizing beamsplitter, PBS: polarizing beamsplitter, PD: photodiode. λ/2: rotating half-wave plate.*

Higher numerical aperture objectives have a broader angular collection, allowing them to capture a larger amount of light.

2.2.1 Wide-field microscopy

In the wide-field configuration, a light-emitting diode (LED) light beam at 400 nm (CooLED pE−100) is employed to illuminate a large area of the sample, with dimensions of 133 µm x 133 µm.

The LED offers an irradiance control with a resolution of 1% of the maximum power (25 W). In this work, a power of 2.5 W is utilized to have an overview of the sample and locate the emitters, while the full power is used to perform measurements of photo-stability in dilution. As illustrated in Figure 2.3a, to direct the LED beam to the sample, a dichroic mirror (Edmund) with a cut-on at 435 nm is employed. The LED light is then focused onto the sample through the oil objective.

The ensemble PL is collected back through the objective lens and filtered from the residual LED excitation using both the dichroic mirror and an additional long-pass filter with a cutoff at 450 nm (THORLABS). After filtering, the fluorescence is imaged on a the camera, controlled via the *HCImage* software. Figure 2.3b shows a representative wide-field microscopy image, where NCs are visible as bright spots on a dark background.

One of the key advantages of this technique is the real-time visualization of the sample, depending on the camera integration time. In our case, the integration time is set at 300 ms, enabling often the direct observation of blinking effects. In contrast, other methods such as spot-by-spot scanning of the sample under confocal light mapping are slower and often less suitable to distinguish individual NCs from small clustered ones.

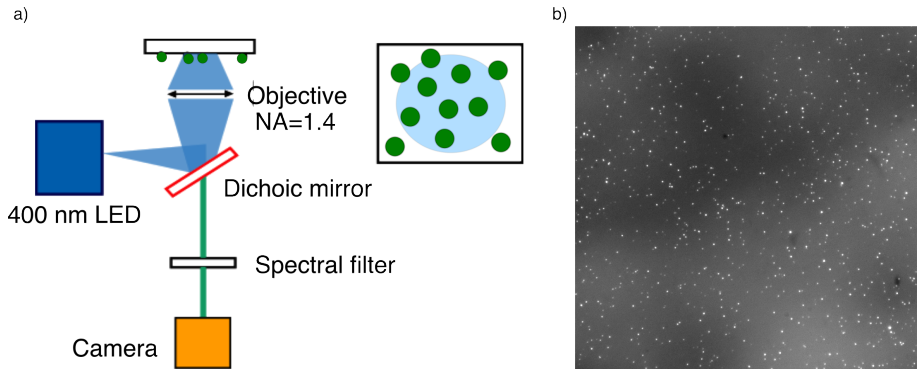

Fig. 2.3 ***Wide-field microscopy scheme.*** *a) Schematic of the wide-field microscopy scheme. b) Example of the imaging of a sample area of* 133 µm *x* 133 µm.

2.2.2 Confocal microscopy

Once the emitter for characterization is selected, the sample on the translation stage can be moved to precisely displace the emitter. The translation stage used offers a high resolution, allowing displacements as small as 95 nm for accurate alignment of the laser excitation with the chosen emitter. This precision ensures that the emitter can be positioned precisely at the center of the camera frame, where the laser spot is located.

The laser employed in this setup is a picosecond pulsed diode laser (LD405-B, PicoQuant), emitting light at a wavelength of 405 nm. Its repetition rate is adjustable, and it is chosen of 2.5 MHz for the measurements presented in this thesis. This results in delay times between two pulses of 400 ns and a pulse width of less than 100 ps. The laser beam is coupled into a single-mode fiber optic patch canble (Thorlabs, P3-405B-FC) to reach the entrance of the microscope. As illustrated in Figure 2.4a, within the microscope, the laser light is reflected by a dichroic mirror (SEMROCK) with a cutoff at 415 nm and directed towards the sample through the objective lens. It is then spectrally filtered using the dichroic mirror and a long-pass filter (SEMROCK) with a cutoff at 405 nm to eliminate any residual laser excitation. The fluorescence emitted by the NC is back-collected by the objective lens. At the output of the microscope, the collected light is collimated using a lens and directed towards the detection part, enabling steady-state and time-resolved fluorescence measurements. Figure 2.4b provides an image of the photoluminescence of a nanocrystal in the confocal microscopy scheme, imaged by the camera.

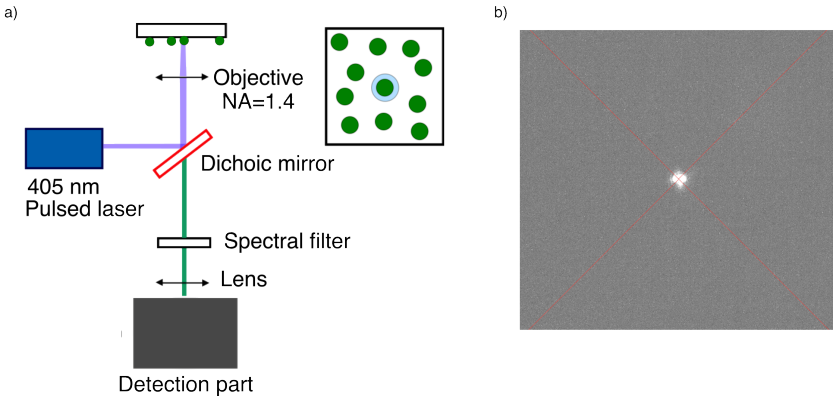

Fig. 2.4 ***Confocal microscopy scheme.*** *a) Schematic of the confocal microscopy configuration. b) Example of the imaging when one individual particle is excited.*

2.3 Steady-state measurements

2.3.1 Photoluminescence spectra

The spectrometer employed in our setup utilizes a Czerny-Turner configuration, incorporating diffraction gratings mounted on a rotating turret and two parabolic mirrors. The light collected from the source is focused onto the entrance of the monochromator using a lens. Once within the monochromator, the beam is collimated by the first curved mirror, impinges on the diffraction grating, leading to dispersion, and is subsequently directed toward the second curved mirror. The second mirror focuses the dispersed beam onto the output ports, and in our case, the entire dispersed beam is imaged by the CCD camera. Control over the spectrometer is managed through the *LightField* software. The acquired spectra are obtained using an integration time of 5 s, and each spectrum represents an average of 5 acquisitions.

In our confocal measurements, the primary goal is to examine individual NCs. Therefore, we specifically target smallest NCs. In cases where the emission spectrum of a selected NC exhibits multiple visible peaks, indicating that it may be part of a cluster, I exclude this emitter from the analysis and proceed to select a different one. No other preselection criteria are applied during the emitter selection process. Since the emission spectrum is the initial measurement conducted on the emitters and their saturation power is not yet known, all spectra are acquired with an excitation fluence around 2.5 µJ/cm^2 with a repetition rate of 2.5 MHz and a spot laser diameter of 1.5 µm. This facilitates a straightforward comparison of the PL counts among different emitters.

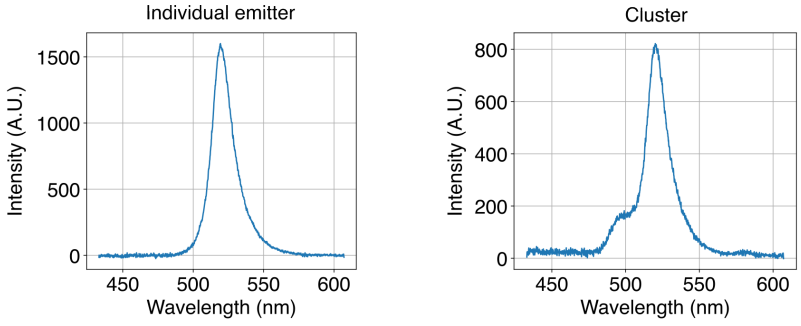

Fig. 2.5 ***Photoluminescence emission spectra.*** *Photoluminescence emission spectra in the case of an individual emitter (left) and a small cluster (right). The spectra are obtained using an integration time of* 5 s*, and each spectrum results from an average of* 5 *acquisitions.*

2.3.2 Saturation measurements

Measuring the saturation power of each NC is crucial when comparing the quantum properties of different emitters. This type of measurement is typically conducted by exciting the NC with increasing laser excitation powers and collecting its photoluminescence, obtaining a saturation curve.

In the experimental setup for this measurement, a shutter is used to block the excitation laser when it is not required, a rotating wave-plate is employed to vary the laser power; a photodiode and a camera are utilized to measure the input and output PL intensities, respectively.

The measurement procedure is as follows:

- **Initial calibration:** the laser's maximum and minimum powers are measured using a power-meter and the corresponding rotation position of the wave-plate are input through the control Python computer interface.
- **Emitter preparation:** the emitter of interest is positioned under the laser spot.
- **Area selection:** a region within the camera frame where the emitter is visible is carefully chosen, excluding irrelevant pixels to enhance the signal-to-noise ratio. The area of this frame is around 5 µm x 5 µm.
- **Measurement initiation:** the measurement sequence begins with the shutter closed, and the wave-plate set to the position of minimum intensity. During each cycle, the wave-plate rotates by a specified degree value, determined by the settings, until the wave-plate reaches the position of maximun intensity.
- **Cycle operations:** several actions are performed at each step within a cycle.
  - With the shutter closed, the camera captures the background to establish the baseline intensity.
  - The miminum excitation power is recorded using the photodiode.
  - The shutter is opened and the emitted PL is measured with the camera. To correctly assess the saturation power, this intensity is acquired three times, and the highest value is retained. This allows to mitigate the impact of blinking on the measurement, minimizing the probability that the emitter is in low emissive state.

  - The shutter is closed, the wave-plate is rotated by the predetermined angle, and the subsequent excitation power is recorded using the photodiode. These steps are iterated around ten times.

- **Data analysis:** once the measurement is concluded, the PL data are plotted as a function of the excitation power.

This systematic procedure ensures the acquisition of reliable data for the emitter's saturation curve. The obtained curve is fitted using the saturation function:

$$I = A[1 - e^{-\frac{P}{P_{sat}}}] + BP \tag{2.1}$$

where P_{sat} is the saturation power, and A and B are two constants that depend respectively on the intensity of the single- and bi-exciton components of the emission, as explained in Section 1.2.3.2. By extracting the P_{sat}, it becomes possible to readily compare the behavior of different emitters.

Let's conclude with some considerations on aging and measurement repeatability. Acquiring the measurement three of four times without degrading the sample is possible, and this results in saturation curves that are almost entirely overlapping in cases where blinking is highly reduced or faster than the photodiode integration time. This is shown in Figure 2.6 for two saturation curves taken a few minutes apart. However, since during the saturation measurement the emitters are excited at much higher powers than their saturation power, the measurement cannot be repeated a large number of times because it would stress the emitters and lead to bleaching.

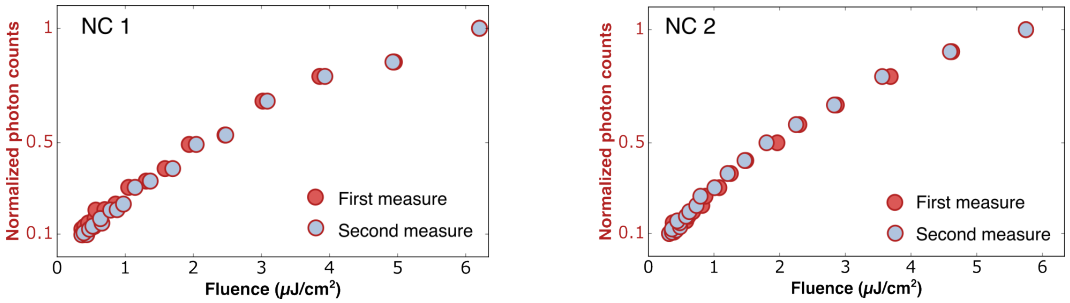

Fig. 2.6 ***Repeatability of the saturation measures.*** *Examples of two saturation measures taken on two different NCs. For each NC, two measures are taken a few minutes apart.*

2.4 Time-Correlated Single Photon Couting (TCSPC)

Our primary objective is to conduct a comprehensive study of the emission's temporal dynamics across various timescales. To achieve this, we employ the Time-Correlated Single Photon Counting (TCSPC) technique, which allows us to determine fluorescence lifetimes, investigate photoluminescence fluctuations (blinking), assess bleaching, and measure the second-order correlation function to assess the single photon purity of the NCs.

To implement the TCSPC technique, we utilize a Hanbury Brown-Twiss (HBT) setup, illustrated by the red dashed line in Figure 2.2. By employing a flip mirror, we redirect the PL signal from the spectrometer path to the HBT setup. This configuration consists of a $50-50$ BS that divides the signal into two parts, each of which is directed to separate avalanche photodiodes (APDs) via single-mode fibers. For signal recording, we employ a Picoquant PicoHarp 300 TCSPC card together with a Picoquant PDL 800 router. In the following paragraph, I will provide a detailed explanation of the data acquisition process, including the information recorded and the data processing procedures.

2.4.1 Data acquisition

In time-resolved fluorescence measurements with TCSPC, the detection of each photon involves a series of steps, as illustrated in Figure 2.7a. The APDs produce TTL output signals, with each output pulse routed to the router. The router converts these optical events into electrical pulses and directs them to a single channel, designated as channel 1, on the PicoHarp card. The synchronization (SYNC) input of the TCSPC device is synchronized with the laser. The SYNC signal, after suitable voltage conversion[2], is then sent to one channel of the PicoHarp card, typically channel 0.

Let's delve into the operation of the PicoHarp 300 card in more detail (Figure 2.7b). When a measurement initiates, it establishes an absolute zero time reference (T_0). The laser synchronization pulse triggers a timer, which halts upon the detection of a fluorescence photon using a time-to-amplitude converter (TAC). The TAC functions as a highly linear ramp generator, starting with one signal and stopping with the other, resulting in a voltage proportional to the time difference between

[2]The laser and the card use a different standard, thus the signal needs to be attenuated and inverted as explained in the PicoHarp manual.

these two signals. This voltage from the TAC is then sent to an Analog-to-Digital Converter (ADC), providing a digital timing value used to address the histogram memory, often referred to as the *Histogrammer*. The histogram memory consists of a series of memory cells or *time bins*, and the width of each bin can be arbitrarily set (in this work, it is set to 128 ps). During the excitation cycles, these memory cells store data whenever a digital signal is received from the ADC.

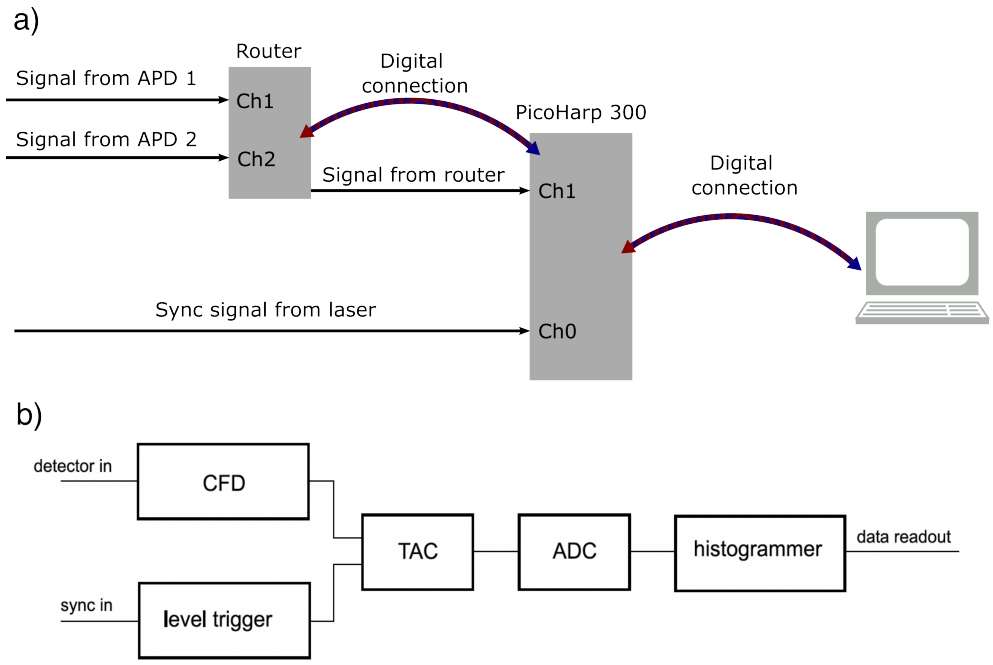

Fig. 2.7 ***Architecture of the TCSPC apparatus.*** *a) Working scheme of the TCSPC apparatus. The router transmits the detected signal to the PicoHarp card, passing the information on which channel the signal arrived from. The PicoHarp card measures the arrival time of the sync signal from the laser, given by the channel 0. The detection signal from the router is received in channel 1. After the stop signal is received, the card has a dead time on the order of hundreds of nanoseconds before being able to detect another signal on the same channel. b) Block diagram of a the PicoHarp card. CFD: Constant Fraction Discriminator, TAC: Time to Amplitude Converter, ADC: Analog to Digital Converter.*

As summarized in Figure 2.8, for each detected fluorescence photon, the following information are recorded:

- The SYNC signal that triggered the photon, represented as an integer number starting from 1 (the first laser pulse sent in the measurement) and increasing with each subsequent pulse, even if no photons are collected.

- The delay between the detected photon and the corresponding SYNC signal, referred as the *microtime (t)*.
- The time elapsed with respect to the absolute zero time (the reference being the first SYNC signal), refered as the *macrotime (T)*.
- The channel (and thus the corresponding APD) on which the photon was detected.

By tagging each fluorescence photon with its absolute arrival time T, delay time relative to the excitation laser pulse t, and the detection channel, it becomes possible to simultaneously measure fluorescence blinking traces, fluorescence decays, and coincidences of the detected photons.

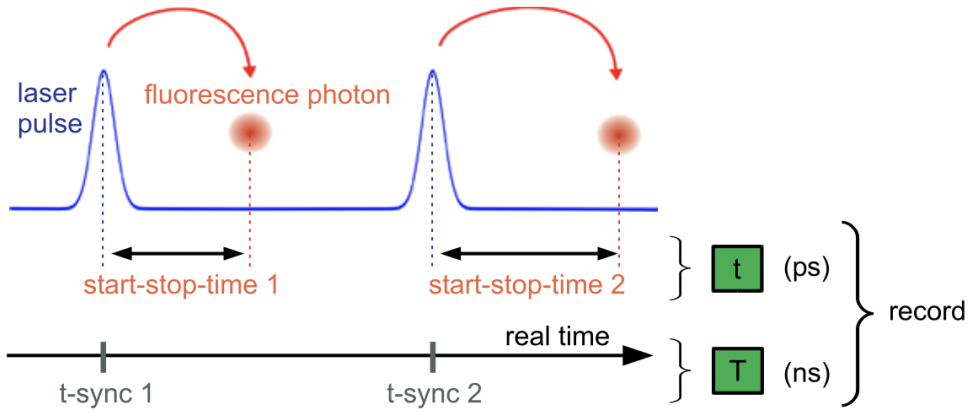

Fig. 2.8 ***TCSPC measured data*** *For each photon triggered by a SYNC signal, the card records the delay between the detected photon and the corresponding SYNC signal(microtime t) and the time elapsed with respect to the first SYNC signal (macrotime T).*

2.4.1.1 Experimental limitation of the TCSPC apparatus

One drawback of the used TCSPC card is that the signals from both APDs are directed to the same channel on the card (channel 1 in Figure 2.7). As a result, channel 1 records all the events. Each time a photon is detected, there is a dead time, referred to as t_{dead}, during which the channel cannot collect any other signals. This poses a significant challenge when measuring coincidences between the two detectors. In fact, the dead time restricts the measurement of delays, denoted as t_δ, shorter than

t_{dead}. We can formally express this limitation by stating that we cannot measure τ if the following condition holds:

$$|\tau| \leq t_\delta \tag{2.2}$$

To overcome this limitation, a workaround can be employed by incorporating a delay line. Introducing a delay, denoted as T_{delay}, in the arrival time of photons from one of the two channels allows us to modify the condition as follows:

$$T_{delay} - t_\delta \leq \tau \leq T_{delay} + t_\delta \tag{2.3}$$

By using a delay line with an appropriate length (in our case a cable of 50 m) that exceeds the interval specified by equation 2.3, we ensure that the interval does not contain $\tau = 0$.

To visualize the effect of the delay line in single photon detection, let's refer to Figure 2.9. An ideal experiment is presented with and without the addition of a delay line, shown at different times. Let's consider two photons emitted almost simultaneously at time t_0. Initially, they follow the same trajectory until they reach a beamsplitter at time t_1, at which point they diverge into separate paths. Although it's possible for the photons to continue along the same path, we will focus on the scenario where they propagate along distinct paths. In the absence of a delay line, both signals arrive nearly simultaneously at time t_2 on different detectors, resulting in only one of them being recorded by the card. However, when a delay line is introduced, one photon arrives later, precisely at time t_3, given by $t_3 = t_2 + T_{delay}$. By subtracting T_{delay} from the time measured by the second detector, we can accurately reconstruct the original signal.

What occurs if both photons are detected by the same detector? This scenario can lead to challenges due to the finite dead time of the detector. When the number of photons detected during a single excitation cycle exceeds 1, the system often registers the first photon while missing subsequent ones. This phenomenon is referred to as *pile-up*. Consequently, this can result in a falsely distorted decay histogram. To ensure the accuracy of single-photon statistics, it is crucial to maintain a low average count rate at the detector. Ideally, the count rate should not exceed $5 - 10\%$ of the excitation rate. For example, when using a diode laser pulsed at a repetition rate of 2.5 MHz, the average detector count rate should not surpass 250 kHz. In our setup configuration, the photoluminescence of perovskite NCs results in signals on the

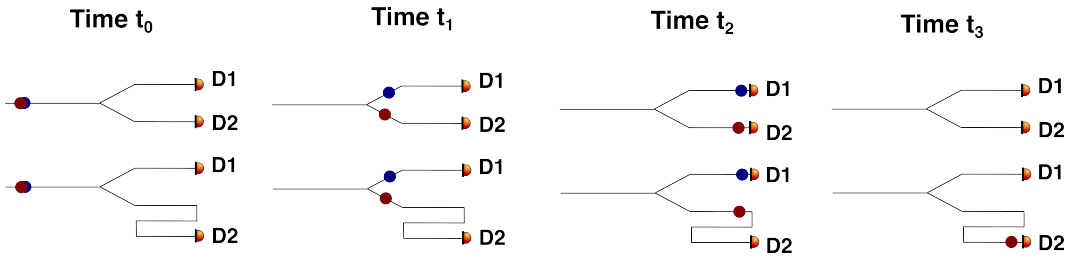

Fig. 2.9 ***Delay line effect on photon detection.*** *In each panel, the configuration without (upper path) and with (lower part) the delay line is represented. At time t_0 two photons are emitted simultaneously, and at the time t_1 they are separated on different paths by the beamsplitter. At the time t_2, in the configuration without delay line, the two photons arrive at the two detectors and only one is recorded. Instead, with the delay line, only one photon arrives on the detector, while the other arrival is delayed. In case with the delay line, at the time t_3 the second photon arrives on the detector and its true arrival time with respect to the first one can be obtained by subtracting $\delta = t_3 - t_2$.*

APDs ranging from approximately 5 KHz to 100 KHz, thus satisfying this constraint.

2.4.2 Data processing

With the acquired data, one can readily derive various quantities discussed in this thesis. These include the photoluminescence decay, the PL-time trace, and the second order correlation function at both short and long time delays.

2.4.2.1 Photoluminescence decay

To obtain the photoluminescence decay, a histogram is constructed using the micro-time data, which represents the time delay between the triggers and the photon detections. To achieve accurate decay measurements, the pulsed laser excitation source must satisfy specific conditions. Firstly, the pulse durations should be considerably shorter than the excited state lifetime, ensuring that the entire lifetime is captured within a single pulse. Second, the period of the laser pulses should be longer than the lifetime to allow sufficient time for the decay process to occur. For example, at room temperature with lifetimes ranging from 1 ns to 100 ns, the PDL 800 laser source can offer a repetition rate of 2.5 MHz (corresponding to a distance of 400 ns between two pulses) and a pulse width of less than 100 ps. To record the fluorescence decay, the measurement is repeated over numerous excitation cycles, and the delay times

between excitation and photon detection are sorted into a histogram. This histogram yields valuable insights for determining the lifetime of the emissive states.

2.4.2.2 Photoluminescence time-trace

The photoluminescence versus time, referred to as the PL time-trace, is derived by constructing a histogram based on the macrotime data. This histogram counts the number of photons detected by the APDs within specific time bins, as illustrated in Figure 2.10.

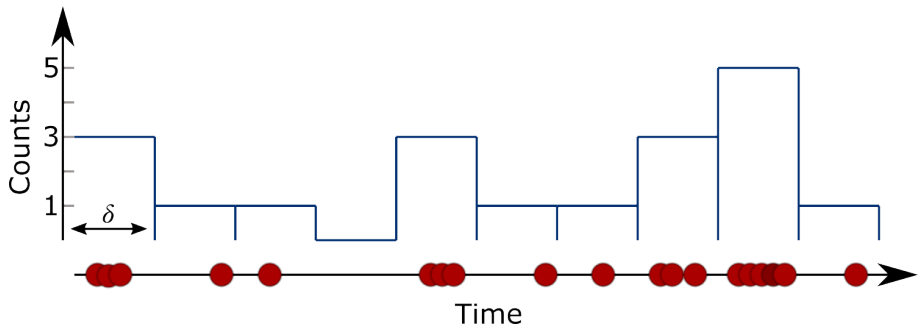

Fig. 2.10 ***Exemplification of the creation of the blinking trace.*** *Each bin δ of the histogram reports the number of photons (in red) arrived in the corresponding time interval.*

It is desirable to choose a small bin time to observe fast intensity fluctuations and avoid excessive averaging of low and high intensity levels. However, there is a limit to how small the time bin can be. The bin size should not be too small due to the need for a good signal-to-noise ratio and/or the finite temporal resolution of the detector. Consequently, the bin size is ultimately constrained by the emission rate of the emitter and collection efficiency of the experimental setup.

For instance, Figure 2.11 presents examples of a PL time traces obtained with a bin time of 1 ms, 10 ms and 50 ms, respectively. The figure also includes the corresponding noise background. In the case of a 1 ms bin, the signal-to-noise ratio is poor, while in the case of a 50 ms bin, this results in significant averaging of the counts. In this thesis, a bin of 10 ms is chosen as good compromise.

2.4.2.3 Second order correlation function $g^{(2)}(\tau)$

Finally, using the microtime, the macrotime and the channel on which each photon is detected, it is possible to compute the photon coincidences between the two APDs,

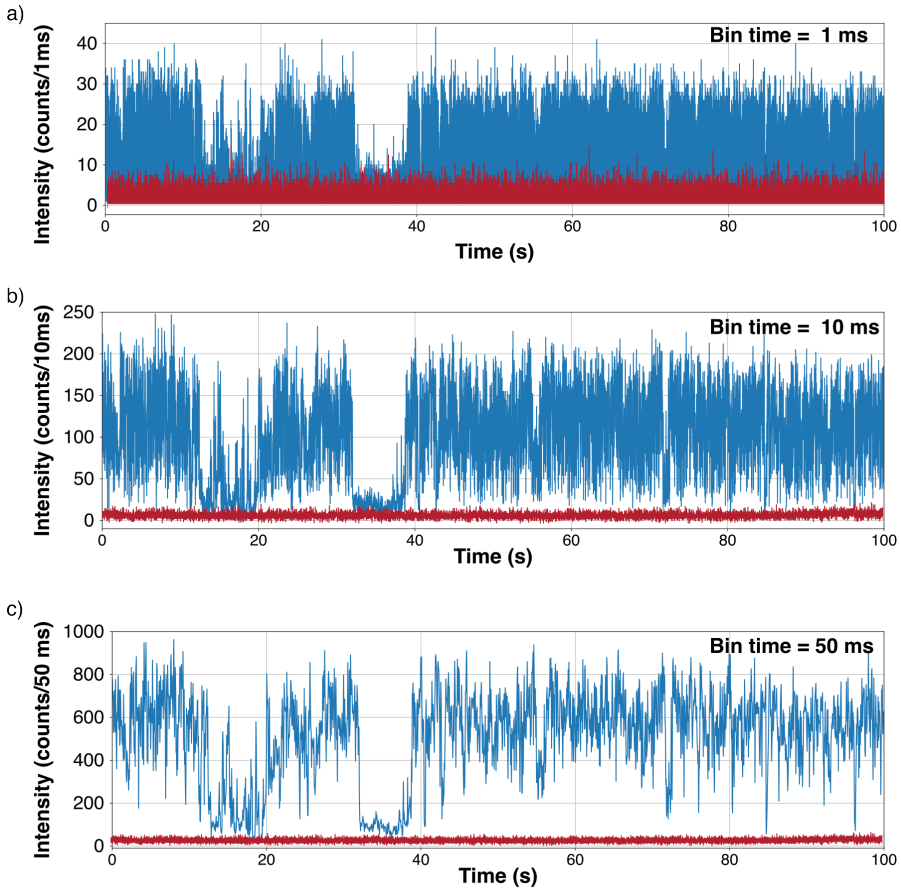

Fig. 2.11 ***Choice of binning time in the PL time-trace)*** *The PL time-trace is reported for a binning time of 1) 1 ms, b) 10 ms, c) 50 ms.*

determining the time delays between the photons detected in one channel and those detected in the other channel. Subsequently, we can construct a histogram of these time delays, as shown in Figure 2.13a. This allows to measure the second-order correlation function $g^{(2)}(\tau)$. The histogram showcases discrete peaks separated in time by the inverse of the laser repetition rate. After normalization, the peak at zero time delay $g^{(2)}(0)$ indicates the probability that both detected photons originated from the same laser pulse, while the adjacent peaks represent coincidence events from consecutive laser pulses. Any residual $g^{(2)}(0) > 0$ can be attributed to the probability of bi-exciton events and subsequent two-photon emission. If examining the $g^{(2)}(\tau)$ histogram at short delays (Figure 2.13a) is essential for assessing single photon purity, the $g^{(2)}(\tau)$ histogram at long delays (Figure 2.13b) can provide valuable insights into the blinking behavior, as shown in next chapters.

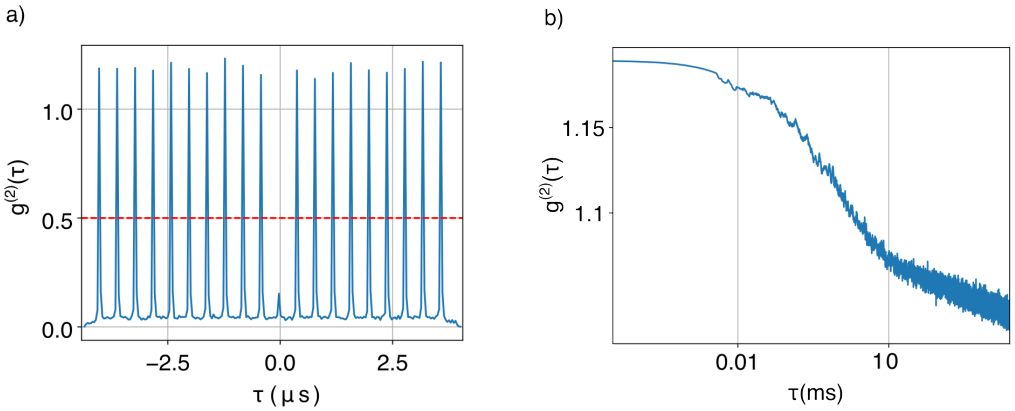

Fig. 2.12 ***g*(2)(τ) histogram.** *a) $g^{(2)}(\tau)$ is visualized at short delays in the range $(-4\mu s, 4\mu s)$. b) $g^{(2)}(\tau)$ is visualized for time delays up to 10 ms.*

Figure 2.13a displays an example of the histogram obtained from the TCSPC card. The y-axis represents the number of measured photon coincidences, and a noticeable shift of the $g^{(2)}(0)$ value (to approximately 300 ns from the origin of the time axis) is observed. This shift is due to the introduction of the delay line, as previously discussed.

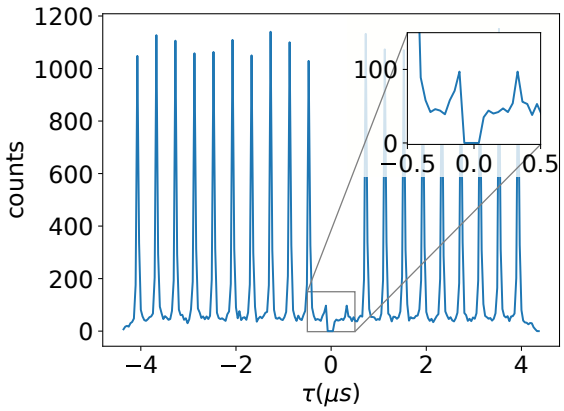

Fig. 2.13 ***g*(2)(τ) histogram before normalization**. *The y-axis reports the number of measured coincidences. The histogram counts are then normalized to the average of the peaks with a delay $\tau > 10ms$. In the inset is clearly visible the dead time of the instrument, that is eliminated in the normalized histogram.*

To obtain the histogram depicted in Figure 2.13b several steps are required:

- Subtract background noise.

- Adjust the zero point of the time axis to eliminate the impact of the delay line.
- Normalize the data to represent the $g^{(2)}(\tau)$ function rather than the number of coincidences.

Regarding background noise, there are four distinct sources of noise to take into account:

- Light from the surrounding room, including emissions from computer screens, etc.
- Residual excitation light.
- Dark counts of the APDs, which correspond to the intrinsic noise of the detector. Thermally-generated carriers within the semiconductor can initiate the avalanche process and resulting in the generation of output pulses. The APDs employed in this study exhibit a typical dark noise level of 100 counts/s.
- Autofluorescence originating from the glass coverslip. In our case, at the excitation power utilized for the nanocrystals and with the specific coverslip employed, the autofluorescence noise from the coverslip is negligible.

Finally, regarding the normalization process, due to the presence of blinking, the $g^{(2)}(\tau)$ function tends to show a super-poissonian behavior at short delays and to converge to 1 at long delays. To normalize, we calculate the average of the maximum values of the peaks with a delay $\tau \geq 10ms$, and then normalize the histogram counts by this average.

Conclusion

In this chapter, I described the experimental setup and the techinques that were employed to characterize the quantum emitters. Specifically,

- I outlined the sample preparation and preservation techniques that were utilized to ensure consistent experimental conditions, preventing aging effects and facilitating reliable measurements and comparisons.
- I provided a comprehensive overview of the experimental setup, covering both wide-field and confocal schemes that were used for characterizing the fabricated samples.
- I detailed the steady-state measurements that were conducted to investigate the optical properties and stability of the emitters. This included the criteria used for selecting emitters and comparing their optical and quantum properties.
- I discussed the time-resolved measurements that were performed to examine the quantum properties and blinking behavior of the emitters, explaining the associated data processing procedures."

This technique and methods are been used to characterized the perovskites emitter in Chapter 3, Chapter 4 and Chapter 5.

Chapter 3

Characterization of $CsPbBr_3$ NCs

Contents

Introduction

Perovskite NCs are highly appealing as potential single photon sources due to their excellent optical properties. However, their instability, particularly due to illumination and moisture, poses a significant challenge. Overcoming these instabilities is imperative to enable their practical use in photonics devices and integrated single photon sources. In this chapter, I delve into a in-depth characterization of $CsPbBr_3$ NCs, as starting point of my optimization study. These NCs were synthesized at the Institut des Nanosciences de Paris (INSP) in Paris, using an approach initially developed for growing $CsPbBr_3$ nanoplatelets, resulting in the formation of $CsPbBr_3$ nanocubes as a side-product of the synthesis, as described in Section 3.1, with an improved stability compared to conventional synthesis. Section 3.2 provides an extensive analysis of the optical properties of these NCs, while Section 3.3 showcases their robust single photon emission and explores the impact of quantum confinement on single-photon purity. In Section 3.4, I investigate the nature of the observed blinking. Section 3.5 is dedicated to studying their stability under exposure to illumination and dilution.

3.1 Synthesis of $CsPbBr_3$ NCs

The $CsPbBr_3$ NCs were synthesized by Dr.Emmanuel Lhuillier (INSP) using a method inspired by the Kovalenko's protocol (detailed in Section 1.3.3.1), with several notable modifications. This adapted approach was initially described by Weidmann et al.[94] for growing CsPbBr3 nanosheets, resulting in the formation of the $CsPbBr_3$ nanocubes as a by-product of the synthesis. Remarkably, we employed this synthesis method for the first time to produce *confined* nanocubes demonstrating single-photon emission.

Compared to Kovalenko's work, there are three significant modifications:

1. **Reduced cesium oleate content**: Less cesium oleate is introduced to favor the growth of a Cs free phase.

2. **Additional ligands**: Two additional ligands with saturated alkyl chains (octanoic acid and octyl amine) are introduced to favor the crystallization of the Cs free phase.

3. **Extended reaction time**: The reaction time is extended from 30 s to 35 min to favor the growth step.

Through this adapted approach, we obtain three distinct products:

- **CsPbBr3 nanoplatelets** as the primary product of the synthesis and presenting an absorption peak at 430 nm, as shown in the absorption spectrum in Figure 3.1a.
- **Cs-free nanoplatelets** showing a peak at 398 nm in the absorption spectrum, as shown in figure 3.1a.
- **CsPbBr3 nanocubes** responsible for the small absorption edge from 450 nm to 500 nm shown in the absorption curve in the inset of figure 3.1a. We are mainly interested to these nanoparticles, which are promising single photon emitters as I will illustrate in the following.

The transmission electron microscopy (TEM) image in Figure 3.1b reveals significant differences in the lateral size among the various populations. Since the nanocubes are much smaller than the nanosheets, they can be effectively sorted through selective precipitation. This process removes the largest compounds, resulting in a solution containing only the small $CsPbBr_3$ NCs, as depicted in the TEM image in Figure 3.1c.

These CsPbBr3 NCs display an asymmetric shape, with one side being bigger than the other two. The size distribution in Figure 3.1d yields important insights into their dimensions, revealing two peaks at approximately 3.6 nm and 11.3 nm. These values correspond to the mean lateral extension and particle thickness, respectively, under the assumption that some nanocubes lie on on their largest facet while others lie on the edge.

The obtained CsPbBr3 NCs exhibit strong quantum confinement together with a excellent colloidal stability under illumination, as discussed in the following sections. These characteristics can be attributed to the modifications made to the conventional synthesis protocol.

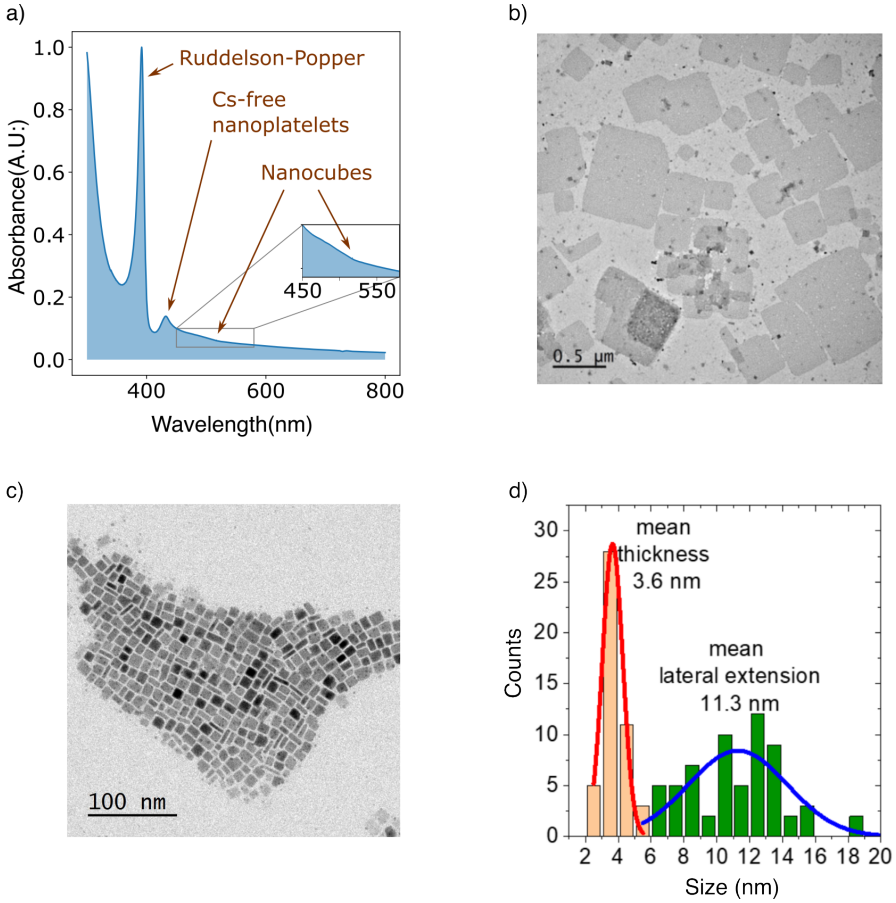

Fig. 3.1 ***Chemical characterization of the CsPbBr$_3$ NCs.*** *a) Absorption spectrum of the products obtained from the synthesis before the last centrifugation. The contribution of the three phases is evidenced.(inset) Portion of the spectrum corresponding to nanocubes contribution. b) TEM image of the products of the synthesis, showcasing distinct populations with various dimensions, including large nanoplatelets and small nanocubes. c) TEM image of the CsPbBr$_3$ NCs obtained from selective precipitation. d) Size histogram for the CsPbBr$_3$ NCs showing two peaks at 3.6 nm and 11.3 nm respectively.*

3.2 Optical properties of $CsPbBr_3$ NCs

At room temperature, the fine structure of the emission, with its distinct energy levels, remains unresolved in the photoluminescence (PL) spectrum. Nonetheless, measuring the emission spectra remains highly advantageous as it serves as the initial step in the characterization process. This step allows us to distinguish between individual emitters and clusters, as clusters often display multiple peaks in their emission spectrum. Additionally, by examining the central emission wavelength (CEW), we can indirectly gain insights into the size of the NCs or any ongoing photo-bleaching phenomena. Furthermore, the analysis of the CEW and the full width at half maximum (FWHM) of a specific NC, togheter with the measured single photon purity can provide a qualitative information about the quantum confinement regime, as discussed in Section 3.3.

Figure 3.2a shows a representative single $CsPbBr_3$ NC emission spectrum, displaying a CEW of 500 nm (2.53 eV) and a FWHM of around 15 nm (72.6 meV).

The perovskite's emission spectrum has an asymmetric shape, characterized by a long tail extending towards longer wavelengths (lower energy). This asymmetric spectrum has been documented since the early synthesis of $CsPbBr_3$ NCs, as showcased in the research conducted by Kovalenko and colleagues in 2015 [23], and shortly thereafter, in the synthesis of perovskite NCs with other compositions and dimensionalities [95, 96]. Other studies have demonstrated that this line shape is temperature-dependent and it is primarily attributed to electron-phonon coupling [97–100].

In this chapter, I report the characterization of 60 $CsPbBr_3$ emitters. Figure 3.2a displays the histogram of the wavelength distribution, revealing that due to the size dispersion, the emitters exhibit a single central emission wavelength (CEW) within the range of 474 nm to 517 nm, with an average value of 498 nm. Figure 3.2c illustrates the FWHMs as a function of the relative CEWs. Within this dataset, the FWHM displays a range spanning from around 63 meV to 87 meV, with an average value of 72 meV. Although it's worth noting that the correlation between these two quantity is not particularly evident, larger FWHM values are more likely associated with higher energy values, then smaller particles. This behavior, also visualized in Figure 3.4, is coherent with a trend often reported in literature [99, 101, 102], which can be explained by the broadening of the linewidth resulting from the coupling with high-energy optical phonon modes, an effect that becomes more pronounced

as the degree of confinement increases. In Figure 3.2d, a typical saturation curve is reported, fitted with equation 2.1. The extracted saturation fluence is typically around 2 µJ/cm^2.

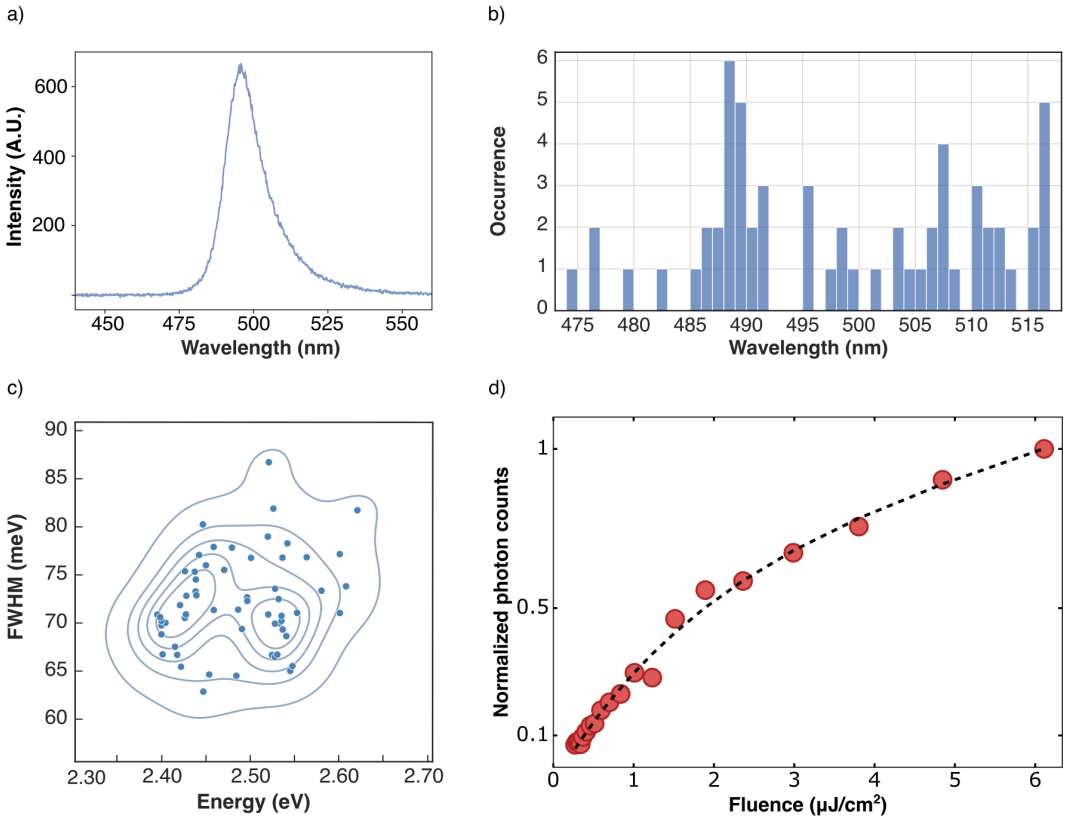

Fig. 3.2 ***Optical properties of CsPbBr$_3$ NCs.*** *a) Typical emission spectrum of a single CsPbBr$_3$ NCs b) Histogram of the central emission wavelength (CEW) distribution for 60 CsPbBr$_3$ NCs. c) Distribution of the FWHM plotted against the relative emission energy for the 60 CsPbBr$_3$ NCs. d) Example of a saturation measurement of a single NC. The red dots are the experimental data while the black line is the fitted function from eq 2.1.*

3.3 Single photon emission in $CsPbBr_3$ NCs

I assessed the single photon purity of 60 $CsPbBr_3$ NCs by measuring the second-order correlation function $g^{(2)}(\tau)$. All measurements were carried out at saturation power to enable a comparison of the quantum properties of the emitters. Figure 3.3 presents the $g^{(2)}(\tau)$ histogram corresponding to the highest single photon purity achieved, with $g^{(2)}(0) = 0.02$. This level of purity is comparable to the best reported values for other colloidal quantum dots (QDs) [103–105].

To investigate the effect of the quantum confinement on single-photon purity, I examined $g^{(2)}(0)$ as a function of emission energy and of the FWHM. Figure 3.4 illustrates that as the energy increases, $g^{(2)}(0)$ decreases. This trend can be attributed to the fact that as the particle size decreases, the quantum confinement is more and more important. Specifically, for the studied CsPbBr3 NCS, a $g^{(2)}(0)$ higher than 0.5 is observed for eneregy lower than approximately 2.43 eV.

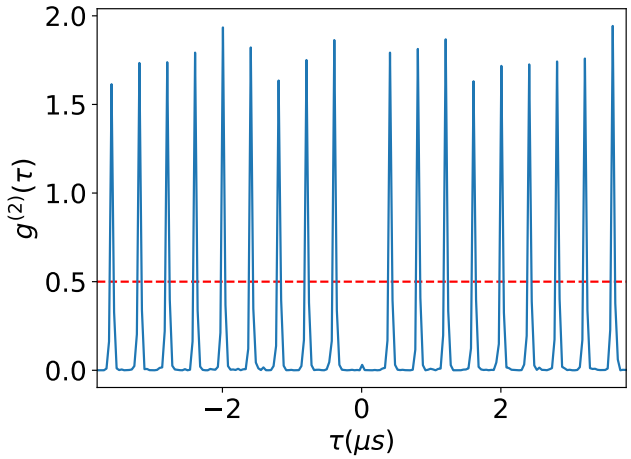

Fig. 3.3 ***$g^{(2)}(\tau)$ histogram for a $CsPbBr_3$ NC.*** *Example of $g^{(2)}(\tau)$ function of a single NC emitting high quality single photons, measured with a repetition rate of 2.5 MHz. The red-line indicates the threshold for single-photon emission claim. Due to the presence of blinking, the $g^{(2)}(\tau)$ function tends to show a super-poissonian behavior at short delays and to converge to 1 at long delays.*

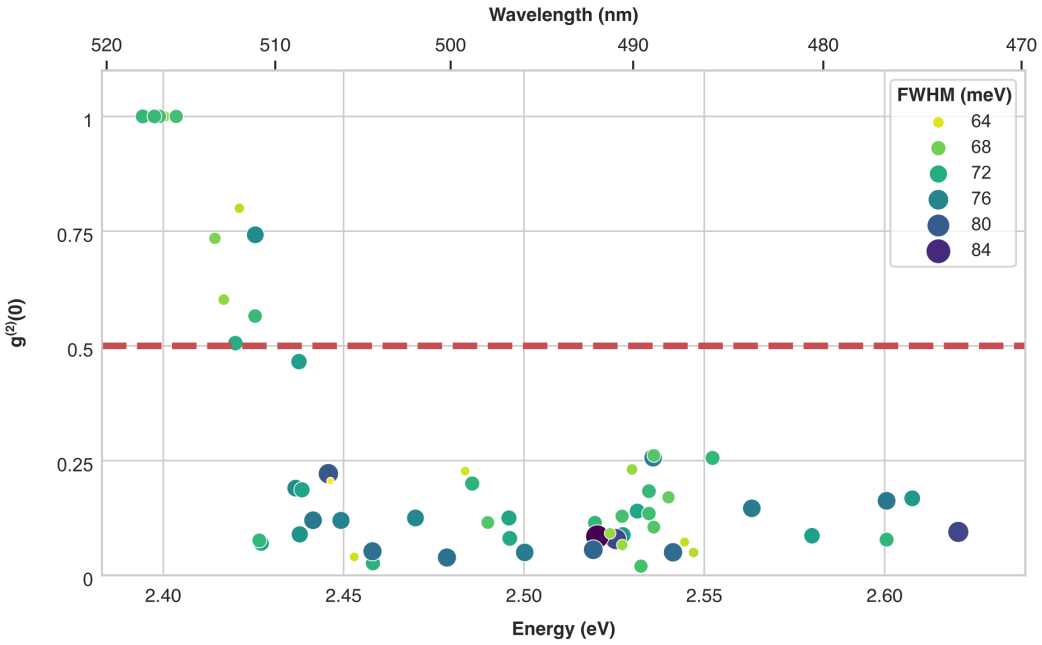

Fig. 3.4 ***Effect of the quantum confinement on sigle photon purity*** *Measured $g^{(2)}(0)$ values as a function of emission energy (bottom axis) and the CEW (upper axis) for 60 NCs. All the emitters were excited at their saturation power. The red-line indicates the threshold for single-photon emission claim.*

3.4 Blinking in CsPbBr$_3$Ncs

Figure 3.5 reports the photoluminescence time-trace of a $CsPbBr_3$ NC, showing fluctuations in the intensity typical of the blinking phenonenon common for the colloidal NCs, described in Section 1.2.3.1. The trace is obtained using a bin time of 10 ms to get a good signal/noise ratio (ad discussed in Section 2.4.2.2) and with an integration time of 600 s. This PL time-trace does not show clear ON-OFF transitions but a PL trajectory with a continuous distribution of intensity as a function of time. This is visible from the intensity histogram in the right panel and in the 50 ms zoom in the bottom panel of Figure 3.5. In this case, we can refer to it as *flickering* [106].

To gain a better understanding of the flickering behavior, it is useful to compare the $CsPbBr_3$ PL time-trace with PL time-traces from other semiconductor single-photon emitters that I also investigated during my PhD, such as unconventional core-shell CdS/CdSe/CdS quantum dots and CdSe/ZnS nanoplatelets, as shown in Figure 3.6 and discussed in Appendix A. These traces, obtained with the same

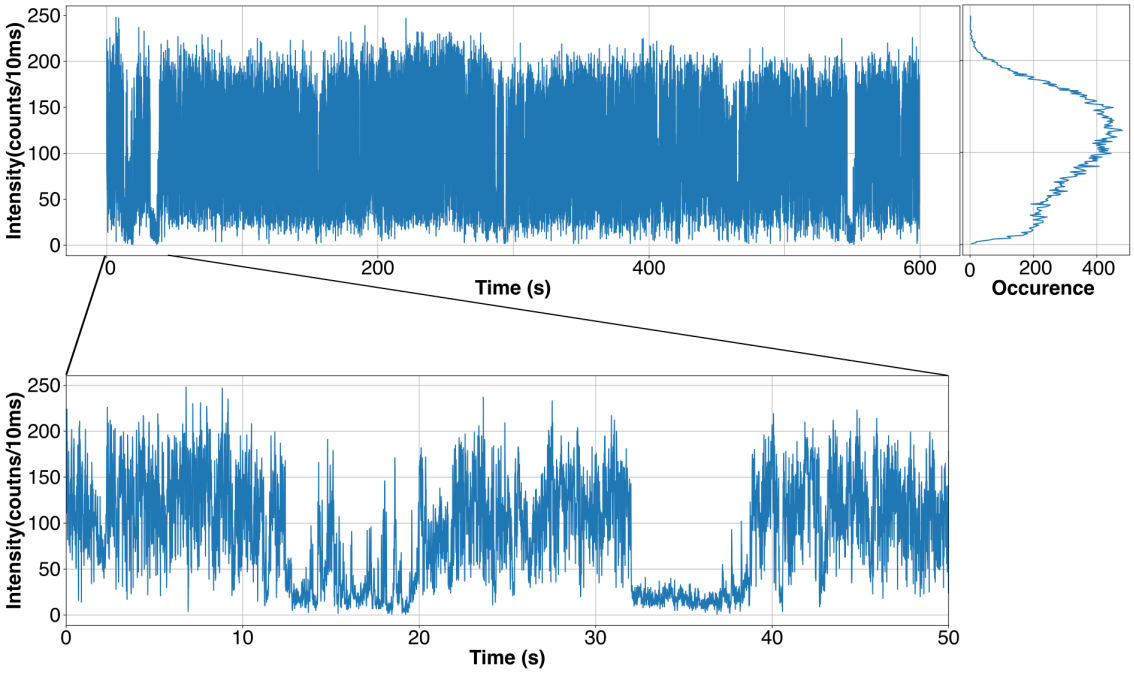

Fig. 3.5 ***PL time-trace of a CsPbBr$_3$ NC.*** *The PL time-trace over 600 s is obtained with a bin time of 10 ms. On the right panel, the histogram of the intensity occurrences On the bottom panel, a zoom of the PL time-trace over the first 50 s.*

binning time of 10 ms, reveal a pronounced telegraphic blinking pattern characterized by clear transitions between high and low emissive states.

Let's investigate the nature of blinking in the case of $CsPbBr_3$ NCs. As discussed in Section 1.2.3.1, the mechanism behind the blinking phenomenon remains a subject of ongoing debate. Typically, blinking scenarios are classified into two categories: type-A blinking, attributed to charging and discharging processes that yield a correlation between PL intensity and lifetime, and type-B blinking, in which short-lived traps are considered the primary cause of blinking, resulting in a nearly constant lifetime despite significant changes in PL intensity.

To analyze this behavior, we first examine the PL decays of $CsPbBr_3$ NCs, as shown in Figure 3.7a. The decay is fitted with a tri-exponential model represented by the equation:

$$I = A_1 e^{(-(t-\tau_0)/\tau_1)} + A_2 e^{(-(t-\tau_0)/\tau_2)} + A_2 e^{(-(t-\tau_0)/\tau_3)} + C \tag{3.1}$$

In this equation, τ_1, τ_2, and τ_3 correspond to the fitted lifetimes, τ_0 represents the

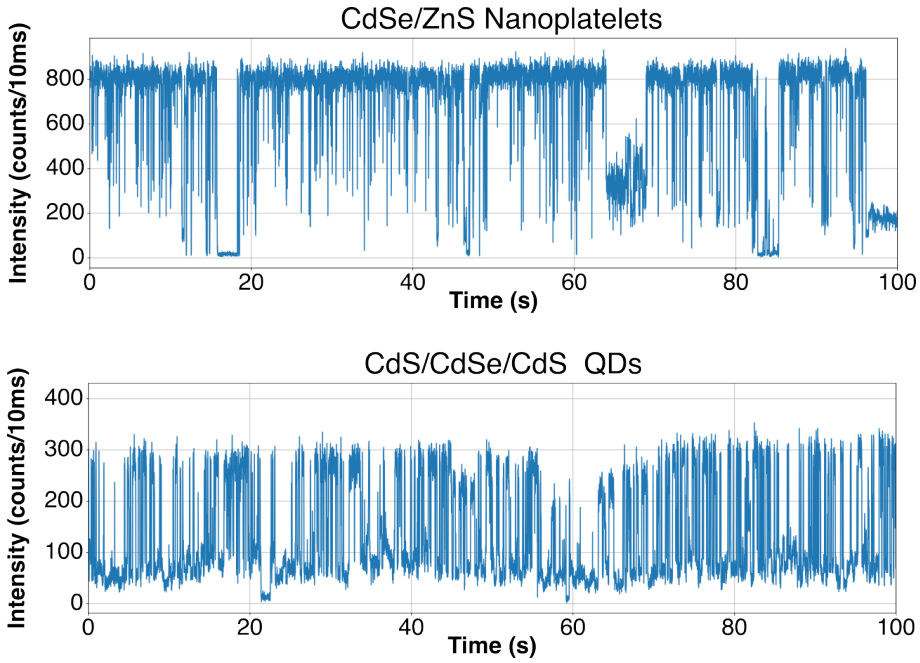

Fig. 3.6 ***Blinking in other semiconductor single photon emitters.*** *PL time-traces over the first 100 s in the case of CsSe/ZnS nanoplateletes and CdS/CdSe/CdS QDs. The bin time is 10 ms. Full traces are reported in Appendix A.*

pulse arrival time, and A_i represents the amplitudes of each decay component, while C accounts for the background signal. The fitted parameters are as follows: $\tau_1 = 2.1$ ns ($A_1 = 0.319$), $\tau_2 = 7.7$ ns ($A_2 = 0.640$), and τ_3 (with $A_3 = 0.038$). We attribute the lifetime τ_1 to the charged exciton (trion) and the lifetime τ_2 to the exciton, while the lifetime τ_3 represents only 3.8% of the emission and can be attributed to noise or could potentially be associated with exciton-phonon coupling [107].

Subsequently, we investigate the relationship between the PL intensity and the lifetime. To achieve this, the top panel of Figure 3.7b provides a close-up view of the PL time-trace for $CsPbBr_3$ NCs over a 10-second duration. In the lower panel of Figure 3.7b, I display the evolution of the lifetime as a function of time, calculated by averaging the arrival times of all the photon detection events registered in the time interval corresponding to the bin of the histogram.

By comparing the lifetime evolution with the PL time-trace in the top panel, we can identify a clear correlation between the intensity state and the lifetime. This correlation is indicative of type-A blinking, where non-radiative Auger recombination of the charged state (trion) competes with radiative recombination, resulting in the

quenching of photon emission through the transfer of exciton energy to an extra carrier (electron or hole). This process leads to lower PL emission and a faster decay.

Another effective way to clearly visualize the correlation between PL intensities and lifetimes is to employ the Fluorescence Lifetime-Intensity Distribution (FLID) analysis [108]. In this analysis each pair of intensity and lifetime values constitutes a data point in the intensity-lifetime space. Figure 3.7c-d presents FLID images for excitation powers of Psat and 1.5 Psat. These images demonstrate that while the system predominantly remains in a state of high emissivity, low-intensity events become more frequent as excitation power increases.

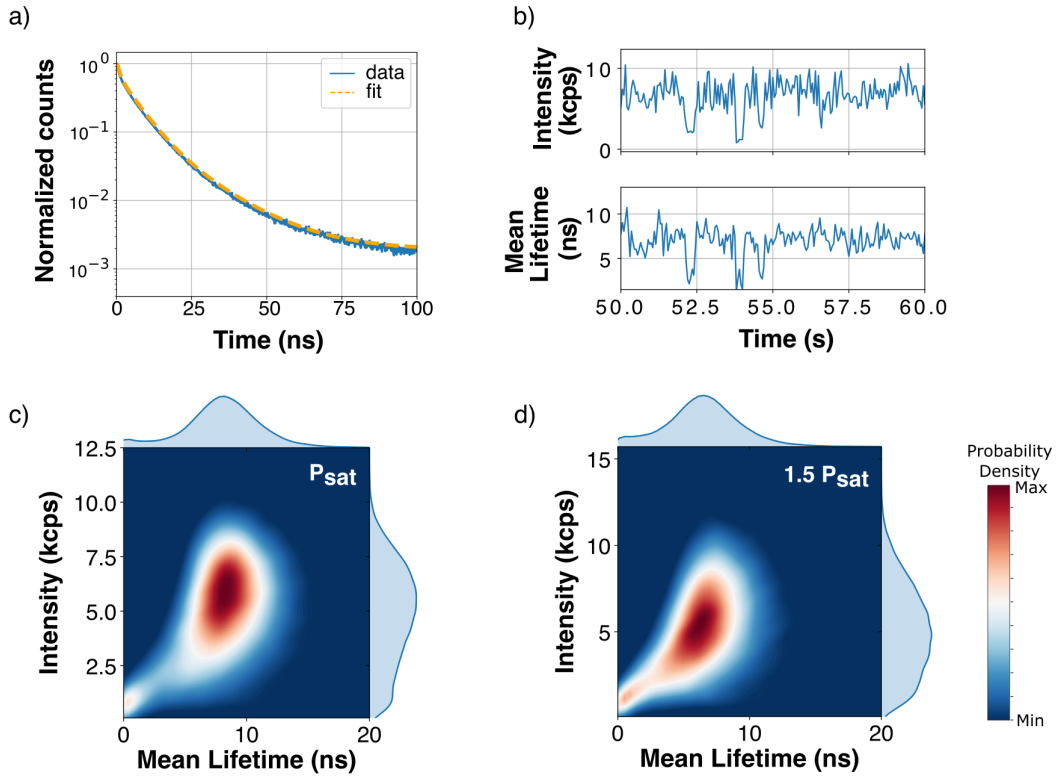

Fig. 3.7 ***FLID analysis on CsPbBr$_3$ NCs.*** *a) PL decay of CsPbBr$_3$ NC. Data are fitted with a triple exponential decay model. b) Zoom of the PL time-trace acquired for a CsPbBr$_3$ NC excited at the saturation intensity (top panel) correlated with the time-trace of the mean measured lifetime (bottom panels). c-d) Fluorescence lifetime-intensity distribution (FLID) images of a single emitter, excited at P_{sat} and $1.5P_{sat}$, respectively.*

We can compare these distributions with the results reported by Park et al.[24] on CsPbBr$_3$ synthetized with the conventional Kovalenko's protocol[23]. In their work,

FLID analysis was carried out at excitation powers below saturation, particularly at excitation powers two orders of magnitude lower than ours, as shown in Figure 3.8. As the excitation power increases, their emitters predominantly exhibit a low emissive state. In contrast, our emitters, excited at or beyond saturation power, consistently maintain bright emission. This characteristic highlights the robustness of the emitters produced using our synthesis method.

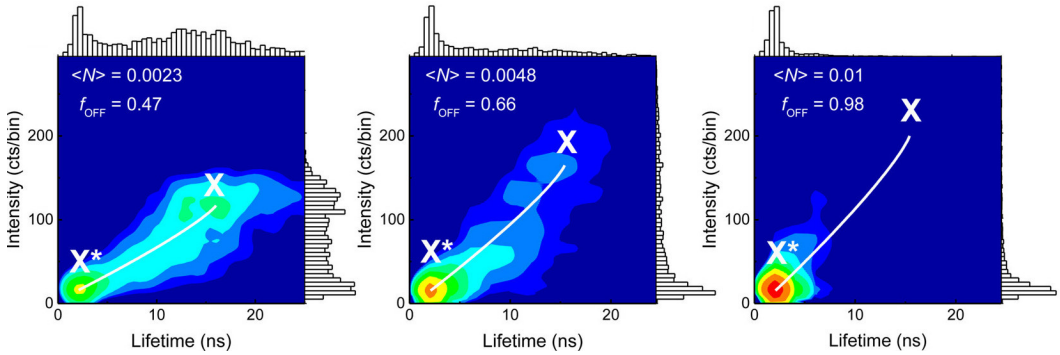

Fig. 3.8 ***FLID images of conventionally synthesized CsPbBr$_3$ NCs.*** *FLID images reported by Park et al.[24] obtained at excitation powers two orders of magnitude lower than ours, showing the predominance of the low-intensity state. (Figure reproduced from reference[24]).*

3.5 Photostability in CsPbBr$_3$ NCs

As previously mentioned, one of the main drawbacks with perovskite NCs is their degradation under light illumination and moisture. The colloidal stability of perovskite NCs mainly depends on surface chemistry, due to their high surface-to-volume ratio. The highly dynamic binding between capping ligands and the ionic NC lattice can cause the detachment of ligands and halide atoms from the surface, leading to a disordered surface with defects that reduces the long-term stability.

Indeed, these defects act as trap sites for optically excited charge carriers and excitons, leading to non-radiative recombination processes and to a significant reduction in the photoluminescence quantum yield (PLQY). Furthermore, some defect traps may undergo photochemical reactions, such as photo-oxidation, causing the degradation and structural collapse of the NC and resulting in photo-bleaching. This behavior is further accelerated in presence of moisture.

To meet the requirements for applications in photonic devices and integrated

single-photon sources, which is our objective, it is essential to maintain high colloidal stability of the NCs.

3.5.1 Photostability under illumination

In literature, the monitoring of the spectral stability over few minutes is often used to evaluate the photostability, as proposed by Rainò et al.[109]. Their investigation of $CsPbBr_3$ perovskite NCs, synthesized using the Kovalenko's protocol, is presented in Figure 3.9. In their study, they observed a large blue shift of over 10 nm after few tens of seconds for perovkite NCs directly deposited on a glass-plate. Also for perovskite NCs encapsulated with polystyrene, the longest measurement time recorded was around 100 s.

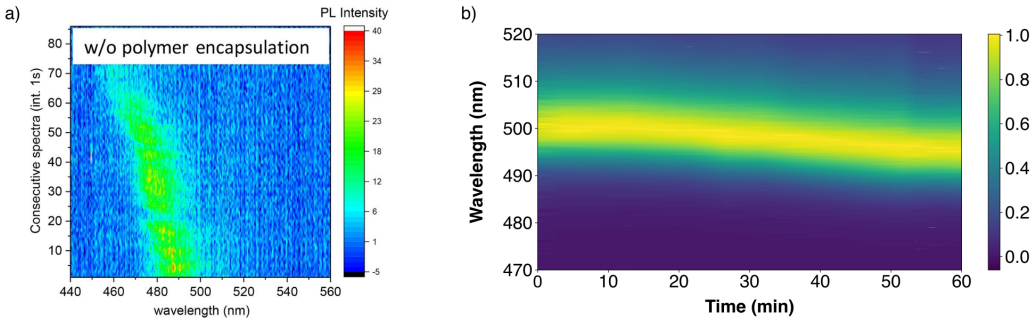

Fig. 3.9 ***Spectral stability for CsPbBr$_3$ NCs.*** *a) Degradation of the emission spectrum of a single $CsPbBr_3$ NC synthesized with the Kovalenko's protocol[23]. The green trace shows the evolution of the wavelength of the emitted photons during time. (Figure reproduced from reference[109]). b) Evolution of the fluorescence spectra as a function of time for a single $CsPbBr_3$ NC, that we synthesized using a different protocol than the conventional Kovalenko's one, as described in Section 3.1. The emitter was excited at the saturation intensity. In order to clear the image from the effect of the blinking, each spectrum is normalized to its maximum value. A blue-shift of about 5 nm after one hour is visible.*

In my research, I employed a similar approach to evaluate the photostability, illuminating a single photon emitter at saturation power with a pulsed 405 nm laser while tracking the spectral evolution over time. Figure 3.9b illustrates our findings, revelealing a blue shift of the emission wavelength with a significantly different timescale. Exciting the NC over 1 hour, I observed a blueshift of about 5 nm. This blue shift is likely attributed to the degradation of the external layers of the emitters,

leading to a reduction in size and subsequently shifting their CEW towards the blue. Our perovskite NCs, synthesized using a different protocol than the conventional one used by Raino et al., show then a significant improvement of the photostability of the emitters under illumination.

3.5.2 Photostability under dilution

On the other hand, the robustness of the NCs is strongly dependent on the concentration of the emitters in the solution, and drops fast when we dilute the sample. Our final objective is to couple a single emitter to a tapered optical nanofiber to develop an integrated single photon source, as I will discuss it in Chapter 6. To do this, we need to use a strongly diluted sample to isolate a single emitter. It is then crucial to investigate the behavior of the emitters as a function of the dilution, that for perovskites is typically done in toluene. To study this behaviour, I prepared 5 samples with different dilution factors, respectively 1 : 1, 1 : 2, 1 : 10, 1 : 20 and 1.40.

The specific solvent-to-solute ratios employed for these dilutions, while keeping the total volume constant at 1 mL, are provided in Table 5.1.

Dilution factor	Solvent	Solute
1 : 2	0.50 mL	500 µL
1 : 10	0.9 mL	100 µL
1 : 20	0.95 mL	50 µL
1 : 40	$\sim$ 0.975 mL	25 µL

Table 3.1: **Solvent-to-solute ratios for CsPbBr$_3$ NCs dilutions.** NCs solution with a original molar concentration of approximately 1 µM were diluted with toluene at various dilution ratios, ranging from 1 : 2 to 1 : 40, while keeping the total volume constant at 1 mL.

The samples to be characterized were prepared using the spin-coating technique, under identical conditions. To study the photobleaching evolution with dilution, the samples were exposed to intense LED light at a wavelength of 400 nm in wide-field configuration. The emission from each of the five samples was sequentially recorded by the CCD camera placed at one output of the microscope. The recorded sample area measures 133 µm x 133 µm, matching the sizes of the camera frame. A frame was captured every 20 s seconds over 20 minutes for each sample. By counting the number of emitting NCs in each frame, as depicted in Figure 3.10a, and normalizing

it to the number of NCs in the initial frame, we can track the temporal evolution of ensemble emission as a percentage, as reported in Figure 3.10b.

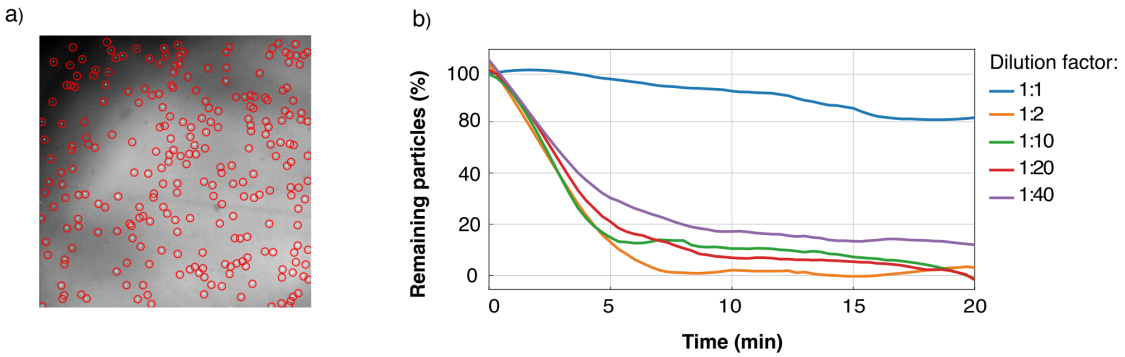

Fig. 3.10 ***Stability in dilution of $CsPbBr_3$ NCs.*** *Percentage of NCs still emitting after 20 minutes under strong illumination as a function of the dilution of the original solution:* 1 : 1, 1 : 2, 1 : 10, 1 : 20, 1 : 50 *where* 1 : *X means x times dilution.*

The important information is contained in the initial slope of the curve, which gives the characteristic lifetime of an emitter under illumination. We can clearly see that only the concentrated sample (1:1 solution) has a high photostability with more than half of the emitters still working after 20 min, while for the other samples (dilutions from 1:2 to 1:40) almost all the emitters have bleached after 5 min, no matter the dilution. Moreover, we observed an increasing number of aggregates for increasing dilutions, indicating that the particles are not colloidally stable anymore. Although our analysis filters out most of the clusters, the applied postselection cannot fully eliminate the smallest aggregates. The residual presence of these aggregates, which last for longer time, results in an overestimation of the number of particles still active after a given time. This explains the fact that the 1:40 solution appears better that the 1:2 one. We attribute the instability in dilution to the dynamic bonding of the ligand to the perovskite nanocrystal surface [110]. Under dilute conditions, the free ligands can hardly find the surface of another nanocrystal. This displaces the equilibrium between bound and unbound ligands toward the latter. As a result, the dilution process leads to poorly passivated nanocrystals which can easily bleach.

Conclusion

In this chapter, I have presented the characterization of $CsPbBr_3$ nanocubes synthesized in collaboration with the Institut Des Nanosciences De Paris (INSP) using an approach initially developed for growing CsPbBr3 nanoplatelets. This method led to the formation of $CsPbBr_3$ nanocubes as a by-product of the synthesis. This synthesis method has been employed for the first time to fabricate confined nanocubes, which exhibit strong single-photon emission. Specifically:

- To investigate the effect of quantum confinement on single-photon purity, I examined the single photon purity as a function of emission energy and their spectral linewidth. The obtained trend shows that as the particle size increases, the quantum confinement is gradually lost.
- These $CsPbBr_3$ nanocubes exhibit improved stability under illumination compared to conventional synthesis methods, showing a blueshift reduction of two orders of magnitude compared to that reported in the literature. They can be illuminated for over one hour and they maintain robustness when excited with powers exceeding the saturation power.
- However, their stability drops down when diluted, as poorly passivated nanocrystals become susceptible to bleaching.

To utilize these NCs in integrated single-photon sources, which is our primary interest, it is important to maintain high colloidal stability even when diluted. Therefore, further optimizations are necessary to achieve this goal. In this context, in collaboration with the Institut des Nanosciences de Paris, we investigated the effect of zinc doping on the NCs to enhance their stability under dilution, as discussed in Chapter 5.

Chapter 4

Color-tunable mixed-cation perovskite NCs

Contents

Introduction

While extensive research has focused on green-emissive lead halide perovskite NCs, a notable obstacle is encountered in achieving stable PL in the red and near-infrared (NIR) spectral regions, where the instability of iodine compounds such as $CsPbI_3$ and $FAPbI_3$ poses a significant challenge. In this chapter, I describe confined mixed-cations $Cs_{1-x}FA_xPbBr_3$ colloidal NCs, aiming to red-shift the emission wavelength while enhancing photo-stability compared to conventional mixed-halide systems. In Section 4.1, I discuss the limits of mixed-halide systems and how engineering mixed-cation perovskites can overcome them. In Section 4.2, I present the synthesis of the $Cs_{1-x}FA_xPbBr_3$ NCs and their crystallographic characterization. In Section 4.3, I show the tunability of their emission wavelength at ensemble and single-particle level. Section 4.4 focuses on the study of their photostability and bliking behaviour. In Section 4.5, I report the first demonstration of single.photon emission from mixed-cation NCs.

The work presented in this chapter was conducted in collaboration with the Nanyang Technological University of Singapore. Specifically, the synthesis of the perovskite NCs and the ensemble measurements were carried out in Singapore, while I characterized the samples at single particle level.

4.1 *Red-wall* of colloidal perovskites

The spectral tunability of perovskite NCs can be readily achieved, as seen, by tuning their size and composition, eliminating the traditional need of external perturbations, such as mechanical strain, electric, and magnetic fields [111–113]. This results in band-gap energies tunable across the entire visible spectrum, including the red and NIR regions. Notably, the development of solid-state single-photon sources operating within the red and NIR regions offers distinct advantages. These include compatibility with silicon-based photonics and electronics, reduced propagation losses in optical fibers [114], and the enhanced capability of long wavelengths to penetrate biological tissues [115]. Then, this renders single-photon sources operating in these spectral ranges very valuable for applications in quantum cryptography, integrated photonics, as well as biomedical imaging and sensing [116–118]. Extensive efforts have been made to develop various platforms for implementing NIR single-photon sources. Currently, leading candidates for these sources are semiconductor materials like indium

gallium arsenide (InGaAs) or indium phosphide (InP), which span the range of 880 nm–1580 nm. These materials exhibit high quantum efficiency, fast decay rates, high purity, near-unity indistinguishability and high extraction efficiency [119–121]. However, they necessitate cryogenic systems for low-temperature operation, which may not be ideal for many practical devices.

4.1.1 Limits of mixed-halide compositions

In 2019, Yoshimura et al.[122] marked a notable milestone in highlighting the capabilities of perovskite NCs for fine-tuning emission wavelength. They accomplished this by showcasing the emission of single photons from mixed-halide $CsPBX_3$ NCs, where X denotes a mixture of chlorine (C), bromine (Br), or iodine (I) halides. For instance, $CsPbBr_3$ QDs with dimensions around 15 nm typically emit green light at approximately 520 nm. Their PL central emission wavelength (CEW) can be blue-shifted by forming $CsPb(Cl_{1-x}Br_x)_3$ compounds. Conversely, forming $CsPb(Br_{1-x}I_x)_3$ compounds leads to red-shifted emissions. However, the latter operation faces challenges due to various thermodynamic and chemical instabilities related to the iodine component. Indeed, when replacing the smaller Br^- anion (with a radius of 0.196 nm) with the larger I^- anion (with a radius 0.220 nm) decreases the Goldsmith tolerance factor t (introduced in Section 1.3.1), and destabilizes the NC [123]. In fact, the resulting $CsPb(Br_{1-x}I_x)_3$ compounds often show in a significant reduction in PLQY and stability, likely attributed to the phase separation between $CsPbBr_3$ and $CsPbI_3$, as well as ion segregation upon continuous illumination [124]. Concerning pure iodine $CsPbI_3$ NCs, despite their theoretical capability to emit light up to 710 nm, their small Cs^+ ion size ultimately triggers thermodynamic instability, resulting in a deterioration of their optical properties. Alternative hybrid (i.e. organic - inorganic) perovskite compounds in the red region are the $MAPbI_3$ ($MA = [CH3NH3]^+$, methylammonium) NCs. However, they suffer from chemical instability as they inevitably transform into PbI_2 along with volatile methylamine and other compounds [125]. A last option involves the use of formamidinium ions ($FA = HC(NH_2)_2^+$) to synthesize $FAPb(Br/I)_3$ NCs. These NCs exhibit high quantum yields ($> 70\%$) in the NIR range (approximately 780 nm for $FAPbI_3$ NCs). However, they also encounter phase instability due to the presence of iodine and environmental-induced instability due to their organic-inorganic nature [126]. This evident difficulty in reaching stable perovskite compound in the red and NIR spectral ranges is commonly referred to as the

perovskite red wall [126].

4.1.2 Mixed-cation perovskites to overcome instabilities

To achieve PL emission at longer wavelengths while ensuring stability, an alternative approach involves synthesizing mixed-cation perovskite materials. A feasible strategy is to partially substitute Cs^+ cations with FA^+ cations in the A site of $CsPbX_3$ emitters, resulting in the formation of $Cs_{1-x}FA_xPbBr_3$ emitters. As Cs^+ cations (with a radius of 0.167 nm) are gradually replaced by larger FA cations (with a radius of 0.205 nm), the composition-averaged Goldschmidt tolerance factor t approaches 1. This change contributes to the structural stability of the perovskite material. The effectiveness of this concept has been demonstrated in photovoltaic and light-emitting devices, where $Cs_{1-x}FA_xPbBr_3$ sources allow for precise tuning of the emission wavelength across a relatively wide range, while maintaining high efficiency and brightness [127–129]. In this chapter, I extend this compositional tunability of mixed-cation perovskites down to the single particle level.

4.2 Mixed-cation $Cs_{1-x}FA_xPbBr_3$ NCs

4.2.1 Synthesis

The synthesis of $Cs_{1-x}FA_xPbBr_3$ NCs was initiated using the Kovalenko's protocol [23], described in Section 1.3.3.1. The substitution of Cs^+ cations with FA^+ cations was achieved by carefully adjusting the molar ratios of cesium bromide (CsBr) and formamidinium bromide (FABr) precursors. A schematic illustration of this procedure is presented in Figure 4.1a, where the stoichiometric ratio x indicates the fraction of FA content present in the precursor solution. Comprehensive synthesis details can be found in Annex B.

Transmission electron microscopy (TEM) analysis was carried out in Singapore using a $JEM-1400$ flash electron microscope operating at 10 kV. To prepare TEM samples, the solution was drop-cast onto 400 mesh copper grids with carbon supporting films. The TEM images displayed in Figure 4.1b showcase the synthesized $Cs_{1-x}FA_xPbBr_3$ NCs with x values of 0, 0.8, and 1.

The NCs exhibit a monodisperse distribution and cubic shape, with average sizes of (10±1) nm for $x = 0$, (11±3) nm for $x = 0.8$, and (10±2) nm for $x = 1$. The gradual

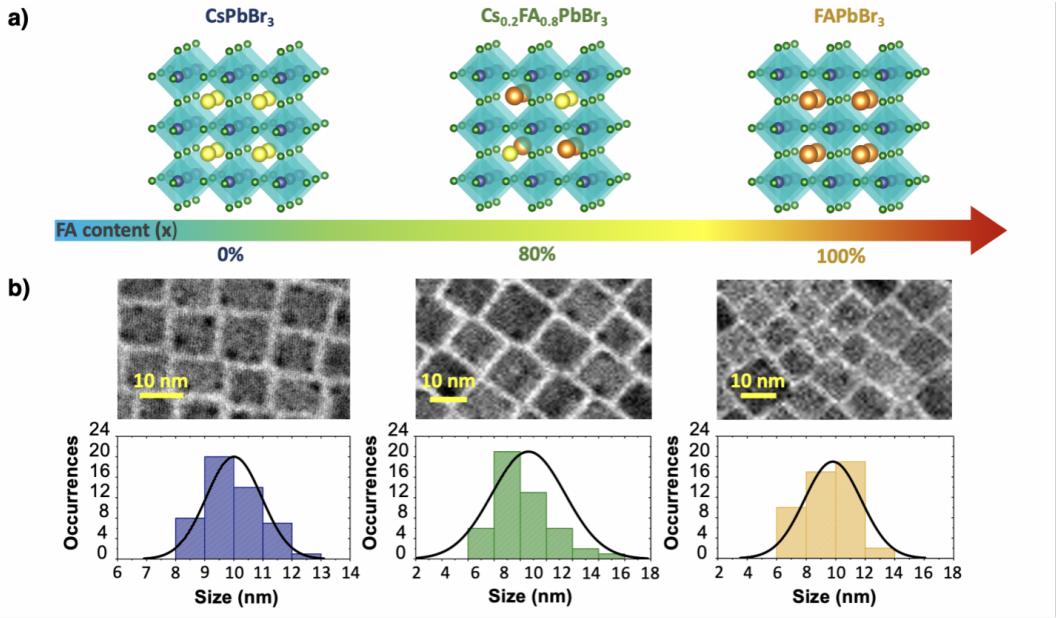

Fig. 4.1 ***Compositionally tunable $Cs_{1-x}FA_xPbBr_3$ QDs (x=0, 0.8 and 1)*** *a) Changes in the crystallographic structures of the $Cs_{1-x}FA_xPbBr_3$ QDs with the addition of the organic FA cation additives. b) Transmission electron microscopy images of the $CsPbBr_3$ (blue), $Cs_{0.2}FA_{0.8}PbBr_3$ (green), and $FAPbBr_3$ (yellow) QDs alongside with their respective size distribution histograms. A sampling size of 50 QDs was recorded for each composition.*

replacement of Cs^+ by FA^+ does not alter the cubic shape of the initial $CsPbBr_3$ NCs and the increase in the FA/Cs ratio does not lead to an obvious change in size, as evidenced by TEM observations. This suggests that the changes in size are unlikely to heavily influence their optical characteristics. Small size NCs with radius comparable to the excitonic Bohr radius (7 nm for $CsPbBr_3$[23] and 8 nm for $FAPbBr_3$[130]) are found in the respective size distribution histograms, suggesting that mixed-cation $Cs_{1-x}FA_xPbBr_3$ NCs could potentially experience quantum confinement effects, then behave as single photon sources.

4.2.2 Crystallographic characterization

Changes in the crystallographic structure due to the introduction of FA^+ cations are evident in both the x-ray diffraction (XRD) measurements and high-resolution transmission electron microscopy (HRTEM), carried out in Singapore. For the XRD analyses, conducted using a Rigaku SmartLab X-ray diffractor, spin-coated samples on glass microscope substrates were prepared. In Figure4.2a, the XRD patterns of

the $Cs_{1-x}FA_xPbBr_3$ NCs are depicted. Remarkably, the diffraction pattern of the $CsPbBr_3$ NCs aligns closely with the cubic $CsPbBr_3$ phase. As the content of FA^+ cations increases, a noticeable shift in the diffraction peaks towards lower angles is observed (as illustrated in Figure 4.2b). This shift implies an expansion in d-spacing[1] due to the incorporation of larger radius FA^+ cations.

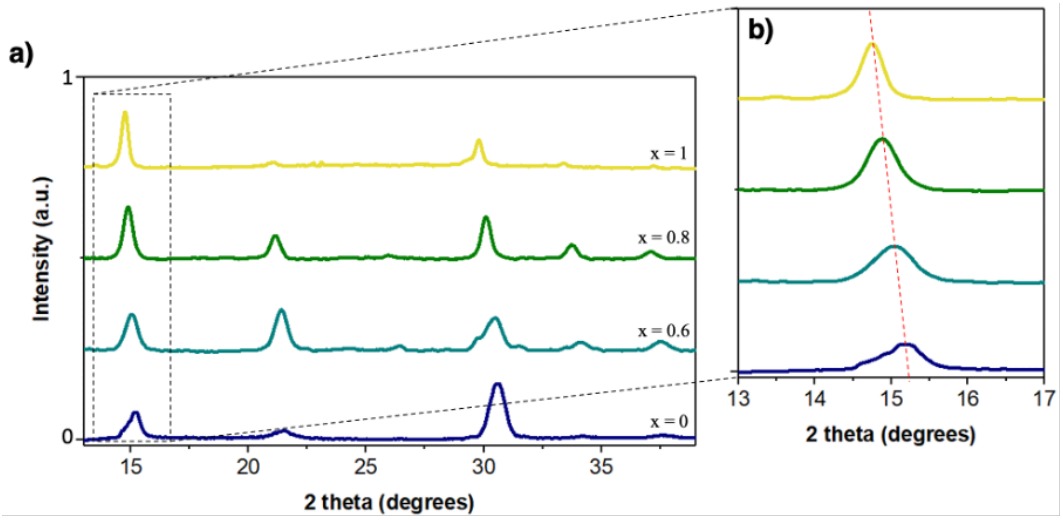

Fig. 4.2 ***XRD patterns of the $Cs_{1-x}FA_xPbBr_3$ NCs.*** *a) XRD pattern of x=0,0.5,0.8, and 1). Diffraction pattern of the $CsPbBr_3$ NCs corresponds to the cubic $CsPbBr_3$ phase. b) Zoom of the diffraction peaks around 15 °C. The gradual shift in the peaks (towards a lower angle is attributed to the substitution of a smaller radius Cs cation with a larger radius FA cation.*

Figure 4.3 presents high-resolution transmission electron microscope (HRTEM) images showcasing the $Cs_{1-x}FA_xPbBr_3$ NCs. The observed increase in d-spacing, measuring 4.1 Å ($x = 0$), 5.3 Å ($x = 0.8$), and 6.0 Å ($x = 1$), aligns with the findings from the XRD analyses. Additionally, HRTEM microscopy highlights the single-crystalline nature and high crystallinity of the samples. Consistent with the TEM observations, no significant alterations are noted in the NC's shape and size upon the introduction of FA^+ cations.

[1]The d-spacing is the distance between successive, parallel planes of atoms.

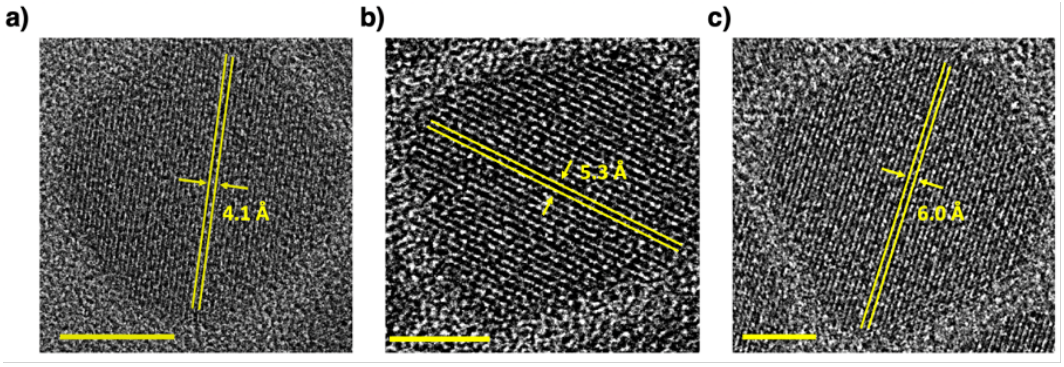

Fig. 4.3 ***HRTEM images of the $Cs_{1-x}FA_xPbBr_3$ NCs.*** *a) $x = 0$, b) $x = 0.8$, and c) $x = 1$. The scale bars represent 5 nm.*

4.3 Spectral tunability of $Cs_{1-x}FA_xPbBr_3$ NCs

4.3.1 Spectral tunability at ensemble level

To investigate the influence of FA addition on the optical properties of the NCs, photoluminescence measurements were conducted on $Cs_{1-x}FA_xPbBr_3$ NCs ensembles with varying compositions ($x = 0, 0.6, 0.8$, and 1). Figure 4.4 shows their photoluminescence absorption [2] and emission spectra. Upon the introduction of FA cations, both the absorption and emission spectra display a red-shift. This phenomenon can be attributed to alterations in the electronic band structure of the NCs.

Analyzing in details the PL spectra presented in Figure 4.5a, the CEW increases from 511 nm ($x = 0$) to 523 nm ($x = 0.6$), 532 nm ($x = 0.8$), and 537 nm ($x = 1$), as clearly depicted in the insert of the figure. This change in the emission wavelength can be attributed to changes in the Pb–Br bond lengths and angles in the $PbBr_6^4$ octahedron when Cs^+ cations are substituted with FA^+. As the valence and conduction bands originate mostly from the Br 4p and Pb 6p orbits, respectively, the modification of Pb–Br bond lengths and angles alters the electronic band structure of the NCs [131, 132]. The full width half maximum (FWHM) of the spectra, respectively of 19 nm ($x = 0$ and 0.6), 20 nm ($x = 0.8$), and 21 nm ($x = 1$) may be slightly affected by inhomogeneous size distribution, electron-phonon coupling, spatial or compositional inhomogeneity of the ensemble.

To gain more insight into PL kinetics, time-resolved PL decays of $Cs_{1-x}FA_xPbBr_3$ ensembles were recorded, as shown in Figure4.5b. Compared to the pure $CsPbBr_3$,

[2] UV-Vis absorbance measurements were performed on an UV-2600i UV-Vis spectrophotometer.

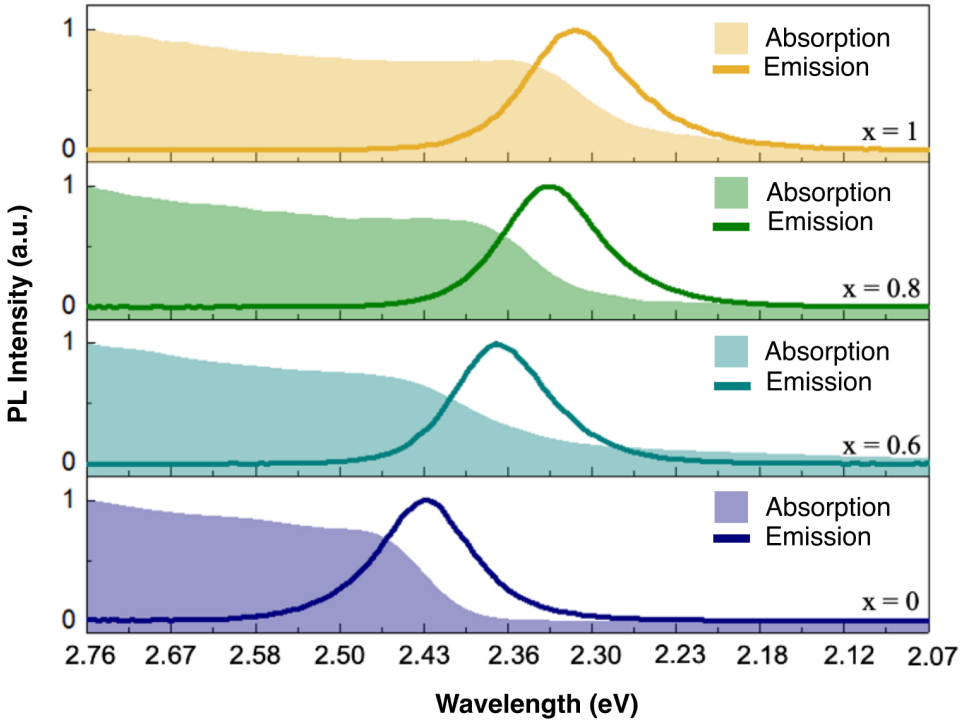

Fig. 4.4 ***Absorption and emission spectra of the $Cs_{1-x}FA_xPbBr_3$ NCs.*** *A red-shift in both the absorption and emission spectra of x = 0,0.6,0.8, and 1 is observed and attributed to the changes in electronic band structure.*

the average PL lifetime of $Cs_{1-x}FA_xPbBr_3$ ensembles is gradually increased with an increase in the FA/Cs ratio (Figure 4.5c, upper panel). This indicates that the decrease in the band gap with the addition of FA^+ cations is probably accompanied by an increase in the exciton binding energy, as already reported in literature [133].

Photoluminescence quantum yield (PLQY) measurements of the $Cs_{1-x}FA_xPbBr_3$ NCs solution were performed by our collaborators in Singapore, with an excitation laser of $\lambda = 435$ nm. Notably, the $Cs_{1-x}FA_xPbBr_3$ NCs show a high PLQY of around 70%, regardless of their relative cation composition (Figure 4.5c, lower panel). Thus, addition of the FA cations does not cause a significant reduction of the quantum dot brightness.

4.3.2 Spectral tunability at single particle level

In this section, the spectral tunability and the optical properties of $Cs_{1-x}FA_xPbBr_3$ NCs are explored at single particle level. Specifically, I examined compositions with

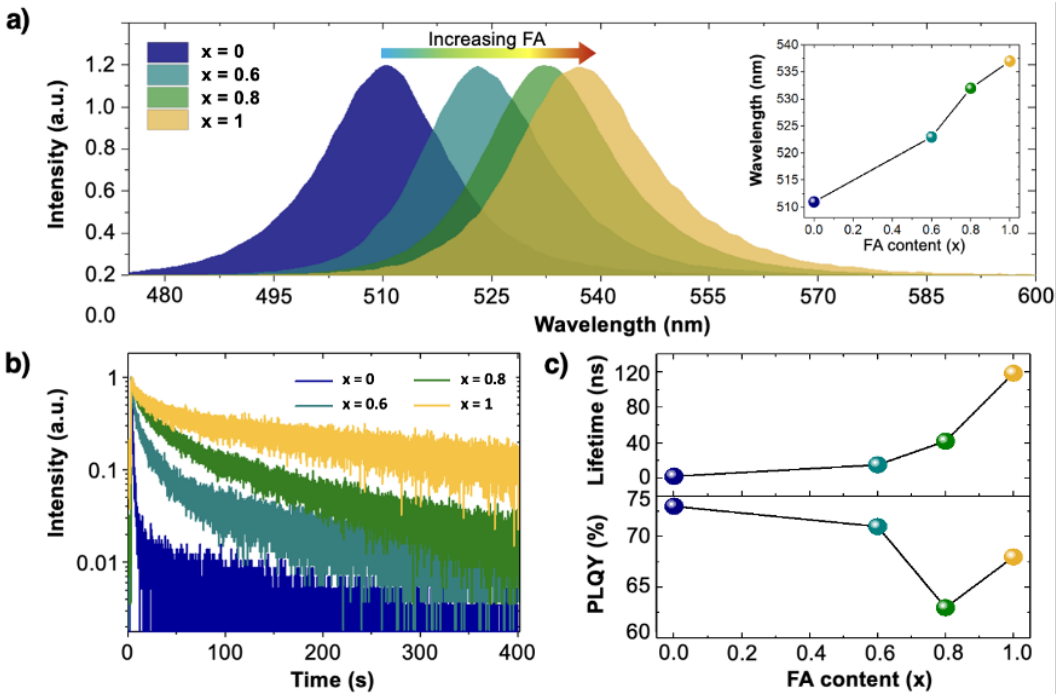

Fig. 4.5 ***Spectral tunability of the $Cs_{1-x}FA_xPbBr_3$ NCs ensembles (x = 0, 0.6, 0.8, and 1).*** *a) Normalized PL spectra of the $CsPbBr_3$ (blue),$Cs_{0.4}FA_{0.6}PbBr_3$ (cyan), $Cs_{0.2}FA_{0.8}PbBr_3$ (green), and $FAPbBr_3$ (yellow) NCs ensembles. The insert illustrates the shift in the CEW with the different amount of FA content. b) Time-resolved PL lifetime measurements of the $Cs_{1-x}FA_xPbBr_3$ NCs. c) Changes in the average lifetime (upper panel) and PLQY (lower panel) with the different amount of FA content.*

x values of 0, 0.4, 0.6, 0.8 and 1. In particular, for the compositions $x = 0$, 0.8, and 1, I conducted a statistical analysis, the results of which are presented below.

Figure 4.6a displays the typical PL spectra of individual $CsPbBr_3$, $Cs_{0.2}FA_{0.8}PbBr_3$ and $FAPbBr_3$ NCs, exhibiting CEW of 509 nm, 519 nm, and 527 nm, respectively. Upon substitution of Cs^+ cations with FA^+ cations, a significant red shift is observed in the PL spectra of individual NCs, aligning with the trend observed in ensembles. The PL spectral broadening, quantified by the FWHM, measures 72.2 meV ($\sim$ 15 nm) for $x = 0$, 79.7 meV ($\sim$ 17 nm) for $x = 0.8$, and 87.6 meV ($\sim$ 19 nm) for $x = 1$. To achieve statistical significance, the optical properties of 20 $Cs_{1-x}FA_xPbBr_3$ emitters were analyzed for each composition, for a total of 60 emitters. All the measures were carried out at the saturation power. Figure 4.6b shows the CEW distribution obtained for the three sets of $Cs_{1-x}FA_xPbBr_3$ NCs ($x = 0, 0.8$ and 1). The respective average CEWs are 505 nm for $x = 0$, 517 nm for $x = 0.8$ and 523 nm for $x = 1$. The

deviations from the mean values arise from the non-uniform size distribution of the NCs.

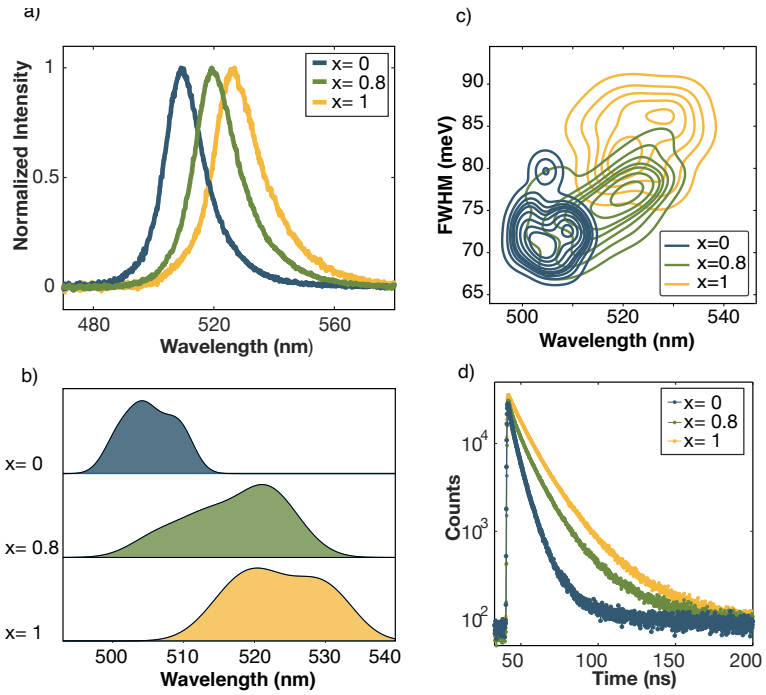

Fig. 4.6 ***Spectral tunability of the Cs1-xFAxPbBr3 NCs (x=0, 0.8 and 1).*** *a) Normalized emission spectra of an individual $CsPbBr_3$ (blue), $Cs_{0.2}FA_{0.8}PbBr_3$ (green), and $FAPbBr_3$ (yellow) NC. The emission spectra are normalized to the peak intensity. b) Typical PL decay of a $CsPbBr_3$ (blue), $Cs_{0.2}FA_{0.8}PbBr_3$ (green) and $FAPbBr_3$ (yellow) QDs. c) Density distribution of the CEW for $CsPbBr_3$ (blue), $Cs_{0.2}FA_{0.8}PbBr_3$ (green), and $FAPbBr_3$ (yellow) NCs. A sampling size of 20 emitters for each composition was recorded. d) Distribution of the FWHM plotted against the relative central emission wavelengths for the $CsPbBr_3$ (blue), $Cs_{0.2}FA_{0.8}PbBr_3$ (green) and $FAPbBr_3$ (yellow) emitters.*

Figure 4.6c shows the distribution of the FWHM of the PL spectra of individual $Cs_{1-x}FA_xPbBr_3$ NCs with compositions $x = 0, 0.8$ and 1, plotted against their CEW. The FWHM ranges from 69 meV ($\sim 14nm$) to 80 meV ($\sim 16nm$) for $x = 0$, from 70 meV ($\sim 14.5nm$) to 82 meV ($\sim 18nm$) for $x = 0.8$ and from 78 meV ($\sim 17.6nm$) to 88 meV ($\sim 19nm$) for $x = 1$. By comparison with the PL linewidth of NCs ensembles, the slightly reduced FWHM can be attributed to the fact that confocal measurements specifically target small particles.

Concurrently, an increase in the average lifetime is observed, as evident in the typical PL decay kinetics of individual $CsPbBr_3$, $Cs_{0.2}FA_{0.8}PbBr_3$, and $FAPbBr_3$

NCs in Figure 4.6d. The PL decays were fitted using the tri-exponential model:

$$I = A_1 e^{(-(t-\tau_0)/\tau_1)} + A_2 e^{(-(t-\tau_0)/\tau_2)} + A_2 e^{(-(t-\tau_0)/\tau_3)} + C \tag{4.1}$$

where τ_1, τ_2, and τ_3 are the fitted lifetimes, t_0 represents the pulse arrival time and A_i are the amplitudes of each decay component. C is a constant to take into account the background signal. Figure 4.7 displays the fit of the PL decays, and the corresponding fitting parameters are given in Table 4.1. The fast decay component τ_1 can be attributed to the recombination of the charged exciton (trion), whereas the component τ_2 corresponds to the radiative exciton recombination, which typically occurs over several tens of nanoseconds. The long τ_3 component observed in the decay curves could potentially be associated with an increase in exciton-phonon coupling within the NCs, particularly in those with higher FA/Cs ratios. In fact, in the case of CsPbBr3 ($x = 0$), this component is negligible.

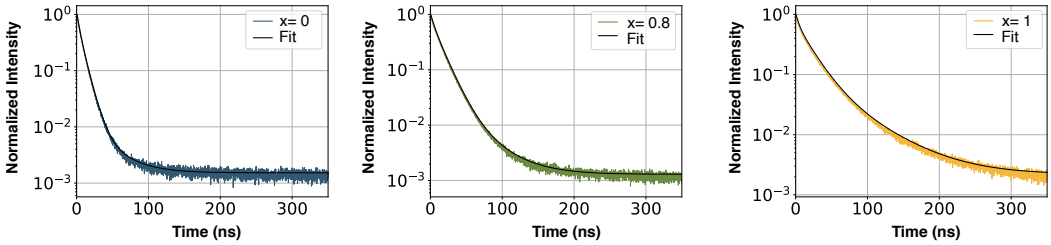

Fig. 4.7 ***PL decays of $Cs_{1-x}FA_xPbBr_3$ (x=0, 0.8 and 1) NCs.*** *The PL decays of $x = 0$ composition (blue decay), $x = 0.8$ composition (green decay) and $x = 1$ composition (yellow decay), are fitted with an tri-exponential model.*

	τ_1	A_1	τ_2	A_2	τ_3	A_3
$x = 0$	3.5	0.309	8.4	0.678	31.6	0.021
$x = 0.8$	4.0	0.259	13.9	0.706	37.8	0.035
$x = 1$	3.9	0.266	19.6	0.634	54.9	0.100

Table 4.1: **Fitting parameters of $Cs_{1-x}FA_xPbBr_3$ (x=0, 0.8 and 1) PL decays**

4.4 Photo-stability and blinking in $Cs_{1-x}FA_xPbBr_3$ NCs

The photo-stability of $Cs_{1-x}FA_xPbBr_3$ NCs was evaluated by measuring their PL time-traces with an integration time of 600 s and binning time of 10 ms. The typical PL time-traces for individual $x = 0, 0.8$ and 1 NCs are reported in Figure4.8. All three compositions exhibit photo-blinking behavior, in which the intermittency of high and low emissive periods is observable. The $x = 1$ composition exhibits the most pronounced blinking compared to $x = 0.8$, and $x = 0$ samples, with low-intensity periods more prolonged. Furthermore, under continuous illumination, a significant decrease in PL intensity is observed, with strongest reduction in the case of $x = 1$, followed by the $x = 0.8$, and $x = 0$ QDs. The decrease in intensity over time is clearly manifested by the width of the high-intensity peak in the PL intensity histograms (right panels): while it is well-defined for $x = 0$, it becomes slightly broader in the case of $x = 0.8$ and spreads widely for $x = 1$ emitters. The observed photo-bleaching is a typical signature of photo-chemical degradation of perovskites NCs [93]. The relatively higher photo-instability observed in the organic-inorganic $FAPbBr_3$ ($x = 1$) perovskites compared to the all-inorganic $CsPbBr_3$ ($x = 0$) is well-documented in literature [134]. Here, by using mixed-cation perovskites to fine-tune the emission, we show that it is possible to mitigate this photo-instability, leading to reduced blinking and bleaching in comparison to organic-inorganic $FAPbBr_3$ ($x = 1$) perovskites.

To evaluate the PL intermittency more quantitatively, the correlations between PL intensity fluctuations and PL lifetime of individual quantum dots are analyzed using the FLID analysis. Starting from the PL time-traces obtained with a binning time of 10 ms in Figure 4.8, the mean arrival time for the photons detected in each bin is calculated, obtaining a corresponding lifetime time-trace. The upper panel of Figure 4.9a,c,e show the PL intensity time-trace of the three compositions within an enlarged period of a few seconds, while the bottom panel show these corresponding lifetime time-traces. Each pair of intensity and lifetime values constitutes a data point in the FLID intensity-lifetime space. The correlation between these two quantities can provide information on the origin of blinking in mixed-cation quantum dots, as explained in Chapter 1.2.3.1. According to this model, the emitter's PL can be reduced by the opening of non-radiative channels, like fast non-radiative Auger decay, which compete with the radiative recombination channel and quench photon emission. In contrast, in type-B blinking PL intensity fluctuations occur without

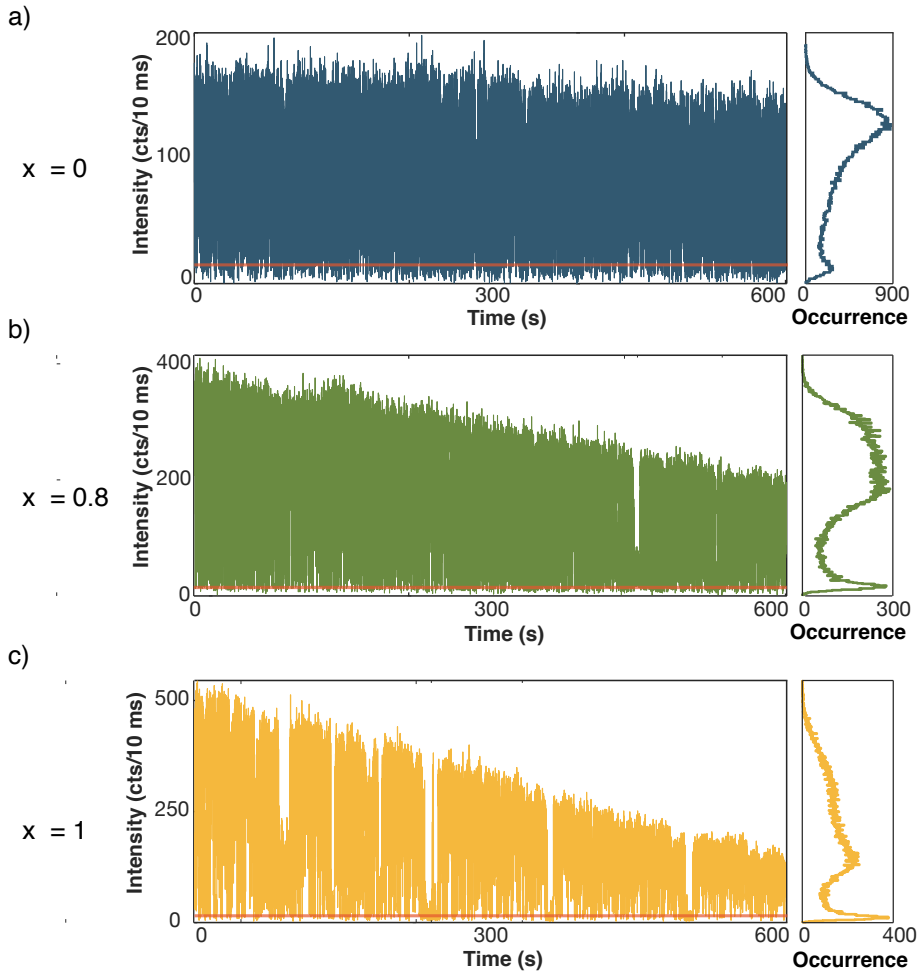

Fig. 4.8 ***Photo-stability and blinking of $Cs_{1-x}FA_xPbBr_3$ NCs (x=0, 0.8, and 1).*** *PL intensity time-traces and relative intensity histograms for single NCs with, respectively, a $x = 0$ (a), $x = 0.8$ (b) and $x = 1$ (c), with a binning time of 10 ms and an integration time of 600 s. The background level is given at 5 counts/10 ms. The threshold for the OFF states is 15 counts/10 ms (red line).*

appreciable changes in lifetime. FLID images obtained using a bin of 10 ms for the three compositions are plotted in false color, changing from blue to red with increasing probability, in Figure 4.9 (panels b, d and f). The resulting FLID trajectory is a curved line, typical of type-A blinking and confirming a correlation between PL intensity and lifetime [108]. Moreover, for the $x = 0$ and $x = 0.8$ emitters, the emission is found to be mostly in the bright state, while low intensity states became frequent for the $x = 1$ emitters (as evidenced by the red spot at shorter times and intensities). Additionally, in $x = 1$ composition the impact of bleaching is more

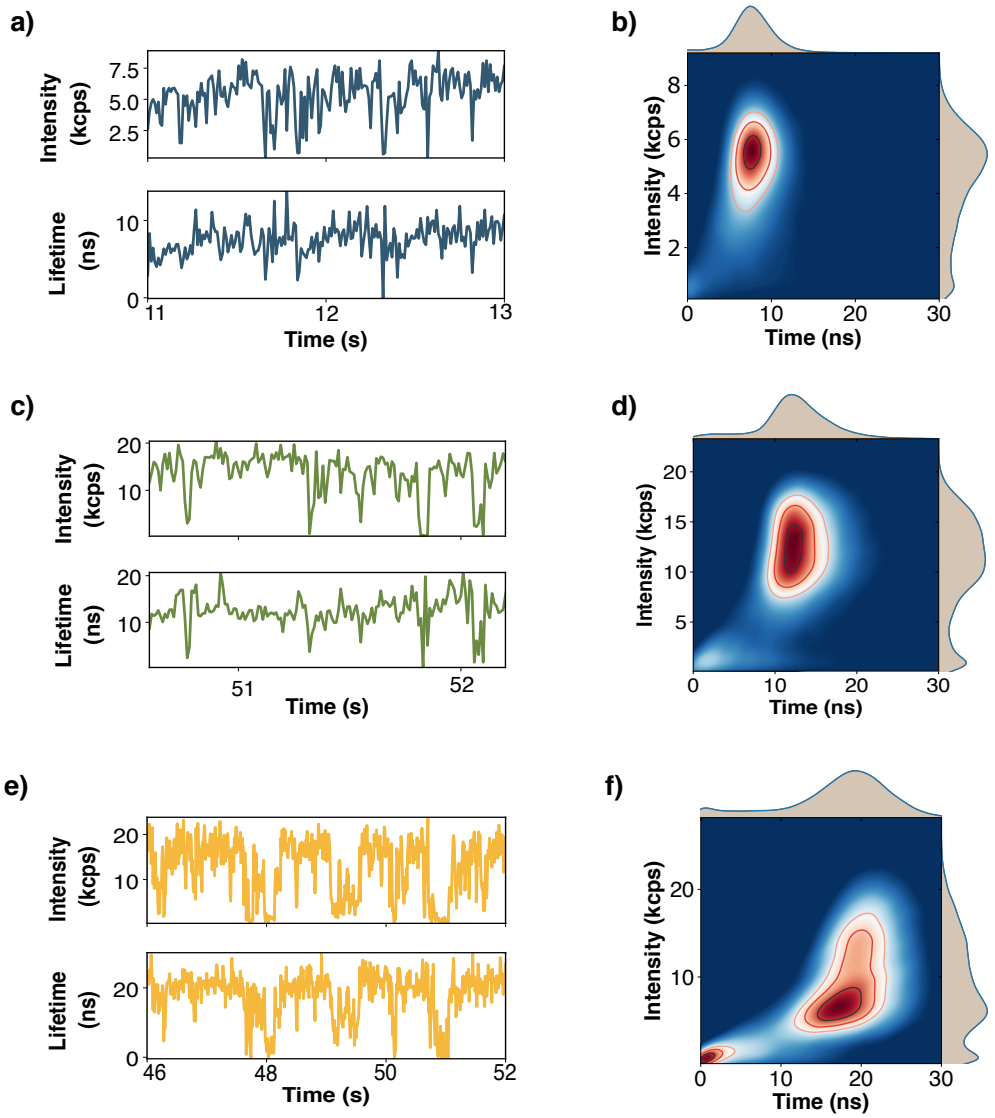

Fig. 4.9 ***Photolumiscence and lifetime time-traces***. *Zoom of PL intensity (upper panel) and lifetime (lower panel) time-traces for single NCs with respectively (a) $x = 0$, (b) $x = 0.8$, and (c) $x = 1$. b), d), f) False color representation of FLID images for NCS with, respectively, x=0, 0.8, and 1, obtained with a bin of 10 ms. A color change from blue to red corresponds to increasing probability of occurrences.).*

pronounced, resulting in a smeared distribution due to the reduction in intensity counts.

4.5 Single photon emission in $Cs_{1-x}FA_xPbBr_3$ NCs

The $Cs_{1-x}FA_xPbBr_3$ NCs have an average size of 10 nm, with a minimum value of 7 nm ($x = 0$) and 6 nm ($x = 0.8$ and 1), as seen in Figure 4.1. Given the excitonic Bohr radii of 7 nm ($x = 0$) and 8 nm ($x = 1$), quantum confinement and single photon emission are to be expected from these NCs. Measurements of the second-order intensity correlation function $g^{(2)}(\tau)$ were conducted with the HBT setup. Figure 4.10 shows the $g^{(2)}(0)$ values plotted in a semilogarithmic scale as a function of their CEW for the three compositions $x = 0$,$x = 0.8$ and $x = 1$.

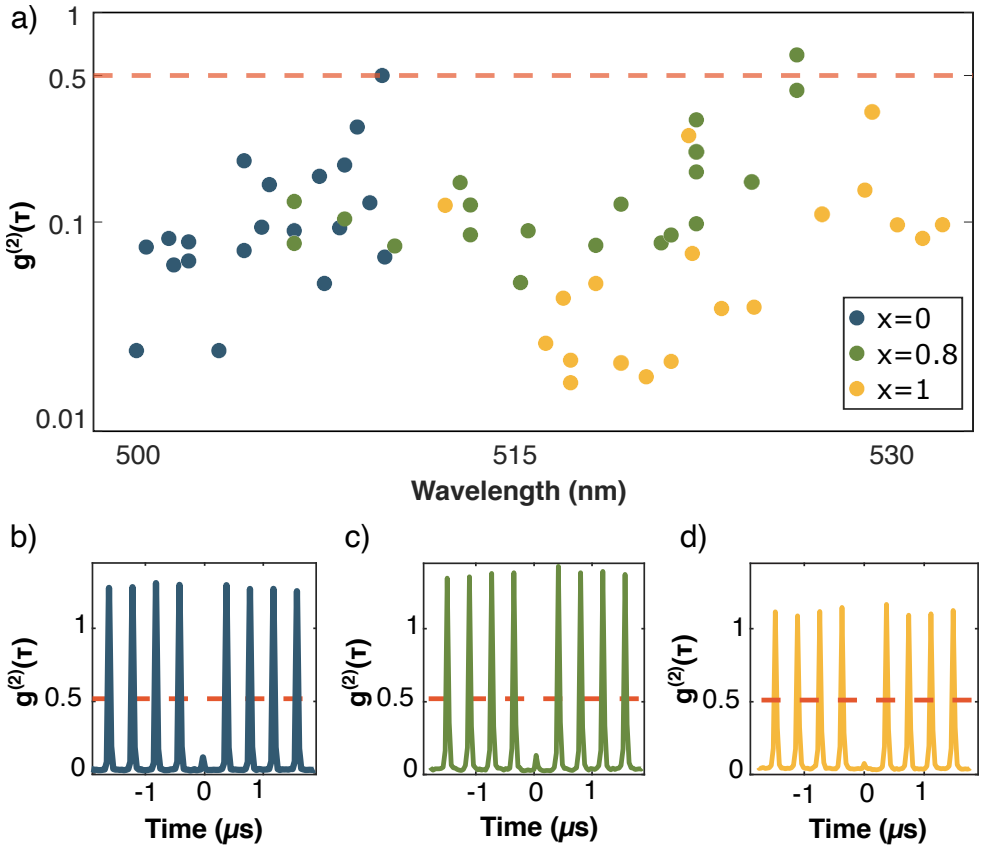

Fig. 4.10 ***Single photon emission of the individual $Cs_{1-x}FA_xPbBr_3$ ($x = 0$, 0.8, and 1) NCs.*** *(a) The measured $g(0)$ values for $CsPbBr_3$ (blue), $Cs_{0.2}FA_{0.8}PbBr_3$ (green), and $FAPbBr_3$ (yellow) in the semi-logarithmic scale as a function of their CEW. A sampling size of 20 emitters per composition were taken and the threshold for antibunching is reported (red dashed line). (b,c, d) $g^2(\tau)$ function of an individual $Cs_{1-x}FA_xPbBr_3$ NCs ($x = 0$, 0.8, and 1).*

I find that approximately 97% of the $Cs_{1-x}FA_xPbBr_3$ NCs show a $g^{(2)}(0)$ value well

below 0.5, clear signature of single photon emission. In particular, the majority of $CsPbBr_3$ (56%), $Cs_{0.2}FA_{0.8}PbBr_3$ (55%), and $FAPbBr_3$ (75%) NCs have $g^{(2)}(0) < 0.1$. It is possible to observe emitters with $g^{(2)}(0)$ values close to or exceeding 0.5, especially among those emitters that exhibit longer CEWs for each composition. As such, assuming a correspondence between the nanocrystal size and the emission wavelength, it is possible to attribute the degradation and/or loss of single photon emission to the increase in the NC's size and to the loss of quantum confinement.

The $g^{(2)}$ histograms with the best anti-bunching behavior recorded for each quantum dot composition are shown in Figures 4.10b-d, yielding $g^{(2)}(0)$ values of 0.05 ($x = 0$), 0.04 ($x = 0.8$), and 0.013 ($x = 1$). For completeness, Figure 4.11 presents two examples of $g^{(2)}$ measurements for NCs with compositions $x = 0.4$ and $x = 0.6$, which exhibit an antibunching value of $g^{(2)}(0) = 0.11$ at $g^{(2)}(0) = 0.09$ respectively.

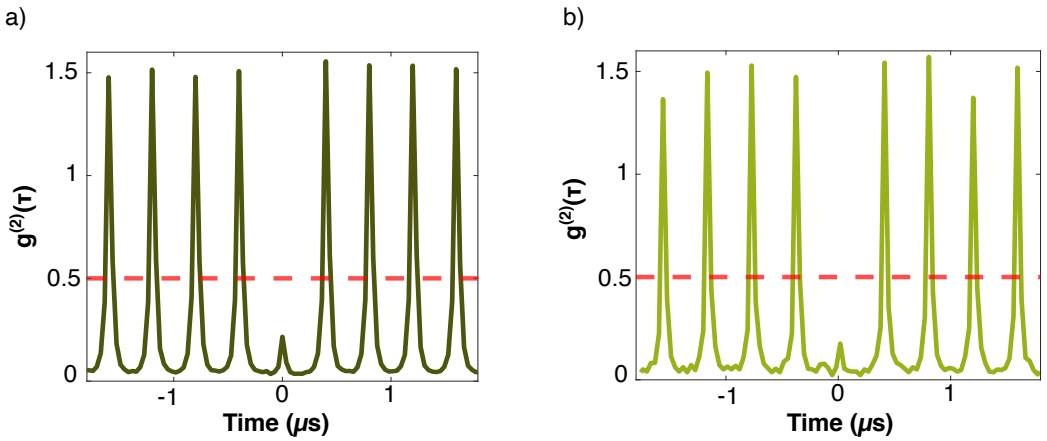

Fig. 4.11 ***$Cs_{0.6}FA_{0.4}PbBr_3$ and $Cs_{0.4}FA_{0.6}PbBr_3$ compositions.*** *a) $g^{(2)}(\tau)$ histogram for a $Cs_{1-x}FA_xPbBr_3$ NC with x=0.4, exhibing a antibunching value $g^{(2)}(0) = 0.11$. b) $g^{(2)}(\tau)$ histogram for a $Cs_{1-x}FA_xPbBr_3$ NC with x=0.6, exhibing a antibunching value $g^{(2)}(0) = 0.09$.*

.

Conclusion

In this chapter, I described confined mixed-cation $Cs_{1-x}FA_xPbBr_3$ NCs, obtained replacing inorganic Cs cations with organic FA cations. Specifically:

- I discussed how the allow to red-shift the emission wavelength while enhancing the photo-stability in comparison to conventional mixed-halide systems, which tend to be unstable in the red and near-infrared spectral regions due to the instability of iodine compounds.
- I showcased the tunability of emission wavelength of $Cs_{1-x}FA_xPbBr_3$ NCs both the ensemble and single-particle levels, with a specific focus on studying their photostability and blinking behavior.
- Notably, I reported what, to the best of our knowledge, this is the first demonstration of single-photon emission from mixed-cation perovskite NCs. The observation of their strong antibunching suggests that the quality of single photons generated by mixed-cation $Cs_{1-x}FA_xPbBr_3$ NCs, is on par with or may even surpass that of other room temperature SPS, such as NV defect centers in diamonds or III-V semiconductor QDs.

These findings lay the groundwork for the potential development of mixed-cation mixed-halide nanocrystals ($Cs_{1-x}FA_xPb(Br_{1-y}I_y)_3$), offering a more stable approach to achieving emission beyond 700 nm.

Furthermore, their broad tunability range may facilitate integration into photonic structures, such as Bragg cavities or metamaterial surfaces. For optimal integration, there remains the possibility of further improving their photostability, either through the use of polymers or through a doping process of the B-site, as described in the next chapter.

Chapter 5

Zn-treated perovskite NCs for enhanced photo-stability

Contents

Introduction

Despite the excellent optical properties and the strong single-photon emission demonstrated by perovskite NCs, their practical use has been hindered by environmental instabilities, such as their high sensitivity to illumination and moisture, as discussed in previous chapters. These instabilities pose a significant challenge in integrating them into various nanophotonic systems. In this chapter, I present an effective strategy to enhance the stability and brightness of $CsPbBr_3$ NCs by incorporating Zn^{2+} ions at the Pb-site. This work was conducted in collaboration with the Institut des Nanosciences de Paris (INSP), where the synthesis of Zn-treated $CsPbBr_3$ NCs was carried out by Dr. Emmanuel Lhuillier. This synthesis represents the outcome of extensive discussions and analysis of the results of the photophysical characterizations that I carried out, ultimately resulting in highly stable emitters for efficient single photon generation here described. After discussing the concept and implementation of the doping in Sections 5.1 and 5.2, I demonstrate the improved stability of the Zn-treated $CsPbBr_3$ NCs under dilution and illumination in Section 5.3. Section 5.4 discusses their single emission properties, while Section 5.5 focuses on the analysis of blinking. In Section 5.6, I show how these doped NCs exhibit high photo-stability and brightness even at excitation powers well above saturation levels. Finally, in Section 5.7, I briefly mention some prospects for further stabilizing these emitters using polymeric ligands.

5.1 Doping of the Pb-site to improve the structural stability

As already explained in Section 1.3.4, large efforts have therefore been dedicated to increase the LHP stability either through better ligand passivation [85–88], by growing a surrounding shell [89–91] or by embedding the NCs in a protective matrix to prevent exposure to moisture [92]. Recently, the doping of the Pb-site cation in the perovskite lattice with metal ions (Sn^{2+}, Cd^{2+}, Zn^{2+}) has been considered as one of the most effective methods to improve the structural stability and the optical performance of LHP-based LEDs and solar cells [135, 136]. In perovskite NCs glasses for white light-emitting diodes (WLEDs) applications, a small amount of ions doping improved the Goldschmidt tolerance factor t (the empirical index to predict the perovskite

structural stability). Importantly, this doping does not alter the crystalline structure of the perovskite [135, 137]. In particular, Zn^{2+} is of significant interest due to its non-toxicity, its high stability against oxidation or reduction compared to other dopants, and its effectiveness in eliminating defect states - contributing to passivate halide vacancy defects on the surface and reduce grain boundary surfaces [138] - where non-radiative recombination typically occurs [139]. As a result, Zn^{2+} has a beneficial impact on both the efficiency and long-term stability of the perovskite bulk-like systems [140].

In this chapter I focus on the Zn^{2+} doping of $CsPbBr_3$ NCs, resulting in Zn-treated $CsPbBr_3$ NCs with improved stability and brightness compared to the pristine $CsPbBr_3$ NCs presented in Chapter 2, while preserving their excellent quantum properties.

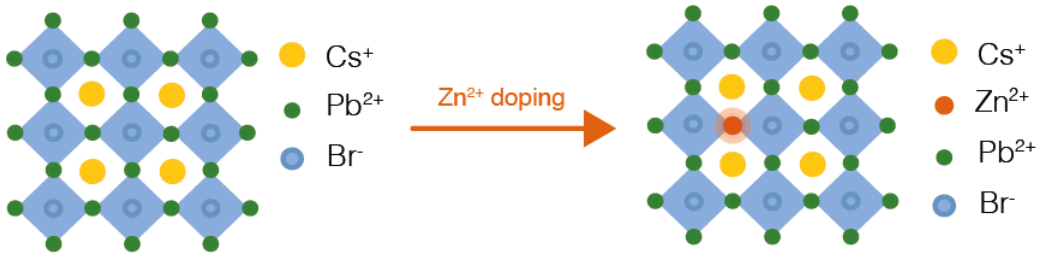

Fig. 5.1 ***Zn^{2+} doping of $CsPbBr_3$.*** *Given the redox state of Zn, the Zn^{2+} doping is likely to replace some Pb^{2+} ions.*

5.2 Synthesis of Zn-treated $CsPbBr_3$ NCs

To synthesize the Zn-treated $CsPbBr_3$ NCs, we start by growing pristine $CsPbBr_3$ NCs using the procedure developed by Kovalenko et al. [23] and described in Section 1.3.3.1. The grown particles present a cuboid aspect with 12 nm edge, as shown in high resolution transmission electron microscopy (HRTEM) images in Figure 5.2a. Some dark spots can be observed that have been associated with the reduction of the Pb^{2+} by the electron beam during the imaging. Subsequently, the grown cubes are mixed with a zinc and sulfur solutions containing molecular precursor as proposed by Ravi et al.[141] and described in Annexe B.

However, the procedure also comes with a significant increase in particle size, with some larger particles reaching sizes of up to 50 nm. Since maintaining small

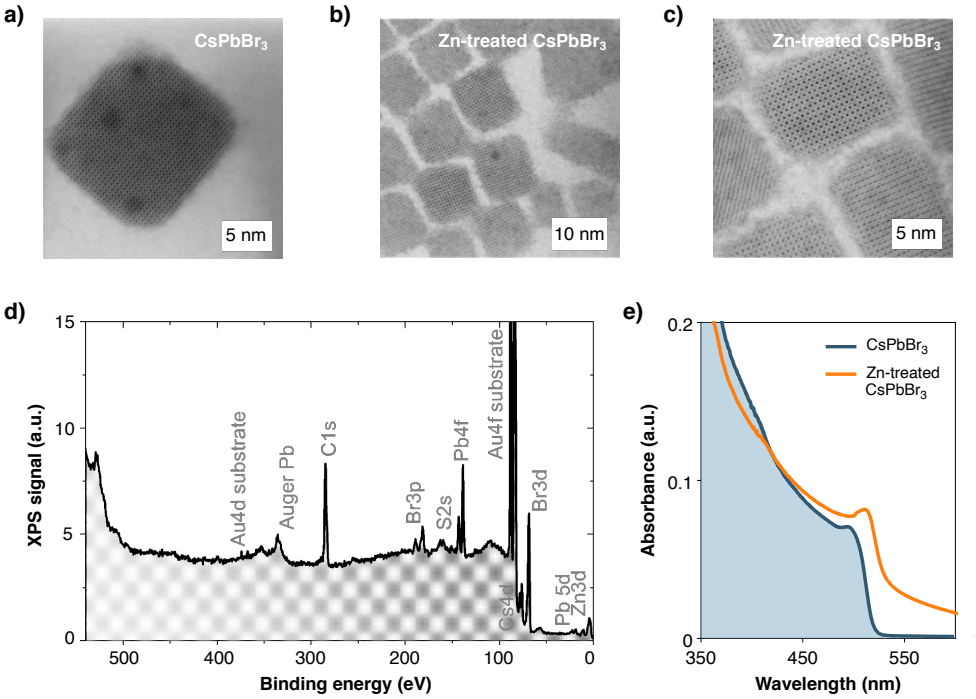

Fig. 5.2 ***Material characterization of Zn-treated $CsPbBr_3$ NCs.*** *a) High magnification HRTEM image of the pristine $CsPbBr_3$ NCs. Low (b) and high (c) magnification HRTEM images of the Zn-trated $CsPbBr_3$ NCs. d) X-ray photoemission survey spectrum for the Zn-trated $CsPbBr_3$ NCs. e) Absorption spectra for the pristine $CsPbBr_3$ NCs before and after their exposure to Zn(DDTC) precusor.*

size is critical to obtain single photon emission properties, we perform a size selection step to discard all the largest particle and presere the smallest. The morphology of the resulting Zn-treated $CsPbBr_3$ NCs is investigated using HRTEM, as shown in Figure 5.2b-c. These size-selected NCs have a size similar to the pristine $CsPbBr_3$, as opposed to what observed by Ravi, in which the particle sizes increases up to 40 nm.

Figure 5.2d shows the absorption spectra of the pristine and Zn-treated NCs, displaying respectively an absorption edge at around 520 nm and 530 nm.

X-ray photoemission spectroscopy (XPS) was carried out at the Synchrotron SOLEIL, to probed the chemical composition of the $CsPbBr_3$ NCs before and after their exposure to the Zn precursor. This analysis confirmed hat a low amount (around 0.5%) of Zn has been incorporated in the NCs (Figure 5.2d), which is consistent with previous report relative to Zn doping and alloying of perovskite NCs [142–145]. Figure 5.3 shows the high-angle annular dark-field scanning transmission

electron microscopy (STEM-HAADF), performed on the Zn-treated NCs to further give insight on the effect of Zn exposure. Zn content is confirmed to be low and no correlation between its localization and the NC surface are found, suggesting that Zn mostly come as a dopant.

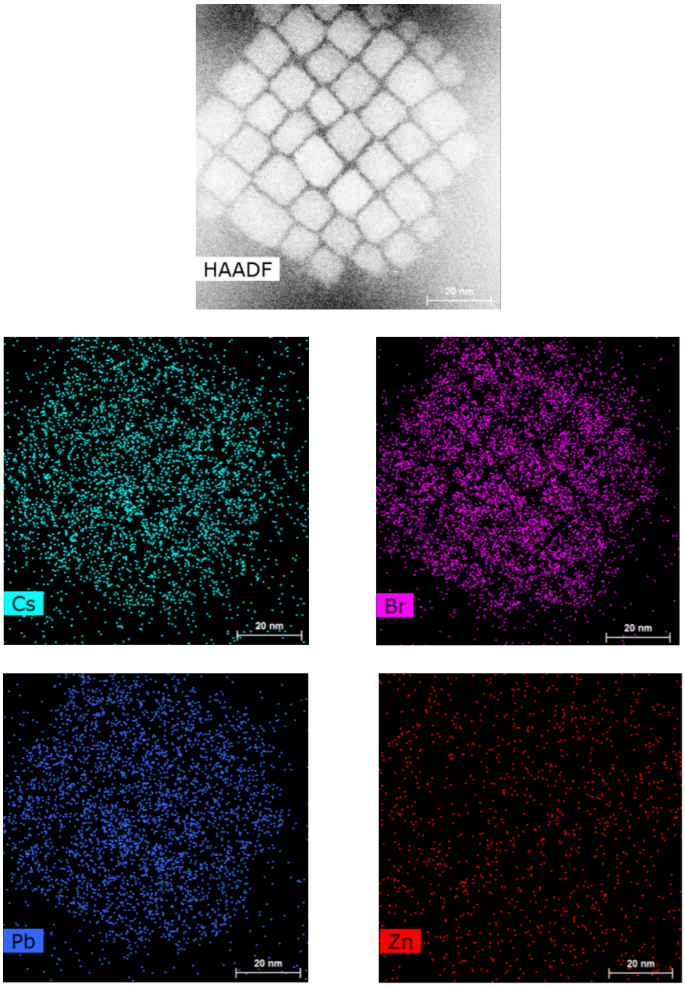

Fig. 5.3 ***High-angle annular dark-field scanning transmission electron microscopy (STEM-HAADF) of Zn-treated $CsPbBr_3$ NCs***, *revealing the localization of Cs, Br, Pb, and Zn contributions. Zn content is confirmed to be low (0.5% atomic ratio) and no correlation between its localization and the NC surface are found, suggesting that Zn mostly come as a dopant.*

5.3 Photostability of Zn-treated $CsPbBr_3$ NCs

The colloidal stability of perovskite NCs mainly depends on their surface chemistry, due to their high surface-to-volume ratio, as already explained in Section 1.3.4. The dynamic binding between capping ligands and ionic NC lattice can lead to ligand and halide atom detachment, causing surface disorder and defects that diminish long-term stability.

As our goal is to couple perovskite NCs with optical nanofibers in order to obtain an integrated single-photon sources, as described in Chapter 6, it is crucial to achieve a high level of colloidal stability even in highly diluted solutions. This stability is necessary for depositing a single emitter onto the nanofiber, and addressing environmental-induced instabilities becomes essential.

5.3.1 Photostability under dilution

I assessed the stability of Zn-trated $CsPbBr_3$ NCs under dilution by studying NCs ensembles using wide-field microscopy [87], using the same method described in Chapter 3 for $CsPbBr_3$ NCs. I prepared five samples by diluting a NCs solution with a molar concentration of approximately 1 µM with toluene at various dilution ratios, ranging from 1 : 10 to 1 : 200. The specific solvent-to-solute ratios employed for these dilutions, while keeping the total volume constant at 1 mL, are provided in Table 5.1.

Dilution factor	Solvent	Solute
1 : 10	0.9 mL	100 µL
1 : 25	0.95 mL	50 µL
1 : 50	0.98 mL	20 µL
1 : 100	0.99 mL	10 µL
1 : 200	$\sim$ 0.995 mL	5 µL

Table 5.1: **Solvent-to-solute ratios for NCs dilutions.** NCs solution with a original molar concentration of approximately 1 µM were diluted with toluene at various dilution ratios, ranging from 1 : 10 to 1 : 200, while keeping the total volume constant at 1 mL.

The samples to characterize were prepared using the spin-coating technique, under identical conditions. To study the photobleaching evolution with dilution, the samples were exposed to intense LED light at a wavelength of 400 nm in a wide-field configuration. The emission of each of the five samples was sequentially recorded

within a squared sample area measuring 133 µm x 133 µm, corresponding to the sizes of the camera frame. A frame was captured every 20 s seconds throughout 1-hour for each sample. By counting the number of emitting NCs in each frame and normalizing it to the number of NCs in the initial frame, we can track the temporal evolution of ensemble emission as a percentage, as depicted in Figure 5.4.

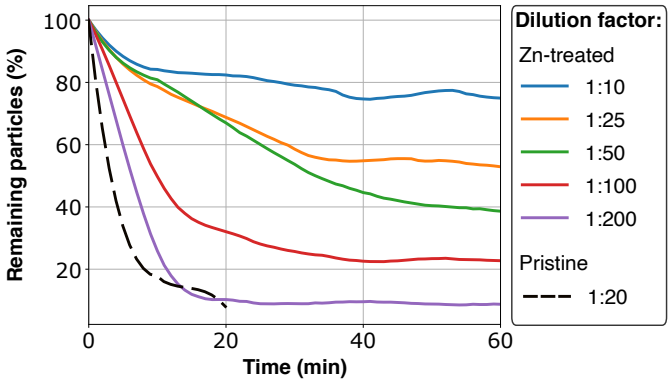

Fig. 5.4 ***Stability in dilution of Zn-treated CsPbBr$_3$ NCs.*** *In color lines, percentage of Zn-trated CsPbBr$_3$ NCs still emitting after 1 hour under strong LED illumination as a function of dilution* $1:X$*, with x going from 10 to 200. In dashed black line, percentage of pristine CsPbBr$_3$ NCs still emitting after 20 minutes in a* $1:20$ *dilution.*

Zn-trated $CsPbBr_3$ NCs exhibit superior resistance to dilution compared to pristine $CsPbBr_3$. For the latter ones photobleaching occurs within 5 minutes regardless of the dilution used, as seen in Chapter 3. This behaviour is reported in Figure 5.4 by the dashed dark line, representing a 1: 20 dilution and serving as a basis for comparison. In the case of Zn-treated NCs, represented by colored lines in the figure, a dilution ratio of 1: 10 exhibits remarkable stability, with over 70% of particles still emitting after 1 hour. For the 1: 25 dilution, approximately 55% of particles continue to emit after 1 hour, followed by 40% for a $1:50$ dilution and 20% for a 1: 100 dilution. Only when reaching a $1:200$ dilution we start to observe bleaching effect, with a bleached time of about 15 min. In this case, a constant residual photoluminescence is observed, which can be attributed to the presence of small aggregates. The improved resistance to dilution in Zn-treated $CsPbBr_3$ perovskites is due to a reduction in defect states resulting from the doping process. This reduction diminishes the degradation of the NCs, even without a polymer encapsulation.

5.3.2 Photostability under illumination

Moving to a confocal microscopy scheme, we monitored then the spectral stability of individual NCs in the 1 : 10 dilution, which allows us to address an individual emitter, as confirmed by its single photon emission, and collect its luminescence. A single NC was excited with the pulsed laser at 405 nm, under a fluence of around $2.5 \mu J/cm^2$. The NC was illuminated for 1 hour, while its emission spectrum was collected every 5 minutes.

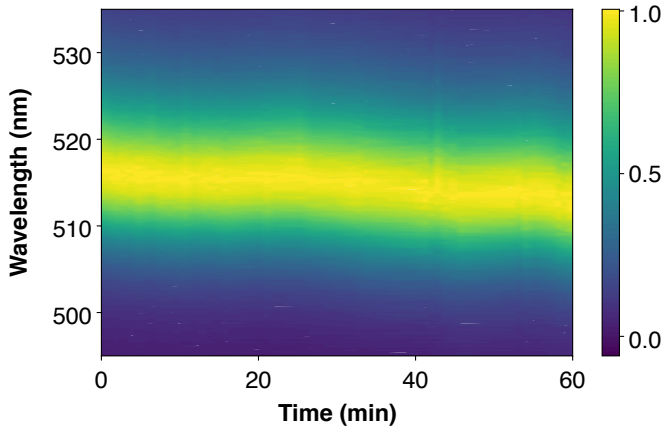

Fig. 5.5 ***Spectral stability in dilution of Zn-treated $CsPbBr_3$ NCs.*** *Evolution of the CEW from a single Zn-treated CsPbBr3 NC excited at its saturation intensity. Each spectrum is normalized to its maximum intensity.*

As discussed in Chapter 3, when conducting measurements under ambient conditions, a continuous blue-shifting of the PL spectrum has been frequently reported in literature [26, 80, 92]. This is a typical signature of photo-induced degradation that leads to a layer-by-layer etching of the NC surface, resulting in a reduction in the size of the QDs and an increase in the band-gap energy [93]. Figure 5.5 shows the 2D colored plot of consecutive PL spectra obtained, showing a blue-shift of the CEW of less than 4 nm in 1 h. The photostability of these emitters demonstrates a slight improvement compared to the pristine $CsPbBr_3$ in Chapter 3, where a 5 nm blueshift occurred over of 1 hour. This improvement is also noteworthy when compared to previously reported results for emitters without encapsulation. In fact, typically $CsPbBr_3$ emitters experience a blue-shift of over 10 nm within just a few tens of seconds, as reported by Rainò et al. [109].

5.4 Single photon emission in Zn-treated $CsPbBr_3$ NCs

I thoroughly analyzed the optical and quantum properties of a set of 60 Zn-treated $CsPbBr_3$ emitters. To establish a reference for the characterization of several emitters, all measurements were performed at the saturation power of each nanocrystal. Figure 5.6a presents the CEWs distribution of the 60 emitters. Due to the slight inhomogeneous size distribution of the NCs, the CEW ranges from 504 to 518 nm (2.46 to 2.40 eV), with an average around 512 nm.

A typical emission spectrum is reported in Figure 5.6b , with a CEW of 512 nm (2.42 eV) and a FWHM of 15 nm (70.69 meV). To verify that the Zn-treated $CsPbBr_3$ NCs behave as sources of quantum light, we evaluate their single photon purity measuring the second order correlation function $g^{(2)}(\tau)$. Figure 5.6c presents a typical histogram of $g^2(\tau)$, showing a photon antibunching value of $g^{(2)}(0) = 0.08$ after background subtraction. I measured the $g^{(2)}(\tau)$ for all 60 emitters and analyzed the $g^{(2)}(0)$ evolution as a function of the emission energy (and corresponding CEW). As the emission wavelength increases with the emitter size, this analysis allows to exploring the effect of quantum confinement on single photon emission. The results are displayed in Figure 5.6d. The $g^{(2)}(0)$ decreases from 1 to 0.1 as the emission energy increases, consistently with the trend reported for $CsPbBr_3$ perovskite NCs in section 3.3. In this case as well, the observed trend strongly indicates that an increase of the degree of quantum confinement corresponds to an increase of the single-photon purity. Below approximately 515 nm, around 94% of the NCs exhibit antibunching behaviour. However, beyond this threshold, only a single nanocrystal was observed to emit single photons, suggesting that for emission wavelengths exceeding approximately 515 nm the quantum confinement regime is no longer maintained.

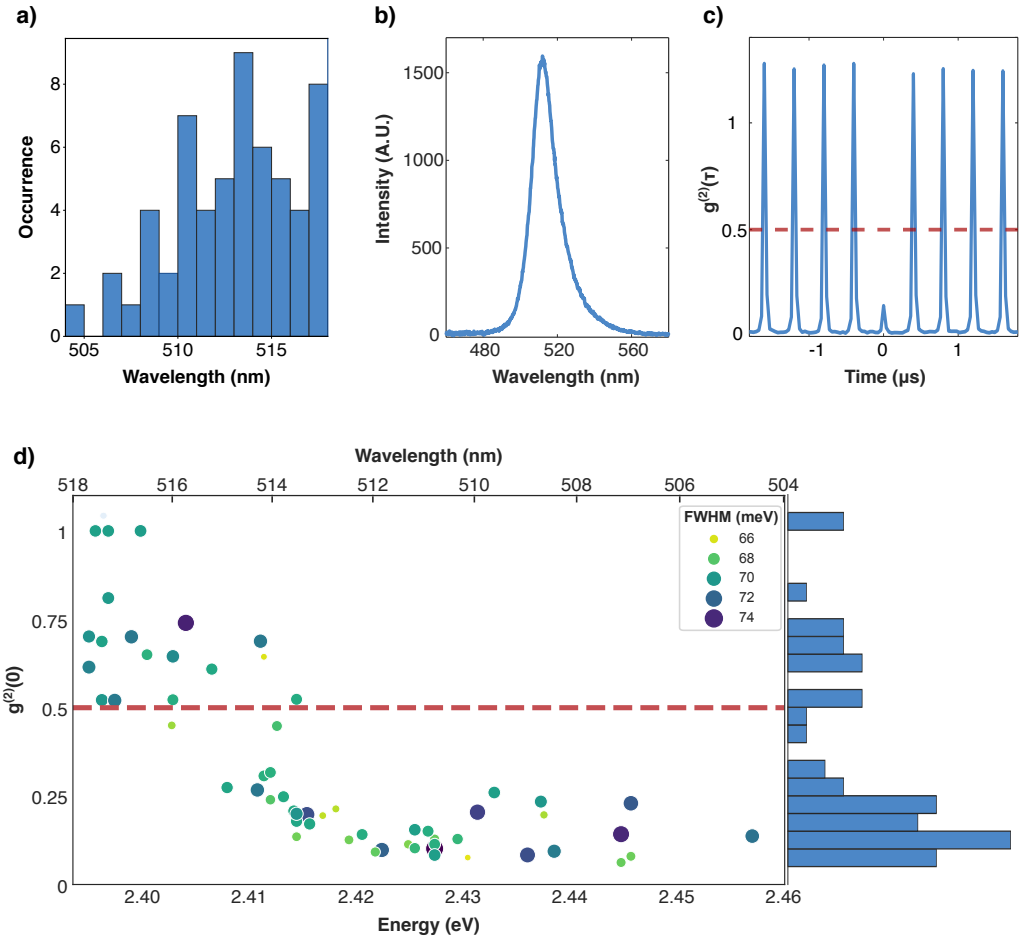

Fig. 5.6 ***Single photon purity of Zn-treated $CsPbBr_3$ NCs.*** *a) Histogram of the measured CEWs for a set of 60 NCs. b) Representative emission spectrum of a single NC. c) Example of second-order correlation function of a single NC emitting high-quality single photons ($g^{(2)}(0) = 0.08$ after background counts subtraction). The red-line indicates the threshold for single-photon emission claim. d) Measured $g^{(2)}(0)$ values as a function of the energy (bottom axis) and CEW (upper axis) for the 60 NCs. All the emitters were excited at their saturation intensity. All the emitters were excited at their saturation intensity.*

5.5 Blinking in Zn-treated $CsPbBr_3$ NCs

Figure 5.7a shows a typical PL intensity time-trace for a single Zn-treated $CsPbBr_3$ NC, together with the corresponding intensity histogram, obtained through a time-tagged time-resolved (TTTR) method with a temporal resolution of 126 ps. The measurement was carried out at the saturation power with a binning time of 10 ms. The results show that the NC maintains a highly stable and bright emissive state, as evidenced by a constant count rate over the entire 600 s integration time. Moreover, as compared to the pristine NCs in Figure 5.12a , the brightness of the Zn-treated $CsPbBr_3$ NCs is improved. To investigate the nature of the blinking, two intensity windows were selected from the intensity time-trace, corresponding to the high-intensity and low-intensity states (see orange and blue areas, respectively, in Figure 5.7a). The corresponding TTTR signals were then pinpointed to retrieve their PL decays, which where compiled for statistics. The results are shown in Figure 5.7b. The PL decays for the two intensity windows were fitted with a mono-exponential model, taking into account the background noise, yielding lifetimes of $\tau_1 = 10.2$ ns and $\tau_2 = 1.3$ ns, respectively for the high-intensity and low-intensity states.

According to the charging/discharging model [108], the high-intensity states can be attributed to radiative excitonic recombinations, while the faster decay of the low-intensity states is indicative of emission from charged excitons (trions). Trions have higher likelihood to experience non-radiative Auger recombination [71] resulting in a reduced PL.

Figure 5.7c shows a zoomed-in view of a 7-seconds segment of the intensity time-trace, with a bin time of 10 ms. In the lower panel of Figure 5.7c, the average lifetime of photons within each bin is plotted as a function of time. Notably, a clear correlation between the photon lifetime and emission intensity is observed, which is indicative of type A blinking behavior.

Blinking dynamics are commonly investigated on time scales of milliseconds and longer by mean of binning and thresholding [64] or change-point analysis [146]. Nevertheless, these approaches rely on the binning of photon detection events and may not provide reliable information, especially in the case of fast blinking.

The second-order correlation function can enable, when measured for higher delays, to accurately assess the amplitude and rate of blinking at short time scales that would not be accessible through the binning of the signal [147, 148]. Figure 5.7d displays this function for time delays between 1 µs and 1 s. Notably, at short delays

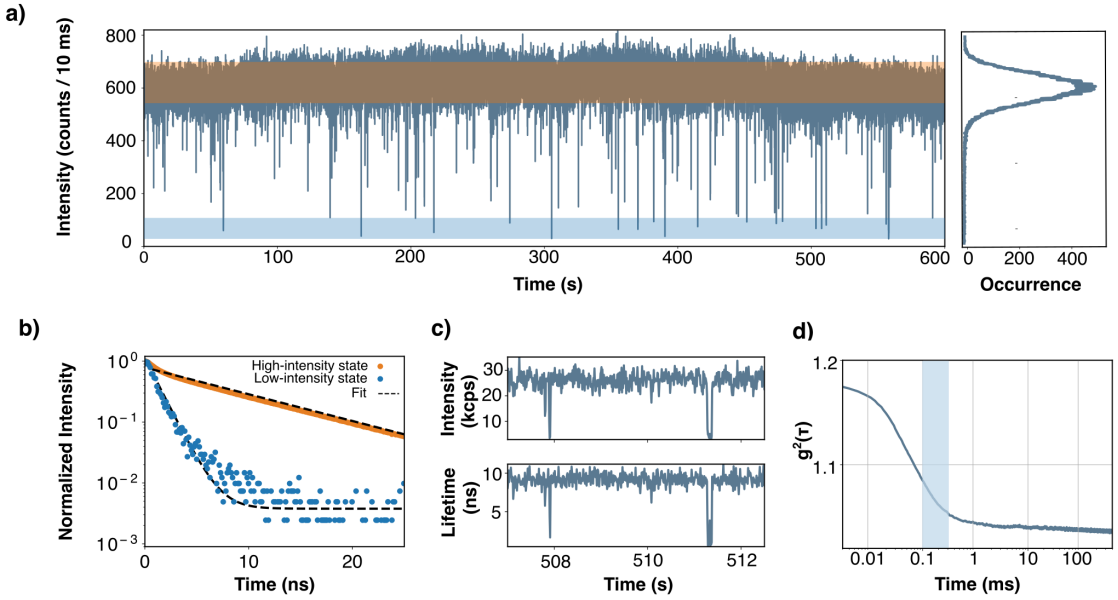

Fig. 5.7 ***Blinkig dynamics in Zn-treated $CsPbBr_3$ NCs.*** *a)Intensity time trace of a single NC, and corresponding relative histogram of intensity occurences. b) Decays for the low-intensity states (blue) and high-intensity states (orange). c) Zoom-view of the intensity time-trace (upper box) and lifetime (lower box) of a single NC. d) $g^2(\tau)$ at large time delays for a single NC.*

($\tau < 10\,\mu s$) the $g^{(2)}(\tau)$ function exhibits a super-Poissonian bunching value of 1.18, due to the flickering between the two intensity states [149]. For delays above $100\,\mu s$, the $g^{(2)}(\tau)$ value decreases towards unity, meaning that switching between the two states does not happen on these longer time-scales.

Figure 5.8 shows a comparison between pristine $CsPbBr_3$ NCs (blue curve) and Zn-treated $CsPbBr_3$ NCs (orange curve). Pristine NCs display a $g^{(2)}(\tau)$ value above 1.32 at short delays and exhibit millisecond-scale blinking behavior. In contrast, Zn-treated NCs exhibit significantly diminished blinking-induced bunching, corresponding to a strongly reduced blinking probability, and faster blinking times on a microsecond time scale.

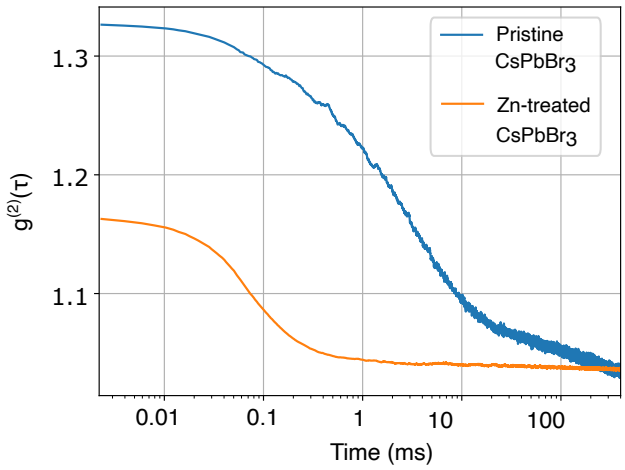

Fig. 5.8 ***g*(2) at large delays for pristine and Zn-treated NCs.*** *At short delays ($\tau < 10\,\mu s$) the $g^{(2)}(\tau)$ function exhibits a super-Poissonian bunching value of 1.18 for pristine NCs (blue curve) and 1.32 for Zn-treated NCs (orange curve). The curves decreases towards unity after 0.1 ms in the case of Zn-treated NCs and after 10 ms in the case of pristine NCs.*

5.6 Stability of the single photon emission with the power

For 25% of the Zn-treated $CsPbBr_3$ NCs (15 emitters out of 60), measurements were conducted with varying excitation power levels. The primary objective was to investigate how single photon purity evolves with increasing excitation power.

As discussed in Section 1.2.3.2, for an ideal two-level system, emitting one photon per excitation pulse, the emitted intensity would show a perfect saturation as a function of the excitation power and the $g^2(\tau)$ function a perfect antibunching $g^2(0) = 0$ independent of the excitation power. On the other hand, in confined LHPs NCs under high excitation power, the contribution of multiexciton states to the emission, although significantly reduced by an efficient Auger non-radiative recombination[25] results in a non-perfect saturation curve and a power dependent $g^2(0)$ value.

Figure 5.9a shows the PL intensity of a single Zn-treated $CsPbBr_3$ NC measured as a function of the excitation power. The data were fitted with the following model:

$$I = A \cdot \left[1 - e^{-\frac{P}{P_{sat}}}\right] + B \cdot P \tag{5.1}$$

where P_{sat} is the saturation power, and A and B are two constants that depend respectively on the intensity of the single- and bi-exciton components of the emission. The saturation power was extracted from the fitting curve and used for single particle measurements. I measured $g^{(2)}(\tau)$ at different excitation power (respectively with P/P_{sat} = 0.25,0.5,1,1.5,2,3). We observe that $g^{(2)}(0)$ increases below P_{sat} and remains constant for higher excitation powers.

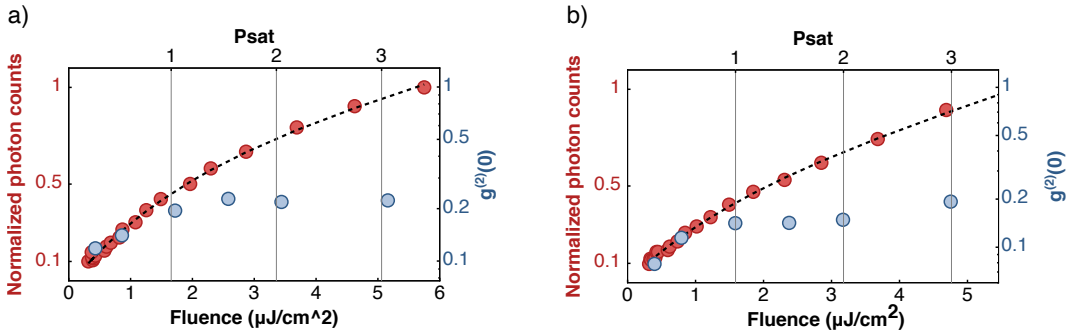

Fig. 5.9 ***Stability of the single photon emission with the excitation power.*** *In red: saturation measurement of two single NCs (a and b respectively). The dots are the experimentally measured counts with the excitation power. The dashed black line is the fitting function from eq 5.1. In blue: evolution of the antibunching $g^2(0)$ values measured for different excitation powers (respectively with P/P_{sat} = 0.25,0.5,1,1.5,2,3).*

Figure 5.10a shows the PL decays as a function of the excitation power. These decays become slightly faster as the excitation power rises. Nevertheless, the negligible bi-exciton contribution is confirmed by the constant value of $g^{(2)}(0)$ as the excitation power increases. In Figure 5.10b, the behavior of $g^{(2)}(\tau)$ at large delays is presented for various excitation power levels (corresponding to 0.25, 0.5, 1, 1.5, 2, and 3 times P_{sat}).

Notably, as the excitation power increases, the blinking becomes more pronounced, particularly evident for time delays shorter than 0.1 ms. For an excitation power of $3P_{sat}$, blinking occurs on a shorter timescale, indicating that for high excitation powers, blinking becomes increasingly significant.

To evaluate the stability of the high-intensity state, we use a Fluorescence Lifetime-Intensity Distribution (FLID) analysis, which, as seen in previous chapters, provides a visual way to analyze correlations between photoluminescence intensities and lifetimes [108].

In particular, from $P_{sat}/4$ to P_{sat} we observe that the emission remains in the

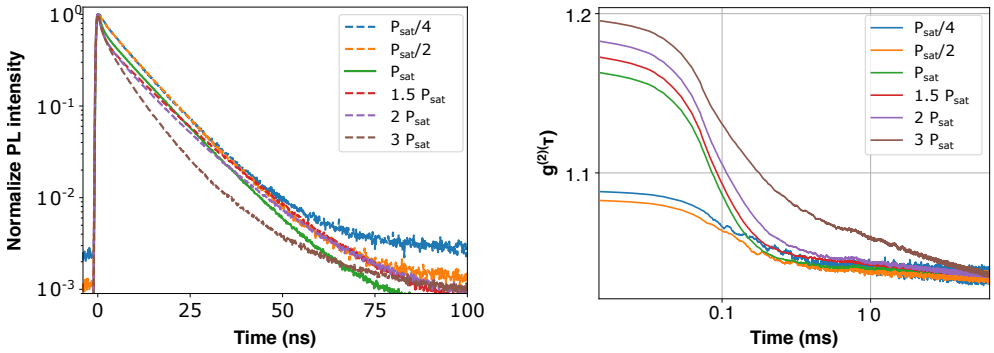

Fig. 5.10 ***PL decays and $g^{(2)}(\tau)$ at large delays varying the excitation power.*** *a) PL decays (a) and $g^{(2)}(\tau)$ at large delays (b) measured for different excitation powers (respectively to* 0.25,0.5,1,1.5,2,3 *times the P_{sat})*

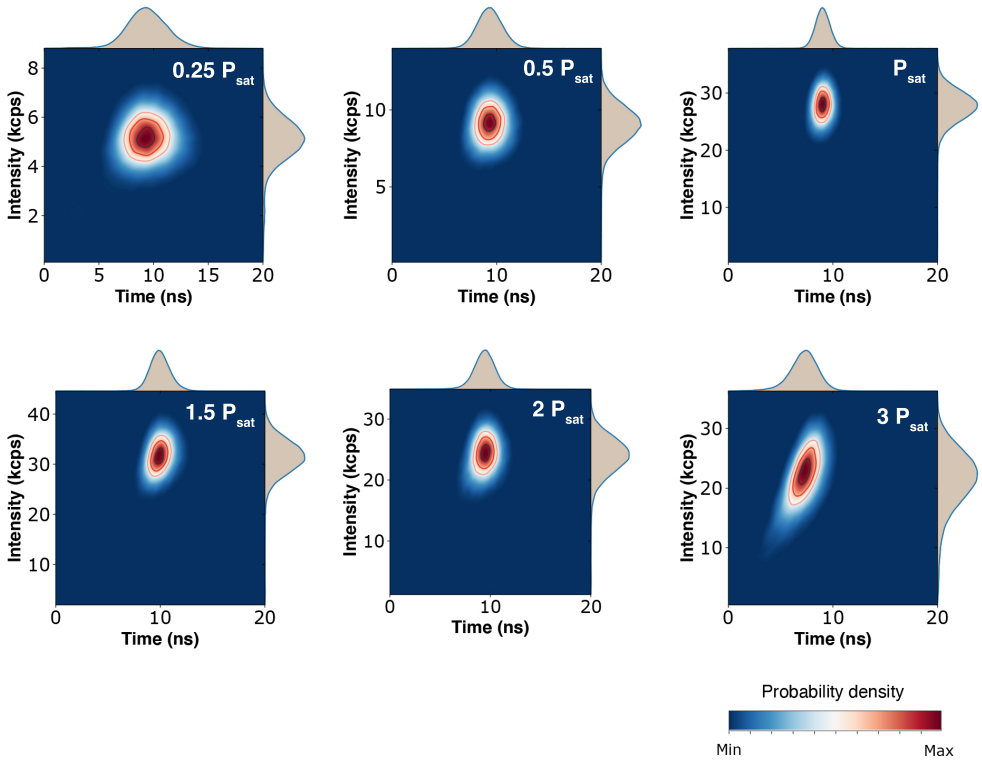

Fig. 5.11 ***FLID images varying the excitation power.*** *Fluorescence lifetime-intensity distribution images of a single emitter, excited respectively at* 0.25,0.5,1,1.5,2,3 *times P_{sat}.*

bright state characterized by significantly reduced blinking and the absence of photobleaching. At an excitation level of $3P_{sat}$, we begin to observe an elongated and smeared distribution. This shape can be attributed to two main factors. First, at

an excitation power of $3P_{sat}$, blinking occurs at a longer time-scale. Second, the elongated shape can be ascribed to a slight reduction in counts, which results from photo-bleaching at such high excitation power.Comparatively, pristine NCs, before Zn-treatment, already showed an important spread at P_{sat}, as shown in Figure 5.12

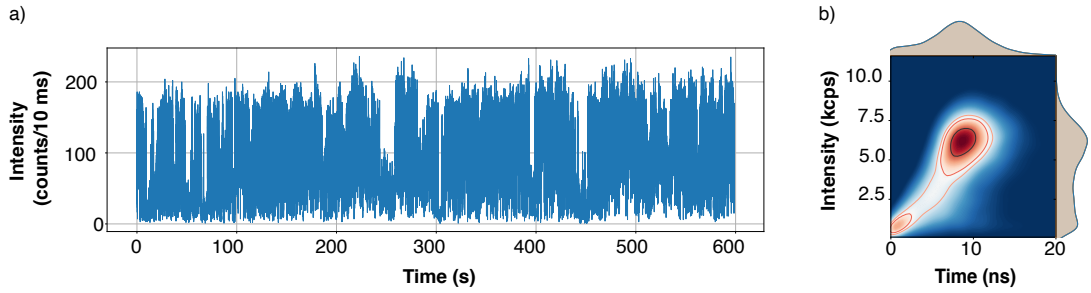

Fig. 5.12 ***FLID analysis of pristine $CsPbBr_3$.*** *a) PL time-trace of pristine $CsPbBr_3$ at saturation power. b) FLID image of pristine $CsPbBr_3$ at saturation power.*

5.7 Alternative ligands to further improve the photo-stability

Conventional perovskite NCs are typically synthesized using a combination of two amine capping ligands, namely oleic acid (OA) and oleylamine (OLA), as described in details in Section 1.3.3. These ligands exhibit dynamic nature and a labile interactions with the NC surface [150]. Considering this, I initiated a preliminary investigation to explore alternative capping ligands with the aim to further improve the stability of the studied Zn-treated NCs. This investigation was motivated by the fact that the use of standard polymers such as PMMA, commonly employed in microscope characterization, is not practical when considering their integration with an optical nanofiber.

For this on-going study, I characterized Zn-treated $CaPbBr_3$ NCs synthesized using three alternative capping ligands:

- **Lecithin**, for which is reported a long-term stability in the case of red-emitting perovskites films [151].
- **Polyethylenimine (PEI)**, a polymer rich in amine groups on its branched chains, used to stabilize perovskites nanoplatelets [152].

- **Hexyl phosphonate (HPA)**, proposed as an alternative to labile OA ligands in the synthesis of blue-emitting perovskite nanoplateletes [153].

The synthesis with PEI yielded confined nanocrystals (NCs) that demonstrated robust single-photon emission and optical properties similar to those obtained with the standard synthesis method used for Zn-treatment. Nevertheless, further optimization of the colloidal solutions are necessary. This is because all the solutions currently exhibit a high percentage of clusters, in particular in the case of Lecithine and HPA, as depicted in the wide-microscopy images in Figure 5.13, which prevents a proper assessment of the emitters' stability.

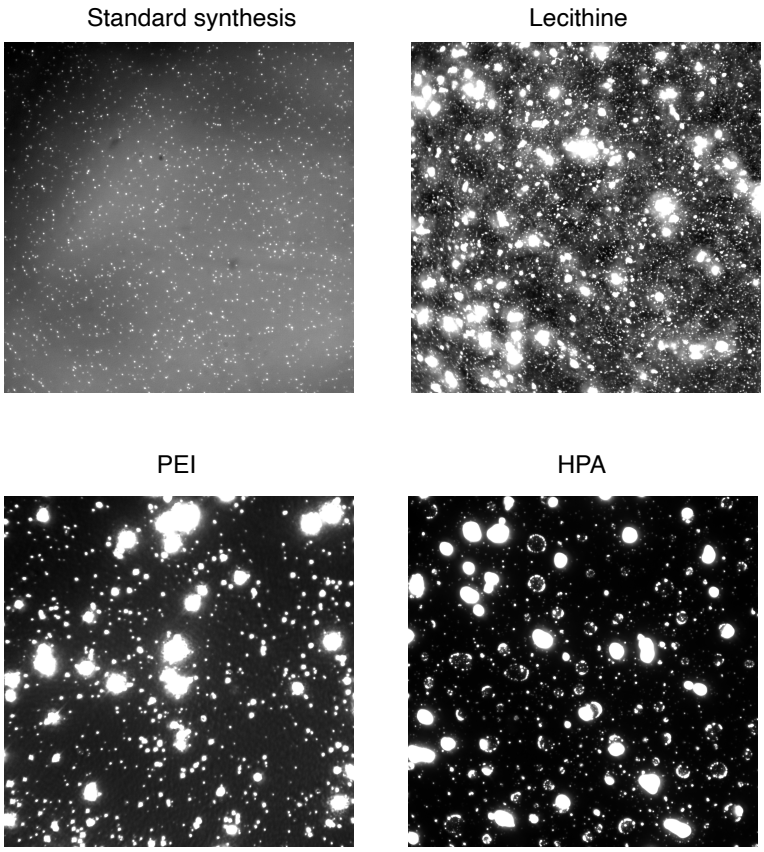

Fig. 5.13 ***Alternative capping ligands.*** *Wide-field microscopy images on samples syntetized using: a) standard Zn-treatment, b) lecithine as capping ligand, c) Polyethylenimine (PEI) as capping ligand, c) Hexyl phosphonate (HPA) as capping ligand.*

Conclusions

In this chapter I demonstrated that the Zn^{2+} doping of NCs is a very efficient approach for enhancing the stability and brightness of LHP NCs.

- The studied Zn-treated NCs exhibit an increased stability under dilution and illumination.
- Thet exhibit high single-photon purity, with values as low as ≈ 0.08.
- A significantly reduced blinking behavior on a sub-millisecond time scale is observed, in contrast to the pristine NCs which exhibit a millisecond time-scale blinking.
- A remarkable stability in both the brightness and single photon purity of the emission across a large range of excitation powers is observed.

This synthesis approach could enable to achieve more stable emissions in the red and NIR spectral ranges, where iodine components are prone to instability. The operation of this new class of highly stable perovskite nano-emitters at cryogenic temperature is also expected to further improve the recent results on the indistinguishability of the emitted photons [154], a must-go for practical quantum technologies applications.

Chapter 6

Hybrid integrated single photon sources

Contents

Introduction

In the previous chapters, we explored the high-efficiency single photon generation with perovskite NCs. However, generating single photons efficiently is useless without the ability to collect and transport them effectively. Consequently, fiber-coupled single photon sources, designed for the long-distance transmission of quantum information, are crucial for the development of future quantum networks [155]. In this chapter, I present the coupling of a perovskite NC with an optical tapered nanofiber, serving as a proof of concept for a compact and integrated single photon source. In Section 6.1, I introduce this platform, elucidating its advantages and applications. Section 6.2 delves into the propagation of light within the nanofiber and the conditions required for achieving single-mode nanofiber behavior. Section 6.3 outlines the nanofiber fabrication protocol and describes the quality control measures I carried out. Section 6.4 provides an in-depth look at the optimizations I made to address key challenges that hinder the practical, optimal use of nanofibers. Finally, in Section 6.5, I describe the coupling of a quantum emitter with the nanofiber, demonstrating how this integrated system functions as a hybrid single photon source.

6.1 Optical tapered nanofibers

An optical tapered nanofiber (ONF) is a cylindrical waveguide that begins and ends like a conventional optical fiber. However, in the central section, it gently tapers down in diameter, typically reaching a waist diameter of few hundred nanometers. This waist diameter is often equal to or even smaller than the wavelength of the guided light. Figure 6.1 provides a visual representation of its geometric structure. As depicted, the standard fiber ends consist of two concentric dielectric cylinders: a *core* with a refractive index here referred to as n_{core}, surrounded by a *cladding* with a lower refractive index here denoted as $n_{cladding}$. In the case of a single-mode fiber, the standard fiber part usually has a diameter of 125 µm. Additionally, the fiber may be enveloped in an elastic and abrasion-resistant plastic coating known as *jacket*, serving to protect the fiber, as illustrated in the inset on the bottom right side of the figure.

ONFs have garnered significant attention due to their advantageous optical and mechanical properties, which include:

- **Intense evanescent fields**: In a typical optical fiber, light propagates for total

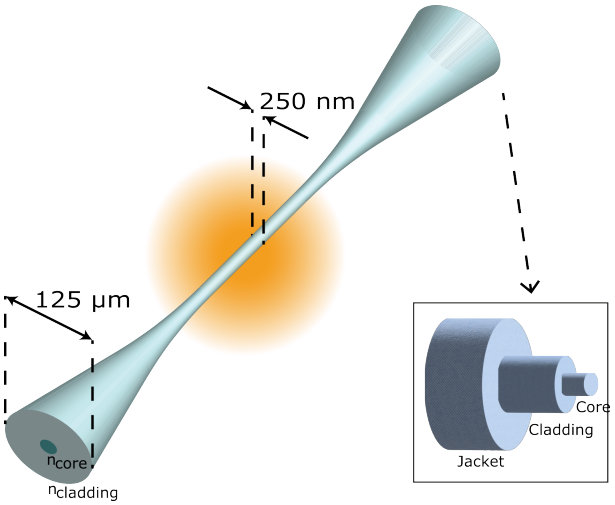

Fig. 6.1 ***Scheme of an optical tapered nanofiber.*** *Optical tapered nanofibers are fabricated by adiabatically stretching optical fibers, then preserving the original dimensions at the input and output ends. The fiber ends have a size of* 125 µm *and consist of a core with a refractive index* n_{core}*, surrounded by a cladding with a lower refractive index* $n_{cladding}$*. Additionally, the fiber are enveloped in a plastic protective jacket (inset on the bottom right).*

internal reflection, if the incident angle falls within the range $0 < \theta < \theta_{max}$. The value of θ_{max} can be calculated using the refractive indexes of the cladding and the core, in accordance with Snell's law, which yields $\theta_{max} = \sqrt{n_{core}^2 - n_{cladding}^2}$. In contrast, when dealing with a sub-wavelength fiber, the boundary conditions of guided light changes due to the substantial mismatch between the refractive index of the cladding and the surrounding air. Consequently, the assumption that light remains entirely confined within the nanofiber no longer holds. Instead, we observe a significant evanescent field extending beyond the nanofiber's boundaries and diminishing into the surrounding air over a few hundred nanometers, with a portion of the light propagating within this evanescent field at the fiber's surface.

- **High transmission**: Depending on the fabrication method employed, nanofibers can achieve very high transmission values. Methods like self-modulated taper-drawing [156, 157], direct drawing from bulk materials [158, 159], and the heat-and-pull technique [160, 161] have been used to create ONFs. Here, I used the heat-and-pull method, ensuring low surface roughness and an outstanding

transmission exceeding 95%[1].

- **Compatibility with fiber networks**: ONFs are fabricated by adiabatically stretching optical fibers, preserving the original dimensions at their input and output ends. This characteristic facilitates seamless, low-loss splicing with standard fibers and straightforward integration into standard fiber networks. In the context of integrated single sources, this in-line characteristic is exceptionally appealing.

This platform was originally proposed as a way to interface light with atomic clouds. In fact, between 2004 and 2007, Le Kien et coworkers [163, 164] introduced a series of theoretical concepts regarding the interaction of neutral atoms with nanofibers. Their proposals encompassed various aspects, such as trapping atoms in proximity to a nanofiber, efficiently channeling single-atom emissions into nanofiber-guided modes [165], and efficient scattering of the nanofiber guided light by a single atom [166]. Shortly thereafter, these theoretical propositions were substantiated by early experimental demonstrations of the atom-nanofiber interface. In 2007, research groups led by A. Rauschenbeutel in Germany/Austria [167] and Hakuta in Japan [168] successfully showcased the efficient channeling of fluorescence from a few laser-cooled atoms into nanofiber-guided modes. This marked the beginning of optical nanofibers serving as a versatile tool for quantum photonics applications. Several significant experimental achievements have then followed, including photon correlation measurements, which confirmed the detection of single-atom fluorescence through nanofiber-guided modes [169, 170], Beyond atoms, single solid-state quantum emitters like quantum dots [171, 172] and nanodiamonds [173, 174] have been interfaced with nanofiber-guided modes. Recent endeavors explore novel setups involving coupling light into resonators by positioning the fiber surface adjacent to a cavity [175], investigating nonlinear optics with warm atoms [176, 177] or studying chiral quantum optics [178, 179].

6.2 Light guiding in optical tapered nanofibers

The propagation of light along an optical nanofiber can be described in terms of a set of guided electromagnetic waves called the *modes* of the optical nanofiber. These can

[1]See the Brambilla and coworkers' review [162]for details about the others fabrication methods.

be derived solving the Maxwell's equations subject to cylindrical boundary conditions at the air-cladding interface of the nanofiber. The solutions to these differential equations are given by Bessel functions, as discussed in the works of Yariv [180], Snyder and Love [181], Sague [182] and Vetch [183]. In particular, in this chapter I will use the formalism presented by Hoffman [184].

6.2.1 Modes of an optical nanofiber

An optical nanofiber, having the structure of a cylindrical fiber, supports four distinct modes: Transverse Electric (TE) modes, Transverse Magnetic (TM) modes, and the HE or EH *hybrid* modes. When considering light propagation along the longitudinal z-axis, TE modes exhibit a zero longitudinal component of the electric field, with the electric field confined to the transverse plane. Similarly, in TM modes, there is no component of the magnetic field in the direction of propagation, and the magnetic field is entirely confined to the transverse plane. In contrast, EH and HE modes are referred to as *hybrid* modes because the electric and the magnetic fields are not confined to the transverse plane, but they have a component in the longitudinal direction. Specifically, when the amplitude of the longitudinal component of the electric field is greater than the longitudinal component of the magnetic field, these modes are classified to as EH modes; in the opposite case, they are categorized as HE modes. These classifications are summarized in Table 6.2.1, while Figure 6.2 provides a schematic visualization for the first HE_{11}, TE_{01}, TM_{01}, HE_{21} and HE_{12} modes.

Mode nomenclature	Longitudinal components	Transverse components
TE	$E_z = 0$ $H_z \neq 0$	E_t, H_T
TM	$E_z \neq 0$ $H_z = 0$	E_t, H_T
HE or EH	$E_z \neq 0$ $H_z \neq 0$	E_t, H_T

Table 6.1: **E- and H-field components for different types of modes in optical nanofibers**

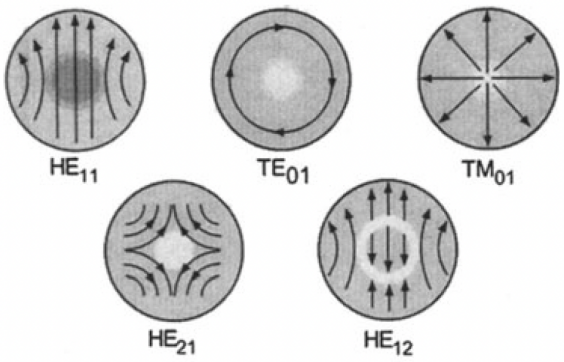

Fig. 6.2 ***Electric field distribution of different modes in an optical nanofiber.*** *The electric field distribution is reported for the five different modes: HE_{11}, TE_{01}, TM_{01}, HE_{21} and HE_{12}. Figure reproduced from [180].*

6.2.2 Single-mode optical nanofibers

To determine how many modes the nanofiber can substain as a function of its diameter, we introduce the *normalized frequency parameter* V, defined as:

$$V = \frac{2\pi a}{\lambda}\sqrt{(n_{cladding}^2 - n_{air}^2)} \tag{6.1}$$

It is a dimensionless quantity which depends on the nanofiber's radius a, the refractive indices of the cladding and the air[2], and the wavelength λ of interest. By introducing an effective refractive index, defined as $n_{eff} = \beta/k$, where β represents the mode propagation constant and $k = \frac{2\pi}{\lambda}$ is the wavenumber, the relationship between n_{eff} and the V-parameter corresponds to the dispersion relation of modes. Figure 6.3 illustrates the first four lower-order modes, which include HE_{11}, HE_{21}, TM_{01}, and TE_{01}[3]. These modes are shown for the case of $n_{cladding} = 1.46$, $n_{air} = 1.00$, and a wavelength of $\lambda = 510$ nm, corresponding to the average emission wavelength of perovskite NCs that I intend to couple with the nanofiber.

From Figure 6.3, it is evident that, with the exception of the lowest-order HE_{11} mode, each mode can only exist for values of V that exceed a certain cut-off, which depends on the specific mode. For a given nanofiber radius, the solutions exhibit continuous values with $n_{air} < n_{eff} < n_{cladding}$. This means that as the fiber diameter

[2]In the nanofiber region, as explained in next sections, the nanofiber cladding assumes the role of the core, as the original fiber core is melted, and the surrounding medium becomes air.

[3]Using an other notation, we can consider these modes as two families of linearly polarized modes LP_{lm}. The lowest order mode is LP_{01}, which corresponds to the HE_{11} hybrid mode. The next-highest mode is LP_{11}, which corresponds to the three modes HE_{21}, TE_{01}, and TM_{01}.

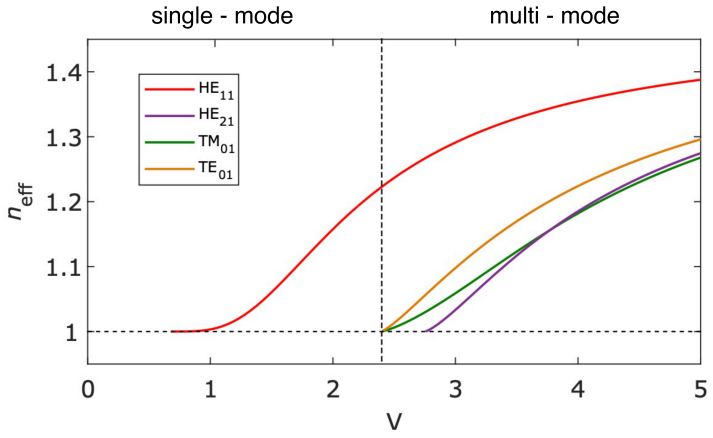

Fig. 6.3 ***Effective refractive index n_{eff} as a function of V*** *The boundary of single mode and multi mode is marked with a vertical dashed line ($V_b = 2.405$). For $V < V_b$, the optical nanofiber propagates only HE_{11} mode.*

increases, the effective index associated with a mode increases, transitioning from the air index $n_{air} = 1$ to the cladding index $n_{cladding} = 1.46$. When a mode appears, it initially interacts predominantly with the surrounding air. As the diameter increases, the mode becomes increasingly guided by the nanofiber, resulting in an increased effective index. In the limit of a very large fiber, the modes propagate primarily within the fiber, with an effective index approaching the cladding's index.

This essential behavior allows us to:

- Distinguish between a single-mode and multi-mode regime for the nanofiber.
- Compute for which diameter the single-mode nanofiber has the maximum evanescent field at its surface.

Let's start with the first point. The number of propagating modes for a certain diameter is found by drawing a vertical line at a corresponding value of V and counting the number of mode lines that are crossed. From Figure 6.3 we can see that for $V < 2.405$, only the HE_{11} mode is supported, while the others are not. This implies that for $V < 2.405$, the nanofiber is single-mode, and for this reason, the HE_{11} mode is referred to as the *fundamental mode* of the nanofiber. As the nanofiber diameter increases, the other modes can propagate as well. My objective was to design a single-mode nanofiber for the coupling with a perovskite NC, whose emission wavelength is around 510 nm. Therefore its diameter has to be smaller than about 280 nm.

At this point, I can focus on the fundamental mode HE_{11} determing its electric and magnetic field components in cylindrical coordinates (r,θ,z), as described in Annex D. In particular, I wanted to determine at which diameter we can obtain the strongest evanescent field at the nanofiber surface to achieve the best coupling with the perovskite NCs I will deposit on the nanofiber. To accomplish this, I examined the intensity distribution profile of the normalized electric field within the cross-section of the nanofiber, varying the fiber radius a. Figure 6.4 shows this simulation in the case of a linear polarization of light along the y-axis. Here, the nanofiber center corresponds to $x = 0$. When the fiber radius is large, for example for diameters exceeding 400 nm (second dashed white line in the figure), most of the light remains confined within the fiber core, and the evanescent part of the mode profile, observable for $x > a$ or $x < -a$, is minimal. As the ONF's diameter decreases, the evanescent field gradually becomes the dominant contribution to the intensity distribution profile, especially when the fiber diameter reaches sub-wavelength dimensions. However, if the fiber diameter becomes exceedingly small (i.e. $a < 50nm$), the decay of the evanescent field slows down significantly, and it can no longer be considered confined to the fiber surface.

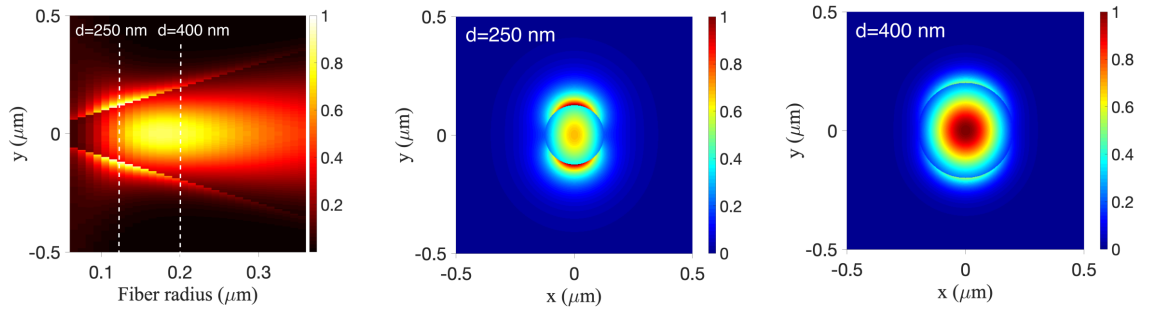

Fig. 6.4 ***Choice of the nanofiber diameter.*** *a) Simulation of intensity distribution profile of the normalized electric field within the cross-section of the nanofiber ($|E_y|^2$), varying the fiber radius a. b) Electric field intensity $|E|^2$ for a diameter of 250 nm and 400nm,respectively. The linear polarization of light is along the y-axis.*

Based on this analysis, we can conclude that for a wavelength of 510 nm, the highest intensity of the evanescent field on the fiber surface corresponds to a fiber diameter of approximately 250 nm, as highlighted by the first white dashed line in Figure 6.4. However, in the range $d \in [220, 280]$ nm, the evanescent field intensity at the fiber surface remains above 90% of the maximum intensity observed at $d = 250$

nm. This range defines a fabrication tolerance, accounting for slight variations in fiber diameters and also in the wavelength emission of the perovskite NC.

To visualize clearly the difference in light propagation for differents diameters, Figure 6.4b-c show the electric field intensity $|E|^2$ for a diameter of 250 nm and 400 nm, respectively. In the first case we have a strong evanescent field at the surface, in the second case the light is predominantly guided by the core.

Finally, Figure 6.5 shows the components E_x, E_y, E_z, H_x, H_y and H_z of the electric and magnetic fields of the fundamental mode HE_{11} in the case of a 510 nm guided light with linear polarization along the y-axis in the 250 nm diameter optical nanofiber. These simulations are obtained using the equations reported in Annex D.

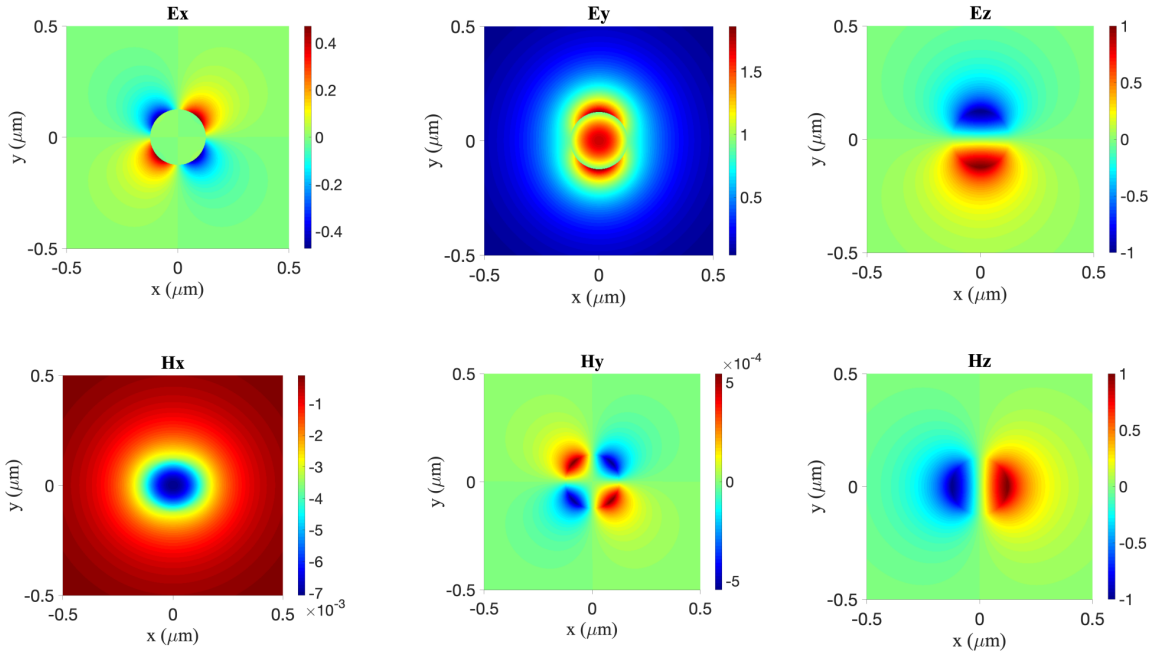

Fig. 6.5 ***Fundamental mode (HE_{11}) structure.*** *The components E_x, E_y, E_z, H_x, H_y and H_z of the electric and magnetic fields of the fundamental mode HE_{11} are simulated for a 250 nm diameter optical nanofiber and in the case of a 510 nm guided light with linear polarization along the y-axis.*

6.2.3 Adiabatic profile in a tapered nanofiber

Once the nanofiber's diameter determined, the subsequent crucial step is the evaluation of the profile geometry of the tapered optical nanofiber. Figure 6.6 gives a schematic of the propagation of the light within it.

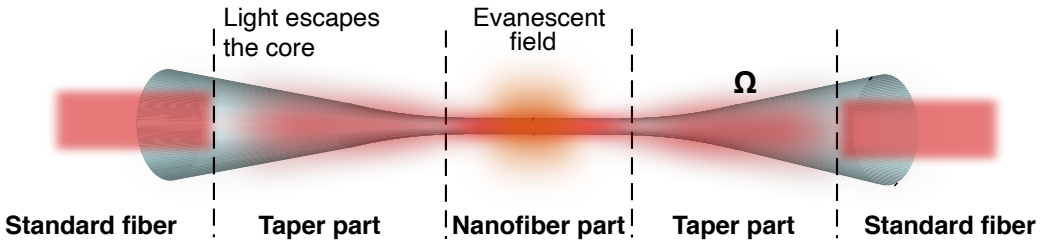

Fig. 6.6 ***Light propagation in a nanofiber.*** *Ω is the slope angle of the tapered part.*

1. Initially, the light is sent into the single mode optical fiber core from the left. In the unmodified standard fiber section, there are only two refractive indexes to consider: n_{core} and $n_{cladding}$. In this part, the light remains confined to the core.

2. Then, the tapered section gradually guides the light from the unmodified fiber core to the nanofiber waist. As the fiber radius continuously decreases during the pulling process, the light leaks from the core into the cladding [181, 185]. In the tapered region three distinct media should be considered: n_{core}, n_{clad} and n_{air}. In addition to the fundamental mode, higher-order modes are present.

3. In the nanofiber waist, what was initially the core at the center of the fiber becomes negligible and the system once again involves only two refractive indexes: n_{clad} and n_{air}. This region, as seen, can only sustain the fundamental mode HE_{11}. The light is guided through the cladding-to-air interface, and due to the significant refractive index difference, the evanescent field becomes prominent.

4. Light couple back to the core.

To achieve high transmission in optical nanofibers, the precise control over the fiber taper geometry is essential. This is especially critical in the taper region where the fundamental mode can couple with higher-order modes that cannot be sustained by the nanofiber part. In such case, light escaping from the core and leaking into the cladding, results in signal losses. To mitigate these losses, the tapered fiber's profile must meet the so-called *adiabatic criterion* [181, 186, 187].

This criterion sets limits on the taper angle Ω relative to the fiber axis. If the taper is too short (with a steep taper angle), the mode evolution becomes non-adiabatic, leading to a drop in transmission. Conversely, with a lengthened taper, the mode conversion becomes more adiabatic, as the energy remains in the fundamental mode throughout the evolution.

To ensure an adiabatic transition, the taper slope Ω should satisfy the condition:

$$\Omega < \frac{r}{L(r)} = \frac{r(\beta_1(r) - \beta_2(r))}{2\pi} \tag{6.2}$$

where r represents the local fiber radius, β_1 and β_2 denote the propagation constants of the fundamental HE_{11} mode and the first excited mode [186] at the radius r, and $L(r)$ is the length of the coupling region where coupled modes can exchange energy. If, at some point, the taper angle Ω approaches $r/L(r)$, the higher-order mode will be excited, and the corresponding power will be lost when the taper reaches the mode cutoff radius (as previously shown in Figure 6.3).

The resulting length for a pulled fiber optimized for 510 nm is around 60 mm, as shown in the profile in Figure 6.7.

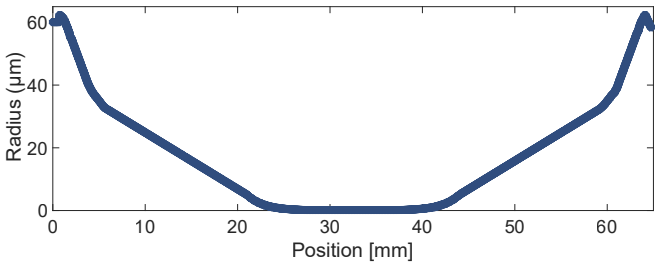

Fig. 6.7 ***Profile of the tapered fiber.***

The quality of the taper sections directly impacts the transmission of ONFs. However, this is not the only constraint. As explained in Section 6.3, another critical aspect is the cleanliness of the fiber during and after the pulling process [156, 188].

6.3 Nanofiber fabrication

The nanofiber is fabricated using the heat-and-pull method, also known as the *brushing technique*. This technique consists in a straightforward process: the standard optical fiber is heated, softened, and then stretched until it reaches the targeted diameter, resulting in a nanofiber adiabatically connected via tapered regions on both sides to the standard fiber. Using this fabrication technique, the transmission of a typical optical nanofiber typically exceeds 95%.

6.3.1 Pulling system

To achieve this, we employ a custom-built pulling system, illustrated in Figure 6.8 and Figure 6.9. This system includes an oxyhydrogen flame capable of heating fused silica to its softening point (1585 °C) and two translation stages with two clamps for holding and pulling the fiber ends.

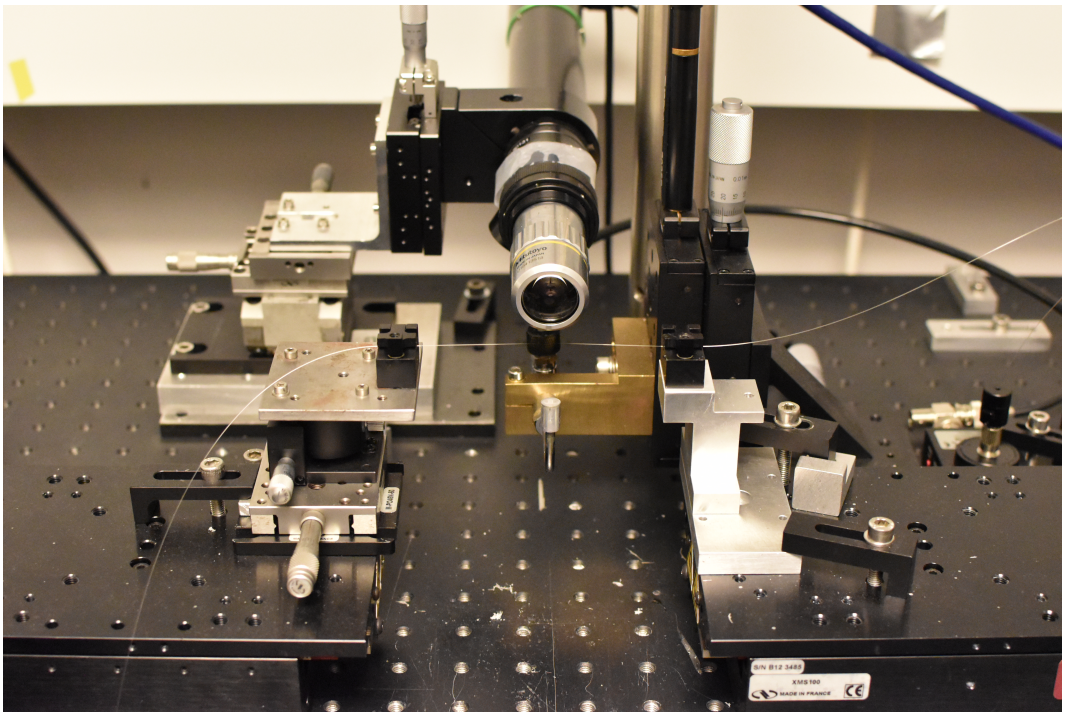

Fig. 6.8 ***Photo of the pulling setup.***

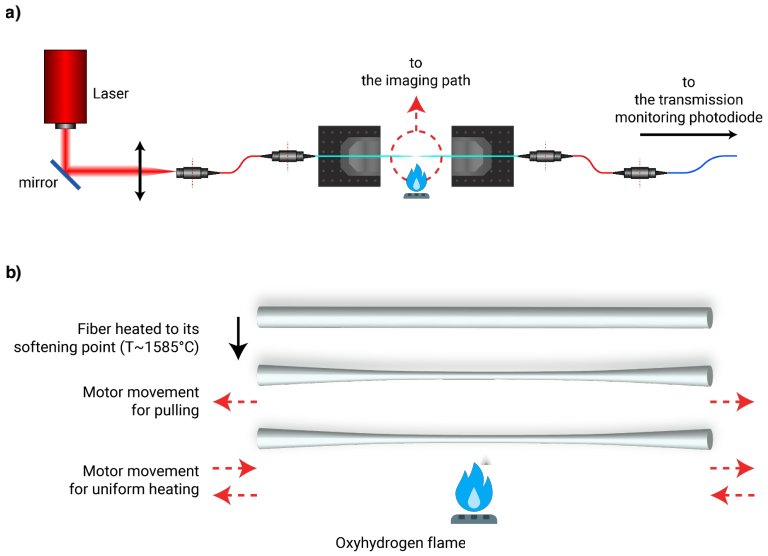

Fig. 6.9 ***Sketch of the pulling setup*** *a) An oxyhydrogen flame heats the silica and two translation stages with two clamps hold and pull the fiber. During the pulling process the fiber is imaged with a camera and the transmission is monitored with a photodiode. b) The stages move apart from each other to stretch the fiber and make it thinner. At the same time, they move in the same direction, shifting the heated portion of the fiber from the fixed heat source.*

The hydrogen-oxygen flame is generated through a stoichiometric mixture of hydrogen and oxygen, with the hydrogen produced via the electrolysis of water. This method ensures clean combustion, as only water is produced, and eliminates the need for storing hydrogen in the lab. After igniting the flame, I allow it to stabilize for a few minutes before starting the pulling. Precise control of the gas flow is maintained using a mass flow controller, ensuring stable and reproducible flame conditions. The flame's x-position (horizontal) remains fixed during the pulling process, while the z-position (vertical) is controlled by a motorized stage. This allows to position the flame below the fiber before initiating the pulling process, and then lift it just before pulling. The flame's height is carefully chosen to ensure sufficient softening of the fiber without causing it to break. In our setup, the typical distance of the tip from this reference point is 0.9 mm. When viewed from above, the flame is centered on the fiber.

The trajectories for these stages, responsible for pulling and the back-and-forth

brushing motion, are predefined in "pvt" files, with each line specifying positions and velocities for a given time increment. These trajectories are computed based on the target taper shapes and nanofiber diameters using a Matlab script, which produces control parameters for motors. The code, written by the former PhD student Dr. Maxime Joos, is closely aligned with the algorithm developed by Florian Warken [189] and the published code by Hoffman (`https://drum.lib.umd.edu/handle/1903/15069`).

The movement of the translation stages can be divided into two components: firstly, they move apart from each other to stretch the fiber and make it thinner; secondly, they move in the same direction, shifting the heated portion of the fiber from the fixed heat source, as sketched in Figure 6.9. This heated portion roughly corresponds to the width of the flame. The speed and range of motion of the translation stages during each pass dictate the final shape of the nanofiber.

During fabrication, maintaining a clean environment is crucial for producing optical nanofibers. Before starting the tapering process, I remove the plastic jacket of the optical fiber. Any particles, dust, remnants of the fiber jacket, or grease from handling can burn when exposed to the flame, potentially causing defects on the fiber surface during pulling. To maintain cleanliness, the pulling setup is placed under a laminar flow system, and I wear clean-room gloves and suitable clothes to prevent dust. The optical fiber is meticulously cleaned with isopropanol on lens tissue to remove most surface particles, followed by acetone to dissolve any remaining small pieces, and finally, a wipe of isopropanol to remove residual acetone. Maintaining a clean environment is also crucial for preventing dust from adhering to the nanofiber after tapering, scattering light and reducing the overall transmission.

6.3.2 Monitoring the transmission

Once the fiber is prepared, the tapering process is initiated via a computer-controlled interface. The flame is lifted, and the two translation stages start to move. The duration of the tapering process varies from a few minutes to around ten minutes, depending on the trajectory.

This process is continuously monitored from the side using a camera with its focus plane adjusted to the fiber. This allows us to observe the reduction in diameter. Notably, during pulling, the hot air from the flame gradually lifts the nanofiber as the weight of the fiber region above the flame decreases (since the diameter decreases). This is a crucial factor to consider, since, if the distance between the flame and the

fiber becomes too large, the fiber may not reach the softening point of silica. To prevent this, I perform several upward jogs of the flame during the pulling process, following the lifting of the nanofiber. Each jog incrementally raises the flame position by 100 µm. The number of jogs required depends on how tightly the fiber is secured in the stage clamps, and this can vary from one operator to another. In my case, I observed that reducing the number of jogs to less than four often leads to fiber breaking because the fiber doesn't reach the softening point of silica during the pulling process. Conversely, increasing too much the number of jogs consistently results in the fiber breaking due to excessive melting.

To monitor the entire process, I measure the transmission of the laser through the fiber using a photodiode. The output signal is normalized to the initial transmission before pulling. Figure 6.10 illustrates a typical transmission curve as a function of the nanofiber's total length (the sum of the tapered parts and the nanofiber zone), showing a transmission of 99.7%. The sinusoidal oscillations observed in the transmission represent the energy transfer between the fundamental mode HE_{11} and the first excited mode that occurs in the tapering region, as explained in section 6.2.3. Once the fiber reaches the nanofiber waist, only the fundamental mode is propagating, and the oscillations cease.

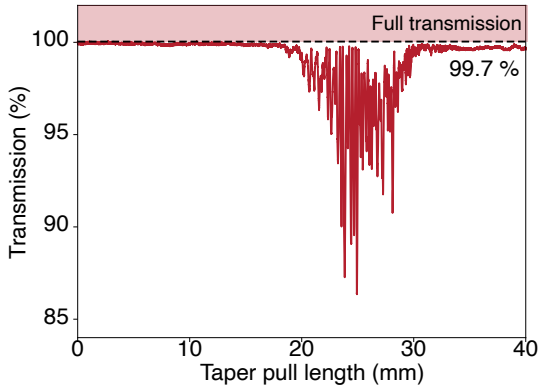

Fig. 6.10 ***Trasmission of the nanofiber*** *The transmission of the nanofiber is monitored using a photodiode and is normalized to the inizial transmission of the standard fiber before pulling.*

6.3.3 Inspection of the fabricated nanofibers

To assess the quality of the fabricated nanofibers, I randomly select a set of nanofibers and I measure the diameter using a Scanning Electron Microscopy (SEM), as shown

in Figure 6.11a. As example, in Table 6.2, I have provided the measured diameters of five nanofibers that I designed to have a target diameter of 360 nm, optimized for a wavelength of 785 nm. These nanofibers were utilized for the fabrication of metallic nanostructures, as described in Chapter 7. Across this selected group, the diameter at the fiber waist consistently falls within the range of 320 nm to 380 nm. The fluctuations observed in the diameter size can be attributed to the slight difference in manual operation. It's worth noting that the transmission efficiency of all these measured ONFs remains above 97.5%, with the signal level transmitted before starting the pulling process considered as 100%.

	Transmission	Diameter (nm)
Fiber 1	99.5%	380.4
Fiber 2	98.7%	357.4
Fiber 3	99.5%	322.5
Fiber 4	99.6%	364.1
Fiber 5	97.5%	358.9

Table 6.2: **Quality Inspection of fabricated ONFs.**

For a more extensive statistical analysis of the transmission values of the pulled nanofibers, Figure 6.11 presents the transmissions for a sample of 59 nanofibers optimized for 785 nm. It is visible that 54% of the nanofibers exhibits transmission values exceeding 99%, with 5% achieving a remarkable 99.8%.

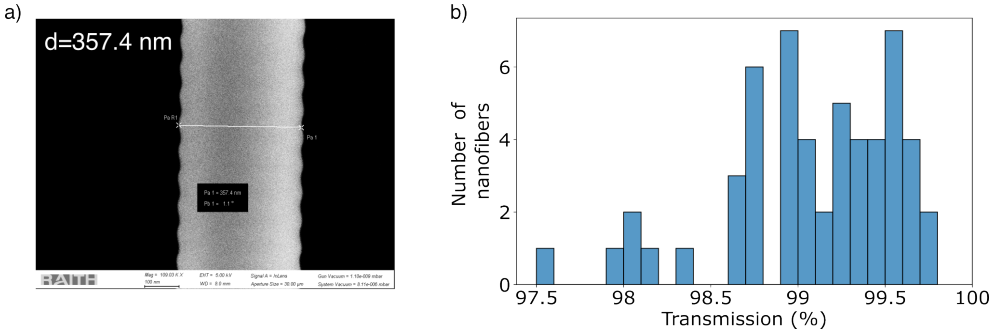

Fig. 6.11 ***Quality inspection of the nanofibers*** *a) With a target diameter of* 360 nm*, the measured diameter at the waist of the nanofiber is* 357.4 nm*. b) The measured transmission is reported for a sample of 59 nanofibers.*

6.3.4 Transportation

After the pulling process is finished, the fibers are fixed to a support, here U-shaped. To achieve this, a translation stage is employed to position the holder directly under the nanofiber until it makes a gentle contact, as illustrated in Figure 6.12a. The fiber is fixed to the holder using UV glue (Figure 6.12b), a task that necessitates meticulous care due to the fragility of the nanofiber zone. Subsequently, the fiber is cut at an appropriate length, dependent on the specific application, usually ranging from 10 to 50 cm at each end of the fiber. These ends will be subsequently connected to the experimental fiber network via a splicing machine to minimize signal losses. To prevent dust accumulation, the nanofibers are stored within a specially clean and hermetically sealed plastic box I designed, as shown in Figure 6.12c.

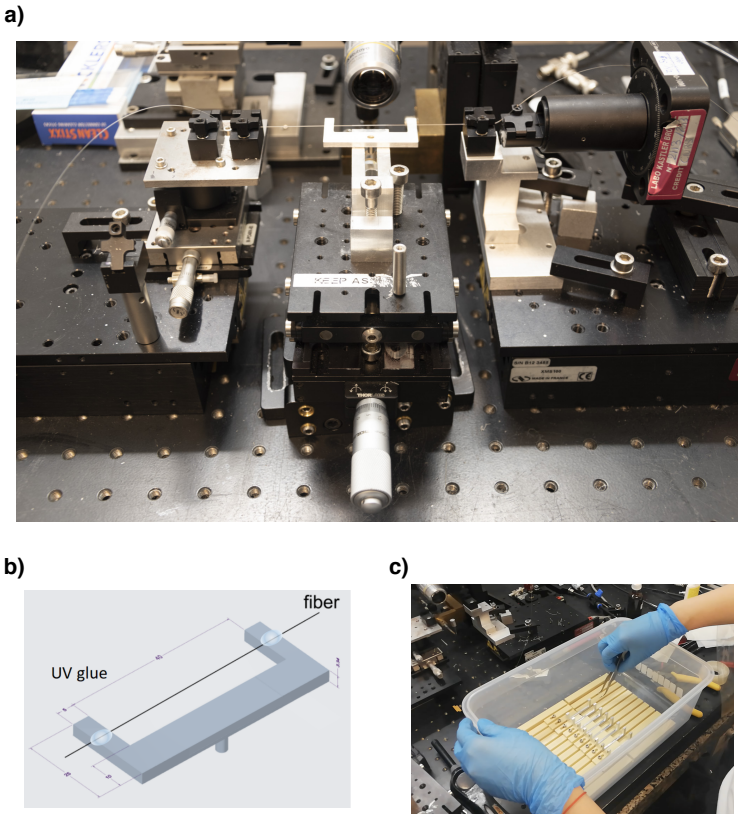

Fig. 6.12 ***Transportation of the nanofibers.*** *a) Translation stage employed to glue the nanofiber to a support. b) U-shaped nanofiber holder. c) Home-designed, clean and hermetically sealed plastic box for transportation.*

6.4 Nanofiber optimization

I enhanced the quality of the fabricated nanofibers by focusing on two critical aspects that hinder the practical, optimal use of nanofibers: tension and cleanliness.

6.4.1 Additional tension

When observed under the scanning electron microscope, the nanofibers exhibited resonant vibrations under the electron beam. I have observed this phenomenon in two scenarios. Firstly, when the ends of 1.5 cm-long nanofibers were glued to a substrate (typically made of silicium) while the nanofiber was left slightly suspended. This configuration is depicted in Figure 6.13a. Secondly, when the intact (not cut) nanofibers were glued to a 5 cm-long metallic U-shaped holder, as shown in Figure 6.13b. Figures 6.13c-d illustrate the visible oscillations during imaging: in the first configuration, we can observe a wavy profile of the nanofiber, while in the second configuration, there are significant oscillations. These oscillations gradually decreased moving from the waist of the nanofiber, which has a diameter of a few hundred nanometers, to the taper region with a diameter of the tens of micrometers. Ultimately, they disappeared at the standard fiber ends. Resolving this issue was crucial for the fabrication of metallic nanostructures on the nanofiber, as detailed in Chapter 7.

Notably, modifying the electron beam parameters did not resolve these issues. To address this challenge, after the heat-and-pull process, I introduced an additional tension to the nanofiber by elongating it by a length ΔL, as depicted in Figure 6.14d. I systematically fabricated nanofibers with varying values of additional tension, ranging from 0 µm to 200 µm, and assessed the resulting behavior under the electron beam. This extra tension effectively diminished the amplitude of the nanofiber's oscillations when exposed to the electron beam, as illustrated in Figure 6.14d. However, it's worth noting that for elongations exceeding $\Delta L > 125\mu m$, there was a increased risk of the nanofiber breaking. Consequently, I selected an intermediate range of $75 - 125\mu m$ for the additional tension. Specifically, I pulled the fibers with an elongation of $\Delta L = 100\mu m$.

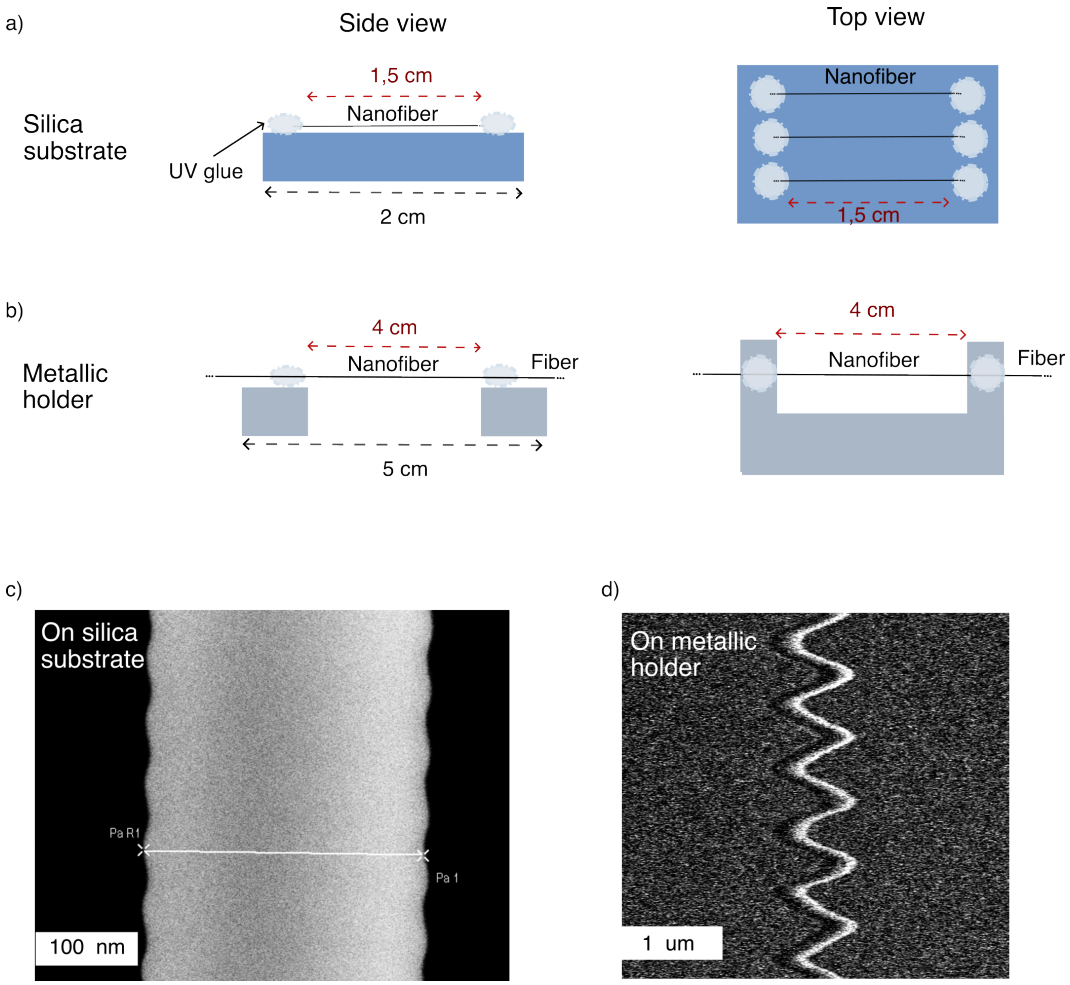

Fig. 6.13 ***Oscillations of the nanofiber under electron beam***: *a-b) Schematic of two configurations used to measure the diameter of the nanofibers in the SEM. In (a) the nanofibers are cut and glued to a flat substrate. In (b) the nanofibers are glued to a U-shaped holder preserving the entire nanofiber length. c-d) SEM image of the nanofiber waist showing oscillations in the first and second configuration, respectively.*

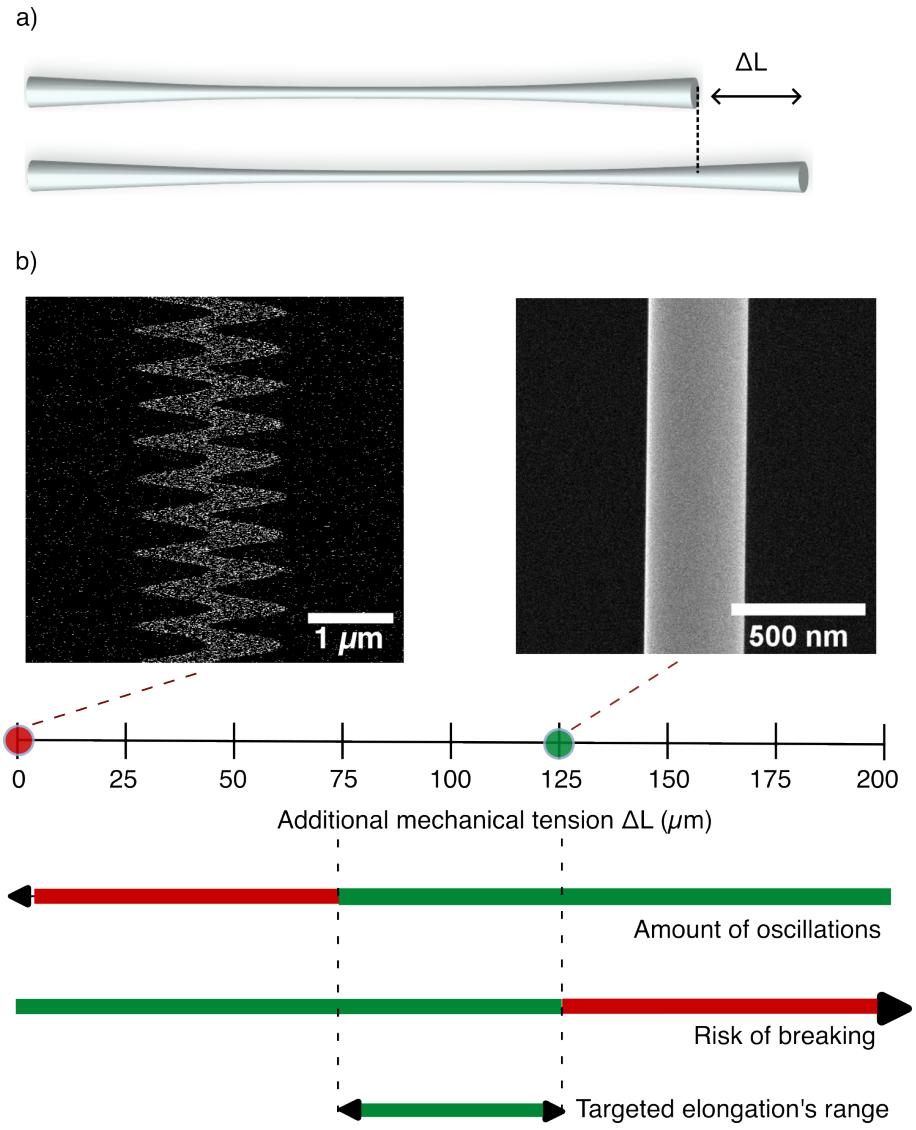

Fig. 6.14 ***Optimizing the nanofiber tension.*** *a) Schematic of the elongation technique. b) Schematic illustrating the optimization process, which shows the reduction of nanofiber oscillations with increasing elongation, along with the growing risk of fiber breakage. The resulting compromise was found to be in the range of* $75 - 125\mu m$.

6.4.2 Plasma oxygen treatment

Despite storing the nanofiber in an air-tight box, it tends to accumulate dust after prolonged exposure to the SEM environment. One plausible explanation is that the nanofiber becomes charged by the electron beam, exacerbating the dust attraction issue. This poses a significant problem, as the presence of dust leads to a drastic reduction in transmission, often dropping below 10%. To address this issue, I devised a solution involving the use of a plasma oxygen treatment, performed using a plasma cleaner.

Plasma cleaning is a well-established and effective method for flat surface preparation, known for its cost-efficiency and environmental safety. It is commonly used to clean macroscopic flat substrates. Specifically, oxygen plasma cleaning is highly effective to remove contaminants at the nano-scale when compared to traditional wet cleaning methods, such as solvent cleaning.

In my case, I utilized vacuum plasma cleaning to remove dust and contaminants from the nanofiber surface, providing a rapid, effective, and reproducible cleaning process. Figure 6.15 provides an overview of the process: first, the nanofiber is placed under vacuum conditions, and then ultraviolet light is generated within the plasma. This UV light is highly effective in breaking down most organic bonds present in surface contaminants, including oils. The second cleaning step involves the energetic oxygen species generated in the plasma. These species react with organic contaminants, primarily forming water and carbon dioxide, which are continuously removed (pumped away) from the chamber during the process. After treatment, we are left with an atomically clean and contamination-free surface. I conducted this plasma oxygen treatment on the nanofibers for 25 minutes at 30 Watts in a vacuum environment.

Figure 6.15a-b are particularly useful to visualize the effectiveness of this treatment. Figure 6.15a shows the effect of light scattering from dust when a laser is sent into a nanofiber. In this way it becomes nearly impossible to distinguish between a particle and the dust, as both act as scattering centers. Instead, Figure 6.15b shows the result after the plasma cleaning, when the a particle becomes clearly visible without the interference of dust.

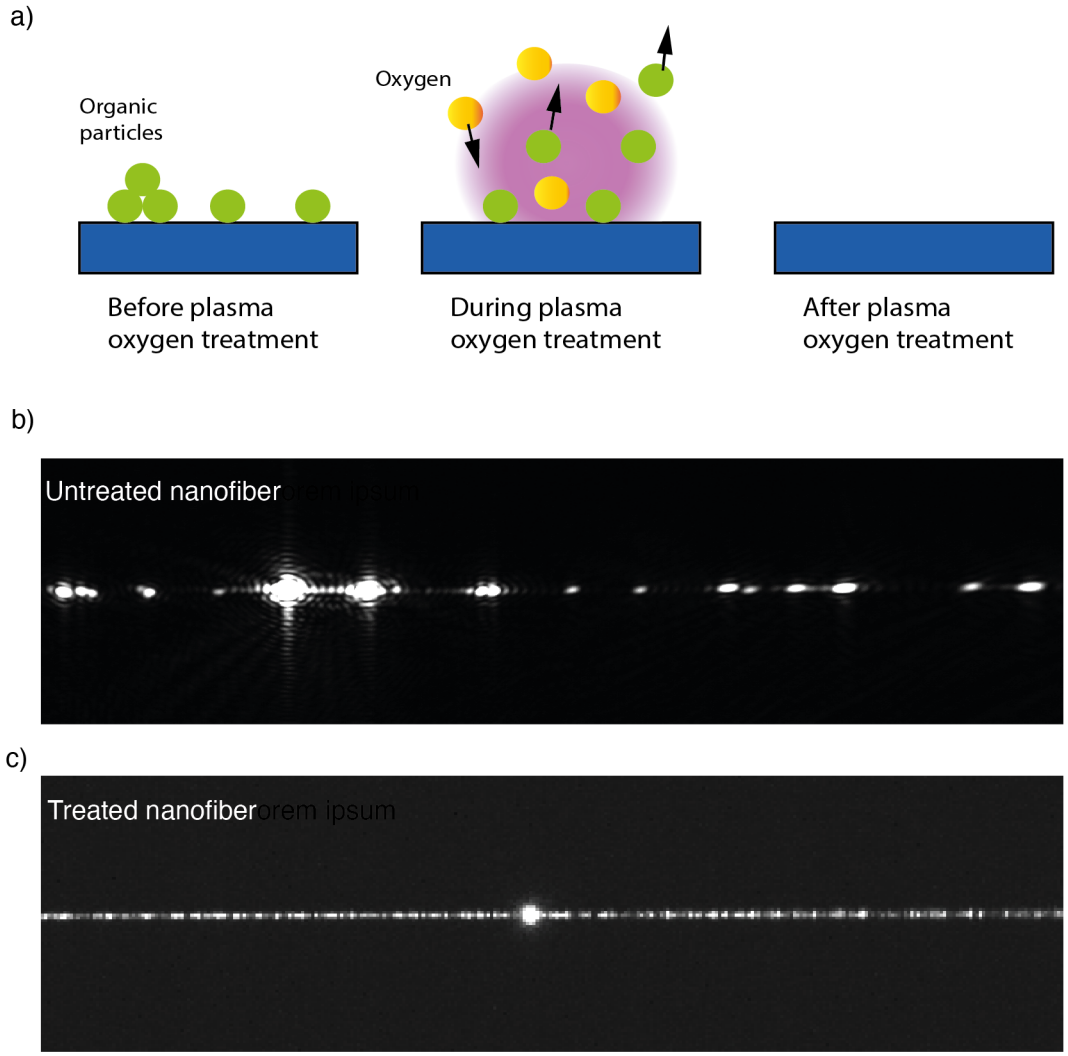

Fig. 6.15 ***Cleaning of a nanofiber.*** *a) Schematic of the Plasma oxygen treatment b) Scattering from the dust before the plasma oxygen treatment of the nanofiber c) Without dust, when depositing a particle, it is easy to locate it. The scattering points visible on the nanofiber are glass imperfections.*

6.5 Coupling of a perovskite NC with the optical nanofiber

I achieved the first coupling of a perovskite NC, specifically a $CsPbBr_3$ NC described in Chapter 3, with an optical nanofiber via the strong evanescent field present at the nanofiber's surface.

6.5.1 Emitter deposition on the nanofiber

Various techniques exist for depositing an emitter onto a nanofiber. For atoms, this is achieved by placing the nanofiber in vacuum and trapping atoms near it using optical trapping. Conversely, with solid emitters, deterministic deposition can be accomplished by using an AFM tip to place the emitter precisely at the desired position. In my case, I opted for a deposition technique by gently touching the nanofiber with a droplet of solution containing the NCs. Compared to other methods, this approach offers a faster and simpler deposition process for fragile emitters.

In order to do this, it's essential to substantially reduce the nanocrystal concentration to enhance the chances of depositing just one NC. I start by drawing a 20 µL droplet of the diluted nanocrystal solution using a micropipette. With the droplet positioned at the micropipette's tip, I move it towards the fiber until it makes contact. Once the droplet touches the fiber, I gently withdraw it. The procedure is schematically outlined in Figure 6.16a. To ensure precise control, I employ a 3-axis translation stage to manipulate the micropipette's position and monitor the procedure with the objective lens, as shown in Figure 6.16b. This process results in the deposition of one or more emitters onto the fiber, which can be easily confirmed by sending the laser into the fiber and imaging the perovskite NCs' emission with a camera Figure 6.16c-d shows cases where multiple perovskite nanocrystals and a single perovskite nanocrystal are deposited, respectively.

6.5.2 Experimental setup

The nanofiber used for this experiment had a diameter of 250 nm and was designed for a wavelength of 510 nm which matches the emission wavelength of the $CsPbBr_3$ NC. To verify that I deposited a single NC, I measured the single photon purity of the light detected at the end of the fiber, measuring the $g^{(2)}$ function using a HBT setup, as illustrated in Figure 6.17. A photo of the setup is provided in Figure 6.18. This setup enables the excitation of the emitter on the fiber from both the nanofiber and the free space, via the confocal microscope. To protect the nanofiber, the section of the setup where it is placed is in a box under a clean laminar air-flow. In our case, I excite the nanofiber from free space using a pulsed 405 nm laser and I collected the PL emission at the end of the fiber, which is connected to the Hanbury Brown and Twiss (HBT) setup, indicated by the red dashed line. Alternatively, through the objective lens, the emitted PL from the emitter can be collected, sent to the camera

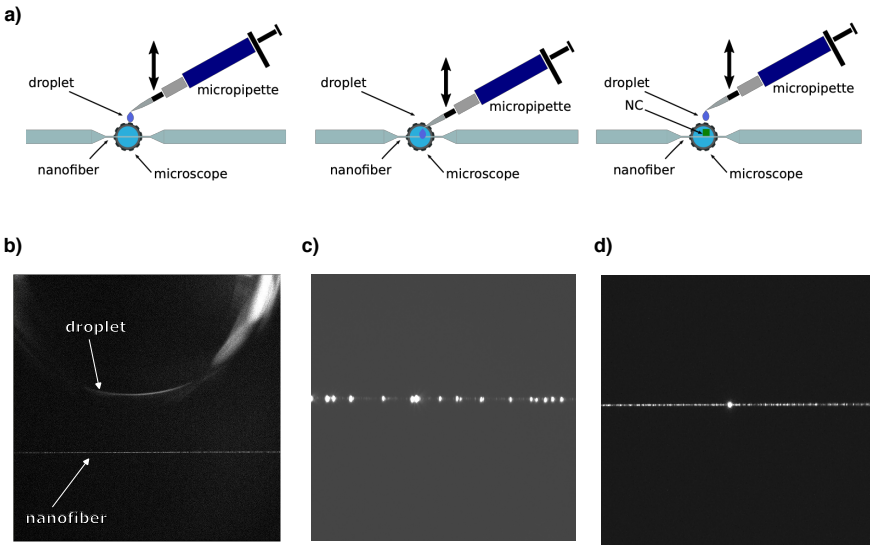

Fig. 6.16 ***Emitter deposition on the nanofiber.*** *a) Sketch of the deposition process. b) View of the deposition through the camera. c) Example of a deposition resulting in many NCs on the nanofiber surface. d) Example of a deposition resulting in one single NC on the nanofiber surface.*

or to the spectrometer, or directed to a second HBT setup.

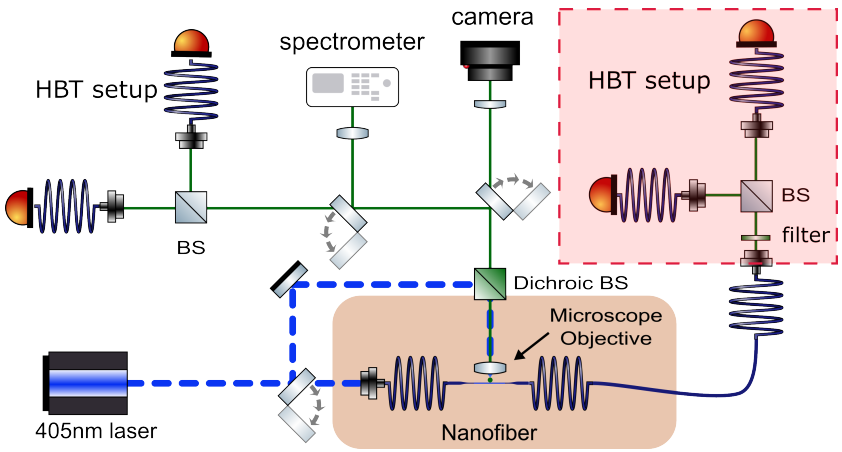

Fig. 6.17 ***Experimental setup for the nanofiber****: the* 405 nm *pulsed laser can excite the emitter both from the nanofiber and from the free-space. The single-photon purity measurement, using the HBT setup, can be performed via the nanofiber of via the free-space. The NC's PL emission can be imaged using a camera. The part surrounded by orange rectangle is placed in a box under a clean laminar air-flow.*

a)

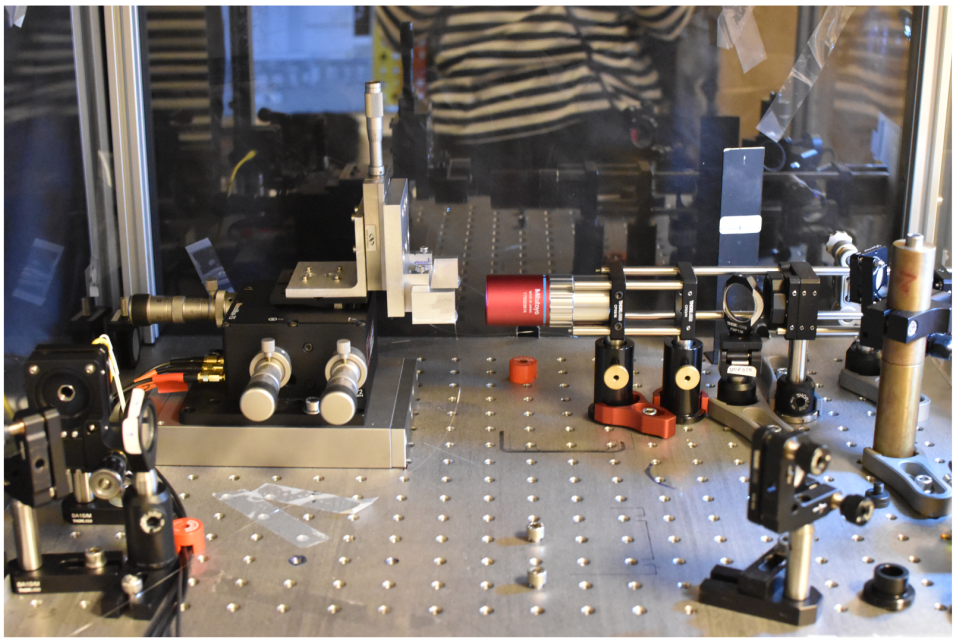

b)

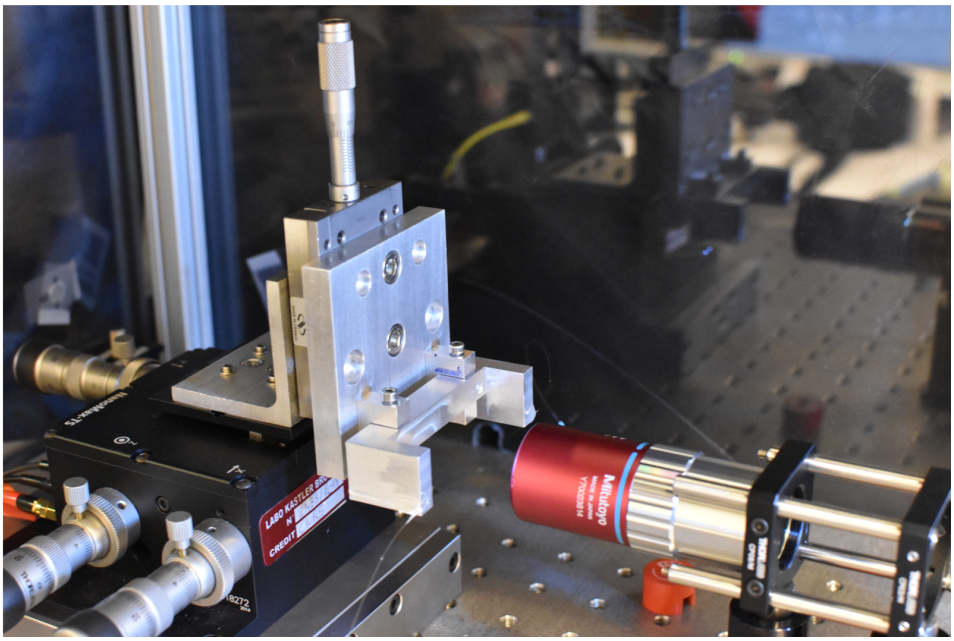

Fig. 6.18 ***Photo of the nanofiber experimental setup***: *a) Section of the setup hosting the nanofiber is protected by a box with a clean laminar air-flow. b) The fiber is glued to an U-shaped metallic holder.*

6.5.3 Measure of the single-photon purity

By illuminating the $CsPbBr_3$ nanocrystal through the nanofiber with a continuous 532 nm laser, which is effectively guided by the nanofiber, it becomes possible to locate the emitter. In this way, we can observe the scattering of the emitted light from the emitter using a camera. Consequently, we can precisely position the perovskite NC in correspondence with the laser spot of the pulsed 405 nm laser that is incident on the fiber from free space via the microscope objective. The photons channeled into the fiber are detected with the same TCSPC scheme and data processing methods presented in Chapter 2. The measure was conducted for 5 minutes, after this time the NC bleached. The measured second-order correlation function $g^{(2)}(\tau)$, shown in Figure 6.19, exhibits an antibunching behavior with a $g^{(2)}(0) = 0.24$. This confirms the deposit of a single NC and that is emission is channeled in the nanofiber.

Compared to the values obtained during the characterization under the microscope, this $g^{(2)}(0)$ value is higher. Due to the emitter's high instability in dilution, as observed in Chapter 3, we did not measure the emission spectrum of the nanocrystal or its saturation curve in this experimental configuration. The higher $g^{(2)}(0)$ value could potentially be attributed to the size of the nanocrystal. Another hypothesis, that could also explain the significant bunching amplitudes for the peaks adjacent to $\tau = 0$, is the scenario where the excitation power exceeds significantly the saturation power specific to this emitter. This would justify the higher $g^{(2)}(0)$ value and the rapid bleaching of the emitter.

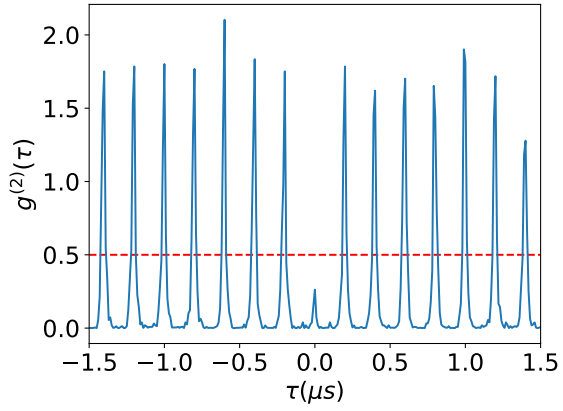

Fig. 6.19 ***Antibunching measurement via the nanofiber***. *Histogram of the second order correlation function measured via the nanofiber.*

Conclusion

In this chapter, I have demonstrated that optical nanofibers with subwavelength diameters can serve as an effective platform for light-matter interaction, thanks to the strong evanescent field present at their surfaces.

- I initially introduced the concept of light guidance by optical nanofibers, describing the means by which I ensured that the nanofiber operates in a single mode.
- I provided a detailed explanation of how I fabricate these nanofibers and outlined how I test their quality.
- I delved into the optimizations I introduced during the fabrication of nanofibers to ensure their optimal usage. These optimizations include addressing the electron beam-induced oscillations observed in nanofibers within the SEM and the treatment of their surface with plasma oxygen to effectively clean their surface.
- I described the coupling of a perovskite nanocrystal with the optical nanofiber. By exciting the nanocrystal on the nanofiber's surface and collecting the emitted light via the nanofiber, I demonstrated the possibility of coupling the single photon emission of a perovskite NC directly inside the nanofiber. This constitues a prototype of a compact and integrated perovskite-based single photon source.

Chapter 7

Metallic nanostructures for plasmon-enhanced light-interaction

Contents

Introduction

This chapter introduces an innovative approach for creating metallic nanostructures on optical tapered nanofibers, representing an interesting prototype of nanofiber-based cavities automatically coupled to fibers. This method has the potential to enable the efficient coupling of emitted photons by harnessing the enhancement of the quantum emitter's spontaneous emission rate by its surrounding environment. In Section 7.1, I introduce the role of the plasmonics increasing the photon generation of an emitter and in Section 7.2 I explained why it is interesting fabricating plasmonic nanostructures on optical nanofibers and which are the limitation to date. In Section 7.3, I present a proposal of a unconventional technique to fabricate metallic nanostructures on nanofibers via Electron Beam Induced Deposition (EBID) and explaining how this method, traditionally employed for flat surfaces, can be adapted to the nanofiber platform. In Section 7.4, I present the fabricated nano-structures, nanopillars and nanoatenna, and I detail their optical characterization, focusing on the study of the spectra and the polarization of the scattered light, and how the Plasma Oxygen Treatment (POT) can enhance their quality. Finally, in Section 7.5, I give the perspectives of this work, explaining how this fabrication method can be extendend to dialectric nano-structures and how quantum emitters can be integrated with these systems.

The protocol and findings presented in this chapter, for which a patent application is currently on-going, have been developed within the context of the European project NanoBRIGHT, designed for applications in biology and optogenetics. NanoBRIGHT's primary objective is to create minimally invasive devices able to exploit unconventional combinations of optics and photonics to interface with brain tissue. The aim is to utilize light for controlling and monitoring physiological processes that are currently beyond the reach of existing techniques in optogenetics. These devices are intended to address severe brain disorders, including brain tumors, epilepsy, and traumatic brain injuries, as outlined in Figure 7.1. Interestingly, the technologies developed within this project have also shown great promise for applications in quantum technology.

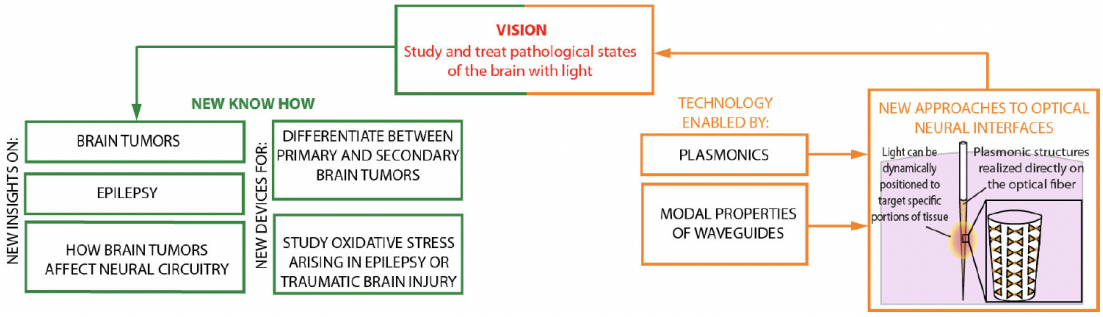

Fig. 7.1 ***Nanobright project.*** *Schematic representation of NanoBRIGHT's objectives.*

7.1 Increasing the photon generation via Purcell effect

In 1946, E. Purcell predicted that spontaneous emission is not solely an intrinsic property of the emitter but is also influenced by the local photonic environment[190]. The transition probability between states of a quantum system, as dictated by Fermi's golden rule, crucially depends on the number of available final states for the transition. The number of states accessible to an emitter is quantified by the density of optical states (DOS) which, in a homogeneous medium, depends on the refractive index and the frequency of the emitted light. Modifying the photonic environment of an emitter results in a modified local density of optical states (LDOS). This new environment can either enhance or inhibit the relaxation of the excited state through photon emission, thereby altering its lifetime. Specifically, creating a resonant environment for a specific frequency significantly increases the LDOS at that frequency. Then, an emitter exposed to this increased LDOS emits photons faster, leading to a reduction in its excited state lifetime[1] and enhanching the final photon count rate. This concept is commonly referred to as the *Purcell effect*.

The Purcell factor can be expressed as:

$$F_p = \frac{3\lambda_c^3}{4\pi^2}\frac{Q}{V} \tag{7.1}$$

where Q represents the quality factor of the cavity, V is the volume of the resonant mode, and λ_c corresponds to the wavelength within the medium. Here, λ_c is defined as λ/n, where λ denotes the wavelength in vacuum, and n signifies the refractive

[1]For semiconductor quantum emitters in free space, this lifetime typically ranges from 1 to 30 ns.

index of the medium. As the Purcell factor scales as Q/V, the spontaneous emission can be efficiently controlled in an optical cavity presenting a high quality factor and/or a strongly confined mode. Concentrating light within deep sub-wavelength volumes can be achieved through plasmonics. This involves employing nano-metallic structures that support *surface plasmons* — electromagnetic waves guided by the interface between a metal and a dielectric material and coupled to the free electrons of the metal.

Several promising geometric configurations on flat surfaces have been proposed to potentially enhance the emission of single photon sources. These include trapped standing wave-type surface plasmon polariton cavities [191] (Figure 7.2a), surfaces with periodically arranged spherical voids or indented structures capable of confining plasmons [192, 193] (Figure 7.2b), and nanoantenna systems (Figure 7.2c-d). In the latter, a metal structure is positioned above either a metal or dielectric surface [194], or gap plasmon systems can be realized by bringing two nanoantennas close together, effectively squeezing light into even tighter volumes within the gap between them [195]. In particular, nanoantennas are an interesting system to optimize the collection efficiency and ensure that a big fraction of the light produced is detected, as they can be designed to redirect light emission of coupled single photon emitters [196, 197]. This approach represents the current frontier of light confinement, with hotspot diameters easily achievable below 10 nm[198].

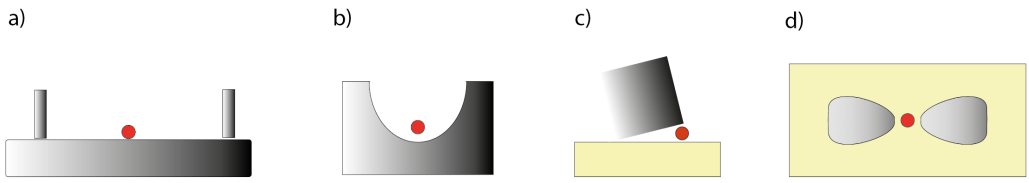

Fig. 7.2 ***Various plasmonic structures.*** *a) Trapped standing wave-type surface plasmon polariton cavities [191]; b) surfaces with spherical voids or indented structures with localized modes [192, 193]. c) nanoantenna systems, where metallic nanoparticles such as gold nanospheres or nanorods are positioned above either a metal or dielectric surface [194] d) gap systems, where highly confined modes are formed in nanometer-sized gaps between pairs of nanostructures [195].*

Single photon sources integrated with plasmonic structures on flat surfaces have been successfully demonstrated using various emitters, including molecules [195], color centers in nanodiamonds [199], epitaxial QDs [115, 200], and colloidal QDs

[197, 201].

7.2 Plasmonic nanostructures on optical nanofibers

Transferring plasmonic nanofabrications to optical tapered nanofibers would present a particularly interesting opportunity because such nanofiber-based devices will be automatically fiber coupled. As detailed in Chapter 6, nanofibers offer several advantages, including strong evanescent field in their waist region, excellent light transmission and low losses when connecting to fiber networks. By implementing these nano-structures onto nanofibers, one can achieve highly efficient coupling of emitted photons, which holds significant appeal for applications in both photonic and quantum technologies.

In literature, several preliminary studies have explored this direction. Plasmonic nanostructures, sush as bow-tie antennas [202, 203], bull's eye phased arrays [204], and double nanohole apertures [205], have been fabricated on the tips of optical fibers and microfibers coated with metal. These systems act like optical tweezers, enabling stable trapping and manipulation of nano-sized particles[206]. Bow-tie antennas have also been integrated onto the surface of microfibers[207], confining electromagnetic fields to very small regions depending on the dimensions of the device gap, resulting in a non-directional radiation pattern.

Turning our attention specifically to nanofibers, top-down approach involving Focused Ion Beam Milling (FIBM) has been proposed as a patterning technique for optical nanofibers (ONFs) using gallium[208] or helium ions[209], and recently the deposition of colloidal quantum dots in close proximity to individual gold nanorods positioned on the surface of an optical nanofiber[210] was reported.

However, to our knowledge, there are no examples nor proposals, in a bottom-up fashion, in literature about plasmonic nano-structures deterministically fabricated on nanofibers. This is primarily due to the absence of suitable protocols for such deterministic fabrication.

7.3 Fabrication of the nanostructures

During my PhD, I focused on addressing the technological gap in the field of plasmonic nanofabrication on optical nanofibers. In April 2021 I spent three weeks at

the Istituto Italiano di Tecnologia in Lecce (Italy) implementing a unconventional nanofabrication technique to fabricate bottom-up metallic nanostructures on optical tapered nanofibers by means of electron beam induced deposition (EBID). I carried out the preparation of the tapered nanofibers used during the fabrications and the post-processing procedures to optimize them. I worked at the adaptation of the Electron Beam Induced Deposition process on the nanotaper, collaborating with Dr. Antonio Balena in finding the optimal fabrication parameters to achieve the fabrication of the nanostructures on the nanometric section of the fiber. I was also involved in the design and optimization of the optical characterization experiments, as well as in the measurement analysis, collaborating with Dr. Chengjie Ding and Dr. Antonio Balena.

7.3.1 Electron Beam Induced Depositon (EBID)

Adapting nanofabrication techniques usually employed onto flat surfaces to achieve nanostructures fabrication on a suspended, dielectric, and nanometric sample, like the nanofibers, represents a significant technological challenge. Indeed, traditional nanofabrication methods are often unsuitable due to the unique properties of the nanofiber platform, in particular for its diameter of few hundreds of nanometers and its pronounced radius. For instance, the diameter of the nanofiber falls below the diffraction limit of most imaging systems coupled with photolithography setups. Moreover, subjecting the substrate to viscous photoresist or electron resist for Electron Beam Lithography (EBL) would result in the fiber breaking due to stress. Also using the FIBM to fabricate metallic nanostructures on the nanofiber remains a challenge. One primary concern with FIBM is the ion contamination of the nanofiber during the fabrication process, which can lead to optical losses due to a modification of the nanofiber refractive index or the creation of defects. Another issue is its limited resolution, typically in the range of a few tens of nanometers, insufficient if we want to fabricate nanoantennas with a gap matching these sizes. To overcome these limitations, we opted for the Electron Beam Induced Deposition (EBID) as fabrication method. In this approach, an electron beam in a Scanning Electron Miscroscope (SEM) is focused onto the waist of the ONF and, within the SEM chamber, a Gas Injection System (GIS) introduces a metallic gas precursor, as illustrated in Figure 7.3a. The dissociation of the precursor and the subsequent growth of the nanostructures occur through a mechanism involving complex interactions between the substrate,

precursor, and resulting nanostructures [211]. A key factor in the deposition process is that the dissociation process of the precursor molecules is driven by their interaction with the secondary electrons emerging from the sample upon irradiation with a primary electron beam. The secondary electrons are responsible for dissociating the precursor molecules, initiating the deposition of nanostructures. Notably, secondary electrons are scattered at wide angles with respect to the primary electron beam axis. For this reason, achieving the growth of complex 3D nanoscale structures on a highly curved surface, like that of a nanofiber, presents a significant challenge.

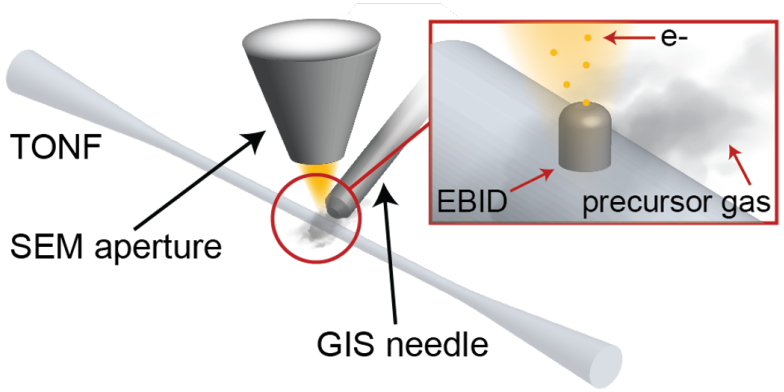

Fig. 7.3 ***Electron Beam Induced Deposition (EBID).*** *Sketch of the technique.*

During this EBID fabrication process, we introduced a novel technique: intentionally defocusing the electron beam. This was achieved by introducing controlled blurring of the beam during exposure, as explained in Section 7.3.2.4. The purpose behind this adjustment was to decrease the electron flux over the exposed area, thus diminishing the mechanical pressure exerted by the electron beam on the ONF. Such pressure, if not reduced, could potentially prevent the precise nanopatterning. While beam blurring is typically seen as a drawback in the field of nanofabrication, in our work, it turned out to be the an effective strategy for achieving the desired fabrication outcomes. Consequently, for the patent application, we have called our technique BEBID, which stands for *Blurred Electron Beam Induced Deposition*.

7.3.1.1 Nanofiber preparation for the SEM

For the experiment, I fabricated around 60 nanofibers nanofibers designed for a wavelength of 780 nm, as detailed in Chapter 6. I designed the profile of the nanofibers to have a length of 4 cm (including both the tapered part and the nanofiber zone). This design allowed me to glue the nanofibers to a custom-designed fiber holder that was 5 cm in length, meeting the size requirements of the SEM chamber's support, as illustrated in Figure 7.4a. After I fabricated and glued each nanofiber, I cut the fiber part at a length of 10 cm from the holder on both sides. This was necessary to enable sample mounting within the machine, matching with the space constraints inside the SEM chamber (slightly over 25 cm along the nanofiber axis). Figures 7.4b-c respectively display a view of the holder support inside the SEM chamber and a perspective view of the SEM chamber. Once the sample is mounted, the SEM's control interface enables simultaneous overhead views of the chamber, a side view of the GIS, and imaging views of the sample.

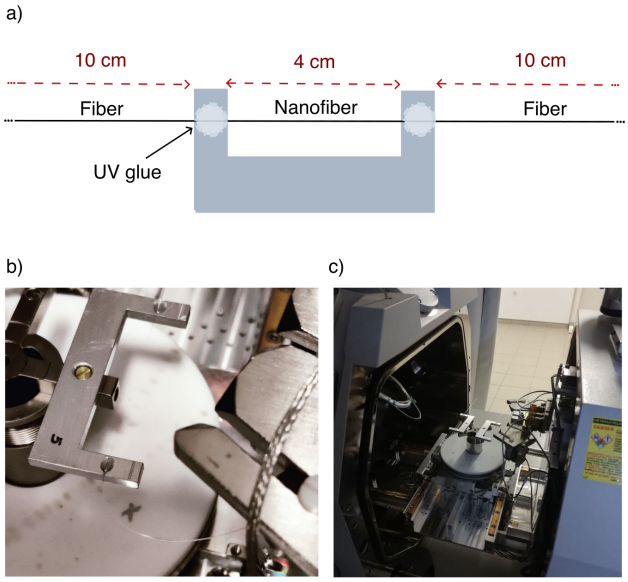

Fig. 7.4 ***Placement of the ONF in the SEM.*** *a) Sketch of the holder where the nanofiber is glued. The nanofiber part (including both the tapered part and the nanofiber zone) has a length of 4 cm and the fiber part is cut at a length of 10 cm from the holder on both sides. These sizes where requested to enable sample mounting within the machine. b) Top view of the of the holder support inside the SEM chamber. c) Perspective view of the SEM chamber.*

7.3.1.2 Adjusting mechanical tension of nanofibers

As previously seen in Chapter 6, the nanofibers displayed oscillations under the electron beams, which here posed significative challenges for fabricating nanostructures. Therefore, as detailed in Section 6.4, I conducted an optimization of the nanofiber's mechanical tension. I fabricated a set of nine nanofibers, incrementally elongating each one with additional tension in steps of 25 µm, ranging from 0 to 200 µm. Figure 7.5 summarizes this optimization, showing that without additional tension (image on the left), strong oscillations were visible under the electron beam. However, by applying a mechanical tension of 125 µm (image on the right), we achieved a clear focus on the surface. In this condition, we were able to successfully fabricate nanostructures on the surface.

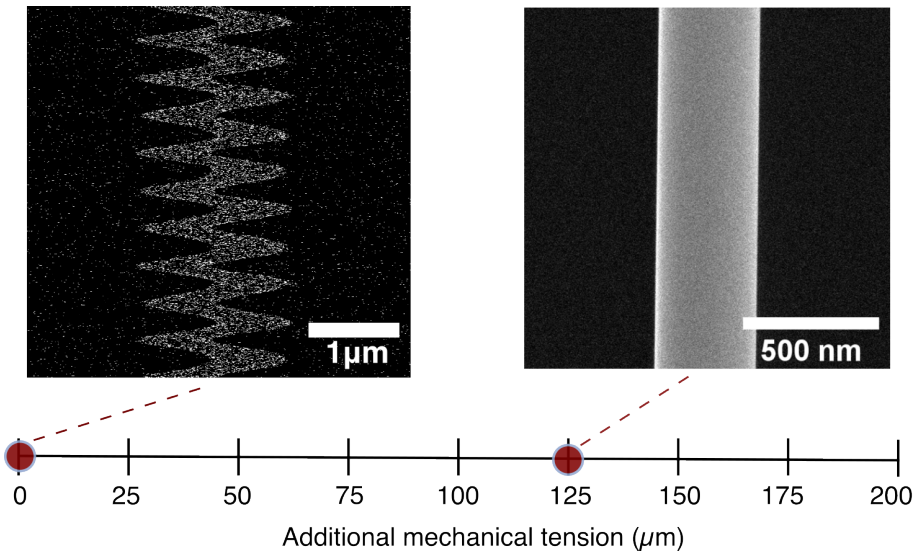

Fig. 7.5 ***Additional mechanical tension on the nanofiber.*** *Summary of the optimization study of nanofiber tension, as described in Chapter 5.9. Nanofibers were fabricated by incrementally elongating each one with additional tension in steps of 25 µm, ranging from 0 to 200 µm. Without additional tension, strong oscillations were visible under the electron beam (SEM image on the left). In contrast, when applying a mechanical tension of 125 µm, the nanofiber surface was well-focused during imaging (SEM image on the right).*

7.3.2 Fabrication protocol

The fabrication process necessitated extensive efforts to determine optimal parameters, including vacuum level, voltage, current, defocusing, and dwell time (that is the time the electron beam pauses on a particular point during line by line scanning [212]), to achieve the desired geometries for the structures, along with the assessment of their repeatability. In the following, we will delve into each of these aspects in detail.

7.3.2.1 Precursors and vacuum level

To fabricate the plasmonic nanostructures we used a dual configuration Focused Ion Beam/Scanning Electron Microscopy (FIB-SEM) system (FEI Helios NanoLab 600i) equipped with a GIS with three gas channels. We employed Platinum as precursor, specifically using $C_9H_{16}Pt$ (Methylcyclopentadienyltrimethyl platinum). We chose this precursor for the typical ease in fabrication. However, alternative metals can also be considered. The precursor was locally injected through the nozzle on the upper side of the sample and its temperature was set at 80 °C to reduce variations in the growth rate. The fabrication starts when a target vacuum level inside the chamber of $\sim 5 \cdot 10^{-7}$ mbar is reached: the GIS needle is then inserted and it fluxes the $C_9H_{16}Pt$ precursor. After starting the gas flux, we waited for the gas pressure inside the chamber to stabilize at $0.8 - 1.2 \cdot 10^{-5}$ mbar. In order to prevent any unintended material deposition due to exposure of leftover precursor gas to the electron beam, after each fabrication we waited until the initial vacuum level of $5 \cdot 10^{-}7$ is restored (no leftover gas in the chamber).

7.3.2.2 Voltage and current parameters

Materials deposited via EBID from organometallic precursor gases are known to contain significant levels of carbonaceous impurities resulting from the dissociation of the precursor molecules. To assess the composition of our fabrications, we fabricated on a flat surface arrays of nanoplatelets with dimensions of $800 \cdot 800 \cdot 500$ nm^3 varying the accelerating voltage V_{acc} from 1 to 10 kV and the electron beam current I_{beam} from 5.4 pA to 340 pA, as shown in Figure 7.6. These arrays were characterized via Energy Dispersive X-ray Spectroscopy (EDS) to quantify the atomic percentage of Pt atoms relative to the combined sum of Pt and C atoms. Platinum concentration

increases for combinations with low accelerating voltages and high beam currents. In Figure 7.6a I put in evidence the Pt percentage in the case of the three nanoplateletes: for $V_{acc} = 10kV$ and $I_{beam} = 5.4pA$ we measured a Pt percentage of around 5%, for $V_{acc} = 5kV$ and $I_{beam} = 86pA$ a Pt percentage of 10% and for $V_{acc} = 1kV$ and $I_{beam} = 340pA$ a Pt percentage of 46%. The findings, reported for all the measurements in Figure 7.6b, suggest that the dielectric properties of the structures can be adjusted by manipulating the mentioned fabrication parameters. This characterization process facilitated the identification of optimal set of parameters that meet the low accelerating voltage requirements for preventing the nanofiber from charging (highlighted by a dashed red line in Figure 7.6b) and the high current ones to maximize the Pt content within the nanostructure. As a result, the structures were manufactured using $V_{acc} = 1$ kV and $I_{beam} = 86$ pA, corresponding to a Pt content of around 46% (highlighted by a yellow dashed square in Figure 7.6).

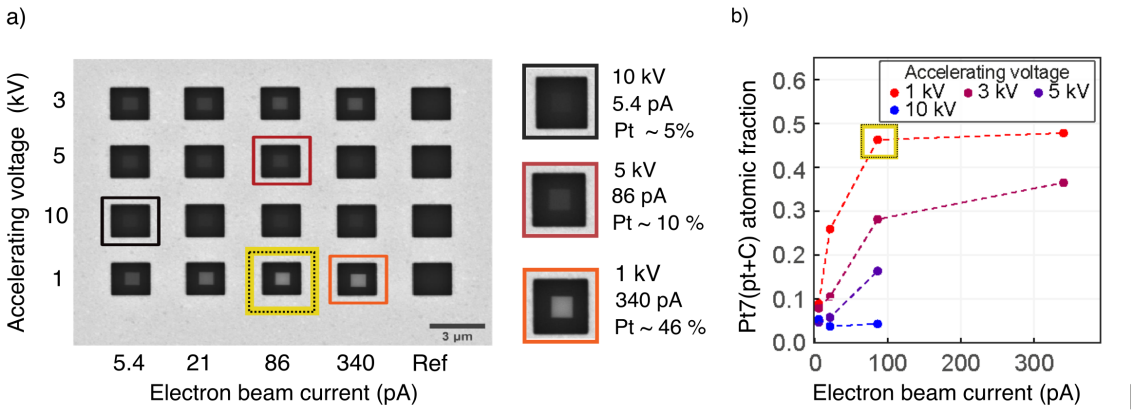

Fig. 7.6 ***Energy Dispersive X-ray Spectroscopy (EDS) tests.*** *a) Arrays of nanoplatelets with dimensions of* $800 \cdot 800 \cdot 500$ nm^3 *were fabbricated varying the accelerating voltage* V_{acc} *and beam current* I_{beam}*. b) The arrays were characterized via Energy Dispersive X-ray Spectroscopy (EDS) to quantify the percentage of Pt atoms relative to the combined sum of Pt and C atoms. The dashed yellow line highlights the chosen voltage and current values, suitable for preventing the nanofiber platform from charging under the electron beam.*

7.3.2.3 Fabrication tests on a flat surface

We initiated our experiments on a flat surface. Through an evaporation process, a silica glass slide was coated with a layer of gold to prevent any charging effects on the surface. The initial test focused on fabricating pillars by adjusting both the focus of the electron beam and the height of the structures, while keeping the base constant. Figure 7.7 shows three rows of structures, with increasing height from left to right. The central row was fabricated with the beam precisely focused on the surface, the upper row involved defocusing downward, and the lower row entailed defocusing upward. With the measurements on the flat surface serving as a reference, we subsequently moved to the fabrication on the nanofiber.

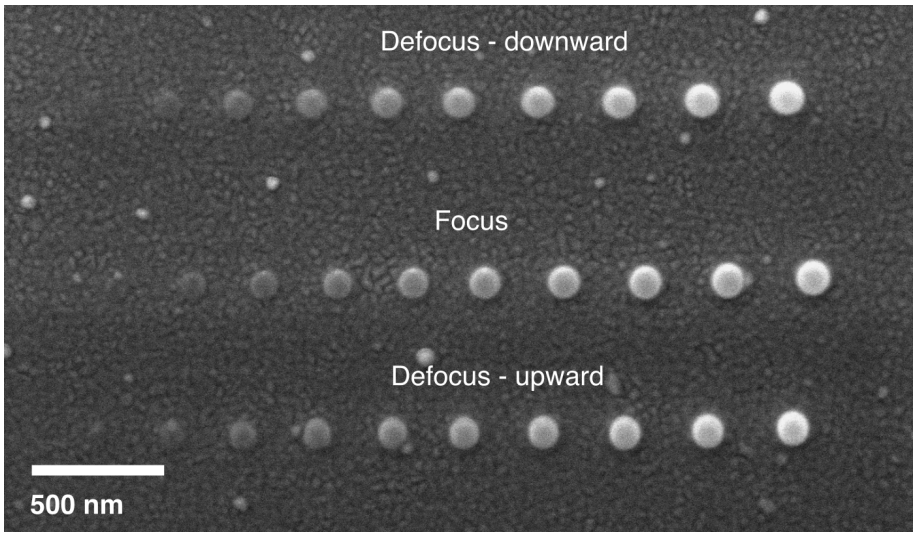

Fig. 7.7 ***Fabrication tests on a flat surface.*** *Plasmonic nanostructures were fabricated varying the height of the structures and focusing respectively donward (upper row), on the substrate surface (centered row) and upward (lower row.*

7.3.2.4 Blurring and dwell time of the electron beam

Compared to the standard EBID technique on a flat surface, our approach on a nanofiber involves using a defocused electron beam during the fabrication process. This choice is made because the mechanical pressure exerted by a tightly focused beam prevents the desired fabrication outcome. In particular, when the beam is focused, its diameter on the fiber's surface is approximately 12 nm. On the highly curved nanofiber surface, this configuration does not give the same high-quality output as on a flat surface, as previously shown in Figure 7.7.However, after conducting several tests, we observed that introducing controlled blurriness, with a blurring value b equal to the base diameter of the pillar to be fabricated (Figure 7.8a), resulted in the best matching between the targeted and achieved size. An example of this process, both with and without blurring, is illustrated in Figure 7.8b, where the blurring was set to $b = 100$ nm.

The last fabrication parameter to be determined is the dwell time. As no reference values are available in literature, this parameter was established entirely through empirical experimentations. In the EBID technique we can specify the sizes of the desired 3D structures, which in the case of a pillar are the base diameter and the height. By setting the desired pillar's base size at 100 nm and its height at 500 nm, and using the previously identified optimal parameters, including voltage, current, and blurring, the dwell time was systematically adjusted within the range of 0.5 µs to 1 µs seconds to achieve the set height, as illustrated in Figure 7.8c-d. In this manner, we selected a dwell time of 0.55 µs.

The complete set of parameters used to fabricate the nanostructures are given in Table 7.3.2.4.

Fabrication parameters				
Voltage	Current	Blurring	Dwell time	Pt content
1 kV	86pA	100 µm	0.55 µs	≈ 46%

Table 7.1: **EBID parameters for nanostructures fabbrication.**

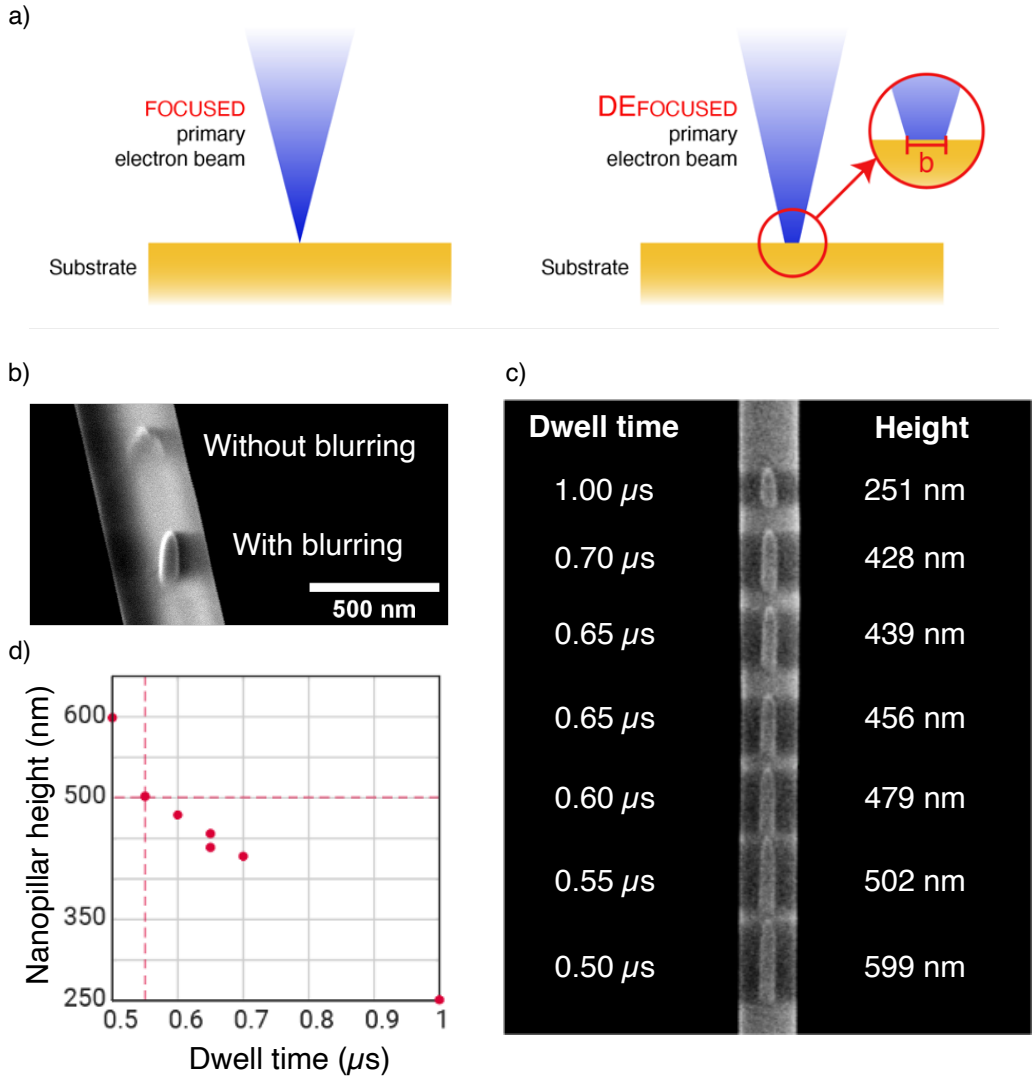

Fig. 7.8 ***Blurring and dwell time optimization*** *a) Sketck of a focused and defocused (blurred) EBID technique b) Nanostructures fabricating without (upper pillar) and with (lower pillar) blurring. The fiber is rotated by 45° on the xy plane and tilted by 52° with respect to the SEM beam axis, to favour visibility. c) Empirical optimization of the dwell time. d) Plot of the obtained heights of the pillars with dwell time variation.*

7.4 Characterization

7.4.1 Targeted structures: nanopillars and nanoantennas

The primary targeted structures were cylindrical nanopillars with a height of 500 nm and a circular cross-section base measuring 100 nm in diameter, as shown in Figure 7.9a. The fabrication process takes approximately one minute to produce a single structure with the identified parameters for current, voltage, blurring and dwell time. To obtain a gap stystem, we target also nanoantennas by combining two pillars with a size gap of the order of tens of nanometers, as illustrated in Figure 7.9e. More than 250 nanostructures were produced, taking into account the parameter optimization study, before achieving the final nanopillars and nanoantennas for optical characterization. An example of the fabricated nanopillars is presented in Figure 7.9b-c. Figure 7.9f-g displays an example of a nanoantenna with a gap.

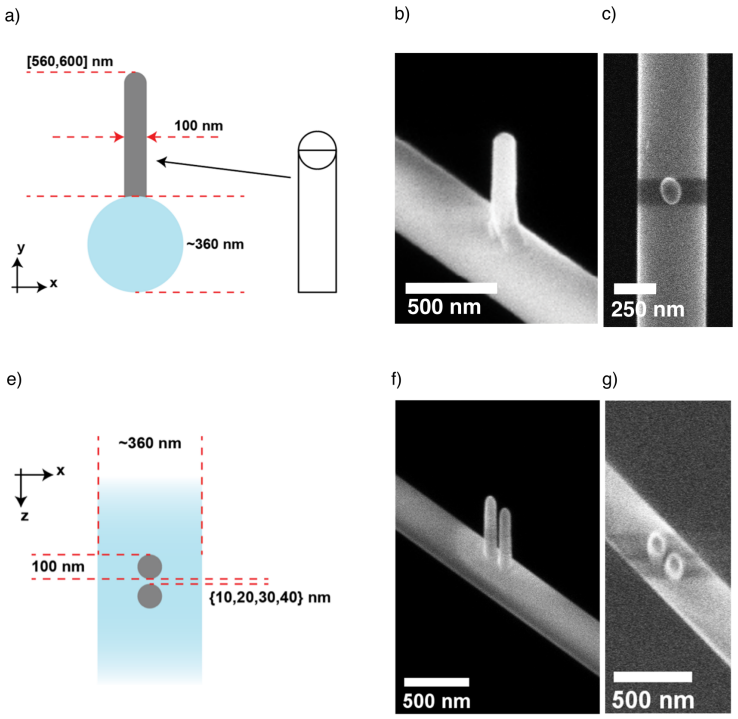

Fig. 7.9 ***Targeted structures.*** *a) Sketch of a nanopillar. b-c) Fabricated nanopillar with a height of 500 nm and a diameter of around 100 nm. e) Sketch of a nanoantenna. f-g) Fabricated nanoantenna with a 20 nm gap.*

7.4.1.1 Repeatability and resolution

Out of the more than 250 nanostructures produced, approximately a hundred were dedicated to assessing the repeatability of the fabrication process. The fabrication demonstrated a good repeatability, with a relative error, between the $\sim \pm 5\%$ of the transverse dimension and the $\pm 10\%$ of the longitudinal one. In terms of the base dimensions, an analysis of the SEM images, as depicted in Figure 7.10, revealed that the pillars exhibited an average longitudinal dimension of 111 ± 13 nm and an average transverse dimension of 90 ± 6 nm at the base. To measure the height of the pillars, we tilted the sample at a angle of 45°, moving from a top-view to a lateral view, and measured the height during imaging. We adjusted the obtained values by dividing them by the sine of the tilt angle. Furthermore, in the case of the nanoantennas, the pillars can be positioned with 10 nm controlled-size nanogaps. For smaller gap sizes, it was not feasible to fabricate two separate pillars, as the nanostructures tend to merge during growing.

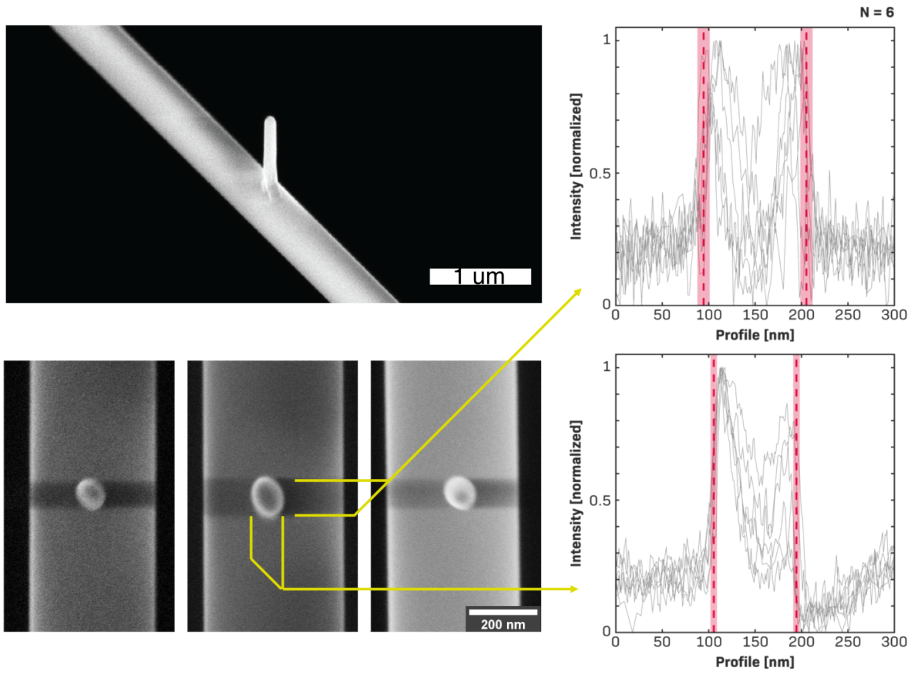

Fig. 7.10 ***Repeatibility of the fabbrications.*** *From an analysis of the SEM images, the fabricated pillars exhibited an average longitudinal dimension of* 111 ± 13 *nm and an average transverse dimension of* 90 ± 6 *nm at the base.*

7.4.2 Optical characterization of the structures

Nanofibers with a nanopillar and a nanoantenna consisting of two pillars separated by a gap of 20 nm, were optically characterized at LKB, amounting to approximately 30 nanofibers. The fibers to be characterized were initially cleaned using the Plasma Oxygen Treatment (POT), presented in Chapter 6.4.2, to remove dust. This cleaning process ensured that the structures were clearly visible and not confused with dust particles, which can produce similar bright scattering points.

7.4.2.1 Spectral characterization

The initial step of the study was devoted to the measurement of the spectrum of the scattered light for both the nanopillars and the nanoantennas. To accomplish this, we employed the experimental setup depicted in Figure 7.11. In this configuration, a supercontinuum laser was sent to one end of the nanofiber through a single-mode fiber. To protect the nanofiber from dust, it was placed in a protective chamber with a window to access to the nanofiber zone, as shown in the inset image at the bottom left. With this setup, we were able to measure the spectrum of the light transmitted by the nanofiber or the spectrum of the light scatterd by the nanostructures collecting it with an objective. For these measures, we used a Princeton Instruments Acton Series SP2500i spectrometer. Alternatively, by using a beam splitter, it was possible to direct the scattered light to a camera for alignment purposes. In the inset image at the bottom right, I have included the spectrum of the light transmitted by a nanofiber without any structure. This serves as a reference for comparison.

Figure 7.12 displays the spectra of light scattered from the nanopillar (in blue) and the nanoantenna (in red) in the range between 600-800 nm, with a noticeable shift in the central peak wavelength between the nanopillar and the nanoantenna. The peak wavelength for the nanopillar is around 690 nm, while for the nanoantenna, it is approximately 760 nm. This shift was confirmed by simulations conducted using the finite time method (FEM) with the software Comsol Multiphysics, realized by Dr. Muhammad Fayyaz Kashif from the Istituto Italiano di Tecnologia in Lecce.

Additionally, in Figure 7.12, a spectral analysis was conducted at 785 nm for both the nanopillar and nanoantenna, revealing a higher intentisity in the case of the nanoantenna.

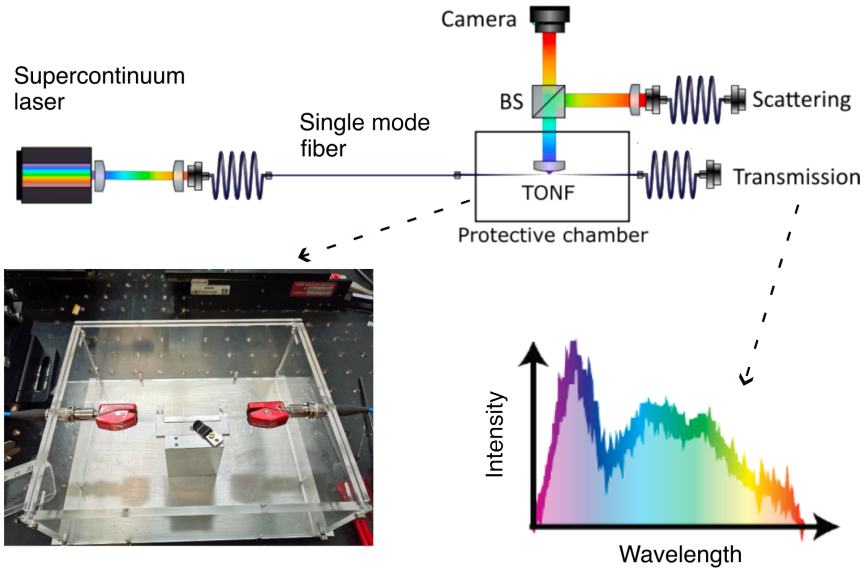

Fig. 7.11 ***Setup for the spectral characterization.*** *A supercontinuum laser is sent to the fiber, which is placed into a protective chamber (insert at bottom left). It is possible to measure the spectrum of light trasmitted by the nanofiber or the spectrum of the light scattered by the nanostructures. The insert at bottor right show the spectrum of the transmitted light for a nanofiber without structures.*

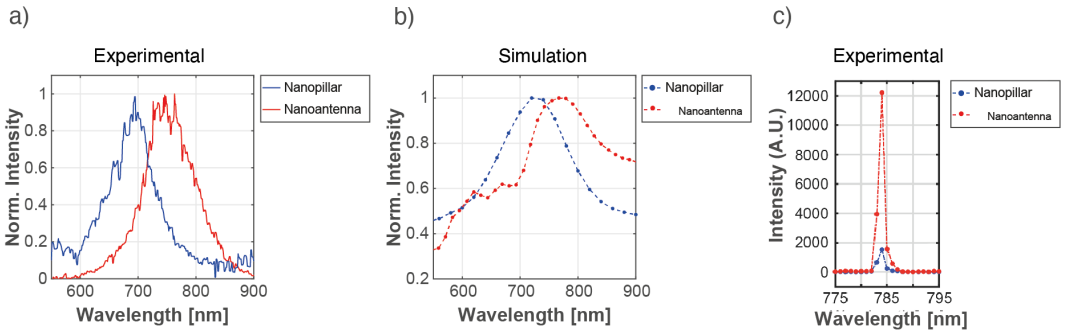

Fig. 7.12 ***Spectral characterization of the scattered light.*** *a-b) Measured spectrum of the scattered light for the nanopillar (blue) and nanoantenna (red) using supercontinuum and relative simulation. c) Measured spectrum of the scattered light for the nanopillar (blue) and nanoantenna (red) using 785 nm laser.*

7.4.2.2 Polarization

The subsequent phase of this study focused on evaluating the degree of polarization in the light scattered by the nanostructures. This investigation specifically addressed the characterization of:

1. The intensity of the scattered light as a function of the polarization of the input light sent into the nanofiber, as illustrated in Figure 7.13a.

2. the polarization of the scattered light with fixed input polarization, as illustrated in Figure 7.13b.

In the first configuration, using the setup in Figure 7.12, a continuous-wave (CW) laser (Toptica Photonics) light with a wavelength of $\lambda = 785$ nm passed through a $\lambda/2$ wave plate (WP) optimized for the working wavelength before being injected into one end of the nanofiber. The nanofiber was kept unbent to avoid introducing asymmetrical stress on its cross section, preserving the polarization of light propagating through it. The scattering from the nanostructure was monitored using a sCMOS camera while continuously rotating the wave plate to identify the polarization producing the maximum scattered intensity, considered then as the zero rotation degree. The scattered intensity at this angle was recorded using the spectrometer, and the wave-plate was then rotated by $\pi/18$ radians (10°) between consecutive measurements.

The obtained results are depicted in Figure 7.13a (blue and red colors correspond to the nanopillar and nanoantenna, respectively) and were fitted with a cosine square function:

$$I(\theta_{rot}) = a \cdot \cos^2(\theta_{rot}) + b \tag{7.2}$$

where θ_{rot} represents the rotation angle of the waveplate. The parameter a quantifies the difference in intensity between the minimum and maximum, and the parameter b the offset of the minimum respect to zero. Therefore, the parameter b gives information of how well the structure scatter light compared to the ideal case where $b = 0$. Due to the asymmetric distribution of the evanescent field on the nanofiber surface, as shown in Figure 7.13b, optimal coupling occurs when the polarization orientation aligns with the azimuthal position of the plasmonic structures. This results in a coupling efficiency that varies from a maximum (along the y-axis) to a minimum (along the x-axis). The single nanopillar exhibits a more pronounced dependence on

the input polarization than the nanoantenna, with a minimum relative intensity of $b_{\text{pillar}} < 0.1$, while for the nanoantenna, $b_{\text{antenna}} \approx 0.2$. The lower performance of the nanoantenna may be attributed to a slight displacement of the two nanopillars along the azimuthal direction introduced during the EBID fabrication, allowing partial coupling between the structure and the x-polarized component of the electromagnetic field. In the second configuration (as shown in Figure 7.13c), a 785 nm beam linearly polarized along the y-axis, where the evanescente field is maximum, was sent into the nanofiber to maximize coupling with the EBID nanostructures. The scattered light passed through a half-waveplate and a polarizer. Since linearly polarized light along the y-axis was sent into nanofiber, the electric field's y- and z-components were primarily coupled to the plasmonic nanostructure. In particular, the y-component dominated the electric field intensity, while the component along the longitudinal axis made a minor contribution to the overall intensity, and the effect of the third component contribution was negligible. However, the y-component cannot be observed from the top of the nanopillar. Therefore, the scattered signal on the xz-plane is polarized along the z-axis.

The polarization state of the scattered signal on the xz-plane can be described as the superposition of two orthogonal components along the polarized (z-axis) and unpolarized (x-axis) axes. This state can be quantified using the degree of polarization (DOP), defined as: $P = \frac{I_{max}-I_{min}}{I_{max}+I_{min}}$. Figure 7.13c shows that the light scattered by the nanoantenna on ONF exhibited an higher degree of polarization (DOP) than the nanopillar. The single nanopillar on ONF exhibited a lower DOP of 0.65, while the nanoantenna on ONF showed a DOP of 0.92, both polarized along the z-axis. These behaviors were supported by simulations, as indicated by the dashed lines in Figure 7.13c. The simulations were realized using the finite-difference time-domain (FDTD) with the software Comsol Multiphysics by Dr. Muhammad Fayyaz Kashif from the Istituto Italiano di Tecnologia in Lecce.

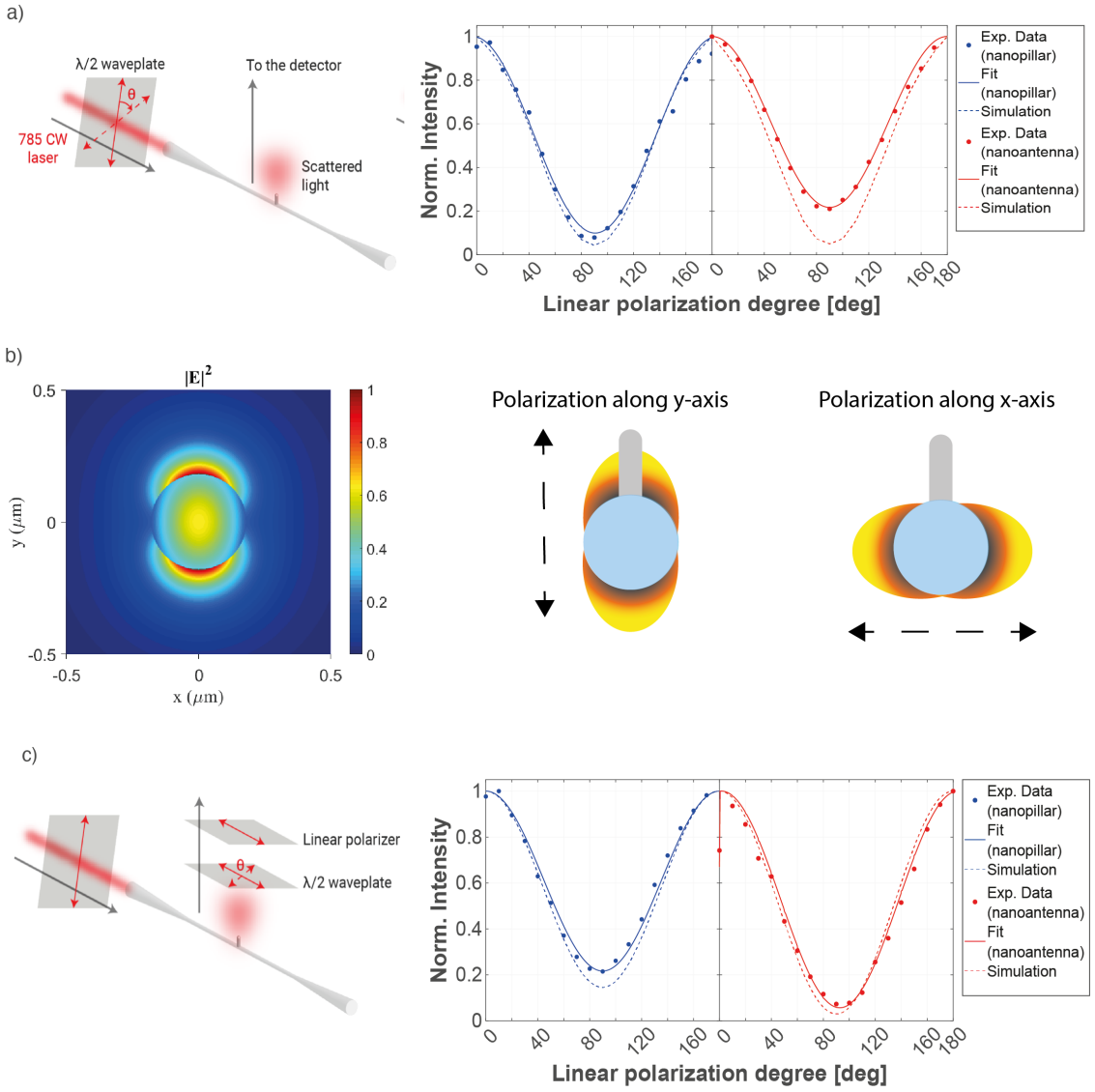

Fig. 7.13 ***Polarization mesaurements*** *a) Input polarization dependence for nanopillar (NP in blue) and nanoantenna (NA in red), respectively. b) Simulation of the evanescente field for a nanofiber of 360 nm designed for a wavelength of 780 nm. c) Scattered light polarization for nanopillar (NP in blue) and nanoantenna (NA in red), respectively.*

7.4.3 Plasma oxygen treatment: a way to enhance intensity

The Plasma Oxygen Treatment (POT), which was employed to clean the nanofiber by removing surface dust as described in chapter 6, not only enhances the cleanliness of the nanofiber but also leads to improvements in the quality of the fabricated nanostructures. Its purification effects on the compositional and electrical properties of the EBID material have previously been documented by Botman and coworkers [213], where an increase in the metal content after the treatment was reported. Comparing the scattering intensity of a single pillar treated firstly with a low oxygen flux and then with a high oxygen flux, we observed a significant increase in the scattering intensity of more than four orders of magnitude (Figure 7.14a). This increase is attributed to a series of oxide-reduction reactions that reduce the carbon concentration in the nanostructure, thus increasing the overall metal content. In turn, this treatment have influences on the dimensions of the nanostructures, potentially reducing both the diameter and the height from tens to a few tens of nanometers.

To demonstrate these effects, Dr. Antonio Balena fabricated several pillars on a flat surface. Figure 7.14b shows two images of one pillar on a flat surface before and after the POT, revealing differences in the imaging brightness. This is usually attributed to a change in composition, toward a higher metallic content. By analyzing the intensity profile in the SEM images of the pillars before and after POT, as presented in Figure 7.14c, he extracted information about the diameter and height sizes before and after POT, as shown in Figure 7.14d-e. This change in size results in a quantifiable and predictable effect. In conclusion, when designing the structures that will be optically characterized we considered the effect of the POT on the nanostructures, which reduces the height and the diameter of approximately the $5 - 10\%$.

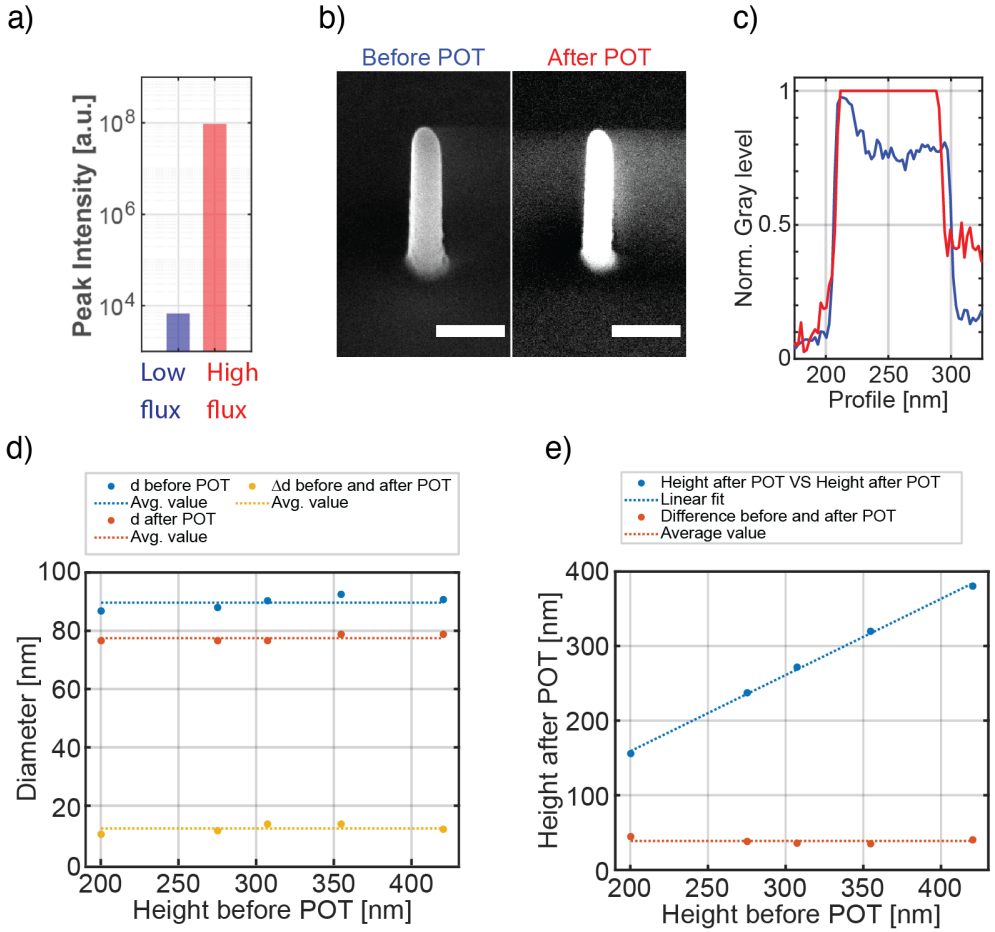

Fig. 7.14 ***Effects on the plasma Oxygen Treatment (POT).*** *a) Set of pillars fabricated on a flat surface b) SEM image of a pillar on a flat surface before and after POT treatment. c) Example of image analysis of the intensity profile of the pillars. d) Measured diameter of the pillar before and after POT varying the height of the pillars. e) Measured height of the pillar after POT respect of the measured height before POT.*

7.5 Perspectives

7.5.1 Nanostructures composition and coupling efficiency

In Section 7.3.2.2, we have seen that it is possible to modify the metal content of the nanostructures by adjusting voltage and current parameters in the fabrication. This approach allows for the potential fabrication of structures with a lower refractive index, approaching a dielectric material. Such structures may offer the advantage of reduced losses and absorption compared to all-plasmonic ones. It would be interesting to compare the coupling efficiency of the device by varying the composition of the material. Figure 7.15 reports this comparison for a system consisting of four nanopillars fabricated on the nanofiber and a dipole (with which we schematize the emitter) oriented along the y-axis. It is visible that for structures with a refractive index around $1.7-2$, the coupling efficiency β can reach $50-60\%$, depending on the pillar's dimensions. This simulation was realized by the intern Lucien Belzane, who joined our team in October 2023.

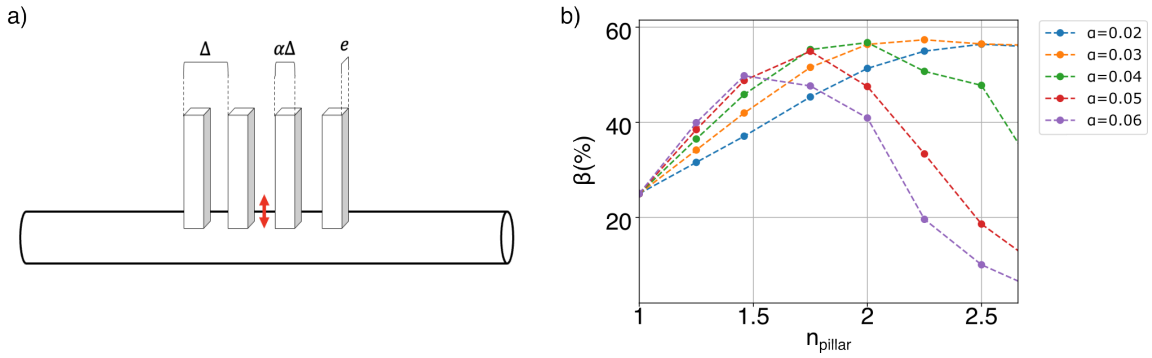

Fig. 7.15 ***Coupling efficiency of the device*** *a) Schematic of the coupling of one dypole with four pillars on the nanofiber. The pillars have a distance Δ and a thickness $\alpha\Delta$. The dypole orientation is along y-axis. b) Simulation of the coupling efficiency β varying the refractive index of the pillar and the thickness of the pillars.*

7.5.2 Quantum emitter placement

A fundamental requirement to use nano-antennas for single-photon sources is the precise positioning of quantum emitters at the antenna hotspot with nanoscale accuracy. Various methods have already been explored, such as probabilistic deposition

(as discussed in Section 6.5.1), atomic force microscopy or two-step electron-beam lithography. In this chapter, the precise control of the plasmonic gap ideally provides the opportunity to deposit particles in a colloidal solution touching the nanofiber with a droplet of diluted solution, and then subsequently fabricate the nano-antenna around the particle. I first tested this approach by depositing a 50 nm gold particle onto a nanofiber with a diameter of 360 nm and then fabricating two pillars with a height of 500 nm on its sides, as shown in Figure 7.16a. However, it's important to note that this protocol requires the use of quantum emitters that can withstand exposure to the electron beam without experiencing bleaching or degradation, which is not feasible for perovskite NCs. To explore this possibility, I initiated preliminary studies in collaboration with the University of Technology of Troyes (UTT) on GeV centers [51] embedded in nanodiamonds of approximately 20-50 nm in size (Figure 7.16b-c), which are expected to be more robust under exposure to the electron beam. The critical aspect under investigation is the impact of the electron beam on the optical properties of these emitters and the potential effects of depositing layers of the EBID precursor on their optical properties. Other aspects to explore include determining whether an emitter placed in proximity to a metallic surface undergo new nonradiative decay processes that lead to a decrease in fluorescence intensity. Additionally, it is crucial to assess how this configuration might affect the single photon purity of the emitters, as the presence of linear and nonlinear processes, though initially insignificant, can become prominent (i.e biexciton generation, electron-Raman scattering, and metal luminescence, among others)[214].

7.5.3 Other photonic surfaces

To enable the application of perovskite nanocrystals (NCs) for studying the Purcell effect, I am working in collaboration with Nanyang University of Singapore to conduct preliminary studies on alternative devices. These include the investigation of distributed Bragg reflector (DBR) cavities constructed as a layered sandwich of TiO_2 and SiO_2 layers (Figure 7.17a) and dielectric metasurfaces (Figure 7.17b). Notably, the latter devices are of particular interest because they inherit many of the functionalities provided by optical nanoantennas, like enhancing emission via the Purcell effect and narrowing the emission spectrum. On these devices the perovskite NCs are deposited with the spin-coating technique, and the feasibility of employing polymers for their stabilization can be explored.

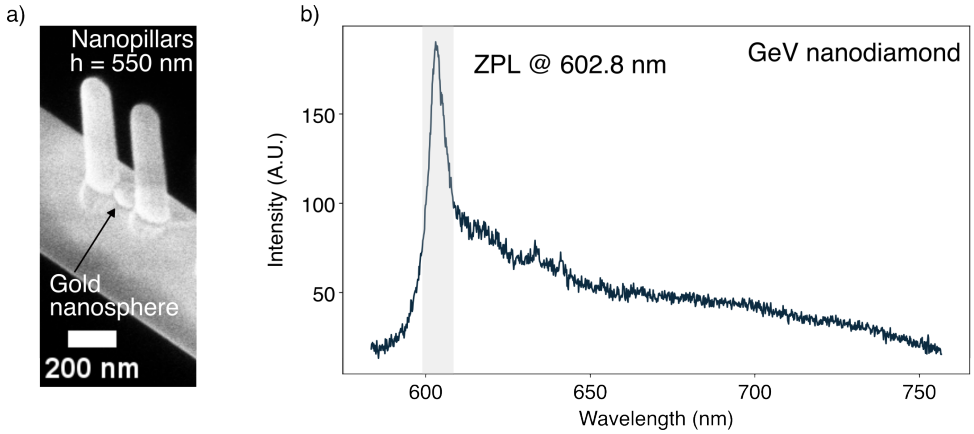

Fig. 7.16 ***Quantum emitter integration.*** *a) Gold nanoparticle with a 50 nm diameter deposited on the nanofiber before the antenna fabrication. b) Wide-field microscopy image of GeV nanodiamonds spin-coated on a glass coverslip after ultra-sonification to desegregate them. b) Example of a room temperature PL emission spectrum of a GeV nanodiamond exhibiting the typical zero-phonon line (ZPL) at 602.8 nm. Other transitions are visible.*

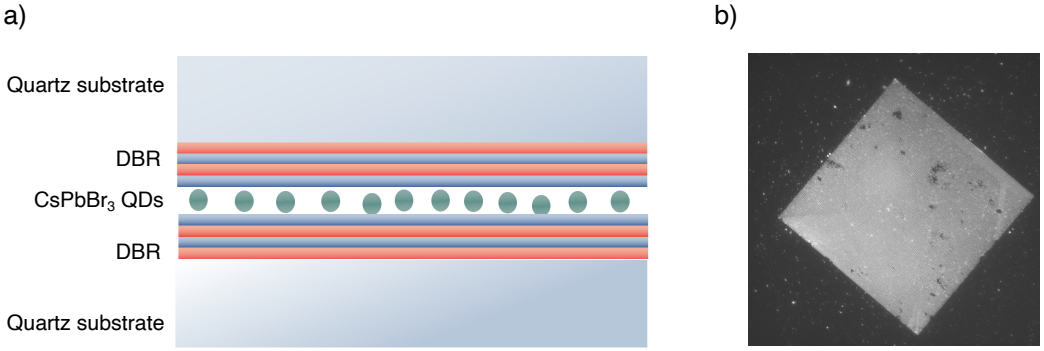

Fig. 7.17 ***Other photonics surfaces.*** *a) Sketch of a DBR cavity constructed as a layered sandwich of dielectric TiO_2 and SiO_2 layers. $CsPbBr_3$ perovskite NCs are deposited between the two DBRs. b) Wide-field microscopy image of a quasi bound states in the continuum (QBICs) metamaterial fabricated on a quartz substrate. Mixed-cation $Cs_{0.2}FA_{0.8}PbBr_3$ perovskite NCs are spin-coated on the substrate.*

Conclusion

In this chapter, I introduced an unconventional technique for fabricating metallic nanostructures on nanofibers using Electron Beam-Induced Deposition (EBID), with the goal of creating a prototype of nanofiber-based cavities automatically coupled to fibers.

Specifically:

- I explained how the EBID technique, typically employed on flat surfaces, was adapted for fabricating nanostructures on a suspended dielectric nanofiber. My focus was on creating nanopillars in platinum and nanoantennas, which consist of two pillars forming a gap system.
- I discussed the process of optimizing the nanofiber for this nanofabrication technique.
- I described the fabrication process and the parameters needed to achieve the desired geometries for the structures. I also emphasized the repeatability of the process.
- I covered the optical characterization of nanopillars and nanoantennas, including the measurement of the spectrum of the scattered light. It was observed that the nanoantennas exhibited increased light intensity. Additionally, I discussed the study of the polarization of light scattered by the nanostructures, noting that the nanoantennas displayed a higher degree of polarization (DOP) compared to the nanopillars.
- I introduced the concept of Plasma Oxygen Treatment (POT) as a method to enhance the cleanliness of the nanofiber and purify the fabricated nanostructures, leading to an increase in the metal content.

The chapter concluded with a discussion of future perspectives, including the potential fabrication of structures with a lower refractive index, approaching a dielectric material or the precise positioning of quantum emitters at the antenna hotspot with nanoscale accuracy.

Conclusions and perspectives

Single photons are a central resource in a wide array of applications, including quantum computation, communication, and metrology. Advances in these fields rely heavily on the continuous improvement of techniques for generating, manipulating, and detecting single photons. Furthermore, the seamless integration of single photons with nanophotonic systems is an essential step towards their pratical usage in existing networks.

The focus of this thesis was the development of a prototype of compact and efficient integrated single-photon device designed to operate at room temperature. This achievement was realized by coupling a perovskite NC with an optical tapered nanofiber. This goal was driven by two primary objectives. The first objective was to optimize perovskite NCs to achieve stability beyond the current state-of-the-art, ensuring robust and reliable single-photon emission. Second, I focused on optimizing the optical nanofiber platform to improve its transmission and to enable the fabrication of nanostructures on its surface.

To lay the groundwork for this research, Chapters 1 and 2 introduced the essential theoretical and experimental tools, providing the necessary knowledge and methodology for the comprehensive study of solid-state semiconductor quantum dots, with a specific focus on perovskite NCs.

In Chapter 3, I delved into the characterization of $CsPbBr_3$ NCs synthetized with an protocol used for the first time to obtain confined NCs and demonstrating improved stability compared to conventional synthesis methods. These $CsPbBr_3$ NCs exhibited strong single-photon emission and demonstrated impressive stability under illumination. In Chapter 4, I introduced confined mixed-cation $Cs_{1-x}FA_xPbBr_3$ NCs, aiming to address the well-know instability of conventional mixed-halide systems in the red and near-infrared spectral regions. In this chapter, I showcased the tunability of their emission wavelength and focused on their photostability and blinking behav-

ior. Furthermore, I reported the first demonstration of single-photon emission from mixed-cation perovskite NCs.

Chapter 5 explored the use of a Zn^{2+} doping to enhance the stability and brightness of $CsPbBr_3$ perovskite NCs. The studied Zn-treated $CsPbBr_3$ NCs presented increased stability under illumination and dilution, reduced blinking on a sub-millisecond timescale, and maintained stability in the bright state for excitation powers well above the saturation point. These findings emphasized the potential of these synthesis approaches to optimize the performance of perovskite-based SPSs, opening up promising prospects for their integration into nanophotonic systems for quantum technology applications.

After optimizing the quantum emitters, my focus shifted to their coupling with the nanofiber platform. In Chapter 6, I detailed the optimizations made to obtain high-performance single-mode optical nanofibers with subwavelength diameters for effective light-matter interaction. In this chapter, I demonstrated the succesful measurement of the single-photon emission from a $CsPbBr_3$ perovskite NC deposited on the nanofiber's surface. This device represents a prototype of a compact and integrated perovskite-based single-photon source. In Chapter 7, I introduced a non-conventional technique for fabricating metallic nanostructures on nanofibers via Electron Beam-Induced Deposition (EBID). This approach aimed to create nanofiber-based structures that are automatically coupled to fibers. This technique has the potential to enable the efficient coupling of emitted photons by harnessing the enhancement of the quantum emitter's spontaneous emission rate via Purcell effect. Specifically, I described how nanofibers were optimized to be suitable for this nano-fabrication technique. I also explained how this EBID technique, typically used on flat surfaces, was adapted for fabricating nanostructures on suspended dielectric nanofibers. In this context, I focused on fabricating nanopillars in platinum and nanoantennas, which consisted of two pillars forming a gap system. I then described the fabrication process, including the optimal parameters required for achieving the desired structure geometries. I also discussed the optical characterization of nanopillars and nanoantennas, focusing on the spectra and the polarization of light scattered by these nanostructures. Notably, the light scattered by the nanoantennas exhibited higher brightness and higher degree of polarization (DOP) compared to the nanopillars.

The work presented in this thesis opens up several perspectives for further enhancing perovskite stability and the efficiency of coupling with the nanofiber platform. For example, future research may investigate new ligands and doping treatments

for perovskite compositions emitting in the red and NIR spectra regions, aiming to improve their stability in regions of interest for telecommunications.

In terms of coupling quantum emitters with the nanofiber platform, precise positioning of quantum emitters at the antenna hotspot and the study of the effects of emitters' proximity to metallic surfaces are key areas of interest. Additionally, to enhance the efficiency of nanofiber-based structures, it is intriguing to explore the fabrication of structures with a lower refractive index, approaching a dielectric material. Such structures may offer the advantage of reduced losses and absorption compared to all-plasmonic structures.

Furthermore, to facilitate the use of perovskite nanocrystals (NCs), which are sensitive to the electron beam, is it possible to employing Distributed Bragg Reflector (DBR) cavities and metamaterials. These components are of particular interest due to their ability to inherit many functionalities provided by optical nanoantennas, such as enhancing emission via the Purcell effect.

Appendices

Appendix A

Core/shell colloidal semiconductor emitters

In addition to perovskite NCs, during my PhD I characterized colloidal quantum emitters of group II-VI semiconductors in collaboration with the Institut de Nanosciences de Paris (INSP). In order to compare their optical and quantum properties with those of perovskites, I briefly present some results related to core/shell CdSe/ZnS nanoplatelets synthesized at the INSP and core/shell CdS/CdSe/CdS quantum dots synthesized at the Columbia University.

A.1 CdSe/ZnS nanoplateletes

These nanoplatelets exhibit a central emission wavelength (CEW) of approximately 630 nm with a full-width at half maximum (FWHM) of approximately 14 nm, as depicted in Figure A.1a. The photoluminescence (PL) decay, as illustrated in Figure A.1b, is longer than that of perovskite NCs and can be fitted by a tri-exponential model, resulting in lifetimes of $\tau_1 = 2.8$ ns, $\tau_2 = 15.3$ ns, and $\tau_3 = 56.0$ ns in the case of the QD in figure.

The photoluminescence time-trace, acquired with a binnig time of 10 ma, reveals visible blinking between high and low-intensity states, as depicted in Figure A.1c. Nevertheless, the Fluorescence Lifetime-Intensity Distribution (FLID) image in Figure A.1d demonstrates that the high emissive states are more likely than the low emissive ones. These emitters also exhibit strong antibunching, as evidenced in Figure A.1e, where the QD displays a $g^{(2)}$ value of 0.05.

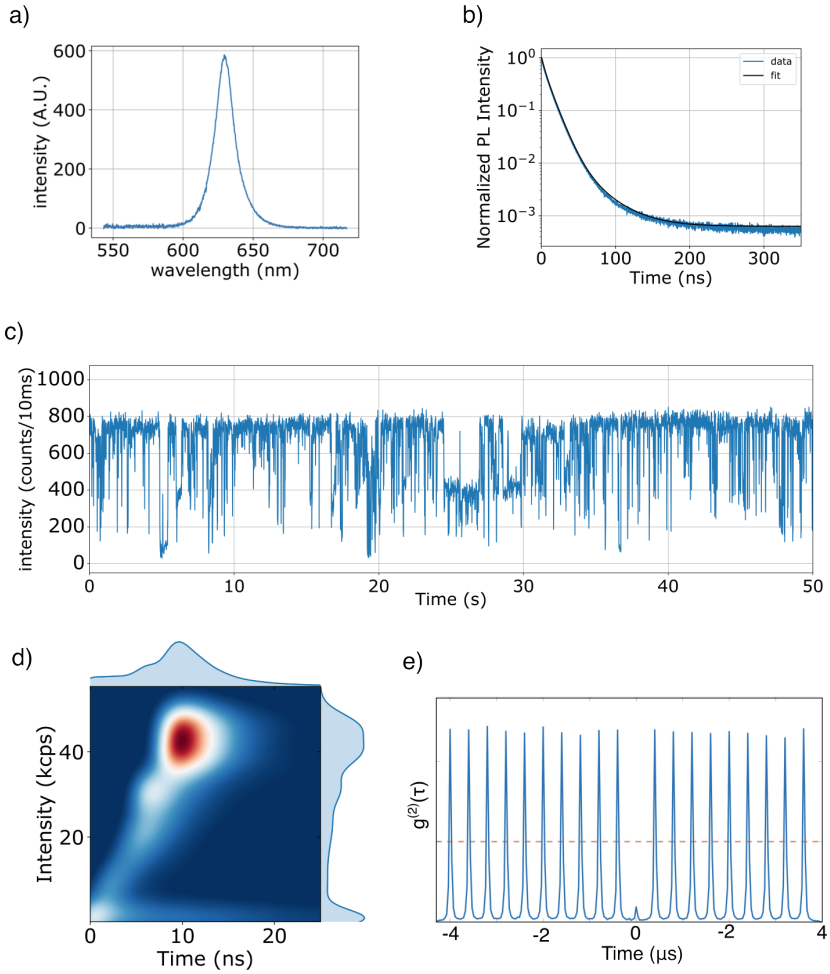

Fig. A.1 ***CdSe/ZnS nanoplateletes*** *a) PL emission spectrum. b) PL decay fitted by a tri-exponential model. c) PL time-traces acquired with a 10 ms binning time. d) FLID image acquired with a 10 ms binning time. e)$g^{(2)}(tau)$ histrogram showing single photon emission. The red-line indicates the threshold for single photon emission claim.*

A.2 CdS/CdSe/CdS core/shell QDs

CdS/CdSe/CdS core/shell QDs have an unconventional core-shell structure. In fact, these QDs feature a CdS/CdSe/CdS configuration, where the CdSe component serves as the emissive core, resembling a spherical quantum well. Further details on these QDS can be found in reference [215].

These emitters exhibit a central emission wavelength (CEW) of approximately 625 nm with a full-width at half maximum (FWHM) of approximately 20 nm, as depicted in Figure A.2a. The photoluminescence (PL) decay, as illustrated in Figure

A.2b, can be fitted by a tri-exponential model, resulting in lifetimes of $\tau_1 = 3$ ns, $\tau_2 = 14$ ns, and $\tau_3 = 51$ ns in the case of the QD in figure.

The photoluminescence time-trace, recorded with a binning time of 10 ms, displays pronounced telegraphic blinking behavior characterized by extended periods of low intensity. This is clearly visible in Figure A.2c and is further highlighted in the Fluorescence Lifetime-Intensity Distribution (FLID) image shown in Figure A.2d. These emitters demonstrate strong antibunching, as indicated by a $g^{(2)}$ value of 0.04 reported in Figure A.2e.

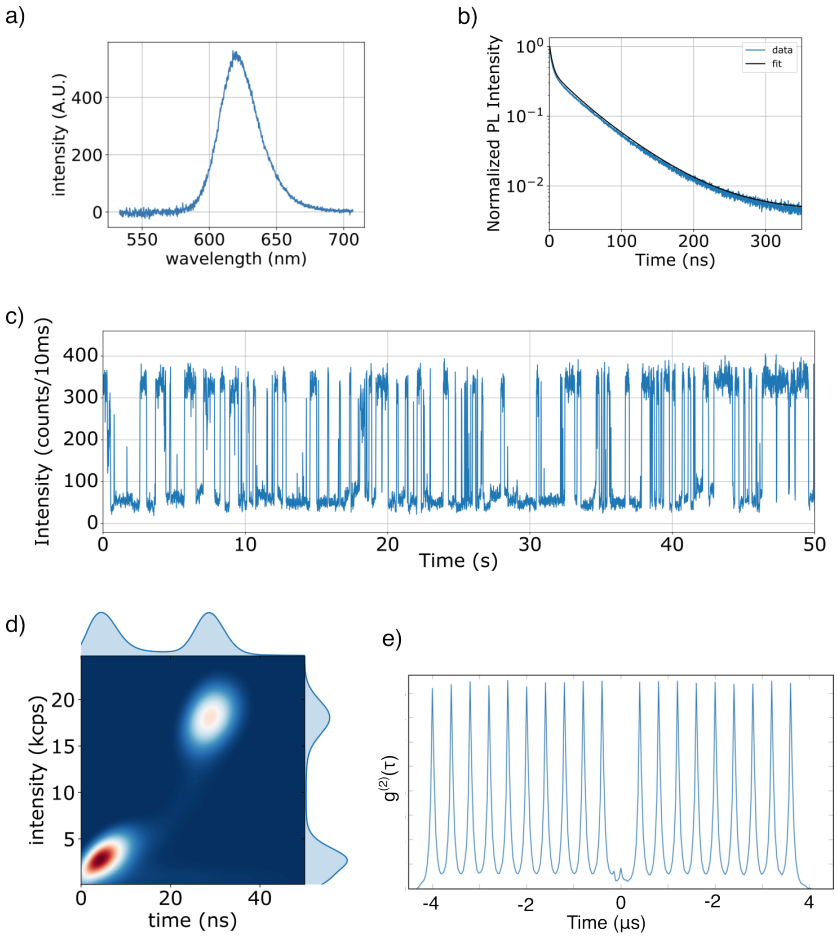

Fig. A.2 ***CdS/CdSe/CdS core/shell QDs*** *a) PL emission spectrum. b) PL decay fitted by a tri-exponential model. c) PL time-traces acquired with a 10 ms binning time. d) FLID image acquired with a 10 ms binning time. e)$g^{(2)}(tau)$ histrogram showing single photon emission. The red-line indicates the threshold for single photon emission claim.*

Appendix B

Synthesis of $Cs_{1-x}FA_xPbBr_3$ perovskite NCs

This Appendix reports the synthesis of $Cs_{1-x}FA_xPbBr_3$ perovskite NCs, realized by our collaborators in Nanyang Technological University of Singapore.

B.1 Chemicals

Cesium carbonate (Cs2CO3, 99.9% trace metal basis), formaminidium bromide (FABr, $\geq$ 98%) lead (II) bromide (PbBr2, 98%), oleylamine (OLA technical grade, 70%), N, N-Dimethylformamide (DMF, 99.8%), and toluene (99.8%) were purchased from Sigma-Aldrich. Octadecene (ODE, technical grade 90%), and oleic acid (OA, technical grade 90%) were purchased from Alfa Aesar.

B.2 Synthesis of $CsPbBr_3$ nanocrystals

For the synthesis of Cs-oleate, 0.326 g of Cs_2CO_3, 18 mL of ODE and 1 mL of OA were loaded into a 100 mL three-neck flask. The mixture was heated under vacuum at 100° for an hour and subsequently raised to 150° under nitrogen flow. After complete dissolution, the solution was kept at 150 °C to avoid solidification. For the synthesis of the $CsPbBr_3$ quantum dots, 0.067 g of $PbBr_2$, 5 mL of ODE, 0.5 mL of OA and 1 mL of OLA were loaded into a separate 100 mL three-neck flask. The mixture was heated under vacuum at 100 °C for an hour and subsequently raised to 150 °C under nitrogen flow. After complete dissolution, the solution was further

heated up to 170 °C. 0.6 mL of the as-prepared Cs-oleate was quickly injected to induce crystallization of the quantum dots. The solution was immediately placed into an ice-water bath and cooled to room temperature. To purify the resulting solution, ethyl acetate was subsequently added into the solution and the solution was centrifuged at 6000 rpm for 5 minutes. The precipitate was collected and re-dispersed into toluene. The solution was again centrifuged at 6000 rpm for 5 minutes and the supernatant was stored in a nitrogen filled environment to prevent degradation of the solution.

B.3 Synthesis of $Cs_{1-x}FA_xPbBr_3$ nanocrystals

In a typical synthesis of $Cs_{0.2}FA_{0.8}PbBr_3$ NCs, 0.04 mmol of CsBr, 0.16 mmol of FABr, and 0.2 mmol of PbBr2 were dissolved in 5 mL of DMF. After complete dissolution, 100 µL of OA and 50 µL of OLA were added into the solution. 200 µL of the precursor solution was injected into 5 mL of toluene under stirring to induce crystallisation of the NCs. The solution was left stirring for 24 hours before storage. All synthesis was conducted at room temperature and pressure. NCs of different Cs and FA cation composition were achieved by varying the stoichiometric amount of CsBr, FABr, and $PbBr_2$.

Appendix C

Synthesis of Zn-treated $CsPbBr_3$ perovskite NCs

This Appendix reports the synthesis of Zn-treated $CsPbBr_3$ perovskite NCs, realized by our collaborators in Institut des Nanosciences de Paris (INSP) in Paris.

C.1 Chemicals

$PbBr_2$ (Alfa Aesar, 98.5%), Cs_2CO_3 (Alfa aesar, 99,99%), oleylamine (OLA, Acros, $80-90\%$), oleic acid (OA, Sigma-Aldrich), octadecene (ODE, Acros Organics, 90%), toluene (VWR, rectapur), Bromic acid (HBr, ABCR, 48% aqueous solution), Ethyl acetate (JT baker), zinc diethyldithiocarbamate (ZnDDTC, alfa Aesar $17-19.5\%$ in weight).

C.2 Caesium oleate precursor

We mix in a 50 mL three-neck flask, 412 mg of Cs_2CO_3, 20 mL of ODE and 1.25 mL of OA. The content of the flask is stirred and degased under vacuum at room temperature for 25 min. The flask is heated at 110 °C for 30 min. The atmosphere is switched to nitrogen and the temperature raised to 150 °C. The reaction is carried on for 30 min. At this stage, the salt is fully dissolved. The temperature is cooled down below 100 °C and the flask degased under vacuum. Finally this solution is used as a stock solution.

C.3 Oleylamonium bromide (OLABr)

We mix 10 mL of OLA with 1 mL of HBr in a 25 mL three-neck flask that is then heated at 80 °C under vacuum. The atmosphere is then switched to nitrogen and the temperature raised to 120 °C for 2 h. This solution is then transfered to the glove box using air free method and used as stock solution.

C.4 $CsPbBr_3$ NCs synthesis

In a three neck flask, 280 mg of $PbBr_2$ are mixed with 20 mL of ODE. The flask is degased under vacuum at room temperature for 15 min. Then, the temperature is raised to 110 °C. Then 2 mL of OLA are injected. Once the vacuum and temperature have recovered, we inject 2 mL of OA. The solution is further degased at 120 °C for 30 min. The atmosphere is switched to nitrogen and the temperature raised to 180 °C. Around 2 mL of CsOA solution are injected, and the solution turns yellow. The reaction is conducted for 30 s and finally quickly cooled-down by removing the heating mantle and using a water bath. The solution is transferred to plastic tube and centrifuged. The supernatant is discarded. The pellet is dispersed in 5 mL of toluene. The same volume of ethylacetate is added and the mixture is centrifugated again for 5 min at 6000 rpm. The obtained dried pellet is stored in the air free glove box.

C.5 Zn shelling

30 mg of $CsPbBr_3$ NCs are mixed with 20 µL of OLABr, 16 mg of ZnDDTC and 3 mL of ODE. The mixture is then sonicated, before being transfered to a 25 mL three-neck flask. The flask is heated at 120 °C. The duration is tuned from 5 to 60 min. The color tends to swicth from green to brown green but PL remains green. Then the mixture is centrifugated. The obtained is redispersed in toluene. The same volume of ethyl acetate is added and the mixture is centrifugated again. NCs are centrifuged in toluene and the pellet is discarded to save only the small particules in solution, more likely to be better confined and stable..

C.6 Absorption spectra

For absorption, we used dilute solution of NC in hexane. The spectra were acquired using a Jasco V730 spectrometer.

C.7 Transmission electron microscopy

A drop of diluted NCs solution was drop-casted onto a copper grid covered with an amorphous carbon film. The grid was degassed overnight under secondary vacuum. Imaging was conducted using a JEOL 2010 transmission electron microscope operated at 200 kV. Complementarily, TEM/STEM observations were made on a Titan Themis 200 microscope (FEI/Thermo Fischer Scientific) equipped with a geometric aberration corrector on the probe. The microscope was also equipped with the "Super-X" systems for EDX analysis with a detection angle of 0.9 steradian. The observations were made at 200 kV with a probe current of about 35 pA and a half-angle of convergence of 17 mrad. HAADF-STEM images were acquired with a camera length of 110 mm (inner/outer collection angles were respectively 69 and 200 mrad).

C.8 X-ray photoemission measurements (XPS)

For photoemission spectroscopy, we used the Tempo beamline at synchrotron Soleil. Films of NCs were spin-casted onto a gold coated Si substrate with an 80 nm tick gold layer. To avoid any charging effect during measurements, the ligands of the nanocrystals were exchanged by dipping the film in ethyl acetate. Samples were introduced in the preparation chamber and degassed until a vacuum below 10^{-9} mbar was reached. Then samples were introduced to the analysis chamber. The signal was acquired by a MBS A-1 photoelectron analyzer. Acquisition was done at constant pass energy (50 eV) within the detector. Photon energy of 150 eV was used for the acquisition of valence band and work function while 600 eV photon energy was used for the analysis of the core levels. A gold substrate was employed to calibrate the Fermi energy. The absolute value of the incoming photon energy was determined by measuring the first and second orders of Au4f core level peaks. Then for a given analyzer pass energy, we measured the Fermi edge and set its binding energy as zero. The same shift was applied to all spectra acquired with the same pass energy. To determine the work function, an 18 V bias was applied, and its exact

value was determined by observing the shift of a Fermi edge. Additional spectra have bene acquired with on a Omicron Argus X-ray photoelectron spectrometer, using a monochromated Al Kα ($h\nu = 1486.6$ eV) radiation source having a 300 W electron beam power. The emission of photoelectrons from the analyzed sample at a takeoff angle of 45° under ultrahigh vacuum ($10^{\breve{}}{}^{8}$ Pa). The spectra are collected with a 20 eV pass energy.

Appendix D

Electromagnetic field of HE_{11} mode

The fundamental mode of an optical nanofiber (HE_{11} mode) is given by the three components of electric and magnetic fields E_x,E_y,E_z and H_x,H_y,H_z in a cylindrical coordinates (r,θ,z):

For $r < a$ (inside the fiber),

$$\begin{aligned}
E_x =& - jA\beta\frac{a}{u}\left[\frac{(1-s)}{2}J_0\left(\frac{u}{a}r\right)\cos\psi - \frac{(1+s)}{2}J_2\left(\frac{u}{a}r\right)\cos(2\theta+\psi)\right],\\
E_y =& jA\beta\frac{a}{u}\left[\frac{(1-s)}{2}J_0\left(\frac{u}{a}r\right)\sin\psi + \frac{(1+s)}{2}J_2\left(\frac{u}{a}r\right)\sin(2\theta+\psi)\right],\\
E_z =& AJ_1\left(\frac{u}{a}r\right)\cos(\theta+\psi),\\
H_x =& - jA\omega\varepsilon_0 n_1^2\frac{a}{u}\left[\frac{(1-s_1)}{2}J_0\left(\frac{u}{a}r\right)\sin\psi + \frac{(1+s_1)}{2}J_2\left(\frac{u}{a}r\right)\sin(2\theta+\psi)\right],\\
H_y =& - jA\omega\varepsilon_0 n_1^2\frac{a}{u}\left[\frac{(1-s_1)}{2}J_0\left(\frac{u}{a}r\right)\cos\psi - \frac{(1+s_1)}{2}J_2\left(\frac{u}{a}r\right)\cos(2\theta+\psi)\right],\\
H_z =& - A\frac{\beta}{\omega\mu_0}sJ_1\left(\frac{u}{a}r\right)\sin(\theta+\psi).
\end{aligned} \tag{D.1}$$

For $r > a$ (outside the fiber),

$$
\begin{aligned}
E_x =& - jA\beta\frac{aJ_1(u)}{wK_1(w)}\left[\frac{(1-s)}{2}K_0\left(\frac{w}{a}r\right)\cos\psi + \frac{(1+s)}{2}K_2\left(\frac{w}{a}r\right)\cos(2\theta+\psi)\right],\\
E_y =& jA\beta\frac{aJ_1(u)}{wK_1(w)}\left[\frac{(1-s)}{2}K_0\left(\frac{w}{a}r\right)\sin\psi - \frac{(1+s)}{2}K_2\left(\frac{w}{a}r\right)\sin(2\theta+\psi)\right],\\
E_z =& A\frac{J_1(u)}{K_1(w)}K_1\left(\frac{w}{a}r\right)\cos(\theta+\psi),\\
H_x =& - jA\omega\varepsilon_0 n_0^2\frac{aJ_1(u)}{wK_1(w)}\left[\frac{(1-s_0)}{2}K_0\left(\frac{w}{a}r\right)\sin\psi - \frac{(1+s_0)}{2}K_2\left(\frac{w}{a}r\right)\sin(2\theta+\psi)\right],\\
H_y =& - jA\omega\varepsilon_0 n_0^2\frac{aJ_1(u)}{wK_1(w)}\left[\frac{(1-s_0)}{2}K_0\left(\frac{w}{a}r\right)\cos\psi + \frac{(1+s_0)}{2}K_2\left(\frac{w}{a}r\right)\cos(2\theta+\psi)\right],\\
H_z =& - A\frac{\beta}{\omega\mu_0}s\frac{J_1(u)}{K_1(w)}K_1\left(\frac{w}{a}r\right)\sin(\theta+\psi),
\end{aligned}
\tag{D.2}
$$

where ψ is the polarization angle, $s = [(w)^{-2} + (u)^{-2}] \,/\, [J_1'(u)/uJ_1(u) + K_1'(w)/wK_1(w)]$, $s_1 = \beta^2 s/(k^2 n_1^2)$, $s_0 = \beta^2 s/(k^2 n_2^2)$, β is the propagation constant, $u = a\sqrt{n_1^2 k^2 - \beta^2}$ and $w = a\cdot\sqrt{\beta^2 - n_2^2 k^2}$ ($u^2 + w^2 = V^2$, V is the normalized frequency). J_n and K_n are the Bessel functions of the first kind and the modified Bessel functions of the second kind, respectively, and the prime stands for the derivative.

- -

Bibliography

[1] R. P. Feynman; "There's plenty of room at the bottom: An invitation to enter a new field of physics"; Caltech Engineering and Science **23**, p. 5 (1960). Cited page xv

[2] P. Zoller, T. Beth, D. Binosi, R. Blatt, H. Briegel, D. Bruss, T. Calarco, J. I. Cirac, D. Deutsch, J. Eisert *et al.*; "Quantum information processing and communication: Strategic report on current status, visions and goals for research in Europe"; The European Physical Journal D-Atomic, Molecular, Optical and Plasma Physics **36**, pp. 203–228 (2005). Cited page xv

[3] E. Diamanti, H.-K. Lo, B. Qi & Z. Yuan; "Practical challenges in quantum key distribution"; npj Quantum Information **2**, pp. 1–12 (2016). Cited page xv

[4] P. W. Shor & J. Preskill; "Simple proof of security of the BB84 quantum key distribution protocol"; Physical review letters **85**, p. 441 (2000). Cited page xv

[5] V. Giovannetti, S. Lloyd & L. Maccone; "Quantum metrology"; Physical review letters **96**, p. 010401 (2006). Cited page xv

[6] V. Giovannetti, S. Lloyd & L. Maccone; "Advances in quantum metrology"; Nature photonics **5**, pp. 222–229 (2011). Cited page xv

[7] P. Schindler, M. Müller, D. Nigg, J. T. Barreiro, E. A. Martinez, M. Hennrich, T. Monz, S. Diehl, P. Zoller & R. Blatt; "Quantum simulation of dynamical maps with trapped ions"; Nature Physics **9**, pp. 361–367 (2013). Cited page xv

[8] R. Barends, L. Lamata, J. Kelly, L. García-Álvarez, A. G. Fowler, A. Megrant, E. Jeffrey, T. C. White, D. Sank, J. Y. Mutus *et al.*; "Digital quantum simulation of fermionic models with a superconducting circuit"; Nature communications **6**, p. 7654 (2015). Cited page xv

[9] M. W. Doherty, N. B. Manson, P. Delaney, F. Jelezko, J. Wrachtrup & L. C. Hollenberg; "The nitrogen-vacancy colour centre in diamond"; Physics Reports **528**, pp. 1–45 (2013). Cited page xv

[10] C. Toninelli, I. Gerhardt, A. Clark, A. Reserbat-Plantey, S. Götzinger, Z. Ristanović, M. Colautti, P. Lombardi, K. Major, I. Deperasińska *et al.*; "Single organic molecules for photonic quantum technologies"; Nature Materials **20**, pp. 1615–1628 (2021). Cited pages xvi, 9, and 10

[11] B. Lounis & W. E. Moerner; "Single photons on demand from a single molecule at room temperature"; Nature **407**, pp. 491–493 (2000). Cited pages xvi and 9

[12] C. Kurtsiefer, S. Mayer, P. Zarda & H. Weinfurter; "Stable solid-state source of single photons"; Physical review letters **85**, p. 290 (2000). Cited page xvi

[13] E. Neu, D. Steinmetz, J. Riedrich-Möller, S. Gsell, M. Fischer, M. Schreck & C. Becher; "Single photon emission from silicon-vacancy colour centres in chemical vapour deposition nano-diamonds on iridium"; New Journal of Physics **13**, p. 025012 (2011). Cited pages xvi and 10

[14] N. Somaschi, V. Giesz, L. De Santis, J. Loredo, M. P. Almeida, G. Hornecker, S. L. Portalupi, T. Grange, C. Anton, J. Demory *et al.*; "Near-optimal single-photon sources in the solid state"; Nature Photonics **10**, pp. 340–345 (2016). Cited pages xvi and 10

[15] P. Michler, A. Imamoğlu, M. Mason, P. Carson, G. Strouse & S. Buratto; "Quantum correlation among photons from a single quantum dot at room temperature"; Nature **406**, pp. 968–970 (2000). Cited page xvi

[16] L. Manna; "The Bright and Enlightening Science of Quantum Dots"; Nano Letters (2023). Cited page xvi

[17] C. R. Kagan, L. C. Bassett, C. B. Murray & S. M. Thompson; "Colloidal quantum dots as platforms for quantum information science"; Chemical reviews **121**, pp. 3186–3233 (2020). Cited page xvi

[18] P. Lodahl, S. Mahmoodian & S. Stobbe; "Interfacing single photons and single quantum dots with photonic nanostructures"; Reviews of Modern Physics **87**, p. 347 (2015). Cited pages xvi and 9

[19] J. Claudon, J. Bleuse, N. S. Malik, M. Bazin, P. Jaffrennou, N. Gregersen, C. Sauvan, P. Lalanne & J.-M. Gérard; "A highly efficient single-photon source based on a quantum dot in a photonic nanowire"; Nature Photonics **4**, pp. 174–177 (2010). Cited page xvi

[20] O. Gazzano, S. M. De Vasconcellos, K. Gauthron, C. Symonds, J. Bloch, P. Voisin, J. Bellessa, A. Lemaître & P. Senellart; "Evidence for confined Tamm plasmon modes under metallic microdisks and application to the control of spontaneous optical emission"; Physical review letters **107**, p. 247402 (2011). Cited page xvi

[21] M. Gschrey, A. Thoma, P. Schnauber, M. Seifried, R. Schmidt, B. Wohlfeil, L. Krüger, J.-H. Schulze, T. Heindel, S. Burger *et al.*; "Highly indistinguishable photons from deterministic quantum-dot microlenses utilizing three-dimensional in situ electron-beam lithography"; Nature communications **6**, p. 7662 (2015). Cited page xvi

[22] N.-G. Park; "Perovskite solar cells: an emerging photovoltaic technology"; Materials today **18**, pp. 65–72 (2015). Cited page xvii

[23] L. Protesescu, S. Yakunin, M. I. Bodnarchuk, F. Krieg, R. Caputo, C. H. Hendon, R. X. Yang, A. Walsh & M. V. Kovalenko; "Nanocrystals of cesium lead halide perovskites (CsPbX3, X= Cl, Br, and I): novel optoelectronic materials showing bright emission with wide color gamut"; Nano letters **15**, pp. 3692–3696 (2015). Cited pages xvii, 14, 25, 28, 57, 63, 65, 72, 73, and 89

[24] Y.-S. Park, S. Guo, N. S. Makarov & V. I. Klimov; "Room temperature single-photon emission from individual perovskite quantum dots"; ACS nano **9**, pp. 10386–10393 (2015). Cited pages xvii, 10, 14, 63, and 64

[25] C. Zhu, M. Marczak, L. Feld, S. C. Boehme, C. Bernasconi, A. Moskalenko, I. Cherniukh, D. Dirin, M. I. Bodnarchuk, M. V. Kovalenko *et al.*; "Room-temperature, highly pure single-photon sources from all-inorganic lead halide perovskite quantum dots"; Nano Letters **22**, pp. 3751–3760 (2022). Cited pages xvii and 99

[26] S. Pierini, M. d'Amato, M. Goyal, Q. Glorieux, E. Giacobino, E. Lhuillier, C. Couteau & A. Bramati; "Highly photostable perovskite nanocubes: toward integrated single photon sources based on tapered nanofibers"; ACS photonics **7**, pp. 2265–2272 (2020). Cited pages xviii and 94

[27] M. D'Amato, Q. Y. Tan, Q. Glorieux, A. Bramati & C. Soci; "Color-tunable mixed-cation perovskite single photon emitters"; ACS Photonics **10**, pp. 197–205 (2023). Cited page xviii

[28] M. D'Amato, L. Belzane, C. Dabard, M. Silly, G. Patriarche, Q. Glorieux, H. Le Jeannic, E. Lhuillier & A. Bramati; "Highly photostable Zn-treated halide perovskite nanocrystals for efficient single photon generation"; Nano Letters **23**, pp. 10228–10235 (2023). Cited page xviii

[29] C. Soci, G. Adamo, D. Cortecchia, K. Wang, S. Xiao, Q. Song, A. L. Schall-Giesecke, P. J. Cegielski, M. C. Lemme, D. Gerace *et al.*; "Roadmap on perovskite nanophotonics"; Optical Materials: X **17**, p. 100214 (2023). Cited page xviii

[30] P. Senellart, G. Solomon & A. White; "High-performance semiconductor quantum-dot single-photon sources"; Nature nanotechnology **12**, pp. 1026–1039 (2017). Cited pages 2, 6, and 7

[31] R. J. Glauber; "Coherent and incoherent states of the radiation field"; Physical Review **131**, p. 2766 (1963). Cited page 3

[32] A. M. Fox; *Quantum optics: an introduction*; volume 15 (Oxford University Press, USA) (2006). Cited page 3

[33] R. Loudon; *The quantum theory of light* (OUP Oxford) (2000). Cited page 4

[34] R. H. Brown & R. Q. Twiss; "LXXIV. A new type of interferometer for use in radio astronomy"; The London, Edinburgh, and Dublin Philosophical Magazine and Journal of Science **45**, pp. 663–682 (1954). Cited page 4

[35] C.-K. Hong, Z.-Y. Ou & L. Mandel; "Measurement of subpicosecond time intervals between two photons by interference"; Physical review letters **59**, p. 2044 (1987). Cited page 6

[36] S. Xia, T. Aoki, K. Gao, M. Arita, Y. Arakawa & M. J. Holmes; "Enhanced single-photon emission from GaN quantum dots in bullseye structures"; ACS Photonics **8**, pp. 1656–1661 (2021). Cited page 7

[37] N. Tomm, A. Javadi, N. O. Antoniadis, D. Najer, M. C. Löbl, A. R. Korsch, R. Schott, S. R. Valentin, A. D. Wieck, A. Ludwig *et al.*; "A bright and fast source of coherent single photons"; Nature Nanotechnology **16**, pp. 399–403 (2021). Cited page 7

[38] N. Srocka, P. Mrowiński, J. Grosse, M. Von Helversen, T. Heindel, S. Rodt & S. Reitzenstein; "Deterministically fabricated quantum dot single-photon source emitting indistinguishable photons in the telecom O-band"; Applied Physics Letters **116**, p. 231104 (2020). Cited page 8

[39] S. Félix, N. Gisin, A. Stefanov & H. Zbinden; "Faint laser quantum key distribution: Eavesdropping exploiting multiphoton pulses"; Journal of Modern Optics **48**, pp. 2009–2021 (2001). Cited page 8

[40] Y.-R. Shen; "Principles of nonlinear optics"; (1984). Cited page 8

[41] C. Couteau; "Spontaneous parametric down-conversion"; Contemporary Physics **59**, pp. 291–304 (2018). Cited page 8

[42] V. Giovannetti, S. Lloyd & L. Maccone; "Positioning and clock synchronization through entanglement"; Physical Review A **65**, p. 022309 (2002). Cited page 8

[43] M. Hennrich, T. Legero, A. Kuhn & G. Rempe; "Photon statistics of a non-stationary periodically driven single-photon source"; New Journal of Physics **6**, p. 86 (2004). Cited page 9

[44] A. Kuhn, M. Hennrich & G. Rempe; "Deterministic single-photon source for distributed quantum networking"; Physical review letters **89**, p. 067901 (2002). Cited page 9

[45] M. Keller, B. Lange, K. Hayasaka, W. Lange & H. Walther; "Continuous generation of single photons with controlled waveform in an ion-trap cavity system"; Nature **431**, pp. 1075–1078 (2004). Cited page 9

[46] T. Basché, W. Moerner, M. Orrit & H. Talon; "Photon antibunching in the fluorescence of a single dye molecule trapped in a solid"; Physical review letters **69**, p. 1516 (1992). Cited page 9

[47] J. Hwang & E. Hinds; "Dye molecules as single-photon sources and large optical nonlinearities on a chip"; New Journal of Physics **13**, p. 085009 (2011). Cited page 10

[48] R. Brouri, A. Beveratos, J.-P. Poizat & P. Grangier; "Photon antibunching in the fluorescence of individual color centers in diamond"; Optics letters **25**, pp. 1294–1296 (2000). Cited page 10

[49] N. Mizuochi, T. Makino, H. Kato, D. Takeuchi, M. Ogura, H. Okushi, M. Nothaft, P. Neumann, A. Gali, F. Jelezko *et al.*; "Electrically driven single-photon source at room temperature in diamond"; Nature photonics **6**, pp. 299–303 (2012). Cited page 10

[50] Y. Zhou, A. Rasmita, K. Li, Q. Xiong, I. Aharonovich & W.-b. Gao; "Coherent control of a strongly driven silicon vacancy optical transition in diamond"; Nature communications **8**, p. 14451 (2017). Cited page 10

[51] M. Nahra, D. Alshamaa, R. Deturche, V. Davydov, L. Kulikova, V. Agafonov & C. Couteau; "Single germanium vacancy centers in nanodiamonds with bulk-like spectral stability"; AVS Quantum Science **3** (2021). Cited pages 10 and 157

[52] T. Schröder, F. Gädeke, M. J. Banholzer & O. Benson; "Ultrabright and efficient single-photon generation based on nitrogen-vacancy centres in nanodiamonds on a solid immersion lens"; New Journal of Physics **13**, p. 055017 (2011). Cited page 10

[53] A. Dousse, J. Suffczyński, A. Beveratos, O. Krebs, A. Lemaitre, I. Sagnes, J. Bloch, P. Voisin & P. Senellart; "Ultrabright source of entangled photon pairs"; Nature **466**, pp. 217–220 (2010). Cited page 10

[54] H. Wang, Z.-C. Duan, Y.-H. Li, S. Chen, J.-P. Li, Y.-M. He, M.-C. Chen, Y. He, X. Ding, C.-Z. Peng *et al.*; "Near-transform-limited single photons from an efficient solid-state quantum emitter"; Physical Review Letters **116**, p. 213601 (2016). Cited page 10

[55] F. Hu, H. Zhang, C. Sun, C. Yin, B. Lv, C. Zhang, W. W. Yu, X. Wang, Y. Zhang & M. Xiao; "Superior optical properties of perovskite nanocrystals as single photon emitters"; ACS nano **9**, pp. 12410–12416 (2015). Cited page 10

[56] F. P. García de Arquer, D. V. Talapin, V. I. Klimov, Y. Arakawa, M. Bayer & E. H. Sargent; "Semiconductor quantum dots: Technological progress and future challenges"; Science **373**, p. eaaz8541 (2021). Cited page 13

[57] J. M. Richter, F. Branchi, F. Valduga de Almeida Camargo, B. Zhao, R. H. Friend, G. Cerullo & F. Deschler; "Ultrafast carrier thermalization in lead iodide perovskite probed with two-dimensional electronic spectroscopy"; Nature communications **8**, p. 376 (2017). Cited page 12

[58] J. Fu, Q. Xu, G. Han, B. Wu, C. H. A. Huan, M. L. Leek & T. C. Sum; "Hot carrier cooling mechanisms in halide perovskites"; Nature communications **8**, p. 1300 (2017). Cited page 12

[59] P. Piatkowski, B. Cohen, F. J. Ramos, M. Di Nunzio, M. K. Nazeeruddin, M. Grätzel, S. Ahmad & A. Douhal; "Direct monitoring of ultrafast electron and hole dynamics in perovskite solar cells"; Physical Chemistry Chemical Physics **17**, pp. 14674–14684 (2015). Cited page 12

[60] J. Yang, X. Wen, H. Xia, R. Sheng, Q. Ma, J. Kim, P. Tapping, T. Harada, T. W. Kee, F. Huang *et al.*; "Acoustic-optical phonon up-conversion and hot-phonon bottleneck in lead-halide perovskites"; Nature communications **8**, p. 14120 (2017). Cited page 12

[61] M. B. Price, J. Butkus, T. C. Jellicoe, A. Sadhanala, A. Briane, J. E. Halpert, K. Broch, J. M. Hodgkiss, R. H. Friend & F. Deschler; "Hot-carrier cooling and photoinduced refractive index changes in organic–inorganic lead halide perovskites"; Nature communications **6**, p. 8420 (2015). Cited page 12

[62] C. Javaux, B. Mahler, B. Dubertret, A. Shabaev, A. Rodina, A. L. Efros, D. Yakovlev, F. Liu, M. Bayer, G. Camps *et al.*; "Thermal activation of non-radiative Auger recombination in charged colloidal nanocrystals"; Nature nanotechnology **8**, pp. 206–212 (2013). Cited page 13

[63] L. N. Quan, F. P. García de Arquer, R. P. Sabatini & E. H. Sargent; "Perovskites for light emission"; Advanced Materials **30**, p. 1801996 (2018). Cited pages 13 and 14

[64] M. Kuno, D. Fromm, H. Hamann, A. Gallagher & D. Nesbitt; ""On"/"off" fluorescence intermittency of single semiconductor quantum dots"; The Journal of chemical physics **115**, pp. 1028–1040 (2001). Cited pages 13 and 97

[65] E. Barkai, Y. Jung & R. Silbey; "Theory of single-molecule spectroscopy: beyond the ensemble average"; Annu. Rev. Phys. Chem. **55**, pp. 457–507 (2004). Cited page 15

[66] W. Moerner; "Those blinking single molecules"; Science **277**, pp. 1059–1060 (1997). Cited page 15

[67] C. Bradac, T. Gaebel, N. Naidoo, M. Sellars, J. Twamley, L. Brown, A. Barnard, T. Plakhotnik, A. Zvyagin & J. Rabeau; "Observation and control of blinking nitrogen-vacancy centres in discrete nanodiamonds"; Nature nanotechnology **5**, pp. 345–349 (2010). Cited page 15

[68] E. Neu, M. Agio & C. Becher; "Photophysics of single silicon vacancy centers in diamond: implications for single photon emission"; Optics express **20**, pp. 19956–19971 (2012). Cited page 15

[69] A. L. Efros & D. J. Nesbitt; "Origin and control of blinking in quantum dots"; Nature nanotechnology **11**, pp. 661–671 (2016). Cited page 15

[70] P. Frantsuzov, M. Kuno, B. Janko & R. A. Marcus; "Universal emission intermittency in quantum dots, nanorods and nanowires"; Nature Physics **4**, pp. 519–522 (2008). Cited page 15

[71] M. A. Becker, R. Vaxenburg, G. Nedelcu, P. C. Sercel, A. Shabaev, M. J. Mehl, J. G. Michopoulos, S. G. Lambrakos, N. Bernstein, J. L. Lyons *et al.*; "Bright triplet excitons in caesium lead halide perovskites"; Nature **553**, pp. 189–193 (2018). Cited pages 15, 23, 24, and 97

[72] A. A. Cordones & S. R. Leone; "Mechanisms for charge trapping in single semiconductor nanocrystals probed by fluorescence blinking"; Chemical Society Reviews **42**, pp. 3209–3221 (2013). Cited pages 16 and 17

[73] S. Vezzoli; *Experimental study of nanocrystals as single photon sources*; Ph.D. thesis; Paris 6 (2013). Cited page 18

[74] M. Manceau; *Single CdSe/CdS dot-in-rods fluorescence properties*; Ph.D. thesis; Université Pierre et Marie Curie-Paris VI; Università del Salento (2014). Cited page 18

[75] Y.-S. Park, A. V. Malko, J. Vela, Y. Chen, Y. Ghosh, F. García-Santamaría, J. A. Hollingsworth, V. I. Klimov & H. Htoon; "Near-unity quantum yields of biexciton emission from CdSe/CdS nanocrystals measured using single-particle spectroscopy"; Physical review letters **106**, p. 187401 (2011). Cited page 19

[76] K. Chen, S. Schünemann, S. Song & H. Tüysüz; "Structural effects on optoelectronic properties of halide perovskites"; Chemical Society Reviews **47**, pp. 7045–7077 (2018). Cited page 21

[77] V. M. Goldschmidt; "Die gesetze der krystallochemie"; Naturwissenschaften **14**, pp. 477–485 (1926). Cited page 21

[78] J. Even, L. Pedesseau, J.-M. Jancu & C. Katan; "Importance of spin–orbit coupling in hybrid organic/inorganic perovskites for photovoltaic applications"; The Journal of Physical Chemistry Letters **4**, pp. 2999–3005 (2013). Cited page 23

[79] A. Amat, E. Mosconi, E. Ronca, C. Quarti, P. Umari, M. K. Nazeeruddin, M. Gratzel & F. De Angelis; "Cation-induced band-gap tuning in organohalide perovskites: interplay of spin–orbit coupling and octahedra tilting"; Nano letters **14**, pp. 3608–3616 (2014). Cited page 23

[80] H. Huang, M. I. Bodnarchuk, S. V. Kershaw, M. V. Kovalenko & A. L. Rogach; "Lead halide perovskite nanocrystals in the research spotlight: stability and defect tolerance"; ACS energy letters **2**, pp. 2071–2083 (2017). Cited pages 23, 24, and 94

[81] M. V. Kovalenko, L. Protesescu & M. I. Bodnarchuk; "Properties and potential optoelectronic applications of lead halide perovskite nanocrystals"; Science **358**, pp. 745–750 (2017). Cited page 23

[82] Q. A. Akkerman, G. Rainò, M. V. Kovalenko & L. Manna; "Genesis, challenges and opportunities for colloidal lead halide perovskite nanocrystals"; Nature materials **17**, pp. 394–405 (2018). Cited pages 23 and 30

[83] J. Kang & L.-W. Wang; "High defect tolerance in lead halide perovskite CsPbBr3"; The journal of physical chemistry letters **8**, pp. 489–493 (2017). Cited page 23

[84] J. Butkus, P. Vashishtha, K. Chen, J. K. Gallaher, S. K. Prasad, D. Z. Metin, G. Laufersky, N. Gaston, J. E. Halpert & J. M. Hodgkiss; "The evolution of quantum confinement in CsPbBr3 perovskite nanocrystals"; Chemistry of Materials **29**, pp. 3644–3652 (2017). Cited page 26

[85] B. Zhang, L. Goldoni, C. Lambruschini, L. Moni, M. Imran, A. Pianetti, V. Pinchetti, S. Brovelli, L. De Trizio & L. Manna; "Stable and size tunable CsPbBr3 nanocrystals synthesized with oleylphosphonic acid"; Nano letters **20**, pp. 8847–8853 (2020). Cited pages 29 and 88

[86] F. Krieg, S. T. Ochsenbein, S. Yakunin, S. Ten Brinck, P. Aellen, A. Süess, B. Clerc, D. Guggisberg, O. Nazarenko, Y. Shynkarenko *et al.*; "Colloidal CsPbX3 (X= Cl, Br, I) nanocrystals 2.0: Zwitterionic

capping ligands for improved durability and stability"; ACS energy letters **3**, pp. 641–646 (2018). Not cited.

[87] F. Krieg, Q. K. Ong, M. Burian, G. Rainò, D. Naumenko, H. Amenitsch, A. Süess, M. J. Grotevent, F. Krumeich, M. I. Bodnarchuk *et al.*; "Stable ultraconcentrated and ultradilute colloids of CsPbX3 (X= Cl, Br) nanocrystals using natural lecithin as a capping ligand"; Journal of the American Chemical Society **141**, pp. 19839–19849 (2019). Cited page 92

[88] A. Swarnkar, R. Chulliyil, V. K. Ravi, M. Irfanullah, A. Chowdhury & A. Nag; "Colloidal CsPbBr3 perovskite nanocrystals: luminescence beyond traditional quantum dots"; Angewandte Chemie **127**, pp. 15644–15648 (2015). Cited pages 29 and 88

[89] M. N. An, S. Park, R. Brescia, M. Lutfullin, L. Sinatra, O. M. Bakr, L. De Trizio & L. Manna; "Low-temperature molten salts synthesis: CsPbBr3 nanocrystals with high photoluminescence emission buried in mesoporous SiO2"; ACS Energy Letters **6**, pp. 900–907 (2021). Cited pages 29 and 88

[90] M. Palei, M. Imran, G. Biffi, L. Manna, F. Di Stasio & R. Krahne; "Robustness to high temperatures of Al2O3-coated CsPbBr3 nanocrystal thin films with high-photoluminescence quantum yield for light emission"; ACS Applied Nano Materials **3**, pp. 8167–8175 (2020). Not cited.

[91] A. Loiudice, M. Strach, S. Saris, D. Chernyshov & R. Buonsanti; "Universal oxide shell growth enables in situ structural studies of perovskite nanocrystals during the anion exchange reaction"; Journal of the American Chemical Society **141**, pp. 8254–8263 (2019). Cited pages 29 and 88

[92] S. N. Raja, Y. Bekenstein, M. A. Koc, S. Fischer, D. Zhang, L. Lin, R. O. Ritchie, P. Yang & A. P. Alivisatos; "Encapsulation of perovskite nanocrystals into macroscale polymer matrices: enhanced stability and polarization"; ACS applied materials & interfaces **8**, pp. 35523–35533 (2016). Cited pages 29, 88, and 94

[93] R. An, F. Zhang, X. Zou, Y. Tang, M. Liang, I. Oshchapovskyy, Y. Liu, A. Honarfar, Y. Zhong, C. Li *et al.*; "Photostability and photodegradation processes in colloidal CsPbI3 perovskite quantum dots"; ACS applied materials & interfaces **10**, pp. 39222–39227 (2018). Cited pages 30, 80, and 94

[94] M. C. Weidman, M. Seitz, S. D. Stranks & W. A. Tisdale; "Highly tunable colloidal perovskite nanoplatelets through variable cation, metal, and halide composition"; ACS nano **10**, pp. 7830–7839 (2016). Cited page 54

[95] K. A. Elmestekawy, A. D. Wright, K. B. Lohmann, J. Borchert, M. B. Johnston & L. M. Herz; "Controlling intrinsic quantum confinement in formamidinium lead triiodide perovskite through Cs substitution"; ACS nano **16**, pp. 9640–9650 (2022). Cited page 57

[96] H. Chen, J. Lin, J. Kang, Q. Kong, D. Lu, J. Kang, M. Lai, L. N. Quan, Z. Lin, J. Jin *et al.*; "Structural and spectral dynamics of single-crystalline Ruddlesden-Popper phase halide perovskite blue light-emitting diodes"; Science advances **6**, p. eaay4045 (2020). Cited page 57

[97] L. Ni, U. Huynh, A. Cheminal, T. H. Thomas, R. Shivanna, T. F. Hinrichsen, S. Ahmad, A. Sadhanala & A. Rao; "Real-time observation of exciton–phonon coupling dynamics in self-assembled hybrid perovskite quantum wells"; ACS nano **11**, pp. 10834–10843 (2017). Cited page 57

[98] S. Masada, T. Yamada, H. Tahara, H. Hirori, M. Saruyama, T. Kawawaki, R. Sato, T. Teranishi & Y. Kanemitsu; "Effect of A-site cation on photoluminescence spectra of single lead bromide perovskite nanocrystals"; Nano Letters **20**, pp. 4022–4028 (2020). Not cited.

[99] G. Rainò, N. Yazdani, S. C. Boehme, M. Kober-Czerny, C. Zhu, F. Krieg, M. D. Rossell, R. Erni, V. Wood, I. Infante *et al.*; "Ultra-narrow room-temperature emission from single CsPbBr3 perovskite quantum dots"; Nature communications **13**, p. 2587 (2022). Cited page 57

[100] A. D. Wright, C. Verdi, R. L. Milot, G. E. Eperon, M. A. Pérez-Osorio, H. J. Snaith, F. Giustino, M. B. Johnston & L. M.

Herz; "Electron–phonon coupling in hybrid lead halide perovskites"; Nature communications **7**, p. 11755 (2016). Cited page 57

[101] H. P. Adl, S. Gorji, G. Munoz-Matutano, R. I. Sánchez-Alarcón, R. Abargues, A. F. Gualdrón-Reyes, I. Mora-Sero & J. P. Martinez-Pastor; "Homogeneous and inhomogeneous broadening in single perovskite nanocrystals investigated by micro-photoluminescence"; Journal of Luminescence **240**, p. 118453 (2021). Cited page 57

[102] H. Utzat, K. E. Shulenberger, O. B. Achorn, M. Nasilowski, T. S. Sinclair & M. G. Bawendi; "Probing linewidths and biexciton quantum yields of single cesium lead halide nanocrystals in solution"; Nano Letters **17**, pp. 6838–6846 (2017). Cited page 57

[103] V. Chandrasekaran, M. D. Tessier, D. Dupont, P. Geiregat, Z. Hens & E. Brainis; "Nearly blinking-free, high-purity single-photon emission by colloidal InP/ZnSe quantum dots"; Nano Letters **17**, pp. 6104–6109 (2017). Cited page 59

[104] X. Lin, X. Dai, C. Pu, Y. Deng, Y. Niu, L. Tong, W. Fang, Y. Jin & X. Peng; "Electrically-driven single-photon sources based on colloidal quantum dots with near-optimal antibunching at room temperature"; Nature Communications **8**, p. 1132 (2017). Not cited.

[105] B.-W. Hsu, Y.-T. Chuang, C.-Y. Cheng, C.-Y. Chen, Y.-J. Chen, A. Brumberg, L. Yang, Y.-S. Huang, R. D. Schaller, L.-J. Chen *et al.*; "Very Robust Spray-Synthesized CsPbI3 Quantum Emitters with Ultrahigh Room-Temperature Cavity-Free Brightness and Self-Healing Ability"; ACS nano **15**, pp. 11358–11368 (2021). Cited page 59

[106] C. T. Trinh, D. N. Minh, K. J. Ahn, Y. Kang & K.-G. Lee; "Verification of Type-A and Type-B-HC Blinking Mechanisms of Organic–Inorganic Formamidinium Lead Halide Perovskite Quantum Dots by FLID Measurements"; Scientific Reports **10**, p. 2172 (2020). Cited page 60

[107] P. Tamarat, M. I. Bodnarchuk, J.-B. Trebbia, R. Erni, M. V. Kovalenko, J. Even & B. Lounis; "The ground exciton state of

formamidinium lead bromide perovskite nanocrystals is a singlet dark state"; Nature Materials **18**, pp. 717–724 (2019). Cited page 62

[108] C. Galland, Y. Ghosh, A. Steinbrück, M. Sykora, J. A. Hollingsworth, V. I. Klimov & H. Htoon; "Two types of luminescence blinking revealed by spectroelectrochemistry of single quantum dots"; Nature **479**, pp. 203–207 (2011). Cited pages 63, 81, 97, and 100

[109] G. Rainò, A. Landuyt, F. Krieg, C. Bernasconi, S. T. Ochsenbein, D. N. Dirin, M. I. Bodnarchuk & M. V. Kovalenko; "Underestimated effect of a polymer matrix on the light emission of single CsPbBr3 nanocrystals"; Nano letters **19**, pp. 3648–3653 (2019). Cited pages 65 and 94

[110] J. De Roo, M. Ibáñez, P. Geiregat, G. Nedelcu, W. Walravens, J. Maes, J. C. Martins, I. Van Driessche, M. V. Kovalenko & Z. Hens; "Highly dynamic ligand binding and light absorption coefficient of cesium lead bromide perovskite nanocrystals"; ACS nano **10**, pp. 2071–2081 (2016). Cited page 67

[111] G. Grosso, H. Moon, B. Lienhard, S. Ali, D. K. Efetov, M. M. Furchi, P. Jarillo-Herrero, M. J. Ford, I. Aharonovich & D. Englund; "Tunable and high-purity room temperature single-photon emission from atomic defects in hexagonal boron nitride"; Nature communications **8**, pp. 1–8 (2017). Cited page 70

[112] G. Noh, D. Choi, J.-H. Kim, D.-G. Im, Y.-H. Kim, H. Seo & J. Lee; "Stark tuning of single-photon emitters in hexagonal boron nitride"; Nano letters **18**, pp. 4710–4715 (2018). Not cited.

[113] R. M. Stevenson, R. J. Young, P. Atkinson, K. Cooper, D. A. Ritchie & A. J. Shields; "A semiconductor source of triggered entangled photon pairs"; Nature **439**, pp. 179–182 (2006). Cited page 70

[114] J. Wang, Y. Zhou, Z. Wang, A. Rasmita, J. Yang, X. Li, H. J. von Bardeleben & W. Gao; "Bright room temperature single photon source at telecom range in cubic silicon carbide"; Nature communications **9**, p. 4106 (2018). Cited page 70

[115] B. Somogyi, V. Zólyomi & A. Gali; "Near-infrared luminescent cubic silicon carbide nanocrystals for in vivo biomarker applications: an ab initio study"; Nanoscale **4**, pp. 7720–7726 (2012). Cited pages 70 and 136

[116] H.-K. Lo, M. Curty & K. Tamaki; "Secure quantum key distribution"; Nature Photonics **8**, pp. 595–604 (2014). Cited page 70

[117] C. L. Degen, F. Reinhard & P. Cappellaro; "Quantum sensing"; Reviews of modern physics **89**, p. 035002 (2017). Not cited.

[118] P. Lombardi, M. Trapuzzano, M. Colautti, G. Margheri, I. P. Degiovanni, M. López, S. Kück & C. Toninelli; "A molecule-based single-photon source applied in quantum radiometry"; Advanced Quantum Technologies **3**, p. 1900083 (2020). Cited page 70

[119] A. Musiał, P. Holewa, P. Wyborski, M. Syperek, A. Kors, J. P. Reithmaier, G. Sęk & M. Benyoucef; "High-purity triggered single-photon emission from symmetric single InAs/InP quantum dots around the telecom C-band window"; Advanced Quantum Technologies **3**, p. 1900082 (2020). Cited page 71

[120] H. Wang, Y.-M. He, T.-H. Chung, H. Hu, Y. Yu, S. Chen, X. Ding, M.-C. Chen, J. Qin, X. Yang *et al.*; "Towards optimal single-photon sources from polarized microcavities"; Nature Photonics **13**, pp. 770–775 (2019). Not cited.

[121] K. Rivoire, S. Buckley, A. Majumdar, H. Kim, P. Petroff & J. Vučković; "Fast quantum dot single photon source triggered at telecommunications wavelength"; Applied Physics Letters **98** (2011). Cited page 71

[122] H. Yoshimura, M. Yamauchi & S. Masuo; "In situ observation of emission behavior during anion-exchange reaction of a cesium lead halide perovskite nanocrystal at the single-nanocrystal level"; The Journal of Physical Chemistry Letters **11**, pp. 530–535 (2019). Cited page 71

[123] D. Chen, X. Chen, Z. Wan & G. Fang; "Full-Spectral Fine-Tuning Visible Emissions from Cation Hybrid Cs1–m FA m PbX3 (X= Cl, Br, and I, 0 m 1)

Quantum Dots"; ACS Applied Materials & Interfaces **9**, pp. 20671–20678 (2017). Cited page 71

[124] A. J. Knight, J. Borchert, R. D. Oliver, J. B. Patel, P. G. Radaelli, H. J. Snaith, M. B. Johnston & L. M. Herz; "Halide segregation in mixed-halide perovskites: influence of A-site cations"; ACS Energy Letters **6**, pp. 799–808 (2021). Cited page 71

[125] B. Conings, J. Drijkoningen, N. Gauquelin, A. Babayigit, J. D'Haen, L. D'Olieslaeger, A. Ethirajan, J. Verbeeck, J. Manca, E. Mosconi *et al.*; "Intrinsic thermal instability of methylammonium lead trihalide perovskite"; Advanced Energy Materials **5**, p. 1500477 (2015). Cited page 71

[126] L. Protesescu, S. Yakunin, S. Kumar, J. Bär, F. Bertolotti, N. Masciocchi, A. Guagliardi, M. Grotevent, I. Shorubalko, M. I. Bodnarchuk *et al.*; "Dismantling the "red wall" of colloidal perovskites: highly luminescent formamidinium and formamidinium–cesium lead iodide nanocrystals"; ACS nano **11**, pp. 3119–3134 (2017). Cited pages 71 and 72

[127] A. Hazarika, Q. Zhao, E. A. Gaulding, J. A. Christians, B. Dou, A. R. Marshall, T. Moot, J. J. Berry, J. C. Johnson & J. M. Luther; "Perovskite quantum dot photovoltaic materials beyond the reach of thin films: full-range tuning of A-site cation composition"; Acs Nano **12**, pp. 10327–10337 (2018). Cited page 72

[128] Y.-W. Zhang, G. Wu, H. Dang, K. Ma & S. Chen; "Multicolored Mixed-Organic-Cation Perovskite Quantum Dots (FA x MA1 − x PbX3, X= Br and I) for White Light-Emitting Diodes"; Industrial & Engineering Chemistry Research **56**, pp. 10053–10059 (2017). Not cited.

[129] M. Hao, Y. Bai, S. Zeiske, L. Ren, J. Liu, Y. Yuan, N. Zarrabi, N. Cheng, M. Ghasemi, P. Chen *et al.*; "Ligand-assisted cation-exchange engineering for high-efficiency colloidal Cs1 − x FA x PbI3 quantum dot solar cells with reduced phase segregation"; Nature Energy **5**, pp. 79–88 (2020). Cited page 72

[130] A. Perumal, S. Shendre, M. Li, Y. K. E. Tay, V. K. Sharma, S. Chen, Z. Wei, Q. Liu, Y. Gao, P. J. S. Buenconsejo *et al.*; "High brightness

formamidinium lead bromide perovskite nanocrystal light emitting devices"; Scientific Reports **6**, p. 36733 (2016). Cited page 73

[131] D. Zhang, Y. Yang, Y. Bekenstein, Y. Yu, N. A. Gibson, A. B. Wong, S. W. Eaton, N. Kornienko, Q. Kong, M. Lai *et al.*; "Synthesis of composition tunable and highly luminescent cesium lead halide nanowires through anion-exchange reactions"; Journal of the American Chemical Society **138**, pp. 7236–7239 (2016). Cited page 75

[132] H. S. Jung & N.-G. Park; "Perovskite solar cells: from materials to devices"; small **11**, pp. 10–25 (2015). Cited page 75

[133] L. Protesescu, S. Yakunin, M. I. Bodnarchuk, F. Bertolotti, N. Masciocchi, A. Guagliardi & M. V. Kovalenko; "Monodisperse formamidinium lead bromide nanocrystals with bright and stable green photoluminescence"; Journal of the American Chemical Society **138**, pp. 14202–14205 (2016). Cited page 76

[134] Z. Ahmad, M. A. Najeeb, R. Shakoor, A. Alashraf, S. A. Al-Muhtaseb, A. Soliman & M. Nazeeruddin; "Instability in CH3NH3PbI3 perovskite solar cells due to elemental migration and chemical composition changes"; Scientific reports **7**, p. 15406 (2017). Cited page 80

[135] L. Ding, S. Liu, Z. Zhang, G. Shao, W. Xiang & X. Liang; "Stable Zn-doped CsPbBr3 NCs glasses toward an enhanced optical performance for WLED"; Ceramics International **45**, pp. 22699–22706 (2019). Cited pages 88 and 89

[136] C. Bi, X. Sun, X. Huang, S. Wang, J. Yuan, J. X. Wang, T. Pullerits & J. Tian; "Stable CsPb1–x Zn x I3 Colloidal Quantum Dots with Ultralow Density of Trap States for High-Performance Solar Cells"; Chemistry of Materials **32**, pp. 6105–6113 (2020). Cited page 88

[137] S. Thapa, G. C. Adhikari, H. Zhu, A. Grigoriev & P. Zhu; "Zn-alloyed all-inorganic halide perovskite-based white light-emitting diodes with superior color quality"; Scientific Reports **9**, pp. 1–10 (2019). Cited page 89

[138] A. Kooijman, L. A. Muscarella & R. M. Williams; "Perovskite thin film materials stabilized and enhanced by zinc (II) doping"; Applied Sciences **9**, p. 1678 (2019). Cited page 89

[139] M. Pols, T. Hilpert, I. A. Filot, A. C. Van Duin, S. Calero & S. Tao; "What Happens at Surfaces and Grain Boundaries of Halide Perovskites: Insights from Reactive Molecular Dynamics Simulations of CsPbI3"; ACS Applied Materials & Interfaces **14**, pp. 40841–40850 (2022). Cited page 89

[140] X. Shen, Y. Zhang, S. V. Kershaw, T. Li, C. Wang, X. Zhang, W. Wang, D. Li, Y. Wang, M. Lu *et al.*; "Zn-alloyed CsPbI3 nanocrystals for highly efficient perovskite light-emitting devices"; Nano letters **19**, pp. 1552–1559 (2019). Cited page 89

[141] V. K. Ravi, S. Saikia, S. Yadav, V. V. Nawale & A. Nag; "CsPbBr3/ZnS core/shell type nanocrystals for enhancing luminescence lifetime and water stability"; ACS Energy Letters **5**, pp. 1794–1796 (2020). Cited page 89

[142] A. Swarnkar, W. J. Mir & A. Nag; "Can B-site doping or alloying improve thermal-and phase-stability of all-inorganic CsPbX3 (X= Cl, Br, I) perovskites?" ACS Energy Letters **3**, pp. 286–289 (2018). Cited page 90

[143] C. Bi, S. Wang, Q. Li, S. V. Kershaw, J. Tian & A. L. Rogach; "Thermally stable copper (II)-doped cesium lead halide perovskite quantum dots with strong blue emission"; The journal of physical chemistry letters **10**, pp. 943–952 (2019). Not cited.

[144] N. Mondal, A. De & A. Samanta; "Achieving near-unity photoluminescence efficiency for blue-violet-emitting perovskite nanocrystals"; ACS Energy Letters **4**, pp. 32–39 (2018). Not cited.

[145] S. Zhou, Y. Ma, G. Zhou, X. Xu, M. Qin, Y. Li, Y.-J. Hsu, H. Hu, G. Li, N. Zhao *et al.*; "Ag-doped halide perovskite nanocrystals for tunable band structure and efficient charge transport"; ACS Energy Letters **4**, pp. 534–541 (2019). Cited page 90

[146] Y. J. Bae, N. A. Gibson, T. X. Ding, A. P. Alivisatos & S. R. Leone; "Understanding the Bias Introduced in Quantum Dot Blinking Using Change

Point Analysis"; The Journal of Physical Chemistry C **120**, pp. 29484–29490 (2016). Cited page 97

[147] M. Manceau, S. Vezzoli, Q. Glorieux, F. Pisanello, E. Giacobino, L. Carbone, M. De Vittorio & A. Bramati; "Effect of charging on CdSe/CdS dot-in-rods single-photon emission"; Physical Review B **90**, p. 035311 (2014). Cited page 97

[148] M. Manceau, S. Vezzoli, Q. Glorieux, E. Giacobino, L. Carbone, M. De Vittorio, J.-P. Hermier & A. Bramati; "CdSe/CdS Dot-in-Rods Nanocrystals Fast Blinking Dynamics." ChemPhysChem **19**, pp. 3288–3295 (2018). Cited page 97

[149] G. Messin, J.-P. Hermier, E. Giacobino, P. Desbiolles & M. Dahan; "Bunching and antibunching in the fluorescence of semiconductor nanocrystals"; Optics Letters **26**, pp. 1891–1893 (2001). Cited page 98

[150] N. Fiuza-Maneiro, K. Sun, I. López-Fernández, S. Gòmez-Granña, P. Müller-Buschbaum & L. Polavarapu; "Ligand Chemistry of Inorganic Lead Halide Perovskite Nanocrystals"; ACS Energy Letters **8**, pp. 1152–1191 (2023). Cited page 102

[151] W. J. Mir, A. Alamoudi, J. Yin, K. E. Yorov, P. Maity, R. Naphade, B. Shao, J. Wang, M. N. Lintangpradipto, S. Nematulloev *et al.*; "Lecithin capping ligands enable ultrastable perovskite-phase CsPbI3 quantum dots for Rec. 2020 bright-red light-emitting diodes"; Journal of the American Chemical Society **144**, pp. 13302–13310 (2022). Cited page 102

[152] W. Yin, M. Li, W. Dong, Z. Luo, Y. Li, J. Qian, J. Zhang, W. Zhang, Y. Zhang, S. V. Kershaw *et al.*; "Multidentate ligand polyethylenimine enables bright color-saturated blue light-emitting diodes based on CsPbBr3 nanoplatelets"; ACS Energy Letters **6**, pp. 477–484 (2021). Cited page 102

[153] J. Shamsi, D. Kubicki, M. Anaya, Y. Liu, K. Ji, K. Frohna, C. P. Grey, R. H. Friend & S. D. Stranks; "Stable hexylphosphonate-capped blue-emitting quantum-confined CsPbBr3 nanoplatelets"; ACS Energy Letters **5**, pp. 1900–1907 (2020). Cited page 103

[154] A. E. Kaplan, C. J. Krajewska, A. H. Proppe, W. Sun, T. Sverko, D. B. Berkinsky, H. Utzat & M. G. Bawendi; "Hong–Ou–Mandel interference in colloidal CsPbBr3 perovskite nanocrystals"; Nature Photonics pp. 1–6 (2023). Cited page 104

[155] H. J. Kimble; "The quantum internet"; Nature **453**, pp. 1023–1030 (2008). Cited page 106

[156] L. Tong, R. R. Gattass, J. B. Ashcom, S. He, J. Lou, M. Shen, I. Maxwell & E. Mazur; "Subwavelength-diameter silica wires for low-loss optical wave guiding"; Nature **426**, pp. 816–819 (2003). Cited pages 107 and 115

[157] L. Tong, J. Lou, Z. Ye, G. T. Svacha & E. Mazur; "Self-modulated taper drawing of silica nanowires"; Nanotechnology **16**, p. 1445 (2005). Cited page 107

[158] S. A. Harfenist, S. D. Cambron, E. W. Nelson, S. M. Berry, A. W. Isham, M. M. Crain, K. M. Walsh, R. S. Keynton & R. W. Cohn; "Direct drawing of suspended filamentary micro-and nanostructures from liquid polymers"; Nano Letters **4**, pp. 1931–1937 (2004). Cited page 107

[159] X. Xing, Y. Wang & B. Li; "Nanofiber drawing and nanodevice assembly in poly (trimethylene terephthalate)"; Optics express **16**, pp. 10815–10822 (2008). Cited page 107

[160] J. Hoffman, S. Ravets, J. Grover, P. Solano, P. Kordell, J. Wong-Campos, L. Orozco & S. Rolston; "Ultrahigh transmission optical nanofibers"; AIP advances **4** (2014). Cited page 107

[161] J. Ward, A. Maimaiti, V. H. Le & S. Chormaic; "Contributed Review: Optical micro-and nanofiber pulling rig"; Review of Scientific Instruments **85** (2014). Cited page 107

[162] G. Brambilla; "Optical fibre nanowires and microwires: a review"; Journal of Optics **12**, p. 043001 (2010). Cited page 108

[163] F. Le Kien, V. Balykin & K. Hakuta; "Atom trap and waveguide using a two-color evanescent light field around a subwavelength-diameter optical fiber"; Physical Review A **70**, p. 063403 (2004). Cited page 108

[164] F. Le Kien, V. I. Balykin & K. Hakuta; "State-insensitive trapping and guiding of cesium atoms using a two-color evanescent field around a subwavelength-diameter fiber"; Journal of the Physical Society of Japan **74**, pp. 910–917 (2005). Cited page 108

[165] F. Le Kien, S. D. Gupta, V. Balykin & K. Hakuta; "Spontaneous emission of a cesium atom near a nanofiber: Efficient coupling of light to guided modes"; Physical Review A **72**, p. 032509 (2005). Cited page 108

[166] F. Le Kien, V. Balykin & K. Hakuta; "Scattering of an evanescent light field by a single cesium atom near a nanofiber"; Physical Review A **73**, p. 013819 (2006). Cited page 108

[167] G. Sagué, E. Vetsch, W. Alt, D. Meschede & A. Rauschenbeutel; "Cold-atom physics using ultrathin optical fibers: Light-induced dipole forces and surface interactions"; Physical review letters **99**, p. 163602 (2007). Cited page 108

[168] K. Nayak, P. Melentiev, M. Morinaga, F. Le Kien, V. Balykin & K. Hakuta; "Optical nanofiber as an efficient tool for manipulating and probing atomic fluorescence"; Optics express **15**, pp. 5431–5438 (2007). Cited page 108

[169] K. P. Nayak & K. Hakuta; "Single atoms on an optical nanofibre"; New Journal of Physics **10**, p. 053003 (2008). Cited page 108

[170] K. Nayak, F. Le Kien, M. Morinaga & K. Hakuta; "Antibunching and bunching of photons in resonance fluorescence from a few atoms into guided modes of an optical nanofiber"; Physical Review A **79**, p. 021801 (2009). Cited page 108

[171] M. Fujiwara, K. Toubaru, T. Noda, H.-Q. Zhao & S. Takeuchi; "Highly efficient coupling of photons from nanoemitters into single-mode optical fibers"; Nano letters **11**, pp. 4362–4365 (2011). Cited page 108

[172] R. Yalla, F. Le Kien, M. Morinaga & K. Hakuta; "Efficient channeling of fluorescence photons from single quantum dots into guided modes of optical nanofiber"; Physical review letters **109**, p. 063602 (2012). Cited page 108

[173] T. Schröder, M. Fujiwara, T. Noda, H.-Q. Zhao, O. Benson & S. Takeuchi; "A nanodiamond-tapered fiber system with high single-mode coupling efficiency"; Optics express **20**, pp. 10490–10497 (2012). Cited page 108

[174] L. Liebermeister, F. Petersen, A. v. Münchow, D. Burchardt, J. Hermelbracht, T. Tashima, A. W. Schell, O. Benson, T. Meinhardt, A. Krueger *et al.*; "Tapered fiber coupling of single photons emitted by a deterministically positioned single nitrogen vacancy center"; Applied Physics Letters **104** (2014). Cited page 108

[175] M. Pöllinger, D. O'Shea, F. Warken & A. Rauschenbeutel; "Ultrahigh-Q tunable whispering-gallery-mode microresonator"; Physical review letters **103**, p. 053901 (2009). Cited page 108

[176] S. Spillane, G. Pati, K. Salit, M. Hall, P. Kumar, R. Beausoleil & M. Shahriar; "Observation of nonlinear optical interactions of ultralow levels of light in a tapered optical nanofiber embedded in a hot rubidium vapor"; Physical review letters **100**, p. 233602 (2008). Cited page 108

[177] S. Hendrickson, T. Pittman & J. Franson; "Nonlinear transmission through a tapered fiber in rubidium vapor"; JOSA B **26**, pp. 267–271 (2009). Cited page 108

[178] P. Lodahl, S. Mahmoodian, S. Stobbe, A. Rauschenbeutel, P. Schneeweiss, J. Volz, H. Pichler & P. Zoller; "Chiral quantum optics"; Nature **541**, pp. 473–480 (2017). Cited page 108

[179] M. Sadgrove, M. Sugawara, Y. Mitsumori & K. Edamatsu; "Polarization response and scaling law of chirality for a nanofibre optical interface"; Scientific reports **7**, p. 17085 (2017). Cited page 108

[180] A. Yariv; *Optical electronics* (Saunders College Publishing) (1991). Cited pages 109 and 110

[181] A. W. Snyder, J. D. Love *et al.*; *Optical waveguide theory*; volume 175 (Chapman and hall London) (1983). Cited pages 109, 114, and 115

[182] G. Sagué Cassany; *Cold atom physics using ultra-thin optical fibres*; Ph.D. thesis; Bonn, Univ., Diss., 2008 (2008). Cited page 109

[183] E. Vetsch, D. Reitz, G. Sagué, R. Schmidt, S. Dawkins & A. Rauschenbeutel; "Optical interface created by laser-cooled atoms trapped in the evanescent field surrounding an optical nanofiber"; Physical review letters **104**, p. 203603 (2010). Cited page 109

[184] J. Hoffman; *Optical nanofiber fabrication and analysis towards coupling atoms to superconducting qubits*; Ph.D. thesis; University of Maryland, College Park (2014). Cited page 109

[185] T. A. Birks & Y. W. Li; "The shape of fiber tapers"; Journal of lightwave technology **10**, pp. 432–438 (1992). Cited page 114

[186] J. Love & W. Henry; "Quantifying loss minimisation in single-mode fibre tapers"; Electronics letters **17**, pp. 912–914 (1986). Cited page 115

[187] J. Love, W. Henry, W. Stewart, R. Black, S. Lacroix & F. Gonthier; "Tapered single-mode fibres and devices. Part 1: Adiabaticity criteria"; IEE Proceedings J (Optoelectronics) **138**, pp. 343–354 (1991). Cited page 115

[188] M. Fujiwara, K. Toubaru & S. Takeuchi; "Optical transmittance degradation in tapered fibers"; Optics express **19**, pp. 8596–8601 (2011). Cited page 115

[189] F. Warken; *Ultra thin glass fibers as a tool for coupling light and matter*; Ph.D. thesis; Ph. D. thesis, Rheinische Friedrich-Wilhelms Universitat, Mainz, Germany (2007). Cited page 118

[190] E. M. Purcell; "Spontaneous emission probabilities at radio frequencies"; in "Confined Electrons and Photons: New Physics and Applications," pp. 839–839 (Springer) (1995). Cited page 135

[191] H. Ditlbacher, A. Hohenau, D. Wagner, U. Kreibig, M. Rogers, F. Hofer, F. R. Aussenegg & J. R. Krenn; "Silver nanowires as surface plasmon resonators"; Physical review letters **95**, p. 257403 (2005). Cited page 136

[192] T. Kelf, Y. Sugawara, R. Cole, J. Baumberg, M. Abdelsalam, S. Cintra, S. Mahajan, A. Russell & P. Bartlett; "Localized and delocalized plasmons in metallic nanovoids"; Physical Review B **74**, p. 245415 (2006). Cited page 136

[193] N. Perney, F. G. De Abajo, J. Baumberg, A. Tang, M. Netti, M. Charlton & M. Zoorob; "Tuning localized plasmon cavities for optimized surface-enhanced Raman scattering"; Physical Review B **76**, p. 035426 (2007). Cited page 136

[194] T. B. Hoang, G. M. Akselrod & M. H. Mikkelsen; "Ultrafast room-temperature single photon emission from quantum dots coupled to plasmonic nanocavities"; Nano letters **16**, pp. 270–275 (2016). Cited page 136

[195] A. Kinkhabwala, Z. Yu, S. Fan, Y. Avlasevich, K. Müllen & W. Moerner; "Large single-molecule fluorescence enhancements produced by a bowtie nanoantenna"; Nature photonics **3**, pp. 654–657 (2009). Cited page 136

[196] C. Belacel, B. Habert, F. Bigourdan, F. Marquier, J.-P. Hugonin, S. Michaelis de Vasconcellos, X. Lafosse, L. Coolen, C. Schwob, C. Javaux *et al.*; "Controlling spontaneous emission with plasmonic optical patch antennas"; Nano letters **13**, pp. 1516–1521 (2013). Cited page 136

[197] A. G. Curto, G. Volpe, T. H. Taminiau, M. P. Kreuzer, R. Quidant & N. F. Van Hulst; "Unidirectional emission of a quantum dot coupled to a nanoantenna"; Science **329**, pp. 930–933 (2010). Cited pages 136 and 137

[198] L. Novotny & N. Van Hulst; "Antennas for light"; Nature photonics **5**, pp. 83–90 (2011). Cited page 136

[199] S. Schietinger, M. Barth, T. Aichele & O. Benson; "Plasmon-enhanced single photon emission from a nanoassembled metal- diamond hybrid structure at room temperature"; Nano letters **9**, pp. 1694–1698 (2009). Cited page 136

[200] S.-H. Gong, J.-H. Kim, Y.-H. Ko, C. Rodriguez, J. Shin, Y.-H. Lee, L. S. Dang, X. Zhang & Y.-H. Cho; "Self-aligned deterministic coupling of single quantum emitter to nanofocused plasmonic modes"; Proceedings of the National Academy of Sciences **112**, pp. 5280–5285 (2015). Cited page 136

[201] D. Ratchford, F. Shafiei, S. Kim, S. K. Gray & X. Li; "Manipulating coupling between a single semiconductor quantum dot and single gold nanoparticle"; Nano letters **11**, pp. 1049–1054 (2011). Cited page 137

[202] A. El Eter, N. M. Hameed, F. I. Baida, R. Salut, C. Filiatre, D. Nedeljkovic, E. Atie, S. Bole & T. Grosjean; "Fiber-integrated optical nano-tweezer based on a bowtie-aperture nano-antenna at the apex of a SNOM tip"; Optics express **22**, pp. 10072–10080 (2014). Cited page 137

[203] J. M. Ehtaiba & R. Gordon; "Template-stripped nanoaperture tweezer integrated with optical fiber"; Optics Express **26**, pp. 9607–9613 (2018). Cited page 137

[204] Y. Liu, F. Stief & M. Yu; "Subwavelength optical trapping with a fiber-based surface plasmonic lens"; Optics letters **38**, pp. 721–723 (2013). Cited page 137

[205] R. M. Gelfand, S. Wheaton & R. Gordon; "Cleaved fiber optic double nanohole optical tweezers for trapping nanoparticles"; Optics letters **39**, pp. 6415–6417 (2014). Cited page 137

[206] N. C. Lindquist, J. Jose, S. Cherukulappurath, X. Chen, T. W. Johnson & S.-H. Oh; "Tip-based plasmonics: squeezing light with metallic nanoprobes"; Laser & Photonics Reviews **7**, pp. 453–477 (2013). Cited page 137

[207] A. Khaleque, E. G. Mironov, J. H. Osório, Z. Li, C. M. Cordeiro, L. Liu, M. A. Franco, J.-L. Liow & H. T. Hattori; "Integration of bow-tie plasmonic nano-antennas on tapered fibers"; Optics express **25**, pp. 8986–8996 (2017). Cited page 137

[208] A. W. Schell, H. Takashima, S. Kamioka, Y. Oe, M. Fujiwara, O. Benson & S. Takeuchi; "Highly efficient coupling of nanolight emitters to a ultra-wide tunable nanofibre cavity"; Scientific reports **5**, p. 9619 (2015). Cited page 137

[209] H. Takashima, A. Fukuda, H. Maruya, T. Tashima, A. W. Schell & S. Takeuchi; "Fabrication of a nanofiber Bragg cavity with high quality

factor using a focused helium ion beam"; Optics Express **27**, pp. 6792–6800 (2019). Cited page 137

[210] M. Sugawara, Y. Xuan, Y. Mitsumori, K. Edamatsu & M. Sadgrove; "Plasmon-enhanced single photon source directly coupled to an optical fiber"; Physical Review Research **4**, p. 043146 (2022). Cited page 137

[211] R. K. TP, P. Weirich, L. Hrachowina, M. Hanefeld, R. Bjornsson, H. R. Hrodmarsson, S. Barth, D. H. Fairbrother, M. Huth & O. Ingólfsson; "Electron interactions with the heteronuclear carbonyl precursor H2FeRu3 (CO) 13 and comparison with HFeCo3 (CO) 12: from fundamental gas phase and surface science studies to focused electron beam induced deposition"; Beilstein Journal of Nanotechnology **9**, pp. 555–579 (2018). Cited page 139

[212] A. Sabouri, C. Anthony, J. Bowen, V. Vishnyakov & P. Prewett; "The effects of dwell time on focused ion beam machining of silicon"; Microelectronic engineering **121**, pp. 24–26 (2014). Cited page 142

[213] A. Botman, J. Mulders & C. Hagen; "Creating pure nanostructures from electron-beam-induced deposition using purification techniques: a technology perspective"; Nanotechnology **20**, p. 372001 (2009). Cited page 154

[214] J. T. Hugall, A. Singh & N. F. van Hulst; "Plasmonic cavity coupling"; Acs Photonics **5**, pp. 43–53 (2018). Cited page 157

[215] I. Rreza, H. Yang, L. Hamachi, M. Campos, T. Hull, J. Treadway, J. Kurtin, E. M. Chan & J. S. Owen; "Performance of Spherical Quantum Well Down Converters in Solid State Lighting"; ACS applied materials & interfaces **13**, pp. 12191–12197 (2021). Cited page 168

Marianna D'AMATO **13 Décembre 2023**

Sujet : Optimisation et couplage de nanocristaux de pérovskite avec des nanofibres optiques pour la réalisation de sources de photons uniques efficaces intégrées

Résumé : L'émission de photons uniques purs est essentielle pour plusieurs technologies quantiques, allant du calcule quantique optique à la cryptographie quantique. Parmi les émetteurs de photons uniques à l'état solide, les nanocristaux colloïdaux de pérovskite $CsPbX_3$ ont suscité une attention considérable en raison de leurs propriétés structurales et optiques. Cependant, leur application pratique a été entravée par l'instabilité de la photo-émission.induite par la diluition et l'excitation optique.

Dans cette thèse, j'ai exploré plusieurs stratégies pour éliminer ces instabilités tout en préservant une émission de photons uniques robuste. Ma recherche a porté sur l'étude de nanocristaux colloïdaux à cation mixte, du type $Cs_{1-x}FA_xPbBr_3$, afin de contrôler la longueur d'onde d'émission de photons uniques tout en améliorant la photo-stabilité par rapport aux perovskites conventionnelles à anion mixte, du type $CsPb(Br_xI_{1-x})_3$. Ensuite, j'ai approfondi l'étude des nanocristaux $CsPbBr_3$ dopés en ions Zn^{2+} au niveau du site Pb, démontrant une stabilité considérablement améliorée et en particulier une résistance accrue à la diluition et à l'excitation optique, ainsi qu'une forte réduction du clignotement, qui se produit dans ces émetteurs à une échelle de temps très courte (sub-milliseconde).

L'optimisation des propriétés photo-physiques de ces nanocristaux de pérovskite ouvre des perspectives prometteuses pour leur intégration dans des systèmes nanophotoniques conçus pour des applications quantiques. Dans mon travail, j'ai réalisé le premier couplage d'un nanocristal unique de pérovskite avec une nanofibre optique effilée, premier pas vers source compacte et intégrée de photons uniques à température ambiante. Pour améliorer l'efficacité d'un tel dispositif, j'ai exploré la fabrication de nanostructures plasmoniques directement sur la nanofibre, en utilisant une nouvelle technique basée sur le dépôt induit par faisceau d'électrons defocalisé. Je montre que cette méthode de fabrication permet un contrôle précis de la composition, de l'emplacement et de la forme des nanostructures.

Ces réalisations représentent des étapes prometteuses vers la réalisation d'un dispositif compact et hautement efficace de photons uniques intégrés.

Mots clés : Quantique, Optique, Single photon sources, Perovskites

Subject : Optimization and coupling of perovskite nanocrystals with optical nanofibers for efficient integrated single-photon sources

Abstract: Achieving pure single-photon emission is essential for various quantum technologies, from optical quantum computing to quantum key distribution. Among solid-state quantum emitters, colloidal lead halide perovskite nanocrystals have gained significant attention owing to their unique structural and optical properties, rendering them appealing single-photon sources. However, their practical application has been hampered by environment-induced photo-emission instabilities.

In this thesis, I explored several strategies to overcome these instabilities while preserving robust single-photon emission. My research involved the investigation of mixed-cations $Cs_{1-x}FA_xPbBr_3$ colloidal nanocrystals, aiming to fine-tune the single-photon emission while enhancing photo-stability compared to conventional mixed-halide systems, such as $CsPb(Br_xI_{1-x})_3$. Then, I delved into the study of Zn-treated $CsPbBr_3$ nanocrystals achieved through Zn^{2+} ion doping at the Pb-site, demonstrating significantly improved stability under dilution and illumination, as well as reduced blinking on a sub-millisecond timescale.

The optimization of the photophysical properties of such perovskite nanocrystals opens promising avenues for their integration into nanophotonic systems designed for quantum technology applications. In my work, I present the first coupling of a single perovskite NC with a tapered optical nanofiber, demonstrating the proof of concept for a compact, integrated single photon source. To enhance the efficiency of such device, I explored the fabrication of plasmonic nanostructures directly on the nanofiber, employing a novel technique based on defocused electron beam induced deposition. I show that this fabrication method enables precise control over the composition, the location, and the shape of the nanostructures.

These achievements are promising steps toward the realization of a compact and high-efficient integrated single photon device.

Keywords : Quantum, Optics, Single photon sources, Perovskites